

annual report
2010

I N S T I T U T L A U E - L A N G E V I N



SYNTHESE ECA - Tél. 04 76 90 02 73

I N S T I T U T L A U E - L A N G E V I N



annual report 2010

I N S T I T U T L A U E - L A N G E V I N





DIRECTOR'S FOREWORD	4
ABOUT THE ILL	6
SCIENTIFIC HIGHLIGHTS	8
MILLENNIUM PROGRAMME AND TECHNICAL DEVELOPMENTS	76
EXPERIMENTAL AND USER PROGRAMME	90
REACTOR OPERATION	100
MORE THAN SIMPLY NEUTRONS	104
WORKSHOPS AND EVENTS	110
ADMINISTRATIVE MATTERS	118

PUBLISHING INFORMATION

Editors: Giovanna Cicognani and Andrew Harrison

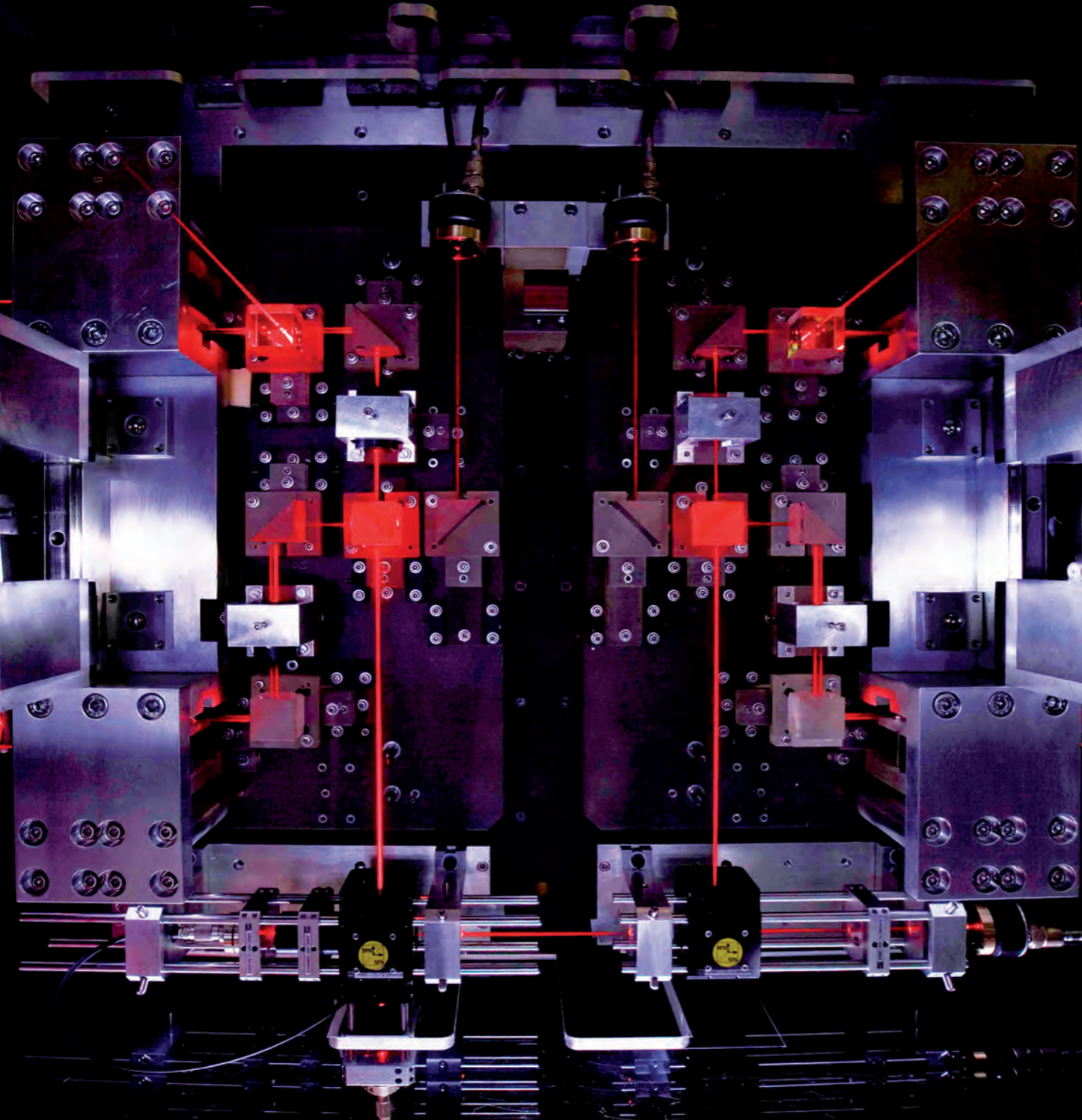
Production team: Giovanna Cicognani, Robert Corner and Susan Tinniswood

Design: www.synthese-eca.com – **Printing:** Imprimerie du Pont de Claix

Photography: by Bernard Lehn (Fotodesign, studio@bernhardlehn.de) – p.4, 8, 76, 90, 104, 110, 118 –,
by Alexis Chezière – p.102 – and by ILL.

Further copies can be obtained from Institut Laue-Langevin
Scientific Coordination Office (SCO)
BP 156 F-38042 Grenoble Cedex 9 (France)
Email: sco@ill.eu – web: www.ill.eu

We warmly thank everyone who contributed to the production of this report.



The high-resolution gamma-ray facility GAMS.

2010 was another eventful year for the ILL. It started off in excellent fashion with the successful replacement of the anti-turbulence grid in the core of the reactor. This was a huge relief to all concerned as it was this component which had caused a shutdown of the Institute's neutron source for almost four years in the early nineties. This has to be contrasted, however, by the news at the year's end of the Associates' decision to make cuts over the years to come in the Institute's budget, as the financial crisis took its toll in some of our Associate countries. It is true that the cuts were considerably less severe than those experienced by most of our six partner institutes in the European EIROforum, but they nevertheless forced Management into a programme of severe savings to balance the budget over the years to come.

The ILL2020 Vision Meeting generated a host of ideas for new and upgraded instruments and neutron infrastructure and represents an excellent step forward in our endeavour to structure the future of our Institute

But now back to the bright side... It is particularly pleasing to be able to report that the projects underway in the second phase of our modernisation programme (M-1) took huge steps forward in 2010 and are right on schedule, thanks to the continuous motivation and commitment of our staff. The ILL 7 guide hall was also successfully extended and the Reactor Division's particularly challenging gaseous decay tank installation brought to completion. The Associates and our Scientific Members did not fail to notice these achievements, and in their expressions of appreciation they also cited the Institute's highly attractive scientific programme, its unparalleled publication record and the

recurringly high demand for beamtime. There can be no doubt that our excellent track record has helped protect us from more severe cuts to our finances and sustains our hopes that our Associates' funding will return to its former level as soon as possible.

In September we organised a highly successful European user meeting, the ILL2020 Vision Meeting. The event generated a host of ideas for new and upgraded instruments and neutron infrastructure and represents an excellent step forward in our endeavour to structure the future of our Institute well into the next decade. This future now includes our eleventh Scientific Member, Poland, who joined us in July, and also India, who arrived as the Institute's twelfth - and first non-European! - Member in January 2011. We remain confident that our Associates and Scientific Members will continue to provide the support we need for the completion of the M-1 phase in 2014 and the subsequent launch of the Millennium Programme's third phase, the "M-2", despite the financial crisis the world is still experiencing.

2010 has therefore provided another year of remarkable achievements and great scientific results by the ILL. You will find quite a few of these in the Annual Report you are now reading. My warm thanks to our staff for their levels of motivation and commitment, their creativity and ingenuity, and for the excellent service they have consistently provided to ILL's broad and still growing user community over the year. They have again made a decisive contribution to the success and international visibility of our institute.

Richard Wagner
Director of the ILL

Richard Wagner



The Institut Laue-Langevin (ILL) is an international research centre at the leading edge of neutron science and technology, where neutrons are used to probe the microscopic structure and dynamics of a broad range of materials from the molecular, atomic and nuclear point of view.

The ILL is owned by three founding countries - France, Germany and United Kingdom. The three Associate member countries contributed a total of about 58 M€ to the Institute in 2010, a sum enhanced by significant contributions from the ILL's Scientific Member countries, Austria, Belgium, the Czech Republic, Denmark, Hungary, Italy, Poland, Spain, Slovakia, Sweden and Switzerland. ILL's overall budget in 2010 amounted to approximately 88 M€. From 1 January 2011, India has also joined the ILL, thus becoming the 12th Scientific Member country.

The Institute operates the most intense neutron source in the world, based on a single element 58.3 MW nuclear reactor designed for high brightness. The reactor functions 24 hours normally during 4 cycles of 50 days each per year, feeding neutrons to a suite of 40 high-performance instruments that are constantly upgraded.

As a service institute, the ILL makes its facilities and expertise available to visiting scientists. Our user community is world-wide: every year, about 2000 researchers

from more than 30 countries visit the ILL, to perform over 800 experiments, which have been selected by a scientific review committee.

The ILL monitors the papers published as a result of the use of our facilities. This gives a figure of more than 600 papers per year. We pay particular attention to papers published in high impact journals. About 80 such papers per year are published from data taken on ILL instruments which is a factor of two higher than the second most productive neutron source in the world.

The Institute has a Director and two Associate Directors, representing each of the Associate countries, appointed on short-term contracts normally of five years. A Scientific Council, comprising external scientists from the member countries, advises the Directors on scientific directions for the Institute, on the evolution of the instrument suite and technical infrastructure to best meet the needs of the user research programme, and to assess the scientific output of the Institute. Our governing body is the Steering Committee, which meets twice-yearly and is made up of representatives of the Associates and the Scientific Partners together with Directors and Staff Representatives. Within the framework of the International Convention, the Steering Committee has the ultimate responsibility for determining operational and investment strategies for the Institute.

Neutrons and society

The scope of the research carried out at the ILL is very broad, embracing condensed matter physics, chemistry, biology, materials and earth sciences, engineering, and nuclear and particle physics. Much of it impacts on many of the challenges facing society today, from sustainable sources of energy, improved healthcare and a cleaner environment to new materials for information and computing technology (see p.95).

For example, neutron-scattering experiments have given us new insights into the structure and behaviour of biological and soft condensed matter, important in designing better drug delivery systems or improving polymer processing. They also provide a unique probe of the phenomena that underpin high-temperature superconductivity or the molecular magnetism that may provide the technology on which the computers of the future are based.

Preparing for the future

In 2000, the ILL launched an ambitious modernisation programme of instruments and infrastructure called the ILL Millennium Programme whose aim was to optimise the ILL's instrument suite (Phase M-0: 2000-2007; Phase M-1: 2008-2014). We are now looking forward and setting the scene – in the framework of our ILL2020 Vision – for developments yet further into the future, maintaining the Institute's world-leading position for another 20 years.

WHY NEUTRON SCATTERING IS USEFUL

Neutron beams have the power, when used as a probe of small samples of materials, to reveal what is invisible using other radiations. Neutrons can appear to behave either as particles or as waves or as microscopic magnetic dipoles and it is these specific properties which enable them to uncover information which is often impossible to access using other techniques.

Wavelengths of tenths of nanometers

They have wavelengths varying from 0.01 to 100 nanometers, which makes them an ideal probe of atomic and molecular structures ranging from those consisting of single atomic species to complex biopolymers.

Energies of millielectronvolts

The associated energies of millielectronvolts are of the same magnitude as the diffusive motions of atoms and molecules in solids and liquids, the coherent waves in single crystals (phonons and magnons) and the vibrational modes in molecules.

An energy exchange between the incoming neutron and the sample of between 1 μ eV (even 1 neV with spin-echo) and 1 eV can readily be detected.

Microscopically magnetic

They possess a magnetic dipole moment which makes them sensitive to magnetic fields generated by unpaired electrons in materials. Precise details of the magnetic behaviour of materials at the atomic level can be investigated. In addition, the scattering power of a neutron by an atomic nucleus depends on the orientation of the spin of both the neutron and the atomic nuclei in a sample thereby providing a powerful tool to detect the nuclear spin order.

Electrically neutral

They are electrically neutral, so can penetrate deep into matter, while remaining non-destructive. This makes them an ideal probe for studying – for example

- biological samples or engineering components under extreme conditions of pressure, temperature, magnetic field or within chemical-reaction vessels.

High sensitivity and electivity

The variation of scattering power from nucleus to nucleus in a sample varies in a quasi-random manner even in different isotopes of the same atom. This means that light atoms are visible in the presence of heavy atoms and atoms neighbouring in the periodic table may be distinguished from each other. This introduces the possibility of using isotopic substitution (for example deuterium for hydrogen or one nickel isotope for another) to allow contrast to be varied in certain samples thereby highlighting specific structural features.

In addition, neutrons are particularly sensitive to hydrogen atoms and therefore they are a powerful probe of hydrogen storage materials, organic molecular materials, and biomolecular samples or polymers.



The horizontal-surface reflectometer FIGARO.

MAGNETISM
 CHEMISTRY AND CRYSTALLOGRAPHY
 MATERIALS
 SOFT MATTER
 LIQUIDS AND GLASSES
 BIOLOGY
 NUCLEAR AND PARTICLE PHYSICS
 MODELLING AND THEORY

Niels Bohr once stated 'Prediction is very difficult, especially about the future'. Nevertheless, for well over a year we have been wondering how best to meet the scientific challenges to come through the development of our instruments and infrastructure. These ideas – in the form of proposals for projects for a further wave of the Millennium Programme – were presented and discussed with our user community at the ILL 2020Vision Meeting in Grenoble on 17-19 September 2010. What was predictable was the demand for yet more flux in all areas of the instrument suite, enabling still smaller samples to be measured even faster. We also saw strong support to be able to probe the structure of materials rapidly over a wider range of length-scales, and explore the behaviour of more complex composite or hierarchical materials. However, the clearest message from the meeting was that the first priority for investing precious resources was in sample environment, and to be more specific, to respond to the needs of the fastest growing sector of our community – soft condensed matter science. A much fuller account of the event may be found at <http://www.ill.eu/news-events/past-events/2010/ill2020/>.

The ILL and its user community have ideas
 and energy in abundance,
 and that, together with appropriate means,
 will allow us to continue to produce
 a wide range of world-beating fundamental
 and applied science for years to come

The burgeoning soft matter community at ILL reflects in part changing trends in the scientific community in general. However, the fact that a commensurate fraction has chosen to apply neutrons to their work may be linked to our efforts to develop some of the instrument suite with them in mind: our new horizontal-surface reflectometer FIGARO is now equipped with a host of complementary equipment to prepare and characterise films and interfaces *in situ*, while the world-leading small-angle neutron scattering instruments D11 and D22 are now fully reintegrated after upgrades or repairs. The Partnership for Soft Condensed Matter (PSCM) also plays an essential role: it now offers a much wider range of technical support, with measurements such as light-scattering routinely enabling much more effective use to be made of our beamtime.

Biology has also consolidated its position as a mainstream part of our research portfolio through a scientific return on investment in instrument development (LADI-III, D19 and D22 again) and the underpinning role of the Partnership for Structural Biology (PSB).

The highlights we report here reflect achievements both in the above fields, and across the rest of the broad and colourful spectrum of science we serve. Indeed, the strongest showing is in our traditional 'heartland' of magnetism and superconductivity, and here we are seeing the fruition of experiments to probe the relationship between magnetism and superconductivity in the latest generation of moderate or high- T_c superconductors, iron pnictides and chalcogenides. These, and the layered cuprates that were the original high- T_c superconductors, continue to elude a definitive theory of the mechanism of the effect. However, all fingers point to magnetism being an integral part, and neutron scattering playing an essential role in establishing this.

Another remarkable result we present is the demonstration of a neutron whispering gallery effect, analogous to the well-known, long-distance propagation of vibrations around a concave surface. This elegant experiment, performed on our reflectometer D17, brought together scientists from the Nuclear and Particle Physics and the Large Scale Structures Group. These unlikely bedfellows bear testament to a creative and often unconventional scientific climate at ILL.

Finally, this year we said goodbye to two of our longest-serving instruments. The single-crystal thermal neutron diffractometer D15 saw its last neutrons at the end of 2010, while our original powder diffractometer D1A was displaced in summer 2010 to make way for the guide for the upgraded IN16 backscattering spectrometer. Despite the advanced years of the latter, it continued to be highly productive right to the end, and went out with a spectacular bang: the results of its last experiment, performed on a highly unusual molecular material that *contracts* when heated, were published in the journal *Science* in early 2011.

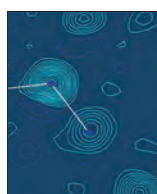
One of the messages we can take from the successes of 2010 is that the ILL and its user community have ideas and energy in abundance, and that, together with appropriate means, will allow us to continue to produce a wide range of world-beating fundamental and applied science for years to come. Just what that science will be, is much harder to predict!

Andrew Harrison
 Associate Director





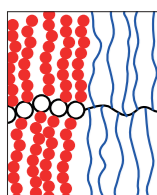
Magnetism:
cf. article "Very high horizontal field investigations using SANS at the ILL" p.18



Chemistry and Structure:
cf. article "Giant deuteron migration in deuterated 3,5-pyridine-dicarboxylic acid" p.32



Materials science and engineering:
cf. article "Optimising the processing of mineral ore at the Styrian Erzberg iron mine" p.34



Soft Matter:
cf. article "Giant surfactants made of amphiphilic dual brush block copolymers and their self-assembly in aqueous solution" p.40

Magnetism

Since the ILL's foundation the study of magnetism and magnetic materials has been a cornerstone of the ILL scientific programme, and it still accounts today for about 30 % of demand. The most recent focus of such activity has been the layered iron pnictides and chalcogenides, structurally similar to the 'original' high- T_c layered cuprates, and shown in 2008 to superconduct at moderate temperatures. Neutrons provide a crucial tool for exploring the role that magnetic interactions may play in their charge transport, exemplified by several of our highlights here. However, a quarter of a century after their discovery, the high- T_c cuprates themselves are still not yet well understood, inspiring work on model low-spin antiferromagnets, also reported here. There is considerable diversity too, from multiferroic ceramics through the so-called single-molecule magnets that may one day provide the qubits for quantum computers in the future, to the only elemental molecular magnet, oxygen.

These scientific advances go hand with technical development: the arrival of a 17 T horizontal-field magnet has already enabled flux-line lattices to be observed by SANS at unprecedented fields, while high pressure techniques are now available to a wider user community through stronger technical support. Improvements to our instruments too promise new ways of doing science. In particular, the increased, continuous angular coverage of the new IN5 detector married with developments in data analysis is opening up a new generation of single-crystal magnetic measurements that may transform the way in which we map out magnetic excitations.

Chemistry and Structure

The point of departure in searching for the reasons why a material behaves the way it does is usually the determination of its structure and composition. Increasingly, the motivation for such work at ILL is the search for better materials for energy capture, storage and conversion, in which the location of hydrogen or oxygen atoms and their associated defects is often the key unknown. Here, conventional structure determination is becoming more frequently augmented by pair distribution function (PDF) analysis, which reveals aspects of the deviations from perfect crystallinity. *In situ* measurements under conditions related to the operation of devices such as cells are also on the rise.

However, our highlights focus elsewhere. The first relates to the structure of polymorphs of cisplatin - the most successful chemotherapeutic drug known - important in understanding how processes such as dissolution and uptake in the body occur. The second concerns the migration of deuterons in model hydrogen-bonded materials to explore the role of such bonds and hydrogen mobility in materials essential for life, or key components of modern technology.

2010 also saw an evolution in our instrument suite. The new CCD-detector Laue instrument CYCLOPS can now produce refinable data from measurements as short as 10 s. We also witnessed the last experiment on our original powder diffractometer D1A as it is dismantled to make way for the guide that will serve the upgraded IN16 spectrometer; fittingly, this saw it out in a spectacular fashion with a result that we expect to highlight in next year's report.

Materials science and engineering

We feature the very broad field of 'Materials' in many other sections of this report; we will therefore focus here on systems with an engineering, earth-sciences or materials-processing component. Perhaps the most strongly represented area is strain-scanning studies of engineering materials, benefitting from the dedicated instrument SALS: a heavy-duty hexapod is now routinely used in experiments and, when combined with tight beam collimation, enables precise studies of very specific parts of heavy engineering components - most recently from nuclear power plants and bridges.

This year our highlights draw attention to a yet wider range of problems and reflect a trend towards increasing *in situ* work. The evolution of the mesoscopic structure of cement precursors during hydration is explored through ultra-small-angle neutron scattering measurements (USANS) on the reflectometer S18. The change in composition of low-grade iron ore during thermal processing was followed by high-flux powder diffraction on D20, providing a way of optimising the process to make it cheaper and less polluting. Finally, the reflectometer D17 has been used to explore the potential for new materials as barriers against copper diffusion in semiconductor devices.

Soft Matter

The strongest growth area in the science we support - judged by user demand - is in soft condensed matter, which has risen to at least 16 % of all proposals in recent rounds. Our Partnership for Soft Condensed Matter (PSCM) is supporting a much wider range of complementary measuring techniques - for example light-scattering - that are essential for performing good neutron experiments. However, the provision of sample environment facilities for the conditions most appropriate for soft-matter systems - around ambient temperature and humidity - needs much development and will be a future priority area.

It is difficult to pick scientific trends in such a diverse field, but research centred on nanoparticles, on self-assembled, often hierarchical supramolecular structures and under kinetic conditions, facilitated by 'faster' upgraded instruments, are certainly more prominent than a few years ago. Our highlights reflect some of this, with work on water-based amphiphiles that self-assemble into aggregates that may be used to disperse otherwise insoluble compounds - very useful in drug delivery - as well as real-time reflectometry measurements on FIGARO that reveal the mechanism of film-formation as a polymer is deposited from solution on a surface. Finally, a combination of SANS and neutron spin-echo measurements have explored the relation between the structure and short-time (ns) dynamics for the clustering of protein molecules, key not only to biological systems, but also the formation of functional materials.

Liquids and glasses

Despite the tremendous breadth of work at ILL on the structure and dynamics of liquids and glassy materials, one or two trends dominate recent work. There has been a change in emphasis from fundamental work - with some very honourable exceptions - towards systems with real or potential applications, in which performance depends on nanoscale inhomogeneities and disorder; examples include new electrolytes for next-generation batteries, and high-performance polymers and composites.

One of our highlights illustrates how neutrons can explore the link between molecular structure and dynamics, and bulk properties such as viscosity in ionic liquids - with the potential to provide greener solvents for chemical synthesis.

Another distinct feature of work in this field of late at ILL has been the key enabling role of technical development, sometimes enabled by our Long Term Proposal (LTP) scheme. One such concerns hydrodynamic laser-heated levitation furnaces, for the structure and spectroscopy of high-temperature melts. This is exemplified by our highlight on a molten yttria-alumina mixture which has been claimed controversially to possess a liquid-liquid transition temperature at 1788 K. A LTP project has also enabled experiments to be performed on D4 to 200°C and 8 GPa, complementing improvements to its monochromator which provides 2.5 times as much flux on the sample. Finally, PDF analysis is increasingly in demand to unravel structural correlations in a broader range of liquids and glassy materials.

Biology

The use of neutrons to unravel structural problems across a broad range of length-scales has increased steadily at ILL over the past decade and now accounts consistently for 15 % of applications. The cold-neutron Laue instrument LADI now holds the record both for the largest system and the smallest crystal ever studied by high resolution neutron diffraction. D19 is also breaking new ground with larger cells and yet smaller crystals that can be studied.

At larger length-scales, the activity on the low-resolution instrument DB21 was transferred on its closure at the end of 2009 to D16, where crystallographic studies of large macromolecular assemblies will benefit from higher neutron flux and the new MILAND detector. Coordinated sample environment developments on D17 and FIGARO will cement ILL's position as a world authority in the study of biomembranes in strong synergy with the needs of the PSCM. D22 has in addition been realigned over the past two winter shutdowns, resulting in up to 50% increase in flux.

Our highlights in this field reflect work at all of these length-scales, from the mechanism of hydrogen transfer in enzymes that could be used in biofuels, to the large-scale structures of membrane proteins, the conformational changes in enzymes acting as part of bacterial immune systems, and the evolution of structure in silk-forming molecules as they are extruded from a silkworm. The last highlight combines SAXS and SANS measurements with electron microscopy to produce the first low-resolution structure of a multienzyme complex implicated in controlling stable glucose levels in a wide range of organisms.

Neutron spectroscopy is less widely exploited in this field than diffraction - possibly because it usually requires larger amounts of material, often with targeted deuteration, and because the interpretation of data is often less direct. Nevertheless, here we report remarkable insights into the influence of cholesterol in model biological membranes as well as the application of BRISP to explore correlations between protein and solvent (water) dynamics at THz frequencies that may be central to protein function *in vivo*; the influence of hydration on the internal dynamics of the protein molecules themselves (timescale) was explored on IN13

Nuclear and Particle Physics

Activity here has always spanned a tremendous range of fundamental science. However, increased economic and political pressure to reduce our reliance on fossil fuels appears to be stimulating a marked increase in experiments in nuclear physics relevant to the improved exploitation of nuclear fission. Here PN1 is ideally placed to explore fission yield products - for example ^{233}U in relation to the ^{233}Th breeding process - while a high priority is given to future developments in γ spectroscopy with strong impact on the study of fission products.

The resolution and dynamic range of the GAMS spectrometers on PN3 provide unrivalled opportunities to study nuclear structure. One highlight here describes the search for evidence that tetrahedral nuclear states can exist - commonplace at a molecular level, but not yet observed for elementary particles bound by strong interactions.

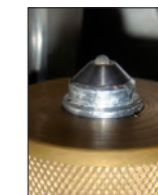
A key enabling technology for much of the fundamental physics at ILL is the production of high densities of ultra-cold neutrons (UCNs) for which two superfluid-helium sources are currently being developed. The first source, for which a UCN density beyond 50 per cc was recently demonstrated, will feed GRANIT - a second-generation ultra-high energy resolution gravitational neutron spectrometer at ILL - which has already received its first delivery of operational levels of UCNs.

Finally, we highlight an elegant experiment to explore a phenomenon called the whispering gallery effect, observed for many years with sound waves near a curved reflecting surface. The effect has been revealed for the first time in cold neutrons with reflectometer D17 - a result that may provide a new method of probing surfaces and neutron optics.

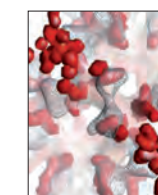
Modelling and theory

'Spectroscopy' in this context covers excitations not included in the other sections of this report, and most notably 'magnetism' (though of course the two are strongly coupled in important cases such as multiferroics and many superconductors). The experimental side of this subject frequently goes hand in hand at ILL with the work of our Computing for Science (CS) Group - boosted in 2010 with the arrival of a new, more powerful computer cluster. Two of our highlights illustrate the impact of such work. The first concerns negative thermal expansion in tellurium-based liquid alloys while the second relates to the interplay between structure and specific atom-atom interactions in alloys of magnesium and zinc, where changes in composition lead to remarkable changes in complexity of structure.

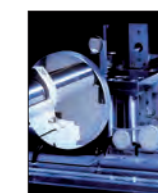
The scope of spectroscopy in solid-state physics and chemistry is broad, but much is related to the challenges society faces in the environment and to improved technology for energy, ranging from diffusion in membranes or solid electrolytes for fuel cells and batteries to sequestration of CO_2 in porous media. However, we continue to have a very strong presence in fundamental work, shown in our third highlight on helium confined to porous media. The ILL has played a key role in exploring quantum condensed phases based on ^3He and ^4He . The latest contribution concerns an amorphous form of ^4He produced through condensation in a porous silicate medium. Diffraction on D20 confirms the amorphous character, while spectroscopy on IN5 may provide insights into a novel form of motion called superflow.



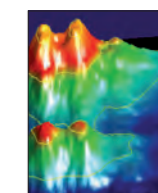
Liquids and glasses:
cf. article "Turning up the heat on the liquid-liquid transition" p.48



Biology:
cf. article "New insights into the E2:E3BP core assembly of the human pyruvate dehydrogenase multienzyme complex (hPDC)" p.52



Nuclear and Particle Physics:
cf. article "A Test of Tetrahedral Symmetry in Nuclei" p.68



Modelling and theory:
cf. article "Anomalous vibrational dynamics in $\text{Mg}_2\text{Zn}_{11}$ " p.72

AUTHORS

D.N. Argyriou, M. Reehuis, S.A.J. Kimber, K. Prokes and S. Matas (HZB, Berlin, Germany)
 A. Hiess (ILL)
 A. Akbari, I. Eremin and M.M. Korshunov (MPI-PkS, Germany),
 T.J. Liu, J. Hu, B. Qian, D. Fobes and Z. Mao (Tulane University, USA)
 A. Rotaru, H. Pharm and L. Spinu (New Orleans University, USA)
 V. Thampy, A.T. Savici, J.A. Rodriguez and C. Broholm (John Hopkins University, USA)
 W. Bao (Renmin University, China)
 Y. Qui, (University of Maryland and NCNR, USA)

From magnetism to superconductivity in FeTe_{1-x}Se_x

The interplay of superconductivity and magnetism in the iron-based superconductors FeTe_{1-x}Se_x has been studied using inelastic neutron scattering. Our experiments shed light on the symmetry of the magnetic and superconducting order parameters as well as on the mechanism of Cooper pair formation.

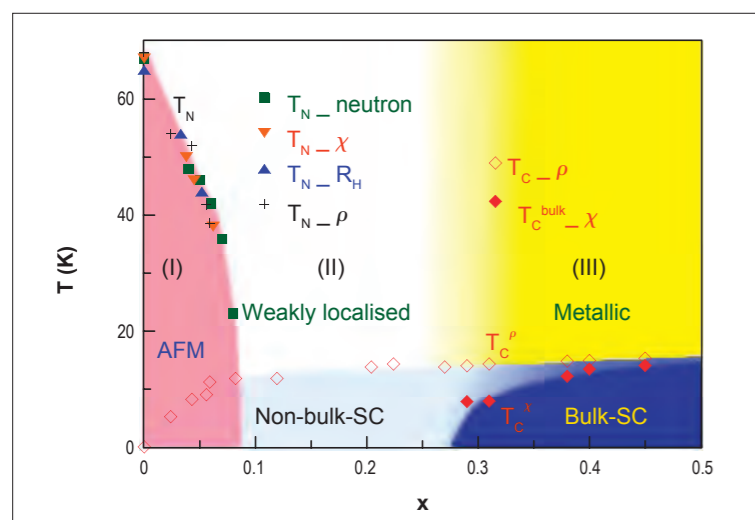


Figure 1: A phase diagram illustrating the magnetic and superconducting properties of FeTe_{1-x}Se_x, with $0 < x < 0.5$ as a function of temperature and doping. The diagram shows the Néel temperature of the AFM phase as determined by neutron scattering (green squares), susceptibility (orange triangles), Hall coefficient (blue triangles) and resistivity (black crosses) measurements. The diagram also shows the onset of the superconducting transition probed by resistivity (open diamonds); bulk superconducting transition temperature (filled diamonds) probed by susceptibility. (taken from [2]).

To investigate the interrelation of magnetism and superconductivity the condensed matter community focuses on materials where both phenomena may not only coexist, but where spin dynamics may actually stabilise a novel unconventional superconducting state. For several decades this possibility has been actively debated, not only for cerium- and uranium-based intermetallic superconductors but also for copper-oxide high-temperature superconductors.

Inelastic neutron scattering (INS) experiments revealed significant changes in the spin dynamics of these compounds related with

the superconducting state. With the discovery of superconductivity at moderate temperature in iron-based pnictides and chalcogenides the research focus has shifted in recent years. The iron chalcogenide FeTe_{1-x}Se_x is structurally the simplest of the iron-based superconductors. The possibility of obtaining large single crystals makes this series an ideal playground for INS investigations, shedding light on the symmetry of the magnetic and superconducting order parameters as well as the spin dynamics relevant for Cooper pair formation. The parent compound FeTe shows magnetic order below $T_N = 65$ K with an in-plane magnetic wave vector $(1/2, 0)$. This contrasts with the pnictide parent compound where the magnetic order has an in-plane magnetic wave vector $(1/2, 1/2)$. Despite these differences the pioneering work by Y. Qiu *et al.* [1] has established that both the pnictides and the chalcogenides exhibit a change in the spin dynamics at the momentum space position $(1/2, 1/2)$ on entering the superconducting state. A central question is therefore how $(1/2, 1/2)$ superconductivity can emerge from a $(1/2, 0)$ instability, i.e., what is the symmetry of the magnetic and superconducting order parameters.

We performed INS experiments using the ILL's thermal three-axis spectrometer IN8, to understand spin dynamics using FeTe_{1-x}Se_x single crystals as a function of doping [2]. In conjunction with bulk measurements we established the phase diagram presented in **figure 1**. Bulk superconductivity (SC) exists when sufficient Te is replaced by Se, with the superconducting volume fraction larger than 75% for $x \geq 0.29$. For $x < 0.29$, only non-bulk-superconductivity exists with the superconducting volume fraction smaller than 3%. The bulk superconductivity and non-bulk superconductivity concentration regions also differ in their normal-state transport property: metallic in the former, non-metallic in the latter. The magnetic soft mode evolving from the $(1/2, 0)$ -type magnetic long-range order is associated with weak charge carrier localisation. Bulk superconductivity occurs as magnetic correlations at $(1/2, 0)$ are suppressed and the mode at $(1/2, 1/2)$ becomes dominant for $x > 0.29$. This suggests competing magnetic interactions but a

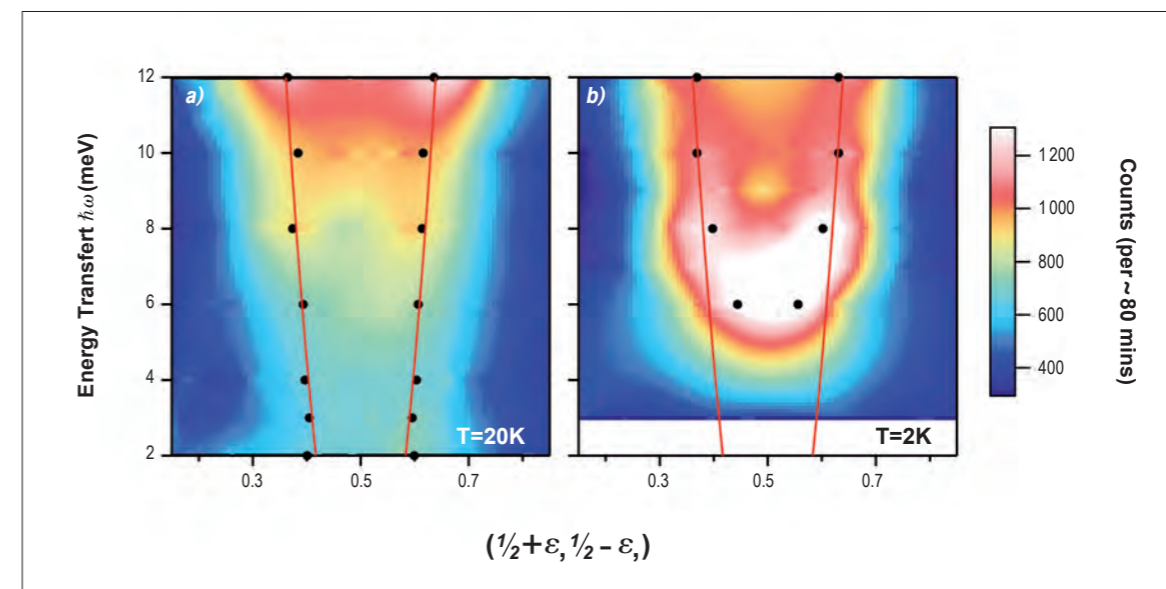


Figure 2: The dispersion relation of the spin dynamics in (a) the normal and (b) the superconducting state of FeTe_{0.6}Se_{0.4}. Here the measured intensity is depicted in colour. The black dots indicate the centre of Gaussian peaks fitted to the experimental data. The dispersion of the normal state is reproduced by red lines in the superconducting state, showing that the higher energy excitations have not changed their position below T_c (taken from [3]).

common magnetic origin for superconductivity in iron chalcogenide and pnictide superconductors, with the $(1/2, 1/2)$ magnetic fluctuations being favourable for superconductivity.

Large single crystals of FeTe_{0.6}Se_{0.4} with a superconducting transition temperature $T_c = 14$ K were used to investigate the momentum space dependence of the spin dynamics close to $(1/2, 1/2)$ [3]. As shown in **figure 2**, the dispersive excitations in the paramagnetic state at $T = 20$ K emerge from incommensurate positions $(1/2 \pm \epsilon, 1/2 \pm \epsilon)$ with $\epsilon = 0.09(1)$.

In the superconducting state, the low energy part of the excitation spectrum is suppressed and a strong inelastic feature (often called 'resonance') positioned at $(1/2, 1/2)$ and $E = 6$ meV is visible, but the higher energy part of the excitation spectrum remains unchanged.

A simple itinerant model describing the Fermi-surface topology of this superconductor with extended S^z symmetry, e.g., considering the superconducting order parameter is modulated in momentum space, qualitatively captures the salient features of the data.

REFERENCES

Y. Qiu *et al.*, Phys. Rev. Lett 103 (2009) 107005 [1]
 T.J. Liu *et al.*, Nature Materials 9 (2010) 716 [2]
 D.N. Argyriou *et al.*, Phys. Rev. B 81 (2010) 220503(R) [3]

K. Prokeš and D.N. Argyriou (HZB, Berlin, Germany)
 A. Kreyssig, P.C. Canfield and A.I. Goldman (Iowa State University, Ames, USA)
 B. Ouladdiaf (ILL)

Four-circle diffractometer with three-axis energy analysis D10

The origin of superconductivity in CaFe_2As_2 under uniaxial pressure

Iron, well known for its ferromagnetic properties, is not generally considered to have properties compatible with classical superconductivity. Ferromagnetically aligned moments on the iron atoms create a local magnetic field that should destroy any Cooper pairs. The announcement by Hosono *et al.* [1] of superconductivity in iron pnictide LaFeAsO therefore came as a big surprise and has initiated exceptional interest and feverish activity around the world. Our work on the CaFe_2As_2 compound has concentrated on detecting structural, magnetic and/or superconducting changes induced by pressure.

Why have these materials generated so much attention? First, these iron-containing compounds form a large group of compounds (second only to the cuprates) in which high-temperature superconductivity is a common phenomenon, related to an identifiable structural feature (iron-arsenide or iron-selenide layers – see **figure 1**). Secondly, it seems that magnetism plays an important role in superconductivity, opening up further possibilities

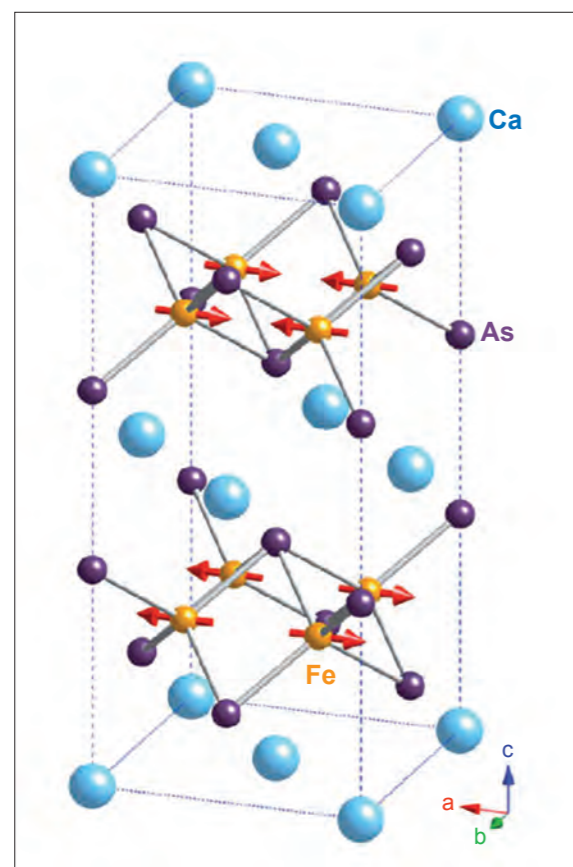


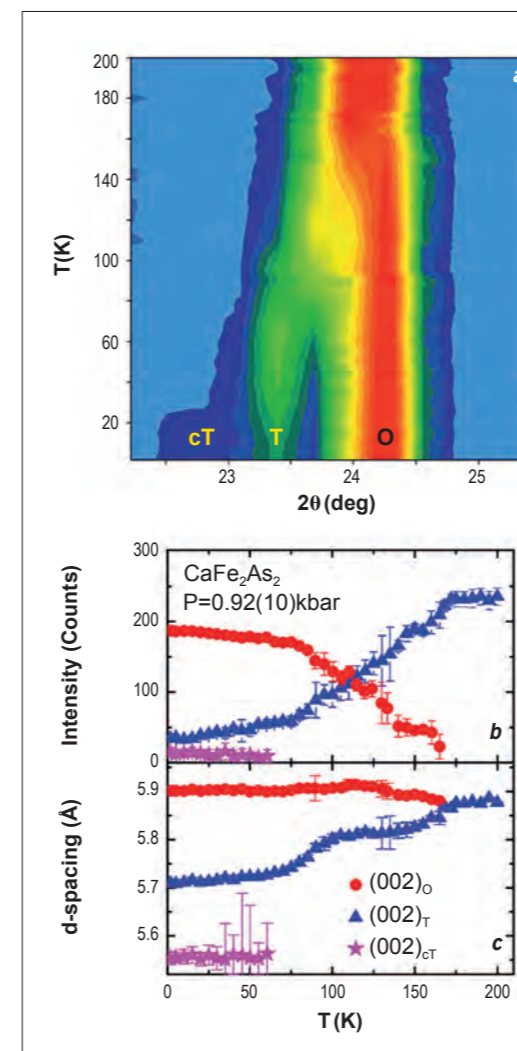
Figure 1: Illustration of the low temperature, antiferromagnetic structure of CaFe_2As_2 . The magnetic unit cell is the same as the orthorhombic chemical unit cell. Iron moments are oriented along the orthorhombic *a*-axis.

for investigating their interplay. Thirdly, iron arsenides differ in several ways from cuprates. For instance, the parent (undoped) compounds are metallic systems rather than Mott insulators, and the superconducting properties of the iron arsenides are clearly three-dimensional. Interestingly, the parent compounds like LaFeAsO [1111 compounds] and AEFe_2As_2 (AE = Ca, Ba or Sr) [122 compounds] are not superconducting at ambient pressure, but become so either after doping or under pressure.

In this study, we concentrated on detecting structural, magnetic and/or superconducting changes induced by pressure on the CaFe_2As_2 compound. At ambient pressure, the high temperature tetragonal phase (T) discontinuously transforms (in CaFe_2As_2 around 172 K) to an orthorhombic phase (O) accompanied by the appearance of a magnetic order [2]. We were able to show that uniaxial pressure stabilises a minute amount of the T phase that hosts superconductivity down to the lowest temperatures, thus solving a puzzle as to why different pressure studies lead to remarkably different results.

In 2008, it was reported [3] that CaFe_2As_2 under hydrostatic pressure greater than 0.3 GPa undergoes a novel structural transition to the so-called collapsed tetragonal (*cT*) phase, and the ordered magnetism disappears. At approximately the same pressure, transport measurements using a liquid medium pressure cell showed the onset of superconductivity. It therefore seemed natural to conclude that the *cT* phase hosts superconductivity. However, more recent transport measurements under truly hydrostatic pressure conditions (He gas cell) have revealed that neither the ambient pressure O phase nor the *cT* phase support superconductivity in this material [4]. Why was superconductivity present during the liquid clamped cell pressure measurements, but not under hydrostatic pressure? One intriguing possibility was that a new phase, stabilised by the non-hydrostatic pressure conditions was present in the former measurements, but absent in the latter.

Uniaxial pressure represents, in some sense, an extreme instance of non-hydrostatic pressure conditions. By using the D10 diffractometer we have verified that CaFe_2As_2 single crystals under uniaxial pressure applied along the *c*-axis exhibit the coexistence



of several structural phases. The room temperature tetragonal phase (T) is stabilised at low temperatures for pressures above 0.06 GPa (**figure 2**), and its volume fraction increases as higher uniaxial pressure is applied.

Additional simultaneous neutron and electrical resistance measurements performed after the D10 experiment strongly suggest that it is the high-temperature tetragonal phase stabilised down to liquid-helium temperatures which is responsible for the superconductivity in CaFe_2As_2 below 10 K. This correlates well with the appearance of the superconducting dome as a function of the uniaxial pressure, as observed in electrical resistance measurements [5]. Moreover, we have shown that there is no competition for volume from magnetism and superconductivity in this material.

Interestingly, the uniaxial pressure required along the *c*-axis to render CaFe_2As_2 superconducting is about an order of magnitude lower than the nominal "hydrostatic" pressure values produced by liquid medium clamped cells, or approximately the same order of magnitude as that expected for the non-hydrostatic component in the clamped cells. We note that the existence of the superconducting "bubble" over only a relatively narrow range of pressure can be nicely explained by considering the development of pressure in the volume fractions of the stabilised T phase [6].

Figure 2: (a) Colour map showing the temperature dependence of a portion of the diffraction pattern taken within the range of various structural (002) reflections of CaFe_2As_2 at 0.092 GPa applied along the *c* axis. Panels (b) and (c) show the temperature dependence of the integrated intensities and positions of reflections shown in panel (a). Various structural phases are denoted by letters: T – high-temperature tetragonal phase, stabilised tetragonal phase, *cT* – the collapsed tetragonal phase, O – orthorhombic phase.

REFERENCES

- Y. Kamihara, H. Hiramatsu, M. Hirano, R. Kawamura, H. Yanagi, T. Kamiya and H. Hosono, *J. Am. Chem. Soc.* 128, 10012 (2006) [1]
- A. Kreyssig, M.A. Green, Y. Lee, G.D. Samolyuk, P. Zajdel, J.W. Lynn, S.L. Bud'ko, M.S. Torikachvili, N.Ni, S. Nandi, J. Leão, S.J. Poulton, D.N. Argyriou, B.N. Harmon, P.C. Canfield, R.J. McQueeney and A.I. Goldman. *Phys. Rev. B* 78, 184517 (2008) [2]
- A.I. Goldman, D.N. Argyriou, B. Ouladdiaf, T. Chatterji, A. Kreyssig, S. Nandi, N.Ni, S.L. Bud'ko, P.C. Canfield and R.J. McQueeney. *Phys. Rev. B* 78, 100506 (2008) [3]
- W. Yu, A.A. Aczel, T.J. Williams, S.L. Bud'ko, N.Ni, P.C. Canfield and G.M. Luke, *Phys. Rev. B* 79, 020511(R) (2009) [4]
- M.S. Torikachvili, S.L. Bud'ko, N.Ni, P.C. Canfield and S.T. Hannahs, *Phys. Rev. B* 80, 014521 (2009) [5]
- K. Prokeš, A. Kreyssig, B. Ouladdiaf, D.K. Pratt, N.Ni, S.L. Bud'ko, P.C. Canfield, R.J. McQueeney, D.N. Argyriou, and A.I. Goldman, *Phys. Rev. B* 81, 180506(R) (2010) [6]

D.H. Ryan (McGill University, Montreal, Canada)

J.M. Cadogan (University of Manitoba, Winnipeg, Canada)

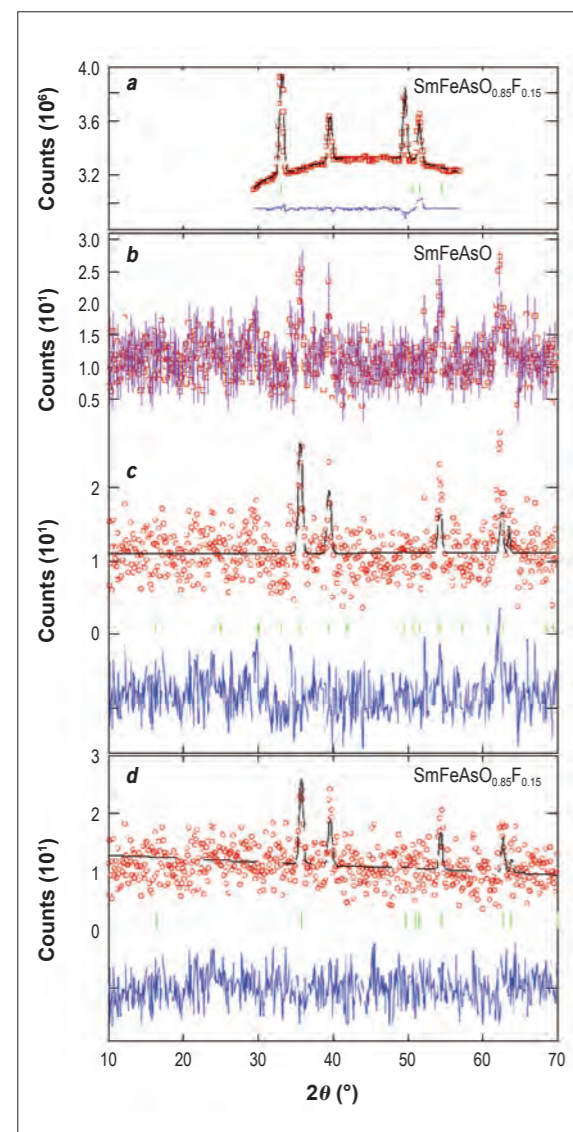
C. Ritter (ILL)

F. Canepa (CNR-INEM and University of Genova, Italy)

A. Palenzona and M. Putti (CNR-INFN-LAMIA and University of Genova, Italy)

Coexistence of long-ranged magnetic order and superconductivity in the pnictide superconductor $\text{SmFeAsO}_{1-x}\text{F}_x$ ($x = 0, 0.15$)

Superconductivity and magnetic order are conventionally considered to be mutually exclusive. However the new RFeAsO or “1-1-1” family of superconductors contains two magnetic elements (iron (Fe) and a rare earth (R)) and in at least two cases ($R = \text{Sm}$, and Gd) not only do magnetic order and superconductivity co-exist, but the compounds in which magnetism is present also exhibit the highest transition temperatures. We have used a newly developed flat-plate sample holder to study the highly absorbing SmFeAsO compound using long wavelength thermal neutrons in order to establish the nature of the magnetic order in this system.



The new generation of iron-based superconductors has shown that materials containing two magnetic elements, both of which can order, can also exhibit superconductivity [1]. In this article, we are concentrating on the RFeAsO, or “1-1-1”, family of compounds where both the iron and rare earth can order. In most cases as the materials are doped in order to induce the superconducting state, magnetism is lost at both the iron and rare earth sites. Remarkably, the two members exhibiting the highest superconducting transition temperatures (samarium and gadolinium) also have magnetically ordered rare earth sites.

Unfortunately, both samarium and gadolinium are highly absorbing for neutrons, making their compounds difficult to study, however indirect evidence from heat capacity [2] and μSR [3] suggests that magnetic ordering of the samarium ions coexists with superconductivity over a wide range of compositions.

It is the direct search for this samarium ordering using neutron diffraction that was the subject of our study. The large thermal neutron absorption cross section for natural samarium (about

Figure 1: Neutron diffraction patterns of SmFeAsO and SmFeAsO_{0.85}F_{0.15} measured at a wavelength of 2.417 Å. (a) Nuclear scattering pattern for SmFeAsO_{0.85}F_{0.15} at 10 K used to set scale and profile factors for the magnetic fits. (b) The difference between the 10 K and 1.6 K patterns for Sm-FeAsO shows the new diffraction peaks due to the ordering of the Samarium moments. The magnetic signal is approximately fifty times weaker than the nuclear signal due to the small samarium moment. (c) Fitted difference pattern for SmFeAsO using the Cm'm'a' magnetic structure. (d) Fitted difference pattern (10 K–1.6 K) for SmFeAsO_{0.85}F_{0.15} showing a weak magnetic scattering pattern similar to that seen for Sm-FeAsO. The solid line shows a fit to the P4/n'm'm' magnetic structure. In each case, where the solid black line shows a fit, Bragg markers (green bars) and residuals (blue line) are given below. The Bragg markers were generated using the reduced symmetry P1 space group, and most have zero structure factors. They serve to emphasise both the presence and absence of possible reflections.

6000 barns, nearly 2.5 times that of cadmium) yields a 1/e thickness for SmFeAsO of about 80 mg/cm², precluding the use of conventional sample holders.

We used a recently developed large-area single-crystal flat-plate sample holder [4] to place about 1.6 g of material in the neutron beam. The scattering measurements were carried out at a wavelength of 2.417 Å on the D20 thermal powder diffractometer at the ILL. For each sample, data sets were obtained at 1.6 K and 10.0 K with counting times of 10 hours (SmFeAsO) and 15 hours (SmFeAsO_{0.85}F_{0.15}) for each temperature. The purely nuclear patterns at 10 K (figure 1a) were fitted to establish scale factors, lattice parameters and the instrument profile function. These were then fixed while the difference patterns (1.6 K–10 K) were fitted to obtain the magnetic structure. All refinements of the neutron diffraction patterns employed the FullProf suite [5, 6].

The Samarium moments were found to order antiferromagnetically along the c-axis in a G-mode which has a +−+− moment sequence. This structure corresponds to the Cm'm'a' group. Figure 2a shows a representation of the derived magnetic structure of SmFeAsO at 1.6 K. Fitting the section of the diffraction pattern shown in figure 1b yields a samarium moment of 0.60(3) μ_B for SmFeAsO at 1.6 K.

A similar analysis of the SmFeAsO_{0.85}F_{0.15} data shown in figure 1d yields a closely related magnetic structure (Shubnikov magnetic space group: P4/n'm'm') and a Sm moment of 0.53(3) μ_B.

The most significant aspect of the pattern shown in figure 1d is not that SmFeAsO and SmFeAsO_{0.85}F_{0.15} adopt closely related magnetic structures, but rather, that the Samarium moments are magnetically ordered in a superconducting sample (this sample exhibits a T_c of 53.5 K) and that the samarium moments are essentially the same in both compounds. This provides direct confirmation that antiferromagnetic order and superconductivity co-exist in the SmFeAsO/F system [7].

We will be extending this project to the GdFeAsO system which should be easier to work with as while gadolinium has a much higher absorption cross-section it also has a larger moment, making the magnetic signal much easier to see.

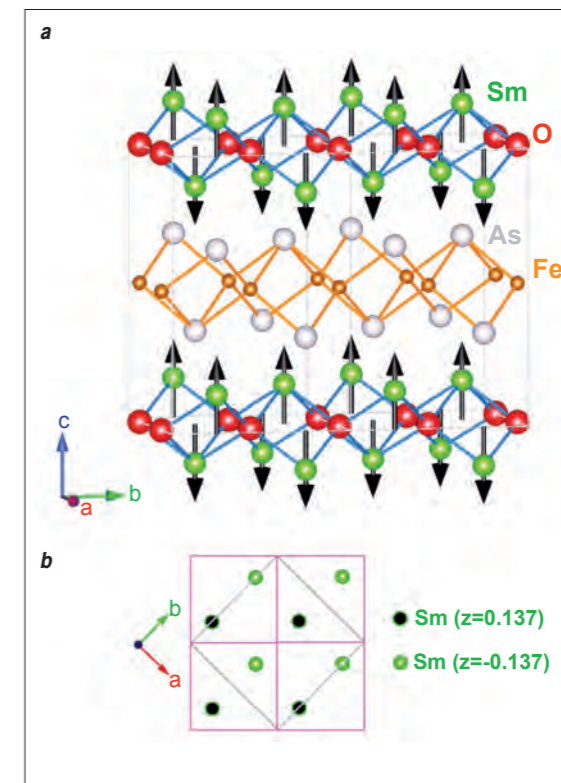


Figure 2: (a) The Sm magnetic structure of SmFeAsO at 1.6 K. The layered nature of both the chemical and magnetic structures is emphasised by showing two unit cells in the b direction. (b) A projection of the magnetic structure onto the basal plane shows the relationship between the magnetic structures of SmFeAsO and SmFeAsO_{0.85}F_{0.15} at 1.6 K. The black discs mark the Sm atoms on the $z = 0.137$ plane that have their moments pointing “up”, while the green discs denote Sm atoms on the \bar{z} plane that have their moments pointing “down”. Four unit cells of the smaller (tetragonal, P4/n'm'm') form of SmFeAsO_{0.85}F_{0.15} each containing two Sm atoms (one each of black and green) are shown by the magenta lines, while the relationship to the larger (orthorhombic, Cm'm'a') cell of SmFeAsO that contains four Sm atoms is shown by the grey lines.

Note: The orthorhombic basal lattice parameters differ by only 0.7% and cannot be distinguished here.

REFERENCES

- M.D. Lumsden and A.D. Christianson, J. Phys. Condens. Matter 22, 203203 (2010) [1]
 L. Ding, C. He, J.K. Dong, T. Wu, R.H. Liu, X.H. Chen, and S.Y. Li, Phys. Rev. B 77, 180510(R) (2008) [2]
 A.J. Drew, F.L. Pratt, T. Lancaster, S.J. Blundell, P.J. Baker, R.H. Liu, G. Wu, X.H. Chen, I. Watanabe, V.K. Malik, et al., Phys. Rev. Lett. 101, 097010 (2008) [3]
 D.H. Ryan and L.M.D. Cranswick, J. Appl. Cryst. 41, 198 (2008) [4]
 J. Rodríguez-Carvajal, Physica B 192, 55 (1993) [5]
 T. Roisnel and J. Rodríguez-Carvajal, Mater. Sci. Forum 378-81, 118 (2001) [6]
 D.H. Ryan, J.M. Cadogan, C. Ritter, F. Canepa, A. Palenzona and M. Putti, Phys. Rev. B80, 220503(R) (2009) [7]

AUTHORS

E.M. Forgan, E. Blackburn, A.T. Holmes, A.S. Cameron, G.R. Walsh and J. Lim (University of Birmingham, UK)
J.S. White (PSI, Villigen, Switzerland)
C.D. Dewhurst, E. Mossou and T. Forsyth (ILL)
M. Savey-Bennett (Cryogenic Ltd, Acton, UK)

Very high horizontal field investigations using SANS at the ILL

We present the first experimental data from the world's highest field cryomagnet for SANS. Its horizontal solenoid design allows a field of 17 T to be reached, at the expense of perpendicular access to the neutron beam, but with $\pm 10^\circ$ access parallel to the beam. This extends the field range available for SANS well beyond the previous limit of 7 T at the ILL. It allows scattering experiments in vacuum from room temperature to 1.6 K, and at atmospheric conditions with an additional room temperature bore. It is available for collaborative use.

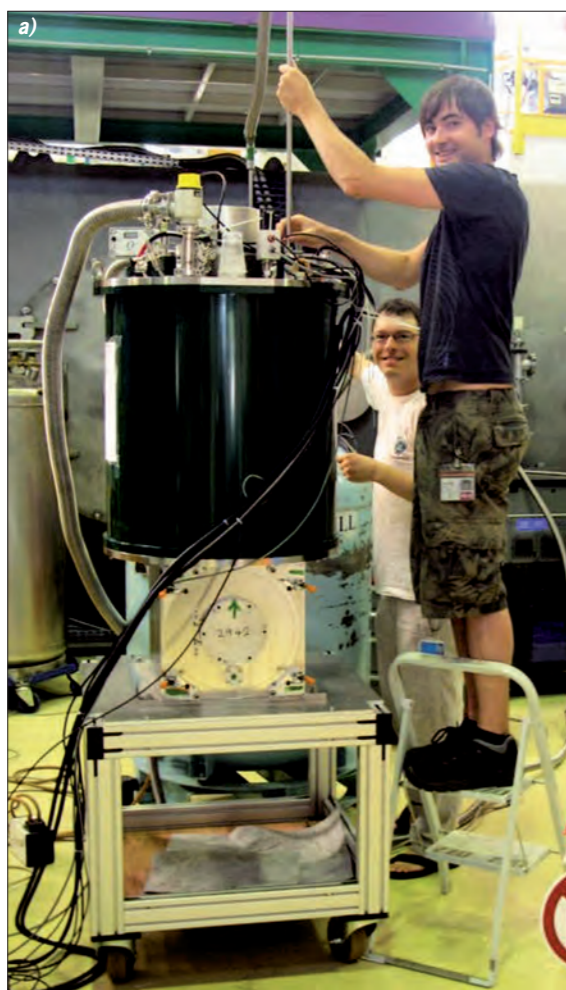


Figure 1: (a) The 17 T cryomagnet being filled with liquid helium by Ken Honniball (ILL), ably assisted by Alex Holmes (University of Birmingham).
(b) Elizabeth Blackburn (University of Birmingham) installing the sample while the cryomagnet is cold.

In August 2010, we carried out a SANS study on $\text{YBa}_2\text{Cu}_3\text{O}_7$ (YBCO) [1] using a new horizontal cryomagnet (**figure 1a**) built by Cryogenic Ltd. and funded by the UK EPSRC. In this study we looked at the flux lines in YBCO in unprecedentedly high magnetic fields. **Figure 2** shows the diffraction pattern characteristic of the flux line lattice at 16 T. The pattern is not quite square, but is distorted in the opposite direction to that observed below 11 T [1]. This means that the angle between the diffraction spots passes through and beyond 90° as the field is increased above 11 T, i.e. the lattice does not lock into a square pattern, as previously seen in tetragonal *d*-wave superconductors [2]. The observed temperature dependence also displays interesting features, including an apparent increase in the perfection of the flux line lattice at high temperatures as pinning becomes less important.

Obviously, sample change in a horizontal solenoid will be unconventional. This is done using a manipulator and airlock designed by Gary Walsh and manufactured in Birmingham. **Figure 1b** shows the detwinned $\text{YBa}_2\text{Cu}_3\text{O}_7$ [3] sample being installed at 100 K using the manipulator chamber, while the cryomagnet remains at 4.2 K.

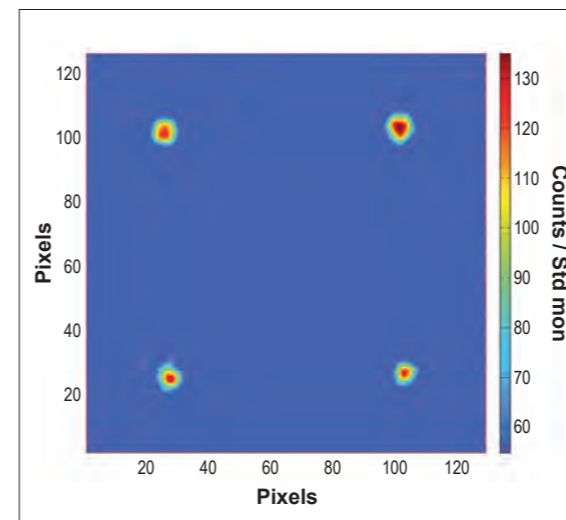
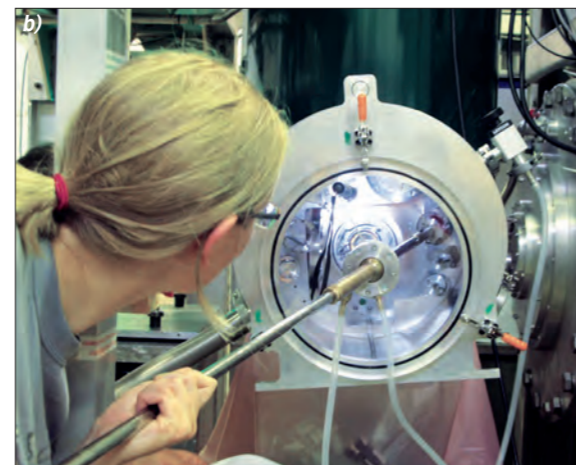


Figure 2: YBCO diffraction pattern at 16 T and 5 K. The vortex lattice phase diagram has been mapped out over the newly accessible field range, and in the future we hope to use the high flux at the ILL to investigate the vortex liquid state.

Use at Room Temperature

The cryomagnet has also been used to align anisotropic structures in water. **Figure 3** shows some initial results for a colloidal suspension of fd bacteriophages in water. These rod-like virus particles, which infect *E. coli* bacteria, are 880 nm long, and have an aspect ratio of about 100. At high concentrations they form liquid crystals, and have proved a valuable tool for the study of such systems. For example, a single mutation in the virus coat causes the chiral twist of the cholesteric metastable phase to change pitch and direction [4]. The scattering from the rods increases significantly when they are aligned parallel by an external field. Most interestingly, on reducing the field back to zero, a new phase (possibly a single domain cholesteric liquid crystal) appears, spontaneously breaking the cylindrical symmetry. These measurements were performed using a room temperature bore insert, which cuts the normal $\pm 10^\circ$ access down to $\pm 7^\circ$, but allows rapid sample changing for biological samples in ambient conditions. A strong magnetic field can also have a big effect on even weakly diamagnetic substances, as demonstrated by the "Moses effect" (**figure 4**).

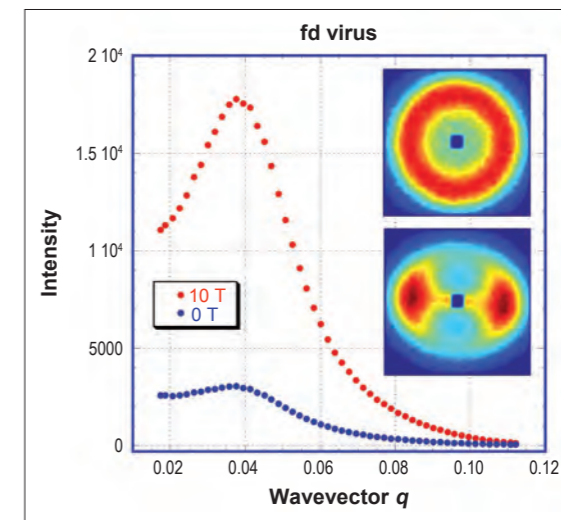


Figure 3: Scattering versus momentum transfer for fd virus. The scattering from randomly oriented rods is greatly increased when they are aligned parallel to a 10 T field which is parallel to the neutron beam, giving the cylindrically symmetric pattern in the upper inset. When the field is reduced to zero, the rods form a phase which spontaneously breaks cylindrical symmetry (lower inset), for reasons as yet unknown.



Figure 4: The Moses effect inside the room temperature bore. The diamagnetism of water and alcohol (the tube contains red wine) causes the liquid to be repelled, bringing about the 'parting of the red wine'.

REFERENCES

- J.S. White *et al.*, Phys. Rev. Lett. 102 (2009) 097001 [1]
- A.D. Bianchi *et al.*, Science 319 (2008) 177 [2]
- A. Junod *et al.*, Physica C 275 (1997) 245 [3]
- E. Barry, D. Beller and Z. Dogic, Soft Matter 5 (2009) 2563 [4]

AUTHORS

M. Enderle (ILL)
 B. Fåk (CEA, Grenoble, France)
 H.-J. Mikeska (Leibniz University, Hannover, Germany)
 R.K. Kremer (Max-Planck Institute for Solid State Research, Stuttgart, Germany)
 A. Prokofiev (University of Technology, Vienna, Austria)
 W. Assmus (Johann Wolfgang von Goethe University, Frankfurt, Germany)

A ballet of pairs and quartets

Like quarks and magnetic monopoles, fractional magnetic excitations are individual entities that only reveal themselves with partners. Such exotic excitations exist in one-dimensional arrays of spins $1/2$, where neighboring spins prefer antiparallel alignment (antiferromagnetic chains). These fractional excitations are called spinons, and are observed only in pairs. In contrast, the excitations in ferromagnetic chains, where neighboring spins are parallel, can be observed as single entities, called magnons. Neutrons can create pairs of spinons, but so far such pairs have only been observed in simple antiferromagnetic chains. We show that spinon pairs and even quartets can be created by scattering neutrons from LiCuVO_4 [1], where the spin- $1/2$ chains have ferromagnetic nearest-neighbor coupling that is a sizeable fraction of the dominating antiferromagnetic coupling between next-nearest neighbors [2].

An individual spinon has a well-defined discrete energy-momentum relationship, but since it is always created as part of a pair, the transferred momentum and energy in a neutron scattering experiment correspond to the sum of two individual momenta and energies. A given pair momentum can be distributed in different ways between the two partners and so allows for a continuous range of individual momenta and hence pair energies. This leads to a continuous spectrum of pair excitations with well-defined energy boundaries that depend on the transferred momentum – this is the signature of fractional excitations.

An example of such a spinon continuum, measured on IN20 in unpolarised set-up, is shown on the left side of **figure 1**. The color reflects the intensity of the inelastic scattering from a 50 mm^3 single crystal of LiCuVO_4 as a function of wave vector k along the chain and energy. The continuum observed in LiCuVO_4 is strikingly asymmetric with respect to $k=1/2$, in contrast to a simple antiferromagnetic chain whose two-spinon boundaries are shown as dashed white lines. We observe a strong transfer

of spectral weight towards lower energy for $k < 1/2$. The intensity for $k < 1/2$ shows a sharp peak slightly below the lower boundary of the two-spinon continuum while for $k > 1/2$ a broad maximum is observed in the middle of the continuum region [1].

We modeled LiCuVO_4 as two interpenetrating antiferromagnetic spin $1/2$ quantum chains (formed by even and odd sites) that are ferromagnetically coupled. Following ideas of Schulz [3], we keep the quantum character of the spinon-pair excitations of the simple antiferromagnetic chains but treat the ferromagnetic coupling in a random phase approximation. The intensity-energy-wavevector relation of all data were then fitted simultaneously with the ferro- and antiferromagnetic coupling as fit parameters. The result, shown on the right side of **figure 1**, describes very satisfactorily the principal features observed in LiCuVO_4 , namely the asymmetry and the shift of the spectral weight of the observed continuum scattering. The sharp onset for $k < 1/2$ seen in the experimental data is shown by our model to arise from a two-spinon bound state below the two-spinon

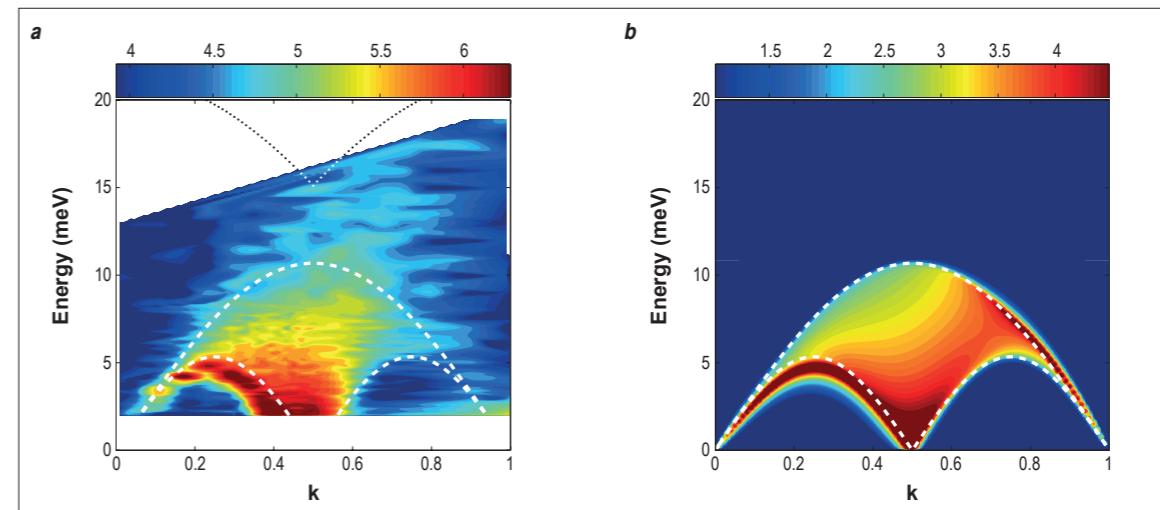


Figure 1: Fractional excitations in LiCuVO_4 , a frustrated spin $1/2$ chain with ferromagnetic nearest-neighbor and antiferromagnetic next-nearest neighbour interactions (taken from [1]). Measured (a) and calculated (b) dynamic structure factor as a function of in-chain wave vector k and energy. The dashed (white) lines show the boundaries of the two-spinon continuum of a simple antiferromagnetic chain and the dotted line the upper boundary of the four-spinon continuum.

continuum boundary. In our data, due to the spectrometer resolution, the bound state is not separated from the continuum.

On closer inspection we observe that the spectrum in **figure 1a** extends to energies well beyond the upper two-spinon boundary. We attribute this extra scattering to "pairs of pairs", spinon-quartets,

that are not covered by our model. The intensity of these quartets is considerably enhanced compared to theoretical predictions for the simple antiferromagnetic chain [4]. We suspect that these multiparticle excitations are enhanced by the strong coupling between the two interpenetrating antiferromagnetic chains – very much like multiparticle states being favoured by strongly coupled quarks.

REFERENCES

- M. Enderle, B. Fåk, H.-J. Mikeska, R.K. Kremer, A. Prokofiev, Phys. Rev. Lett. 104 (2010) 237207 [1]
 M. Enderle, C. Mukherjee, B. Fåk, R.K. Kremer *et al.*, Europhys. Lett. 70 (2005) 237 [2]
 H.J. Schulz, Phys. Rev. B 34 (1986) 6372 [3]
 J.S. Caux and R. Hagemans, J. Stat. Mech.: Theory Exp. (2006) P12013 [4]

AUTHORS

M.A. de Vries (University of Leeds, UK)
J.R. Stewart (ISIS, UK)
P.P. Deen (now ESS Lund, Sweden)
A. Harrison (ILL)
J.O. Piatek, G.J. Nilsen and H.M. Rønnow (Laboratory for Quantum Magnetism, EPFL, Switzerland)

Time-of-flight spectrometer IN4 - Diffuse Scattering Spectrometer D7
Three-axis spectrometer with polarisation analysis IN22 - Time-of-flight spectrometer MARI (ISIS)

Closing in on the resonating valence bond state in a 2D frustrated magnet

When long-range antiferromagnetic order in an insulating antiferromagnet is suppressed, this can in theory lead to an exotic macroscopic quantum state called a spin liquid. It has been conjectured that the high temperature superconducting state observed in the cuprates develops directly from such a spin liquid state [1] when an antiferromagnetic insulator is doped with mobile holes or electrons. We studied an antiferromagnet where the formation of long-range antiferromagnetic order is suppressed due to geometric frustration of the antiferromagnetic bonds. We found strong evidence in favour of a spin-liquid, thus gaining further insight in macroscopic quantum states in solids and in the relationship between high temperature superconducting and antiferromagnetic insulating states.

There has been a long search for antiferromagnetic (Mott) insulators with an exotic spin-liquid ground state that can be pictured as a quantum-mechanical superposition of all possible dimerisations (valence bonds) between (near-neighbour) spins into non-magnetic spin-singlets favoured by strong quantum spin fluctuations. This so-called Resonating Valence Bond (RVB) phase was suggested for triangular and square lattices, and is a fundamental aspect of a theory of high temperature superconductivity [1]. A prime candidate to observe such a state is the kagome antiferromagnet (figure 1a), a 2D lattice of corner-sharing triangles in which the antiferromagnetic exchange interaction between nearest neighbour spins is geometrically frustrated.

The mineral Herbertsmithite $[ZnCu_3(OH)_6Cl_2]$ contains such kagome nets, occupied by Cu^{2+} ions carrying $s = 1/2$ linked by O_2^- ions in OH groups (figure 1b). The only imperfection of this system is that a small fraction (about 6%) of the Cu^{2+} trade places with Zn^{2+} ions, creating weak links between kagome layers and vacancies in the kagome planes [2]. Muon spin relaxation spectroscopy experiments showed that, in agreement with theoretical expectations for the kagome antiferromagnet, the spins do not order in this system even at 50 mK, while the energy scale of the interactions is estimated at about 200 K.

Neutrons are an ideal probe of the structure and dynamics of magnetic moments at atomic length and time scales. We combined conventional neutron spectroscopy data over a wide energy and temperature range, taken at the time-of-flight spectrometers IN4 at ILL and MARI at ISIS, with measurements using XYZ neutron polarisation analysis at D7 and IN22 at ILL, to measure the spin-spin correlations as a function of energy and temperature in a high quality powder sample of Herbertsmithite.

We observed instantaneous antiferromagnetic correlations that are near neighbour only, in the absence of a time-averaged moment - a hallmark property of a quantum spin liquid. These short-ranged dynamic magnetic correlations - or dimer-like antiferromagnetic fluctuations - are spread smoothly over energies between 0 and at least 25 meV (corresponding to about 280 K) and we found that this continuous spectrum depends only weakly on temperature, at least up to 120 K.

Figure 2 shows a part of this magnetic dynamic structure factor. The weak magnetic scattering over this unexpectedly wide range in energies could be verified in detail by a new way to analyse time-of-flight data making use of the very different temperature dependences for the phonons and the magnetic scattering as verified at particular energies and wave vectors using polarised neutron scattering at D7 and IN22. The temperature dependence of the phonon scattering is well described by linear response theory and by comparing data taken at IN4 at a range of temperatures this phonon scattering could be identified and then subtracted, to yield the full magnetic dynamic structure factor, shown in Figure 2b and c.

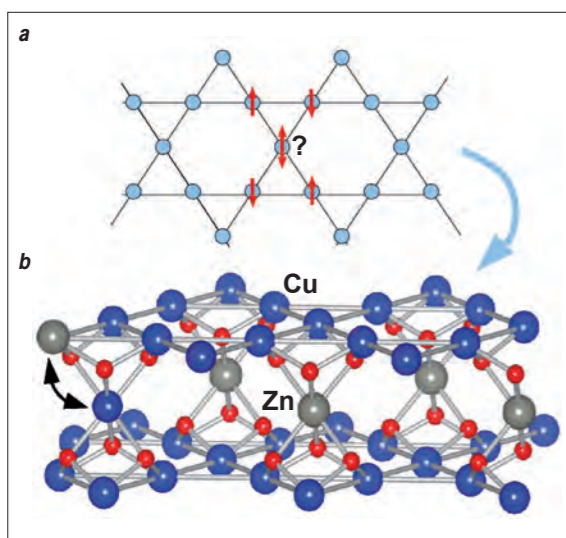


Figure 1: (a) Geometrically frustrated antiferromagnetism on the kagome lattice. There is no unique low-energy orientation for the central spin, as indicated by the question mark. (b) the structure of Herbertsmithite $[ZnCu_3(OH)_6Cl_2]$, with two kagome nets of Cu^{2+} ions (blue) linked by O_2^- ions (red) in OH groups, separated by layers with Zn^{2+} (grey) and Cl ions (not shown). The black arrows indicate the site-disorder due to exchanged Cu^{2+} and Zn^{2+} ions.

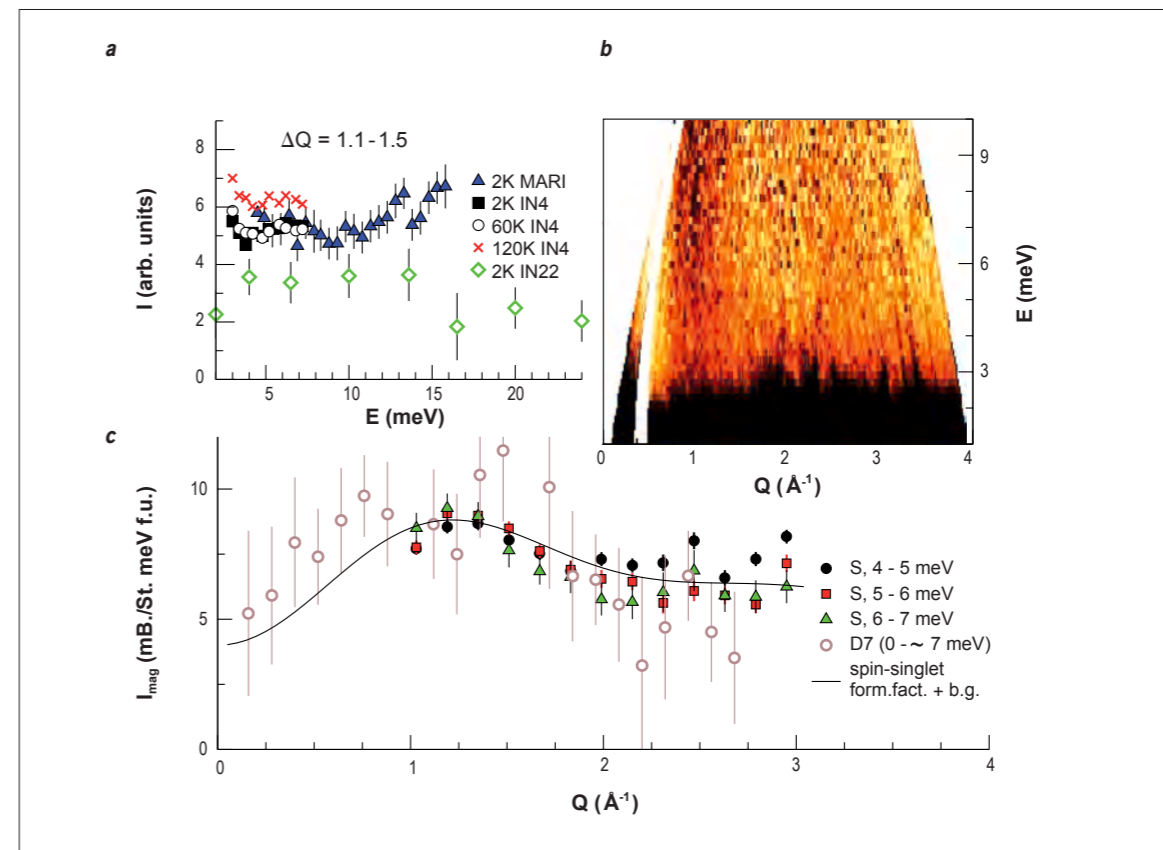


Figure 2: (a) The energy and temperature dependence of the inelastic neutron scattering at the maximum of dynamic antiferromagnetic correlations as measured at MARI and IN4. This is compared with the magnetic scattering measured at IN22, confirming that approximately 2/3 of the inelastic scattering is of magnetic origin. (b) The magnetic dynamic structure factor, obtained by subtraction of the photon spectrum in the IN4 data. (c) Energy cuts of the magnetic structure factor shown in panel (b) compared with the energy integrated magnetic scattering measured at D7. The fit is with the form factor for antiferromagnetic dimers.

The absence of a characteristic energy scale in the neutron spectrum and the weak temperature dependence of the spectrum point to a quantum critical state.

One explanation is that the system is at a quantum critical point as a result of a small Dzyaloshinsky-Moriya interaction [3], an anisotropic exchange interaction that is often found in frustrated compounds and spin glasses.

Another possibility is that the observed phase is a stable quantum critical phase, i.e. primarily due to the absence of symmetry breakings and not due to fine-tuning of particular parameters, as suggested in recent theoretical work where the RVB state is suggested to be an algebraic spin liquid [4], which supports gapless

excitations. However, in a quantum critical state the spin-spin correlations are expected to diverge algebraically as $T \rightarrow 0$ which is clearly not what is observed in herbertsmithite.

The short-ranged dynamic correlations, that could well be due to a disordered arrangement of valence bonds, have been argued to point to a valence bond glass state [5], due to structural disorder in the kagome lattice.

While it is now crucial to address the effect of the inevitable structural disorder [2], our results indicate that we finally have a 2D antiferromagnet in which an RVB-like phase can be studied experimentally.

REFERENCES

P.W. Anderson, Science 235 (1987) 1196 [1]
M.A. de Vries and A. Harrison, Nature (News & Views) 468, (2010) 908 [2]
M. Hermele, Y. Ran, P.A. Lee and Xiao-Gang Wen, Phys. Rev. B 77 (2008) 224413 [3]
O. Cepas, C.M. Fong, P.W. Leung and C. Lhuillier, Phys. Rev. B 78 (2008) 140405 [4]
R.R.P. Singh, Phys. Rev. Lett. 104 (2010) 177203 [5]

AUTHORS

E. Ressouche (INAC/SPSMS/MDN, CEA, Grenoble, France)
V. Simonet and B. Canals (Institut Néel, CNRS/UJF, Grenoble, France)
M. Gospodinov (Institute of Solid State Physics, Sofia, Bulgaria)
V. Skumryev (ICREA, Bellaterra, Spain)

Single-crystal diffractometer D15
Two-axis diffractometer for single crystals D23

Magnetic frustration in an iron-based Cairo pentagonal lattice

The Fe^{3+} ions in the $\text{Bi}_2\text{Fe}_4\text{O}_9$ compound provide the first analogue of a magnetic pentagonal lattice. Neutron diffraction reveals an original non-collinear magnetic structure, made of two sets of four Fe moments forming interpenetrating spin rectangles. This is not a mere propagation of the magnetic arrangement minimizing the energy in each individual pentagon, but actually results from a high geometrical frustration, together with a complex connectivity pattern.

The pentagon has played an important role in mathematics for thousands of years and is found throughout the natural world. It forms the faces of the dodecahedron, one of the platonic solids whose shape is reproduced in biological viruses and in some metallic clusters. The main peculiarity of this polygon is that, unlike triangles, squares or hexagons, it is impossible to tile a plane with congruent regular pentagons. There are, however, several possible tessellations of a plane with non-regular pentagons, the most famous being the Cairo lattice, which was given its name because it can be found on the streets of Cairo and in many Islamic decorations (see figure 1).

We have studied the lattices of Fe^{3+} ions (spin 5/2 and zero orbital momentum) in a single crystal of $\text{Bi}_2\text{Fe}_4\text{O}_9$ that we identified as the first materialization of an analogue of a magnetic Cairo pentagonal lattice [1] (see figure 2). Magnetisation measurements have shown that this compound orders antiferromagnetically

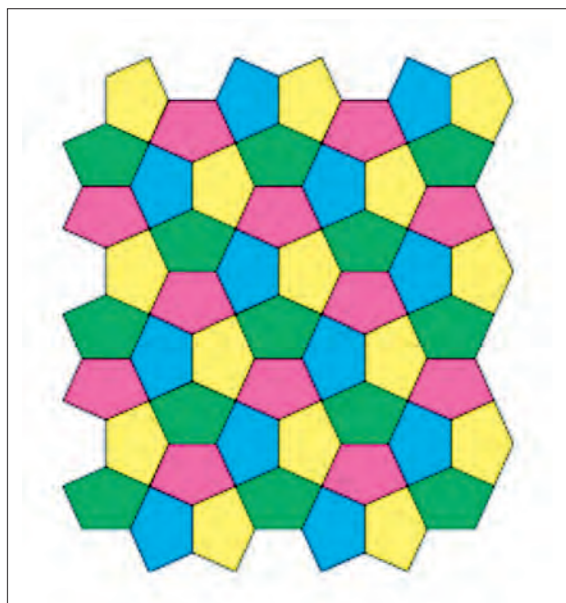


Figure 1: Cairo pentagonal lattice. The pentagons are equilateral but are not regular (non-equal angles).

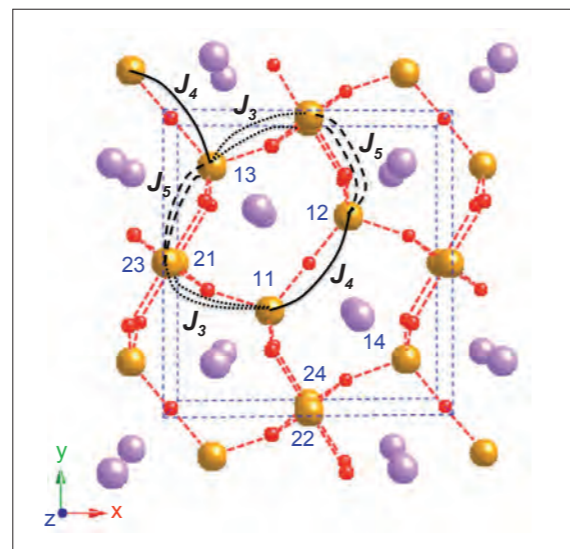


Figure 2: Projection in the (a, b) plane of the atomic structure of $\text{Bi}_2\text{Fe}_4\text{O}_9$. The bismuth, oxygen and iron atoms (on sites 1 and 2) are in purple, red and yellow, respectively. The magnetic interactions are shown in black.

around 240 K, whereas its Curie-Weiss temperature is -1670 K (see figure 3), which denotes strong magnetic frustration. This is expected in the case of antiferromagnetic nearest-neighbour magnetic interactions due to the odd number of bonds per tile in this lattice.

Neutron diffraction measurements were carried out on the two CEA-CRG diffractometers D15 and D23 of the ILL, in order to identify the magnetic structure of the lattice at low temperature. There are two different Fe^{3+} sites in $\text{Bi}_2\text{Fe}_4\text{O}_9$, each with a different crystallographic environment (oxygen tetrahedra and octahedra, respectively) and a different connectivity (3 Fe^{3+} and 4 Fe^{3+} neighbours, respectively). The periodicity of the magnetic structure was found to be doubled in the three space directions with respect to the structural one (propagation vector $(1/2, 1/2, 1/2)$). The magnetic structure was determined by taking into account the presence of two different magnetic domains.

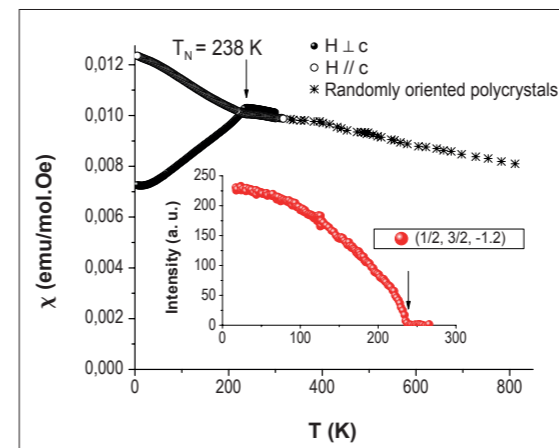


Figure 3: Linear magnetic susceptibility measured with a SQUID magnetometer and a Faraday balance at high temperature on a single crystal. Inset: Temperature dependence of a magnetic Bragg peak.

The magnetic moments lie in the (a, b) plane, where they form, for each site, (anti)parallel pairs of spins at 90° from each other. The resulting picture can be seen as two imbricated rectangles of spins, which cannot result from the crystallographic symmetries without a 4-fold symmetry axis (see figure 4).

Calculations (zero-temperature mean field calculation in reciprocal space and energy minimisation in real space) were carried out in order to understand the origin of such a peculiar magnetic order. Based on a simple examination of the structure, 5 magnetic oxygen-mediated superexchange interactions were taken into account in the model: two inter-plane interactions and 3 interactions within the pentagonal planes (see figure 2). A large set of values of these parameters was found to give both the observed magnetic periodicity and the magnetic arrangement with two imbricated rectangles. To reproduce the observed angle between the two rectangles in $\text{Bi}_2\text{Fe}_4\text{O}_9$, the three intra-plane interactions J_3 , J_4 and J_5 all have to be antiferromagnetic with the additional constraints $J_3/J_5 = 2.15$ and $|J_4| \geq |J_3|$.

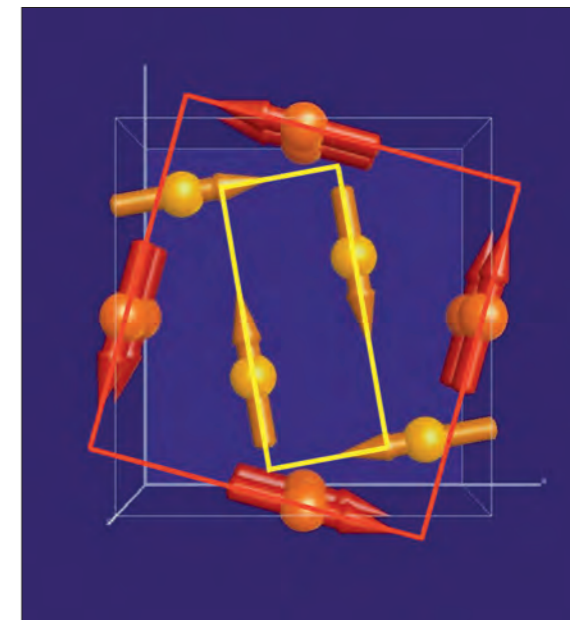


Figure 4: Magnetic arrangement of the Fe^{3+} sublattices in yellow and orange.

These calculations show that the magnetic structure of the $\text{Bi}_2\text{Fe}_4\text{O}_9$ pentagonal lattice can be understood by isotropic exchange interactions alone, which highlights the role of the topology of the lattice. In contrast to what is found in lattices composed of triangles, which provide the most popular frustrated systems, the magnetic order in these pentagon-based systems is not a mere propagation of the spin configuration minimising the energy of each individual plaquette. It is due to their complex connectivity (sites with different coordinations) associated with high magnetic frustration.

Very little theoretical work has been done up to now on pentagonal lattices. We hope that this first experimental study of a magnetic pentagonal lattice [1] will open new perspectives in the field of magnetic frustration and stimulate further work.

REFERENCE

E. Ressouche, V. Simonet, B. Canals, M. Gospodinov and V. Skumryev, Phys. Rev. Lett. 103 (2009) 267204 [1]

AUTHORS

S. Klotz, A.L. Cornelius and J. Philippe (IMPIC, Université Pierre et Marie Curie, Paris, France)
Th. Strässle (PSI Villigen, Switzerland)
T. Hansen (ILL)

Pressed to order

Oxygen is the only elemental molecule which carries a magnetic moment. As it is cooled and solidifies, long-range magnetic order occurs below 24 K, a fact which has been known for precisely a century. Recent diffraction experiments at D20 have shown that magnetic order in oxygen can also be produced by very high pressure, even at temperatures as high as room temperature!

The fact that the oxygen molecule carries a magnetic moment is due to two unpaired spins in the molecular π -orbital, a consequence of the so-called "Hund's rules". Oxygen gas is therefore paramagnetic. When oxygen is cooled it liquefies and then freezes at 51 K. Magnetic susceptibility measurements carried out in the early 20th century by Kamerlingh-Onnes indicated that the solid phases might be magnetically long-range ordered. However, the advent of neutron diffraction was needed to prove this, which it did in the early 1960s [1]. In fact, only one of the three low-temperature phases (α -, β -, γ -O₂) was revealed to be ordered: α -O₂, which is monoclinic, stable below 24 K, and antiferromagnetically ordered. This phase can be regarded as the simplest antiferromagnetic system in nature, since it is made of a single element and both the nuclear and magnetic structures are extremely simple.

In recent experiments at D20, we investigated the possibility of magnetically ordered phases under high pressure, in the 0-10 GPa range (0-100 000 atmospheres) [2]. To achieve these pressures,

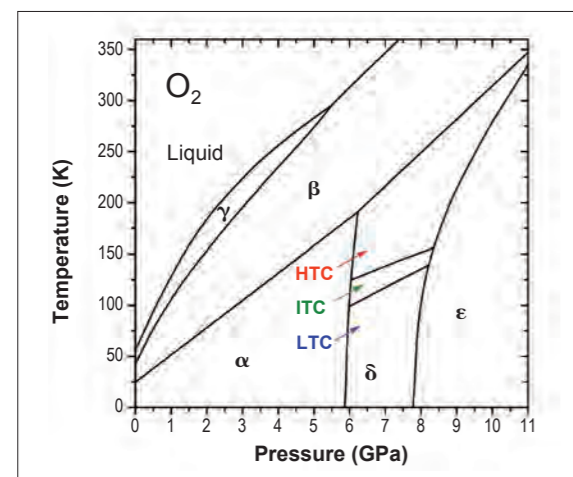


Figure 1: Phase diagram of oxygen in the 0-10 GPa range. Phase δ -O₂ is stable between 6 and 8 GPa. Neutron diffraction measurements at the ILL have shown that there are three distinct antiferromagnetic structures in this phase, denoted as HTC (high temperature commensurate), ITC (intermediate temperature commensurate) and LTC (low temperature commensurate) phases.

we used the ILL Paris-Edinburgh pressure cell and special loading equipment to condense liquid O₂ at 77 K into the sample chamber. Starting from this initial density, a volume reduction of about 50% generates pressures of up to 10 GPa. Under such conditions, two other phases of oxygen appear, δ - and ϵ -O₂, whose nuclear structure is known from X-ray diffraction (figure 1). The measurements at D20 focused on δ -O₂ (orthorhombic) and revealed the existence of three different magnetic structures within the same nuclear phase in the temperature range between 4 and 230 K. A Rietveld analysis of the pattern (figure 2) shows

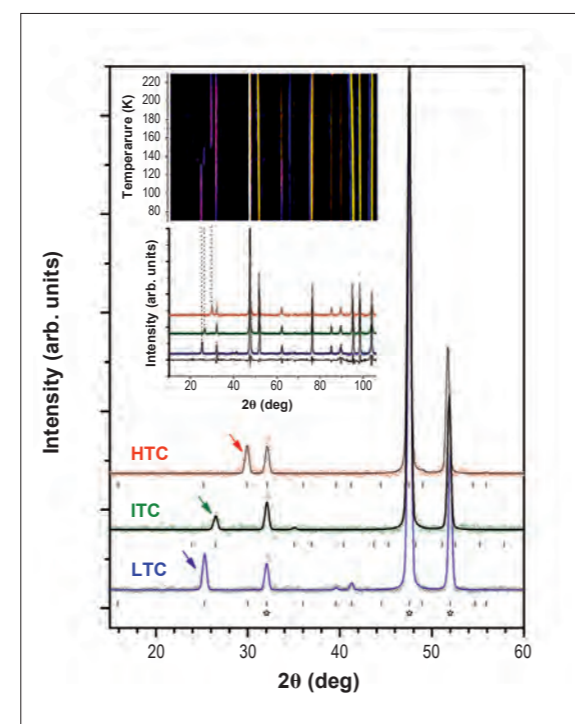


Figure 2: Diffraction patterns collected at D20 at about 7 GPa showing the existence of three magnetic phases as the sample is cooled from 230 K to 4 K (arrows indicate the strongest magnetic reflections). The lines are fits to the data by Rietveld refinements. The inset shows a map of 32 patterns over a temperature range of 160 K.

that in all three cases the spin alignment in the O₂ sheets is antiferromagnetic, but what differs is the stacking sequence of the sheets (figure 3). In the high-temperature phase (HTC, high temperature commensurate phase), the stacking sequence is identical to the one found in the neighbouring α -phase, i.e. antiferromagnetic coupling between nearest-neighbour spins in two different sheets. In the low-temperature (LTC) phase, this coupling is ferromagnetic, and in the intermediate phase (ITC), it alternates between ferro- and antiferromagnetic coupling, which leads to a doubling of the unit cell.

This structural diversity can be explained by the strong dependence of the exchange interaction between O₂ molecules on their mutual orientation, which is known from first-principle calculations [3]. It turns out that for most of the orientations of an O₂-O₂ dimer, the exchange interaction favours antiferromagnetic order, in agreement with the observation that the spins align antiferromagnetically within the O₂ sheets. However, for certain orientations the interaction can switch sign, giving rise to a weakly ferromagnetic exchange.

The orientation of two molecules located in two different sheets ("shifted parallel", see figure 3) is one such case, which explains why the ground-state LTC phase orders in such a way.

As the temperature is raised, the molecular movements ("librons") lead to temporary deviations of such orientations and hence to a weakening of the ferromagnetic exchange in favour of antiferromagnetic coupling, which leads the transitions to the ITC and eventually the HTC phases. Since δ -O₂ is known to exist up to 300 K (figure 1), oxygen is antiferromagnetic at room temperature, if pressed to 8 GPa!

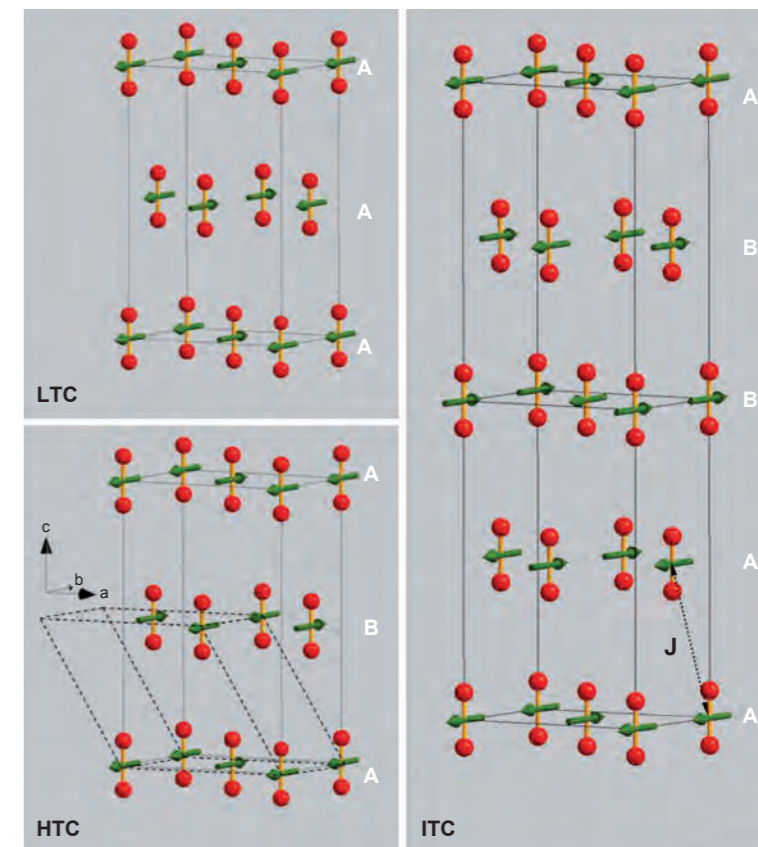


Figure 3: Structures of the HTC, LTC and ITC magnetic phases. "J" denotes inter-plane exchange coupling between "parallel shifted" nearest neighbours, which is ferromagnetic in the LTC phase, antiferromagnetic in the HTC phase, and mixed in the ITC phase. "A" and "B" denote the stacking sequences. The unit cell of α -O₂ is indicated by dashed lines.

REFERENCES

R.A. Alikhanov, Zh. Eksp. Teor. Fiz 45 (1963) 812 (Engl. transl.) JETP 18 (1964) 556 [1]
S. Klotz, Th. Strässle, A.L. Cornelius, J. Philippe, T. Hansen, Phys. Rev. Lett. 104 (2010) 115501 [2]
M.C. van Hemert, P.E.S. Wormers, and A. van der Avoird, Phys. Rev. Lett. 51 (1983) 1167 [3]

The magnetism of high spin cobalt(II) ions in square planar coordination

We have carried out a detailed analysis of layered compounds in which divalent cobalt ions occur in square planar coordination by oxide ions. This is a very unusual coordination environment, and these compounds seem, furthermore, to be rare examples where the cobalt ions are in their high spin state, with three unpaired electrons rather than in the low spin state which is found in the nearest molecular analogues with cobalt in a porphyrin-type ring. We have used neutron diffraction measurements to correlate crystal and magnetic structures and the results are supported by *ab initio* computational investigations.

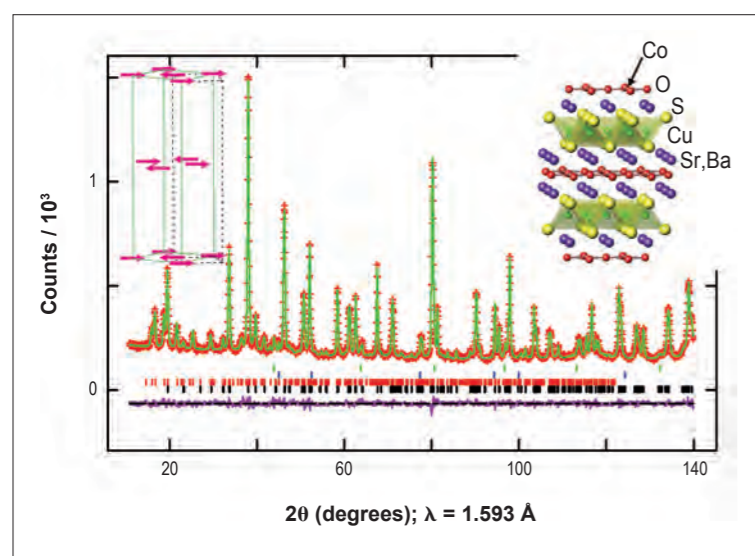


Figure 1: Crystal and magnetic structures of $\text{Sr}_2\text{CoO}_2\text{Cu}_2\text{S}_2$ and $\text{Ba}_2\text{CoO}_2\text{Cu}_2\text{S}_2$ and refinement at 5 K against D2B data collected on $\text{Ba}_2\text{CoO}_2\text{Cu}_2\text{S}_2$.

The compounds are $\text{Sr}_2\text{CoO}_2\text{Cu}_2\text{S}_2$, $\text{Ba}_2\text{CoO}_2\text{Cu}_2\text{S}_2$ [1] and their solid solution (**figure 1**). In $\text{Sr}_2\text{CoO}_2\text{Cu}_2\text{S}_2$ the CoO_4S_2 polyhedron is a highly axially distorted octahedron; the ratio of the Co–S and Co–O distances increases further with increasing size of the alkaline earth ion, so in $\text{Ba}_2\text{CoO}_2\text{Cu}_2\text{S}_2$ the Co^{2+} ion is in a coordination environment which is effectively square planar. These are compounds in which the bandwidth of the Co-3d-based bands is narrow, so the electrons are localised on the Co^{2+} ions by interelectron repulsion and these compounds are Mott-Hubbard type antiferromagnetic insulators.

Low temperature neutron diffraction investigations on D2B (**figure 1**) and D1A, as well as complementary measurements carried out on the diffractometers POLARIS, HRPD and OSIRIS at the ISIS facility revealed firstly that the moments on nearest neighbour Co^{2+} ions are coupled antiferromagnetically in a simple checkerboard arrangement and, secondly that the ordered magnetic moments on the Co^{2+} ions are much larger than can be accounted for by considering the spin moments only and there is a large orbital contribution to the magnetic moment.

This orbital moment increases as the coordination environment for Co^{2+} becomes closer to square planar, and the ordered moment in $\text{Ba}_2\text{CoO}_2\text{Cu}_2\text{S}_2$ is 4.5(1) μB per Co^{2+} ion – much larger than is plausible for a spin-only moment.

The existence of an orbital moment in Co^{2+} systems is well known – in CoO it results from the presence of an orbitally degenerate ground state for octahedral Co^{2+} , but distortion of the octahedron is observed to largely quench this orbital moment. In our systems the distortion from octahedral by axial distortion of the coordination environment is so large that orbital angular momentum carrying states become accessible. Ligand field analysis and *ab initio* calculations carried out at ILL indeed show that the ground state in $\text{Ba}_2\text{CoO}_2\text{Cu}_2\text{S}_2$ should carry a first order orbital moment and the calculations suggest that the size of the orbital moment is larger in $\text{Ba}_2\text{CoO}_2\text{Cu}_2\text{S}_2$ than in $\text{Sr}_2\text{CoO}_2\text{Cu}_2\text{S}_2$. **Figure 2** shows the results of spin-polarized *ab initio* calculations on $\text{Sr}_2\text{CoO}_2\text{Cu}_2\text{S}_2$ and $\text{Ba}_2\text{CoO}_2\text{Cu}_2\text{S}_2$ and shows how the size of the ordered moment on Co in a series of Co^{2+} -containing antiferromagnetic insulators increases as the coordination environment becomes increasingly square planar.

The resolution of D2B is sufficiently high that a structural distortion is evident in $\text{Ba}_2\text{CoO}_2\text{Cu}_2\text{S}_2$. The symmetry is lowered from $I4/mmm$ to $Immm$ as a consequence of a magnetostrictive distortion in which the ordered moment, with its large orbital component, couples to the lattice. Further measurements on the diffractometer ID31 at ESRF – which has an even higher resolution – have revealed that $\text{Sr}_2\text{CoO}_2\text{Cu}_2\text{S}_2$ undergoes a much smaller distortion and in the solid solution extending from $\text{Sr}_2\text{CoO}_2\text{Cu}_2\text{S}_2$ to $\text{Ba}_2\text{CoO}_2\text{Cu}_2\text{S}_2$ there is a universal correlation between the size of the structural distortion and the size of the ordered magnetic moment.

$\text{Sr}_2\text{CoO}_2\text{Cu}_2\text{S}_2$ is a highly air sensitive compound and small changes in the lattice parameters occur on air exposure, although there is no obvious decomposition producing new phases. Our measurements on D2B confirmed that $\text{Sr}_2\text{CoO}_2\text{Cu}_2\text{S}_2$ can exist in a slightly copper deficient form [1]. Refinements against the data showed that a sample of stoichiometric $\text{Sr}_2\text{CoO}_2\text{Cu}_2\text{S}_2$ which had been carefully sequestered from air exhibited an ordered magnetic moment of 3.8(1) μB while a portion of the same sample

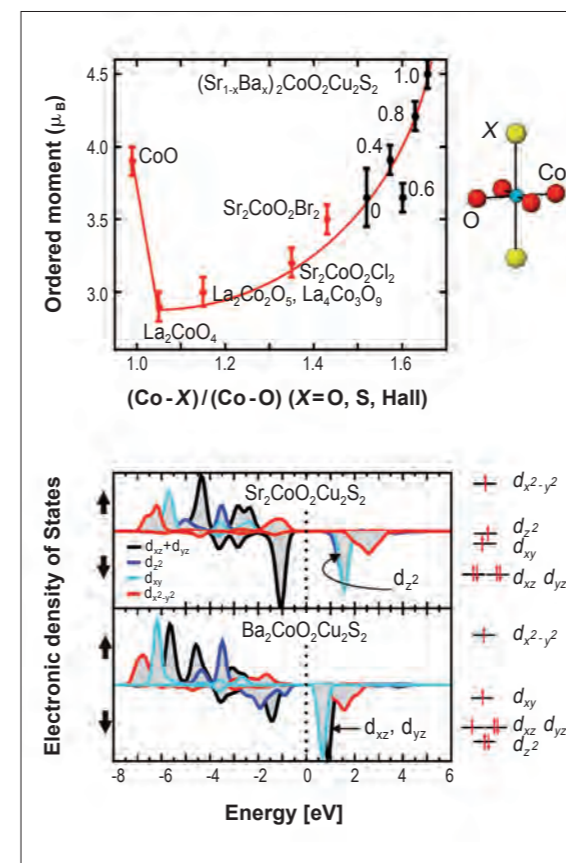


Figure 2 Lower: The calculated spin-polarised density of states for $\text{Sr}_2\text{CoO}_2\text{Cu}_2\text{S}_2$ and $\text{Ba}_2\text{CoO}_2\text{Cu}_2\text{S}_2$ showing relative orbital energies consistent with the cartoons on the right.
Upper: The correlation between long range ordered magnetic moment and the degree of square planarity of the Co^{2+} coordination environment.

which had been exposed overnight to a flow of moist oxygen at room temperature had a greatly reduced ordered moment of only 2.4(1) μB . Refinement of the lattice parameters showed that the exposure of the sample to moist O_2 results in a contraction of nearly 1 % in the volume of the unit cell, and refinement of the site occupancy factor of Cu showed a decrease in the Cu content of about 5 % to produce $\text{Sr}_2\text{CoO}_2\text{Cu}_{1.9}\text{S}_2$. The oxidative deintercalation of Cu results in the formation of poorly crystalline CuO which is just evident in high quality diffraction patterns. The computational investigations and analysis of the structural details suggest that on oxidation it is likely that both Co^{2+} and the states at the top of the Cu-3d/S-3p band are partially oxidised and the oxidation of Co^{2+} and the incorporation of some disorder are responsible for the decrease in the size of the ordered magnetic moment.

Our results show that the behaviour of these materials is complex and unusual. These compounds contain an unusual square planar coordination for high spin Co^{2+} ions [1] and we have shown that we can tune the size of the ordered magnetic moment on Co^{2+} by tuning the coordination environment.

Furthermore, the oxidative deintercalation of Cu from the sulfide layer makes a series of compositions accessible and clearly has a very significant effect on the magnetism of the Co ions in the oxide layer. Previous investigations of samples of nominal composition $\text{Sr}_2\text{CoO}_2\text{Cu}_2\text{S}_2$ included one study [2] which concluded that there was “spin-carrier phase separation” at low temperatures implying electron transfer from the S-3p based states at the top of the valence band onto Co, producing mobile holes in the chalcogenide layer and an insulator to metal transition on cooling.

Our computational investigations show that this is a plausible scenario given the proximity in energy of the Co-3d and S-3p states. However the fact that the composition of this compound is altered by air exposure suggests that further evaluation of the transport properties of $\text{Sr}_2\text{CoO}_2\text{Cu}_{2-\delta}\text{S}_2$ as a function of δ is required.

REFERENCES

- W.J. Zhu, P.H. Hor, A.J. Jacobson, G. Crisci, T.A. Albright, S.-H. Wang and T. Vogt, *J. Am. Chem. Soc.*, 119 (1997) 12398 [1]
S. Okada, I. Terasaki, H. Ooyama and M. Matoba, *J. Appl. Phys.* 95 (2004) 6816 [2]
This article is in press with *J. Am. Chem. Soc.* DOI: 10.1021/jq1095534

Cisplatin - polymorphism and new structural insights into an important chemotherapeutic drug

Cisplatin is the single most well-recognised and successful chemotherapeutic drug used today for the treatment of cancers. Structural elucidation of chemotherapeutic molecules is vital for understanding the utility of active molecules through target receptor interactions, the storage and delivery of the drug and as a means of protecting the intellectual property. Until now full structural information has not been available for either of the two solid forms of cisplatin, which differ in the packing of the square-planar cis -[Pt(NH₃)₂Cl₂] units.

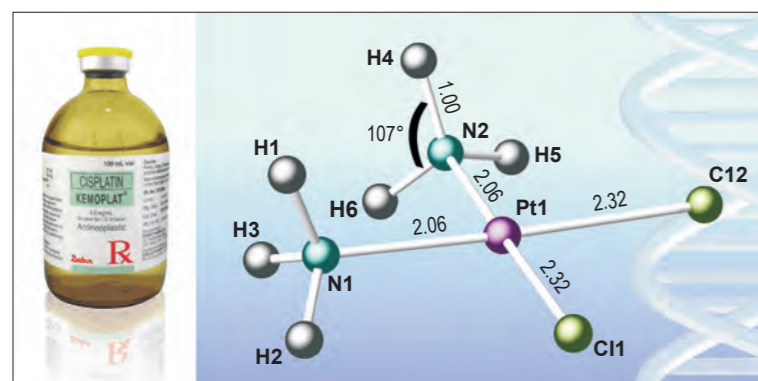


Figure 1: The structure of the square planar molecule cisplatin; distances (Å) and angles are labelled. **Left inset:** pharmaceutical cisplatin.

The only published crystal structure of cisplatin (**figure 1**), is a low resolution determination of the "alpha" polymorph [1], while the solid product of patented, commercial production methods [2] is the "beta" polymorph. The crystal structure of the ubiquitous beta form of cisplatin has never previously been elucidated and crucially the relative thermal stability ranges of the two polymorphs are not known. Accurate determination of the 3D structure of a drug containing a heavy metal centre, and in which hydrogen positions and hydrogen bonding is of importance, is non-routine. To obtain a complete description of the structures of the two polymorphs, including accurate hydrogen positions, we used the powerful combination of single crystal X-ray diffraction (SXD) and neutron powder diffraction (NPD). The collection of the NPD data was optimised for refinement of structural hydrogen positions [3] and used the D20 high-flux powder diffractometer.

Simultaneous refinement of the structures against the SXD data and NPD data sets collected at 100 K and 220 K for the alpha and beta phases respectively, enabled the identification of the hydrogen

atom positions via Fourier difference analysis. This permitted the orientations of the ammonia groups and hydrogen bonding interactions between the square planar moieties, to be determined for the first time.

The full refined structures are shown in **figure 2a** alpha form, **2c** beta form and show the alternating arrangement of the NH₃ groups and the Cl atoms in each stack of square planar molecules along the *c*-axis. In both forms, the central Pt atoms appear staggered along *c*, with Pt-Pt-Pt angles ranging from about 160 to about 170 degrees, as a result of hydrogen bonding which directs the packing of the cisplatin molecules in the solid state.

The full structures of the two polymorphs suggest that small differences in the physical properties of the two solid polymorphs could feasibly exist, affecting, for example, the solubility (which is dependent upon the free energy difference between the solvated and crystalline states, and thus the strength of the hydrogen bonds within the crystal). This could be of import as commercial beta cisplatin has a very low solubility of about 1 mg/mL in aqueous 0.9 % NaCl.

The relative stability of the two polymorphs of cisplatin with respect to temperature was examined via *in-situ* variable temperature NPD experiments on D20. A polycrystalline sample of beta cisplatin at room temperature (RT) was initially cooled to 100 K, then heated to 360 K, and finally returned to RT. Sequential refinements of the relative phase fractions show a transformation of the beta form on cooling below 200 K to the pure alpha form. The alpha form, stable at the lower temperatures, reverted to the beta form above about 340 K. The very large hysteresis in the phase transition temperatures (about 160 K) can be resolved by examining the structural mechanism of the phase transition. On transformation from the low temperature alpha form to the high temperature beta form, every second layer of cisplatin stacks is translated by half a unit cell vector in the directions of the *a*- and *c*-axes (shown by the black arrows in **figure 2b**, accompanied by a slight

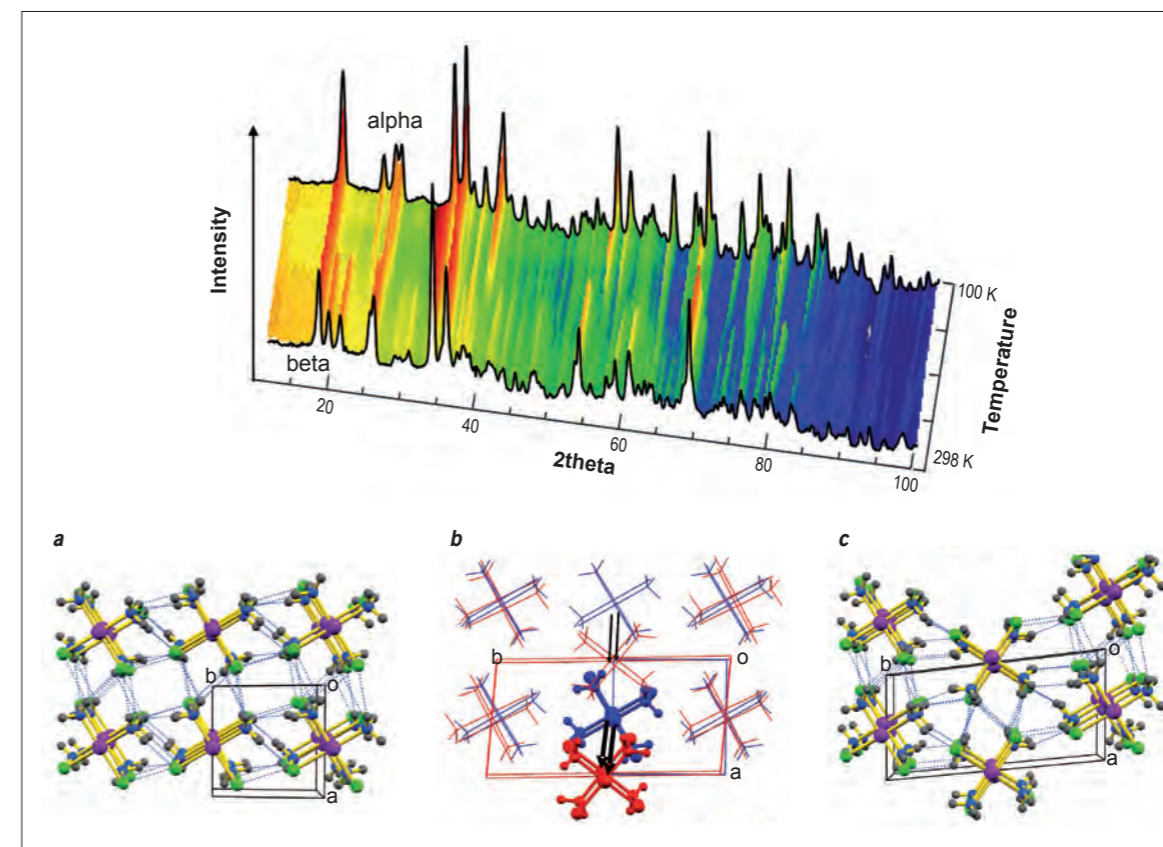


Figure 2: Upper Sequential NPD data sets showing the transformation between the diffraction patterns of the alpha and beta forms of cisplatin with temperature; colours are indicative of the peak intensity. Lower: (a) the structure of the alpha cisplatin; (b) overlaid unit cells of the alpha and beta forms, showing the transformation from the low T alpha form (blue) to the high T beta form (red); (c) the structure of beta cisplatin.

rotation of approximately 25° along the *b*-axis. As a consequence, all hydrogen bonds along the *b*- and half the hydrogen bonds along the *a*-axis are broken and reformed.

This study has highlighted the huge potential for retrieval of accurate and in-depth information on hydrogen positions and hydrogen bonding in polycrystalline pharmaceutical products in

the solid state via the powerful combination of single crystal X-ray diffraction and neutron powder diffraction. The accurate experimental determination of the hydrogen positions in active molecules will facilitate more exact computational modelling of their dissolution and ligand exchange processes, as well as the interactions with their biological targets, providing better understanding of the mechanisms by which they function.

REFERENCES

- G.H.W. Milburn and M.R. Truter, *J. Chem. Soc. (A)* (1966) 1609 [1]
M.A. Kaplan and A.P. Granatek, US Patent 4322391 (1982) [2]
M.T. Weller, P.F. Henry, V.P. Ting and C.C. Wilson, *Chem. Comm.* 21 (2009) 2953 [3]
V.P. Ting, M. Schmidtman, C.C. Wilson and M.T. Weller, *Angewandte chemie Int. Ed.* 49 (2010) 9408 [4]

S.J. Ford (ILL and Durham University, UK)
 J.S.O. Evans and I. Radosavljević Evans (Durham University, UK)
 G.J. McIntyre (ANSTO, Australia)
 M.R. Johnson (ILL)

Very intense vertical axis Laue diffractometer VIVALDI

Giant deuteron migration in deuterated 3,5-pyridinedicarboxylic acid

Short strong hydrogen bonds (SSHBs) often display interesting dynamics, including proton transfer, migration and order-disorder phenomena. These types of behaviour can strongly influence the properties of materials. For example, proton dynamics are of key importance in technologically relevant ferroelectric materials, including the extensively studied family of hydrogen-bonded KH_2PO_4 (KDP) - type ferroelectrics and the more recently discovered family of organic ferroelectrics based on the phenazine and chloranilic acid co-crystals [1]. The relevance of proton migration, however, reaches far beyond small organic molecules; proton transfer in short strong (low-barrier) hydrogen bonds is believed to have a key role in enzymatic catalysis in biological systems. Small organic molecules with short strong hydrogen bonds (such as 3,5-pyridinedicarboxylic acid) are therefore interesting not only in their own right, but also as useful model systems for studies of complex biologically-relevant interactions.

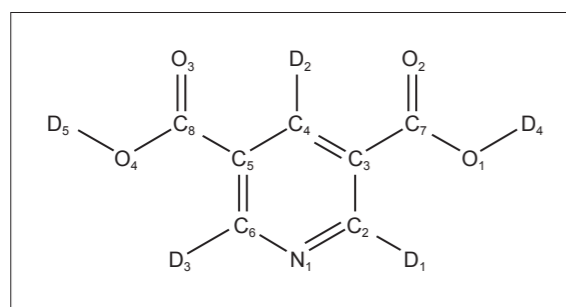


Figure 1: Room temperature molecular structure of d-35PDCA with the atom numbering scheme.

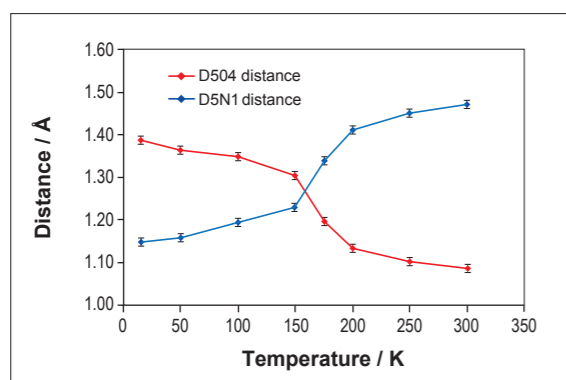


Figure 2: Temperature dependence of the D5-O4 and D5-N1 distances in d-35PDCA (red and blue curve) obtained from single crystal neutron diffraction.

Temperature-induced reversible proton migration has been well characterised in several molecular systems, including urea phosphoric acid [2], 4-methylpyridine pentachlorophenol (4MePy-PCP) [3], 1,2,3,4-tetracarboxylic acid 4,4'-bipyridyl cocrystals (BTA-BPY) [4] and 3,5-pyridinedicarboxylic acid (35PDCA) [5]. The typical magnitude of the proton migration effect in these systems is about 0.1 Å; in other words, the proton moves about 0.1 Å away from the donor atom towards or beyond the centre of the hydrogen bond. Our single crystal neutron diffraction work performed on VIVALDI, in combination with high-resolution powder neutron diffraction data and computational simulations, has enabled us to elucidate the behaviour of deuterated 3,5-pyridinedicarboxylic acid (d-35PDCA, **figure 1**), which exhibits remarkably large deuteron migration, demonstrating a dramatic isotope effect in this material.

We carried out a variable temperature experiment on VIVALDI, collecting data at 300, 250, 200, 175, 150, 100, 50 and 15 K. Excellent quality data sets were obtained at each temperature, enabling us to derive the crystallographic parameters necessary to accurately describe the behaviour of the deuteron in the SSHB. The temperature dependence of the D5-O4 and D5-N1 distances in d-35PDCA obtained from this experiment, shown in **figure 2**, reveals that the deuteron bonded to the oxygen atom at room temperature moves away from it on cooling and becomes bonded to the nitrogen atom.

The D5 - N1 distance increases from 1.159(8) Å to 1.478(6) Å between 15 K and 300 K, while the O4 - D5 distance decreases from 1.374(10) Å to 1.092(7), revealing that the deuteron migrates 0.32(1) Å

from the N donor atom towards and beyond the centre of the hydrogen bond between these two temperatures. The magnitude of this effect is significantly larger than anything observed in similar proton migration systems. Although the integrated diffraction data do not suggest any departure from space group $P2_1/c$ in this temperature range, a careful inspection of the observed Fourier maps suggested a more complex behaviour of d-35PDCA in the temperature range between 150 and 200 K, where the deuteron migration appears to occur (**figure 3**).

The 175 K map shows smeared out nuclear density, suggesting that deuteron migration in d-35PDCA is not a gradual, continuous change from the N-D form at low temperatures into the D-O form at high temperatures, as may at first appear from the evolution of bond distances in **figure 2**.

Variable temperature powder neutron diffraction data analysis has revealed a temperature region of co-existence of the N-D and D-O forms, suggesting that d-35PDCA undergoes an isosymmetric first order phase transition. The structural reorganisation in d-35PDCA which occurs at this phase transition results in a deuteron migration much larger than the proton migration in fully hydrogenous 35PDCA, in which no discontinuities of the structural parameters as a function of temperature are observed.

This is consistent with previous computational simulations of 35PDCA, where integrated molecular dynamics trajectories gave bimodal proton distributions, with protons either close to the N atom or to the O atom, but rarely centred in the hydrogen bond.

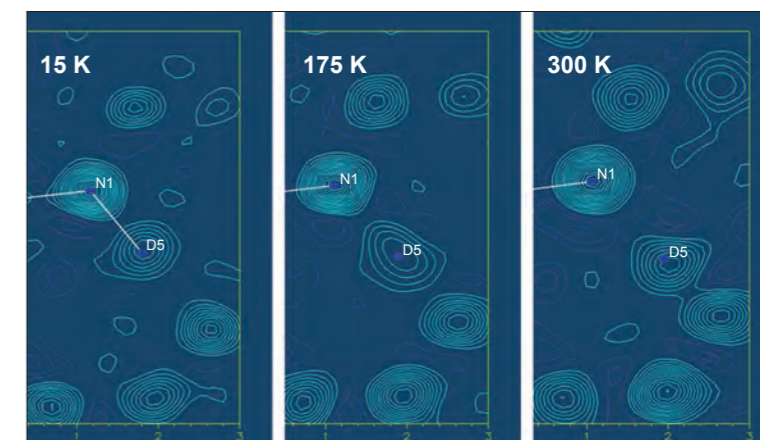


Figure 3: Observed Fourier density maps for d-35PDCA obtained from single crystal neutron diffraction.

The identification of the first-order isosymmetric phase transition as a key factor giving rise to the remarkable deuteron migration in d-35PDCA is therefore very significant, as it provides the first experimental evidence for the bi-stability of this system. Free energy calculations suggest that this phase transition is driven by vibrational free energy stabilisation, which is more pronounced for the deuterated material than for the protonated form.

This work demonstrates a successful and true synergy of experimental neutron diffraction techniques and computational modelling methods, as a necessary combination of approaches which has enabled us to elucidate the origins of the unprecedented proton/deuteron migration in a short strong hydrogen bond and the remarkable isotope effect in 35PDCA.

REFERENCES

- S. Horiuchi, F. Ishii, R. Kumai, Y. Okimoto, H. Tachibana, N. Nagaosa and Y. Tokura, *Nature Materials* 2005, 4, 163 [1]
 C.C. Wilson, *Acta Crystallographica Section B-Structural Science* 2001, 57, 435 [2]
 I. Majerz and M. Gutmann, *J. Journal of Physical Chemistry A* 2008, 112, 9801 [3]
 J.A. Cowan, J.A.K. Howard, S.A. Mason, G.J. McIntyre, S.M.F. Lo, T. Mak, S.S.Y. Chui, J.W. Cai, J.A. Cha and I.D. Williams, *Acta Crystallographica Section C-Crystal Structure Communications* 2006, 62, 0157 [4]
 J.A. Cowan, J.A.K. Howard, G.J. McIntyre, S.M.F. Lo and I.D. Williams, *Acta Crystallographica Section B-Structural Science* 2005, 61, 724 [5]

AUTHORS

A. Boehm (University of Leoben, Austria)
M. Boehm and T. Hansen (ILL)
A. Kogelbauer (VA Erzberg GmbH, Eisenerz, Austria)

High-intensity two-axis diffractometer D20

Optimising the processing of mineral ore at the Styrian Erzberg iron mine

The ever-increasing demand for raw materials from the newly developing economies is stimulating the development of more innovative processes for the efficient and competitive exploitation of comparatively poor mineral deposits in Europe. ILL's work with the Steirische Erzberg iron mine illustrates how neutron powder diffraction may be used to understand and develop new techniques for improved iron mineral extraction while meeting the highest environmental standards.



Figure 1: View of the Steirische Erzberg in the Austrian Alps.

The Steirische Erzberg is Europe's second largest operating iron ore mine (figure 1). The iron is bound in carbonaceous iron ore, which is mined in an open pit operation and delivered to local steel plants at a rate of about 2.1 million tonnes a year. The relatively poor iron content of the ore concentrate, compared to world-leading sources elsewhere (in Brazil, Australia, Ukraine or Canada), has prompted proposals to close the mine over recent decades. The recent rise in demand for raw materials, however, has stimulated the steel industry's interest in domestic ore production. The Erzberg is placing its hopes on new separation technology capable of delivering a competitive product with enriched Fe-content and lower alkaline and SiO₂ levels whilst preserving the local ecology of this Alpine region.

The low iron content of the ore concentrate is the result of the intergrowth of the local iron carbonate *spateisenstein*, or siderite, (Fe, Mn, Mg, Ca)CO₃, containing 42% iron, with ankerite, containing only 17% iron on average. The iron content is too low for industrial use.

Apart from the main ore minerals, the concentrates also contain other carbonates (5% to 10% dolomites and calcites), silicates (quartz) and sulphides with an average sulphur content of 0.06%.

The two minerals display very similar physical properties, having the same cations in their composition, although in different proportions. The industrial technology has traditionally been unable to separate them sufficiently.

The Institute of Mineral Processing at the University of Leoben, in close cooperation with VA Erzberg GmbH and voestalpine AG has now successfully established a procedure for this [1]. Selective magnetising *flash-roasting*, known as the Steiner process, decomposes the valuable *spateisenstein* into a ferromagnetic phase by strictly controlling the temperature settings between 600 and 700°C; the ankerite on the other hand remains paramagnetic.

Standard magnetic separation techniques then attract the ferromagnetic phase and reject the ankerite as well as a large proportion of the silica- and alkaline-bearing minerals. To use the iron-enriched material in the blast furnace, the magnetic product has to be re-agglomerated by grinding and then pelletising.

The idea of heat treatment is not new. What is new is the retention time of *seconds* in a reaction vessel, using oxygen-rich combustion gas as the heat and material transport medium. This not only lowers the specific energy consumption; it also influences the magnetic behaviour and increases the active surface of the new phase.

As a consequence, at the correct process settings, the thermal product absorbs most of the toxic sulphur dioxide which would otherwise need to be extracted from the flue gas by expensive filtering only. The process thus contributes to ensuring compliance with the highest European environmental standards (such as the requirement, for example, that the sulphur released in the heating process from mineral impurities like pyrite remain below the 50 mg/m³ level under normal conditions).

The decomposition of iron carbonates into iron oxides under specific external conditions is very well known [2]. It was therefore surprising that standard laboratory analysis of the final products gave contradictory results on the state of oxidation casting doubt on the validity of phase diagrams under potential non-equilibrium conditions.

We therefore followed the time evolution of the phases under different conditions (temperature ramps, gas atmosphere) in powder diffraction measurements on D20. Typically, 5g of mineral standards prepared from representative ore concentrate samples (1 tonne) were positioned in a quartz glass tube and connected to an artificial gas source containing 12 vol-% oxygen, 6 vol-% CO₂ and 2000 mg/m³ SO₂ in N₂.

The high neutron flux allowed for reliable detection statistics within a time frame of 30 seconds, sufficient for observing the time evolution of the different solid phases (as shown in the example of figure 2). The composition of the off gas was detected simultaneously by electrochemical cells for O₂, CO and SO₂ inside standard flue gas control equipment.

Figure 2 shows that besides the expected hematite, α-Fe₂O₃, a cubic Fd3m phase emerges at the flash-roasting temperature, refined as a ferrite (Fe 89%, Mg 4%, Mn 6% and Ca 1%)₃O₄, with the divalent ions (Ca, Mg) occupying the tetrahedral sites and the trivalent ions (Fe, Mn) occupying the octahedral sites. Maintaining gasification at a constantly high temperature favours the steady increase of hematite at the expense of the ferrite. It is the interruption of the process kinetics in the flash-roasting process that provides the ferrite phase with the required magnetic properties.

The D20 experiments have allowed us to calibrate the degree of alteration reliably as a function of temperature in different gas atmospheres. This provides made-to-measure data for computerised simulations to be performed by the company on site at the plant to improve process control and performance.

The 180 M€ plant has now passed its environmental risk assessment. Its construction will expand employment opportunities in the Erzberg.

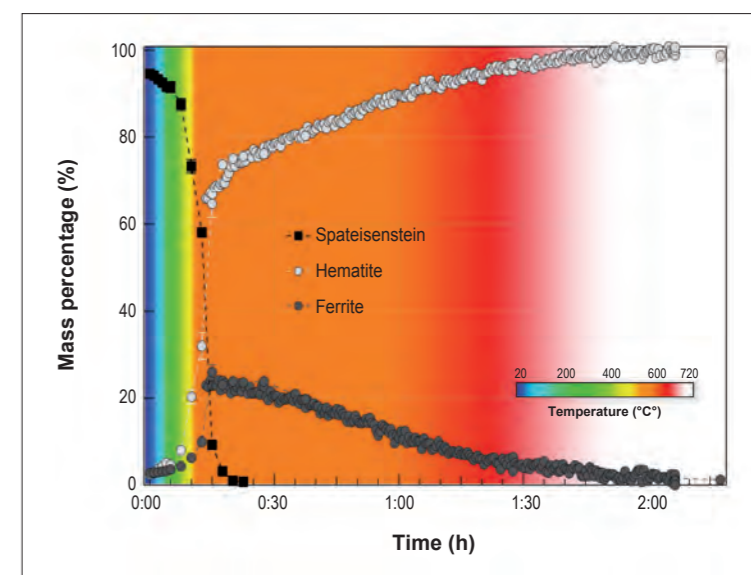


Figure 2: Mass distribution as derived from Rietveld refinement during the decomposition of *spateisenstein*.

REFERENCES

A. Böhm, M. Böhm and A. Kogelbauer, In *Proceedings of the XXIII International Mineral Processing (2006)* [1]
Congress Volume III, Chapter 20 (ed: G. Önal), 2423-2428
Gmelin-DurrerMetallurgie des Eisens, Bd.1a. In *Gmelins Handbuch der anorganischen Chemie, 8.Aufl* (ed: Gmelin-Institut für anorganische Chemie und Grenzgebiete in der Max-Planck-Gesellschaft zur Förderung der Wissenschaften) (1964), 188a-232a [2]

AUTHORS

S. Mazumder, D. Sen and J. Bahadur (Bhabha Atomic Research Centre, Mumbai, India)
J. Klepp (University of Vienna, Austria)
H. Rauch (University of Vienna, Austria and ILL)
J. Teixeira (LLB, France)

Interferometer S18
Small-angle scattering diffractometer PAXE (LLB)

The isotope effect in the temporal evolution of mesoscopic structures during the hydration of cement

The cement manufacturing process contributes about 5-7% of man-made and 4% of total global CO₂ emissions. To improve the lifetime of cement and its macroscopic properties (such as compressive strength, permeability, elastic modulus etc.) it is important to understand the mechanisms determining its hydration and how cement-water mixtures develop their high compressive strength. This study aims to improve our understanding of the mechanisms involved in cement hydration as well as the temporal evolution of the mesoscopic structure of the cement paste which exhibits temporal oscillations, strongly dependent on the hydration medium (H₂O or D₂O). Neutron scattering is a technique ideal to our purpose, since neutrons are particularly sensitive to hydrogen atoms and the scattering power varies significantly in different isotopes of the same element.

Cement has become an essential modern material, indispensable to the construction industry, nuclear energy (it is used to immobilise non-heat-generating low-level radioactive waste) and the petroleum industry (oil wells are lined with cement slurry). Portland cement is a composite material consisting of fine grains of tri-calcium silicate, 3CaO.SiO₂ (C₃S) along with other minor constituents. When cement and water are mixed, a complex series of hydration reactions take place [1] of which the main products are an amorphous calcium-silicate-hydrate (C-S-H) with a gel-like structure and crystalline Ca(OH)₂. Cement has been the object of study for over a century, but our understanding of the mechanisms by which cement-water mixtures turn into gel leaves much to be desired [2].

Because the H₂O and D₂O hydration processes differ, due to the different properties of the hydrogen bonds formed between the substrate and the light or heavy water, we decided to investigate the evolution over time of the mesoscopic structure of cement paste in different hydration media.

We performed ultra-small-angle neutron scattering (USANS) on the interferometer S18 at the ILL to investigate the temporal evolution of the mesoscopic structure of hydrating cement paste. **Figure 1** shows the temporal evolution of C₃S (described by the scattering function S(q=0, t)) for light and heavy water hydration (with time periods of apparent silence in between), albeit with non-regular periodicity. In contrast, for D₂O hydration, S(q=0, t) decreases without any significant oscillatory behaviour, (**figure 1b**).

This proves that - in the case of H₂O hydration - the hydration reaction leads to non-monotonic growth in the cement structure. Cement particles in contact with H₂O initially form a water-rich C-S-H sol and Ca(OH)₂ causing an increase in S(0, t) [3]. After some time - depending on the w/c ratio - the sol in contact with the cement particles transforms into a cement-rich C-S-H gel causing a decrease in S(0, t). The maxima of S(0, t) correspond to the sol-to-gel transition. The periodic variation of S(0, t) with t is due to the fact that the C-S-H gel initially forms a protective layer on the unreacted part of a cement grain. After a certain time, this protective hydration layer breaks, causing a sudden growth of fresh hydration products from unhydrated cement surfaces (shown in the resumption of growth of S(0, t)). The process is repetitive.

For hydration with D₂O, a mass fractal calcium-silicate-deuterate (C-S-D) gel is formed initially. Both the fractal dimension and the linear dimension of the mass fractal C-S-D gel grow in the early stages. Later, when unreacted C₃S and D₂O are considerably depleted, the reaction progresses with a negligible amount of

C-S-D and a relatively large amount of Ca(OD)₂. At this stage, the gel consolidates, resulting in a reduction in size associated with increasing fractal dimension. The hydrated gel attains a uniform internal density with the outer surface exhibiting self-similarity. Overall contraction of the gel and deposition on the surface of the gel continues, leading to the formation of a mass fractal structure with a solid core.

Having observed a striking isotope effect in the temporal evolution of the bulk structure, we considered that it would be useful to examine the temporal evolution of the interface structure of the gel at shorter length scales. Measurements were therefore carried out with a pinhole collimation SANS instrument. **Figure 2(a)** shows S(q, t), measured with the PAXE spectrometer at LLB for C₃S with H₂O and D₂O hydration, with a 5-minute time interval between measurements. **Figure 2(b)** shows the temporal evolution of the Porod exponent, η(t), assuming that S(q, t) is proportional to q^{-η(t)}. While η(t) for all H₂O hydrating specimens lies in the 4.3 - 3.93 range, for D₂O the hydrating specimen η(t) decreases from 4.187±0.083 to 4.09±0.075 at about the 500 minutes mark, then rises to 4.5±0.085 at a time slightly longer than 2000 minutes; it finally decreases monotonically, with different slopes, to 3.86±0.073 at about 4000 minutes.

The positive deviation of η(t) from 4 is indicative of the diffuse interface of the gels. For H₂O hydrating specimens (**figure 2b**), the C-S-H gel has a diffuse interface in the length scale of 10²-10³ Å initially. As time progresses, the interface becomes sharp and tends to have surface fractal morphology after the onset of the reaction. In contrast, for the D₂O hydrating specimen, the temporal evolution of the surface morphology of C-S-D gel is non-monotonic. To begin with, the gel interface is diffuse but its width decreases initially before rising and finally falling, to display surface fractal morphology. The temporal evolution of the surface morphology of the gel is strongly length-scale dependent, in both cases.

In conclusion, the mesoscopic structure of cement paste exhibits isotope effects. The structure exhibits temporal oscillations - strongly dependent on the scale of observation and on the medium of hydration. A sol-to-gel transition is observed for hydration with H₂O. While the formation of Ca(OH)₂ and C-S-H gel is synchronous for hydration with H₂O, the process is non-synchronous for hydration with D₂O. The structures arise from chemical reactions as water diffuses through the porous material within the complex local geometry. The isotopic effect is due to the more stable hydrogen bonds in the case of D₂O. This investigation has taken us a step forward in our understanding of long hydration processes.

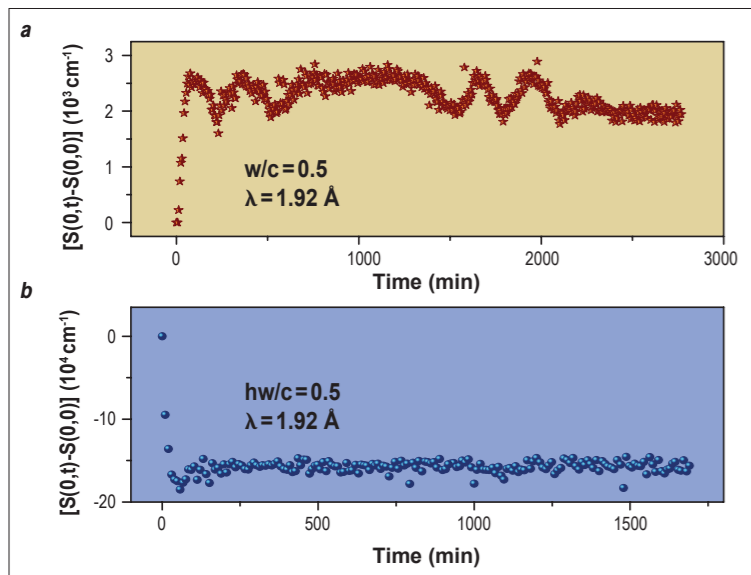


Figure 1: (a) Temporal evolution of S(0,t) for H₂O hydrating C₃S with w/c = 0.5 (b) Temporal evolution of S(0,t) for D₂O hydrating C₃S with w/c = 0.5. Statistical error bars are smaller than the corresponding symbol sizes.

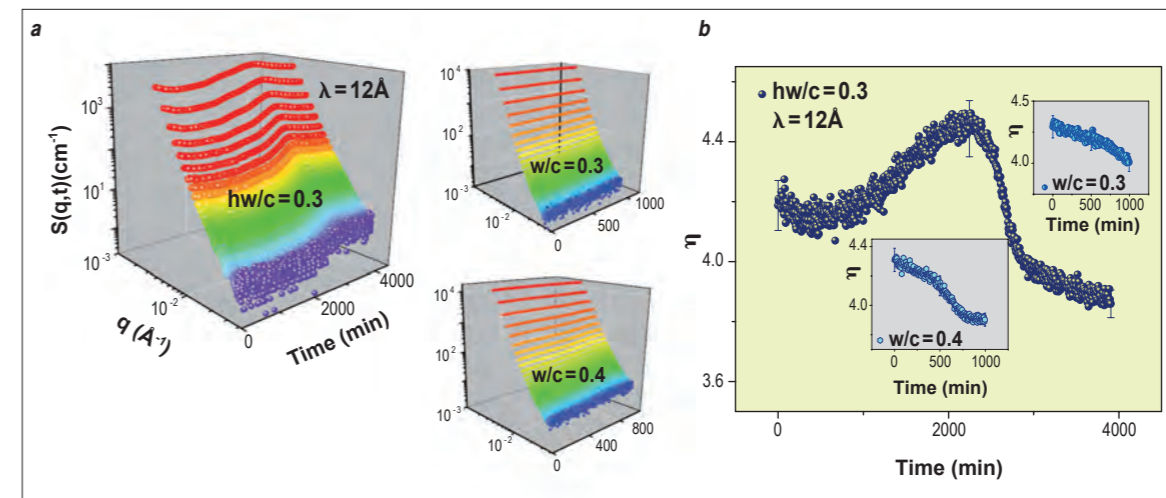


Figure 2: (a) Temporal evolution of S(q,t) for H₂O hydrating C₃S with w/c = 0.3 and w/c = 0.4; and for D₂O hydrating C₃S with w/c = 0.3. Statistical error bars are smaller than the corresponding symbol sizes; (b) Temporal evolution of η(t) associated with power-law scattering, as estimated from ln(S(q,t)) vs ln(q) in the q range 0.0042-0.017 Å⁻¹, for various H₂O and D₂O hydrating specimens.

REFERENCES

H.F.W. Taylor, Cement Chemistry (1990) (Academic Press, London) [1]
H.L. Le Chatelier, Experimental Researches on the Constitution of Hydraulic Mortars (1905) (McGraw, New York) [2]
S. Mazumder et al., Phys. Rev. B. 82 (2010) 064203 [3]

AUTHORS

D. Rébiscoul, T. Morel, C. Jayet and P.H. Haumesser (CEA-MINATEC Grenoble, France)
V. Perrut (31 Degrees Montauban, France)
R. Cubitt (ILL)

Alkoxysilane layers compatible with copper deposition for advanced semiconductor device applications

In semiconductor devices copper is widely used to fabricate interconnects using the *damascene architecture* (figure 1). This architecture – which is necessary because it is not possible to etch Cu - requires barrier/adhesion layers which are generally TiN or Ta/TaN, on a insulating dielectric material. Because of the downscaling of integrated circuit, the thickness of these barrier layers needs to be reduced below 30 Å which is a challenge in process manufacturing. In this context, organic self-assembled monolayers are studied for their ultra-thin thickness (10 to 20 Å) and their barrier properties at the copper/dielectric interface [1]. The knowledge of the morphology and structure of such alkoxysilane layers is mandatory to control their continuity and efficiency as a barrier against copper diffusion.

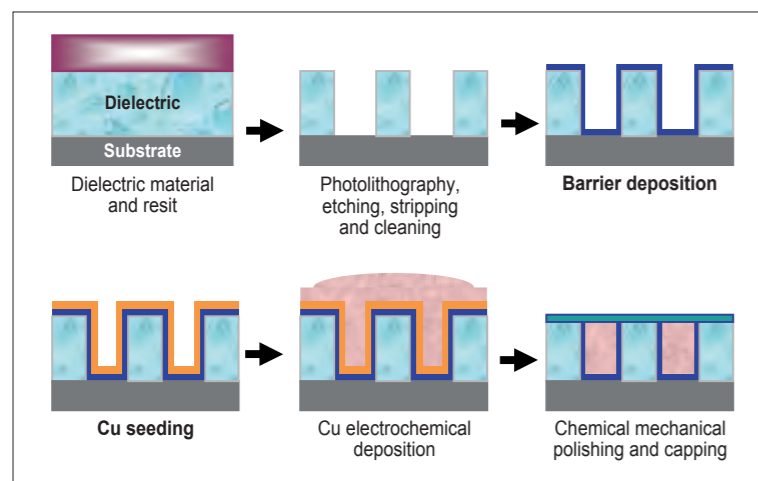


Figure 1: Presentation of the main steps used to manufacture a damascene architecture.

For this study, alkoxysilane films obtained from silanes having various functional head groups, such as amino- (-NH_2 , APTMS), mercapto- (-SH , MPTMS), aminoethylaminopropyltrimethoxysilane (-NH_2 , AEAPTMS) were deposited on a porous dielectric material by supercritical carbon dioxide processes (dynamic and static mode), and coated with copper by Physical Vapor Deposition (PVD) and Metal Organic Chemical Vapor Deposition (MOCVD). The morphological characteristics of the layers, their ability to receive copper deposits and their impact on copper morphology have been investigated by atomic force microscopy and two complementary methods particularly interesting to thin layers characterisation: X-ray and neutron reflectivity (NR).

X-ray reflectivity is sensitive to the electron density (via X-ray-electron interactions) whereas NR responds to the nuclear scattering length density (via neutron - nucleus interactions). Therefore neutron reflectivity is well adapted to characterise alkoxysilane layers - sandwiched between the dielectric and copper - because they have a low coherent scattering length compared to

both surrounding materials. By the complementary use of these techniques, it is possible to extract information on the influence of the chemical nature of the alkoxysilane layers on the quality of the copper films.

The NR measurements performed on the D17 reflectometer and coupled with X-ray reflectivity show that copper PVD is not compatible with a silanised surface degraded by the physical impact of the Cu atoms during the process, whereas the layer remains intact after a MOCVD process at 200°C. Moreover, dense and thin films having small copper grains were obtained with MPTMS and AEAPTMS layers and thick films having low density and large copper grains were obtained with an aminopropyltrimethoxysilane layer (figure 2). In fact, the formation of specific copper film morphologies depends on the capability of the sample surface to immobilise copper atoms, modifying the nucleation and growth of the metal [2].

For the sample without alkoxysilane, copper deposition is not observed on the dielectric. Indeed, copper is known to have a high mobility on SiO_2 surfaces due to the relatively weak interactions between Cu and Si or O atoms. Therefore copper deposition on SiO_2 is difficult [3].

For surfaces having available electron donor atoms such as S and N like the used alkoxysilane layers, copper atoms are probably less mobile on the surface. These donor atoms can act as privileged nucleation sites. Also, the limited mobility of Cu atoms on the substrate is expected to hamper growth which proceeds through diffusion of adatoms. Consequently, copper nucleation is favoured on alkoxysilane layers.

Meanwhile, depending on the structure of the silane layer, the copper film morphology is different. In our previous study [4] we have characterised the structure of these silane layers on dense SiO_2 : MPTMS and AEAPTMS formed thin self-assembled monolayers whereas aminopropyltrimethoxysilane formed thick

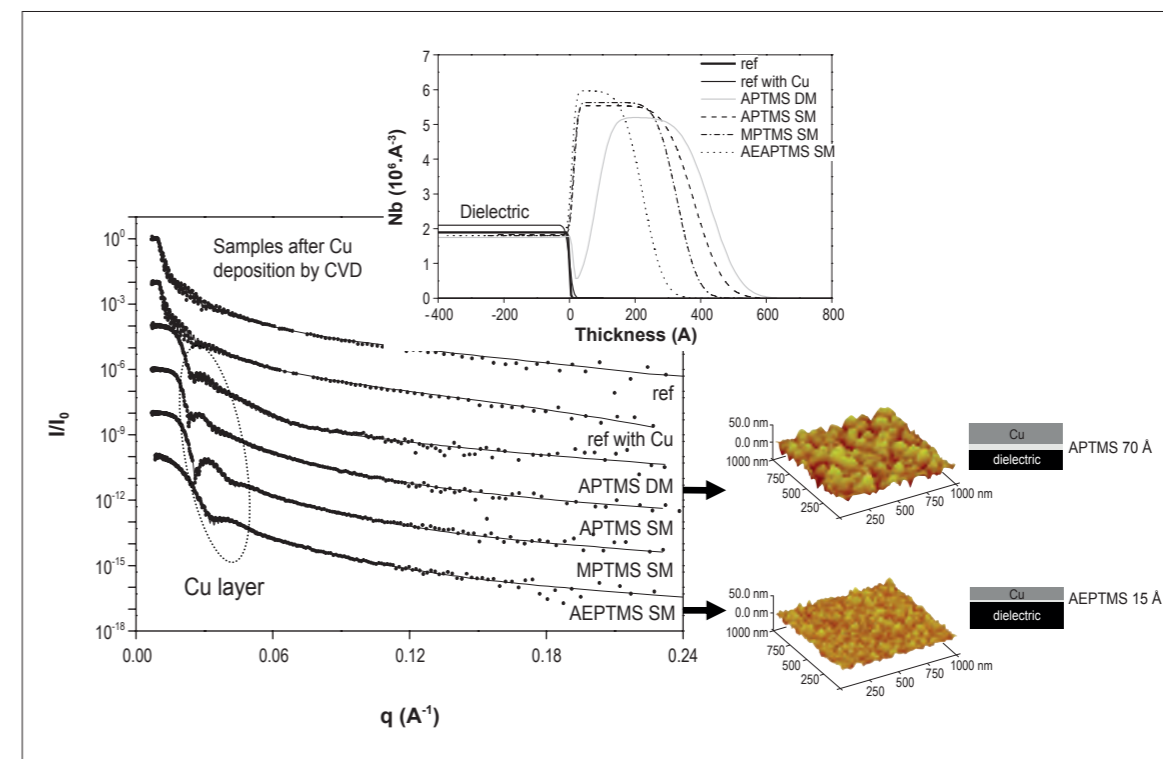


Figure 2: Experimental and simulated neutron reflectivity curves of the samples before and after Cu deposition by MOCVD obtained on the D17 reflectometer. The corresponding scattering length density profiles and the atomic force microscopy images are given in the inset. DM: dynamic mode; SM: static mode.

polycondensed layers. The same types of layers are obtained on porous dielectric material. In self-assembled monolayers, the functional head groups point to the surface leading to a high density of nucleation sites allowing the formation of thin and dense copper films having small grains. On the contrary, for the polycondensed aminopropyltrimethoxysilane layers, molecules are randomly oriented. X-ray photoelectron spectroscopy data and water contact angle of such layers have suggested that some of the -NH_2 head groups are oriented towards SiO_2 surface, exposing alkyl chains. Consequently, the lower density of NH_2 nucleation sites on aminopropyltrimethoxysilane surface leads to higher copper grain sizes. For the AEAPTMS molecule, the presence of an additional N-H in the alkyl backbone of the compound can stabilise

the molecule in vertical position by hydrogen bonding between -NH and H favouring the formation of a monolayer and leading to a high density of -NH_2 head groups pointing to the surface.

In conclusion, we showed that MPTMS and AEAPTMS are the best candidates for the deposition of a thin and dense copper layer by MOCVD process, because of their ultra-thin nature (10 to 15 Å) and their high density of nucleation sites for copper. In the future, the adhesion properties between these silane layers and copper and the impact of annealing on copper diffusion through the porous dielectric material will be investigated in order to determine the reliability of such structure from morphological and electrical point of view.

REFERENCES

- D.D. Gandhi, M. Lane, Y. Zhou, A.P. Singh, S. Nayak, U. Tisch, M. Eizenberg and G. Ramanath, Nature 447 (2007) 299 [1]
- S. Swada, Y. Masuda, P. Zhu and K. Koumoto, Langmuir 22 (2006) 332 [2]
- Z-Z. Liu, Q. Wang, X. Liu and J-Q. Bao, Thin Solid Films 517 (2008) 635 [3]
- D. Rébiscoul, V. Perrut, O. Renault, F. Rieutord, S. Olivier and P-H. Haumesser, J. Supercritical Fluids 51, 2 (2009) 287 [4]

AUTHORS

D. Zehm and A. Laschewsky

J.-F. Lutz (Fraunhofer Institute of Applied Polymer Research, Potsdam, Germany)

P. Heunemann (ILL and TU Berlin, Germany)

R. Schweins (ILL)

J. Gummel (ESRF)

S. Prévost (TU Berlin and HZB, Germany)

M. Gradzielski (TU Berlin, Germany)

Giant surfactants made of amphiphilic dual brush block copolymers and their self-assembly in aqueous solution

We have extended the concept of amphiphilic molecules, such as surfactants or block copolymers, to dual brush block copolymers - "giant surfactants" with a molecular weight (M_w) of several 100.000 g/mol. Brush copolymers have densely grafted side-chains rather than simple polymer chains. They can be synthesised for different brush blocks of hydrophobic and hydrophilic domains and can be disperse in water. Our small-angle neutron and X-ray scattering measurements (SANS and SAXS) have shown that they form well-defined aggregates in aqueous solutions whose size and structure is controlled by packing considerations in a fashion similar to conventional surfactants, thereby revealing a new type of nanostructured self-assembled aggregate.

Water-based amphiphiles conventionally come in the form of surfactants ($M_w = 200-1000$ g/mol) or copolymers ($M_w = 2000-50000$ g/mol) [1]. They are widely employed for dispersing otherwise insoluble compounds in formulation applications ranging from detergency to drug delivery; they typically contain hydrophobic domains with a size range of 2-20 nm.

The amphiphilic molecule model can be extended to much larger sizes if, instead of using straight chain molecules, we use molecules with a brush architecture, i.e., containing grafted side-chains along a backbone [2, 3].

We synthesised these amphiphilic dual brush diblock and triblock copolymers by the overlay of reversible addition fragmentation chain transfer (RAFT) and nitroxide mediated polymerisation techniques (NMP), thereby obtaining copolymers of several hundred thousand M_w . In these polymers poly(ethyleneglycol) brushes (made from Poly(ethylene glycol monomethyl etheracrylate) (PEGA)) form the hydrophilic moiety, while polystyrene (PS) or poly(*n*-butyl acrylate) (PnBA) brushes provide the hydrophobic part [4]. These polymers therefore resemble surfactants from a fundamental structural point of view, although their hydrophilic and hydrophobic units are about a factor 100-1000 larger than in conventional surfactants (see **figure 1**). We studied the aggregation behaviour of these "giant surfactants" in an aqueous solution using a combination of dynamic light scattering (DLS), SANS and SAXS measurements.

The experimental investigation of the polymers with the hydrophobic PnBA component showed that in aqueous solution they form stable mesoscopic, spherical aggregates with sizes in the range of 150 to 350 nm; the size is determined by the length of the stretched polymer molecules. The scattering experiments for the dual brush copolymers (copolymers where both hydrophilic and hydrophobic block have a brush architecture) showed that a compact structure is formed, dominated by the large hydrophobic poly(*n*-butyl acrylate) (nBA) block. **Figure 2**, shows SANS curves for the single brush copolymer $(\text{PEGA})_{192}$ - b - $(\text{CIPEA})_{72}$ - b - $(\text{PEGA})_{192}$ (without the hydrophobic side chains

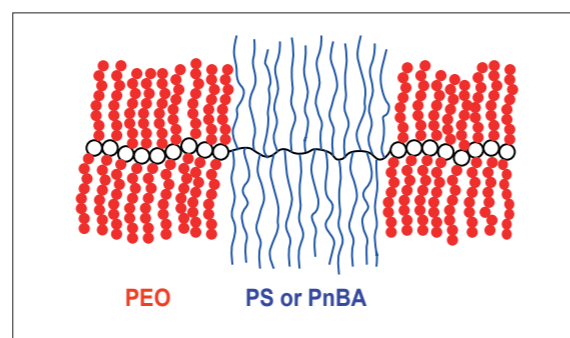


Figure 1: Schematic drawing of the structure of triblock giant surfactants of dual brush structure (central part with the blue lines depicting the hydrophobic side chains PS or PnBA, the outer parts with the red dots depicting the hydrophilic PEO side chains).

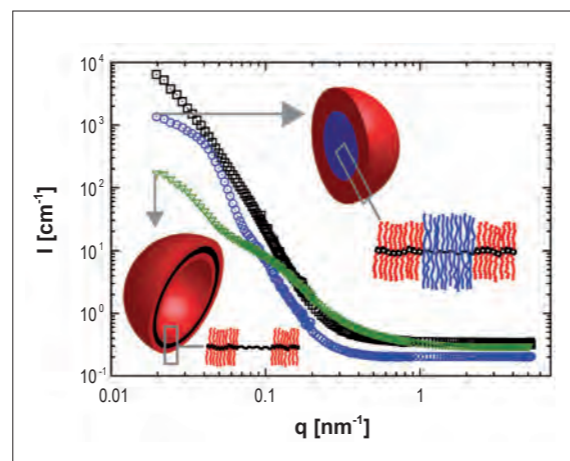


Figure 2: SANS intensity as a function of the magnitude of the scattering vector, q , at 25°C: (∇) 1.0 wt% $(\text{PEGA})_{192}$ - b - $(\text{CIPEA})_{72}$ - b - $(\text{PEGA})_{192}$ in D_2O ; (\square) 0.9 wt% TriB-1 $(\text{PEGA})_{192}$ - b - $(\text{CIPEA-g-BuA}_{51})_{72}$ - b - $(\text{PEGA})_{192}$ in D_2O/DMF (10:1); (\circ) 0.1 wt% TriB-1 in D_2O .

shown in **figure 1** in the centre) and for the dual brush triblock copolymer 1 TriB-1 $(\text{PEGA})_{192}$ - b - $(\text{CIPEA-g-nBA}_{51})_{72}$ - b - $(\text{PEGA})_{192}$ in D_2O and a DMF/ D_2O mixture [4].

The aggregation number for the dual brush is about 10 times higher than for the single brush copolymer, due to the packing requirements for the much bulkier hydrophobic core.

The formation of aggregates is clearly visible in all cases, while for the macroinitiator a vesicular structure is formed (due to the much larger hydrophilic block – and the correspondingly different packing parameter for this molecule); for the dual brush TriB-1 large micelles with a hydrophobic core of 40 nm radius are formed. They are relatively monodisperse in water but much more so in a DMF/water mixture. It is therefore possible not only to form well-defined micellar aggregates from these giant surfactants, which possess an internal hierarchical order, but also tune their aggregation behaviour by the polarity and type of solvent.

Essentially similar aggregation behaviour in aqueous solutions can be observed when switching from PnBA to PS for the side chains of the hydrophobic brush, despite the fact that PS is below the glass transition temperature and PnBA above. The samples were prepared by adding water or water/DMF (10/1) to a concentrated THF solution of the polymers. The SAXS and SANS measurements on identical samples of triblock brush copolymers are presented in **figure 3** for two polymers. The two polymers differ mainly in the length of the hydrophilic brush, which is about 5 times larger for TriB-4 compared to TriB-3. From the combined analysis of the SANS and the SAXS data, the aggregation number can be determined to be 1530 and 440 with Guinier radii of 92 and 58 nm for TriB-3 and TriB-4, respectively [4]. This means that the larger aggregates are formed by the smaller polymer. This is explained by the fact that the ratio of the hydrophilic part to the hydrophobic part is smaller here, favouring the formation of larger aggregates due to the packing conditions.

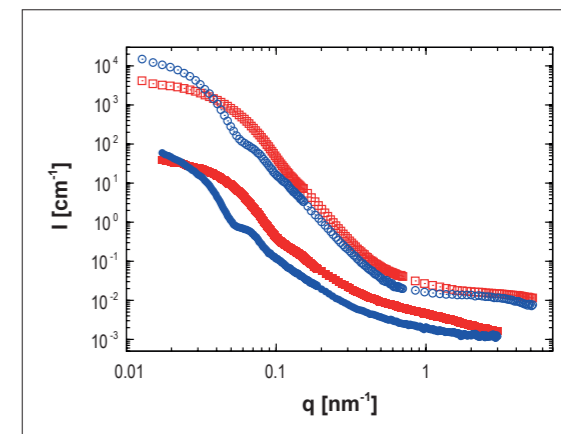


Figure 3: SANS and SAXS intensity as a function of the magnitude of the scattering vector q for 1 wt% samples of TriB-3 $(\text{PEGA}_{32}$ - b - $(\Phi\text{TEA-g-PS})_{88}$ - b - PEGA_{32}) (blue circles) and TriB-4 $(\text{PEGA}_{160}$ - b - $(\Phi\text{TEA-g-PS})_{108}$ - b - PEGA_{160}) (red squares) in D_2O (open symbols: SANS from D11; closed symbols: SAXS from ID02).

In conclusion, these dual brush block copolymers constitute a novel class of amphiphiles appropriately named "giant surfactants". Their aggregation properties are very similar to those of conventional amphiphiles and are determined by the packing parameter. They can be made with very different hydrophobic liquid or glassy cores, from which one can form frozen nanostructured aggregates below their glass transition temperature. The latter ones then can be deposited on surfaces without morphological change [4]. The dimensions of the aggregates reflect the size of the "giant surfactants"; their building blocks show a well-defined microstructure due to the molecular architecture of their constituting molecules. With their hierarchical molecular architecture and the ability to control the local brush structure, these are complex but well-defined self-assembled aggregates which open up interesting perspectives as nano-structured and selective delivery vehicles.

REFERENCES

1. Piirma, Polymeric surfactants. In Surfactant Science Series; Marcel Dekker: New York, 1992; Vol. 42 [1]
2. K. Ishizu, J. Satoh, K. Toyoda and A. Sogabe, J. Mater. Sci. 39 (2004) 4295 [2]
3. Z. Li, J. Ma, C. Cheng, K. Zhang and K.L. Wooley, Macromolecules 43 (2010) 1182 [3]
4. D. Zehm, A. Laschewsky, P. Heunemann, M. Gradzielski, S. Prévost, H. Liang, J.P. Rabe and J.-F. Lutz, Polym. Chem. 2 (2011) 137 [4]
5. D. Zehm, A. Laschewsky, M. Gradzielski, S. Prévost, H. Liang, J.P. Rabe, R. Schweins and J. Gummel, Langmuir 26 (2010) 3145 [5]

Near-surface solvent content profiles during solution casting

Polymer coatings such as paints, corrosion protections, adhesives or organic electronic devices play a key role in science, industry and everyday life. One widely-used processing method is to dissolve the polymer, spread the solution onto the desired support and let the solvent evaporate. This “solution casting” technique permits thicknesses ranging from a few nanometers to millimetres. There is also almost no limitation to the shape of the polymer film.

Solvent evaporation can be one of the driving forces influencing the surface roughness or morphology of polymer coatings; good knowledge of the underlying kinetics is therefore of utmost importance [1]. Solvent loss rates reported in the literature depend on time t as t^k , where k can vary between $1/2$ and 1 . These studies consider the total amount of solvent as a function of time. We, in contrast, focus on the near-surface part of drying polymer films, using *in situ* neutron reflectometry (NR) on ILL's FIGARO. With this method even small concentration variations as a function of distance from the sample surface can be detected.

To be more precise, the near-surface solvent content profile of solution-cast polymer films is monitored as a function of time and of molecular weight. We start from freshly coated, toluene-based poly(*n*-butylacrylate-*stat*-methylacrylate) (P(*n*BA-*stat*-MA)) solutions, which present a model system for pressure-sensitive adhesives, and we perform continuous NR experiments until the extractable solvent has evaporated. By choosing protonated polymers and deuterated toluene we ensure that the neutrons provide very high contrast between the solvent and the polymers; the components of the copolymer are deliberately not distinguishable.

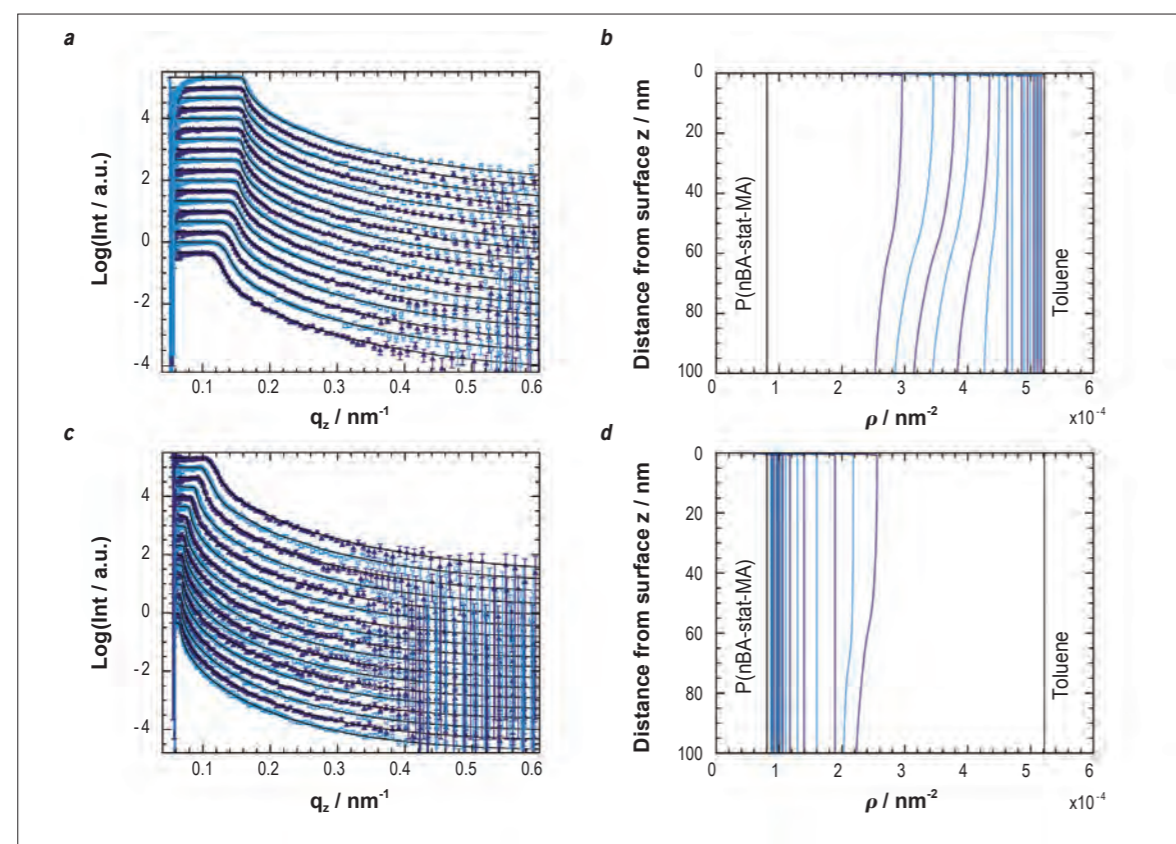


Figure 1: (Left) *In situ* NR data for the drying process of P(*n*BA-*stat*-MA) with a molecular weight $M_w = 600 \cdot 10^3$ g/mol. For clarity, the curves have been shifted along the y-axis and presented in separate graphs. The sample age increases from top to bottom. **(Right)** The corresponding SLD profiles, in which the sample age increases from left to right. The SLDs of the materials involved are marked by the vertical lines (see labels).

Figures 1a and **1c** show (from top to bottom) the evolution with time of the reflectivity curves in the first 5 hours after casting the solution onto the substrate, for a molecular weight of $M_w = 600 \cdot 10^3$ g/mol (symbols). The data of several measurements was summed up on the basis of the counting rates and evaporation speed. The black solid line shows the fit to the data. The first curve is still equal to the NR data of liquid toluene. After this, the shift of the critical edge accelerates before it converges to zero for large t .

Figures 1b and **1d** show the corresponding scattering length density (SLD) profiles. The data is fitted assuming homogeneously distributed toluene except for a time interval of 20 min (see curves 13 to 20 counting from the top). There is a 60 nm region in this time interval at the top of the sample in which the solvent concentration is higher here than in the bulk. The length of the corresponding time interval and the amplitude of the difference in concentration between bulk and surface increase with increasing molecular weight.

To our knowledge, there are no theoretical predictions of this phenomenon, although recent molecular dynamics simulations have shown comparable effects [2]. The free-volume theory [3, 4] may provide an explanation: close to the sample surface the chain end density deviates from the bulk value and this allows further trapping of the solvent.

Figure 2 shows the solvent loss $1-n(t)$ as a function of time, normalised to the point at which deviation from pure toluene NR data is detected; $n(t)$ is the solvent concentration. For the stages of inhomogeneous solvent distribution, $n(t)$ is determined by averaging the SLD profiles over the interval $z \in [0; 100$ nm].

For the samples with the two highest molecular weights, the solvent loss is proportional to time in the early stages; this is also called case II diffusion and is classically predicted for glassy polymers. Beyond the early stages, near-surface solvent evaporation accelerates showing power law behaviour exactly proportional to t^3 . To our knowledge this exceeds all reported evaporation velocities. It has to be considered, however, that our experiment focuses on

the near-surface region. It is possible that the solvent trapped in the enhanced near-surface free volume is released in this phase and contributes in addition to the ongoing case II evaporation.

For the sample with the lowest molecular weight, the early stages of solvent loss cannot be split into two regions. This might be attributable to a lower degree of near-surface solvent trapping. If we neglect the first two data points, a best fit to the data leads to a power law in which the solvent loss is proportional to t^2 . There is still, nevertheless, strong deviation from a case II diffusion.

In summary, the complete near-surface solvent evaporation process for a polymer melt has been monitored *in situ* for the first time. We have revealed a new aspect of the process by focusing on the region close to the sample surface. Further experimentation with other classes of polymer and other solvents would almost certainly provide even more insight.

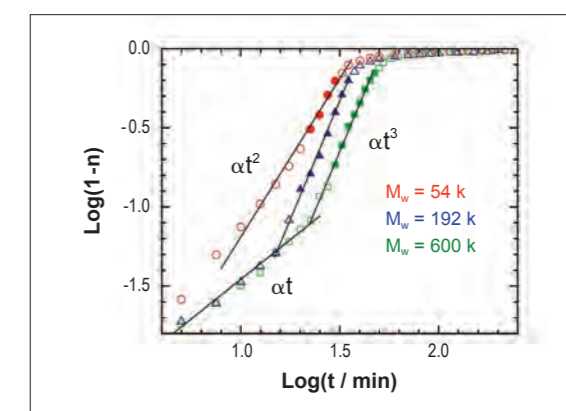


Figure 2: Near-surface solvent loss $1-n$ as a function of time t for P(*n*BA-*stat*-MA) with $M_w = 54 \cdot 10^3$ g/mol (circles), $M_w = 192 \cdot 10^3$ g/mol (triangles) and $M_w = 600 \cdot 10^3$ g/mol (squares). The data points for stages with solvent enrichment at the surface are shown as filled symbols, whereas open symbols represent a homogeneous distribution of the solvent.

REFERENCES

- A. Diether, Y. Peykova, N. Willenbacher, and P. Müller-Buschbaum, ACS Appl. Mater. Interfaces 2 (2010) 2060 [1]
- S. Peter, H. Meyer and J. Baschnagel, J. Chem. Phys. 131 (2009) 014902 [2]
- Z. Yu, U. Yahi, J. McGervey, A. Jamieson and R. Simha, J. Polym. Sci. Part B: Polym. Phys. 32 (1994) 2637 [3]
- A.M. Mayes, Macromolecules 27 (1994) 3114 [4]

AUTHORS

L. Porcar (ILL and University of Delaware, Newark, USA)
 Y. Liu (University of Delaware, Newark and NCNR, Gaithersburg, USA)
 W.-R. Chen and K. Hong (ORNL, Oak Ridge, USA)
 P. Falus (ILL)
 A. Faraone (University of Delaware, Newark and University of Maryland, USA)
 E. Fratin and P. Baglioni (University of Florence, Italy)

Dynamic clusters in lysozyme solution

The phenomenon of protein clustering has attracted a lot of interest in recent years, given its importance in various disease processes and as a promising technique for storing high concentrations of functioning proteins, thus opening up a new route for drug delivery. We present a fundamental first step toward the complete understanding of the cluster formation process for a model protein (lysozyme), probing the static and dynamic protein solution properties using small-angle neutron scattering (SANS) and neutron spin-echo (NSE) techniques.

A great deal of theoretical and experimental expertise has recently been devoted to investigating the structure and dynamics of colloidal systems displaying both short-range attraction and long-range repulsion, which these are ubiquitous in many charged biological systems such as protein solutions. The tuning of these interactions generates rich colloidal phase behaviour that can lead to monomer, cluster, gel, or glass phases. The ability to understand and quantitatively predict the properties of such systems can be of benefit to a wide range of disciplines from the material and life sciences to the pharmaceutical industry.

The current limited microscopic understanding of the physical picture has, however, generated a lot of debate and impeded application to other systems. Since nanometre-size objects like proteins are so small, traditional techniques, such as light scattering or confocal microscopy, provide little useful information. SANS and NSE techniques, however, can play a critical role in determining the structural and dynamical information on the nano-scale, due to their ability to probe the appropriate length and time scales.

The formation of finite-size clusters in protein solutions is fascinating and can lead to a better control of general colloidal structures by simply tuning the potentials involved. But observing these structures has relied on the accurate interpretation of sophisticated scattering data from small-angle neutron and X-ray scattering measurements (SANS and SAXS). The experimental conditions triggering the onset of clustering and its physical origin are still not clear and remain under debate. The extra peak in the SANS/SAXS pattern, that appears at much lower scattering angles with respect to the monomer-monomer interaction peak, has been attributed to the cluster-cluster correlation, and has therefore been named the "cluster peak" [1]. This "cluster" peak has been considered as a characteristic feature of cluster formation. This concept has been challenged using SANS/SAXS techniques, and the absence of clusters in solution has been claimed [2].

Combining SANS and NSE to access the fundamental process of cluster formation, we have investigated the correlation between the structure and the motions of protein in solutions at nanosecond timescales [3]. We have found that there is no direct correlation between the appearance of a "cluster" peak and the formation of clusters in solution. The occurrence of the "cluster" peak is due to the formation of an intermediate range order in solution, determined by the combination of short-range attraction and long-range repulsion [4]. Dynamic clusters only form at relatively high concentrations [3].

Figure 1a shows the SANS pattern – measured on D22 – of 5 wt% lysozyme solution, with the corresponding quantitative analysis of the scattered intensity, using a model fit based on statistical mechanical theories. Interestingly, the extracted structure factor presents two correlation peaks with both a so-called "cluster" peak and a monomer-monomer peak (**figure 1b**). In principle, SANS only provides a snapshot of the structure of a solution. It cannot tell whether proteins can move together, which is a necessary condition for cluster formation.

For this reason the existence of clusters has to be examined by studying the dynamic behaviour of protein solutions, rather than their simple structural characterisation alone. NSE experiments on IN15 were performed to elucidate the cluster's stability and to determine the true nature of the clusters (permanent or dynamic). The normalised intermediate scattering function was measured by NSE for different lysozyme concentrations as reported in **figure 1c** for the 5%wt case. The collective diffusion coefficient at the short time limit was extracted and a hydrodynamic radius of clusters was quantified as shown in **figure 1d**. The change in the hydrodynamic radius shows that there is no dominant clustering effect at 5% although there is a clear low-Q peak. Through more careful data analysis we identified the origin of the "cluster" peak, which is due to the formation of intermediate range order (IRO) structure [4].

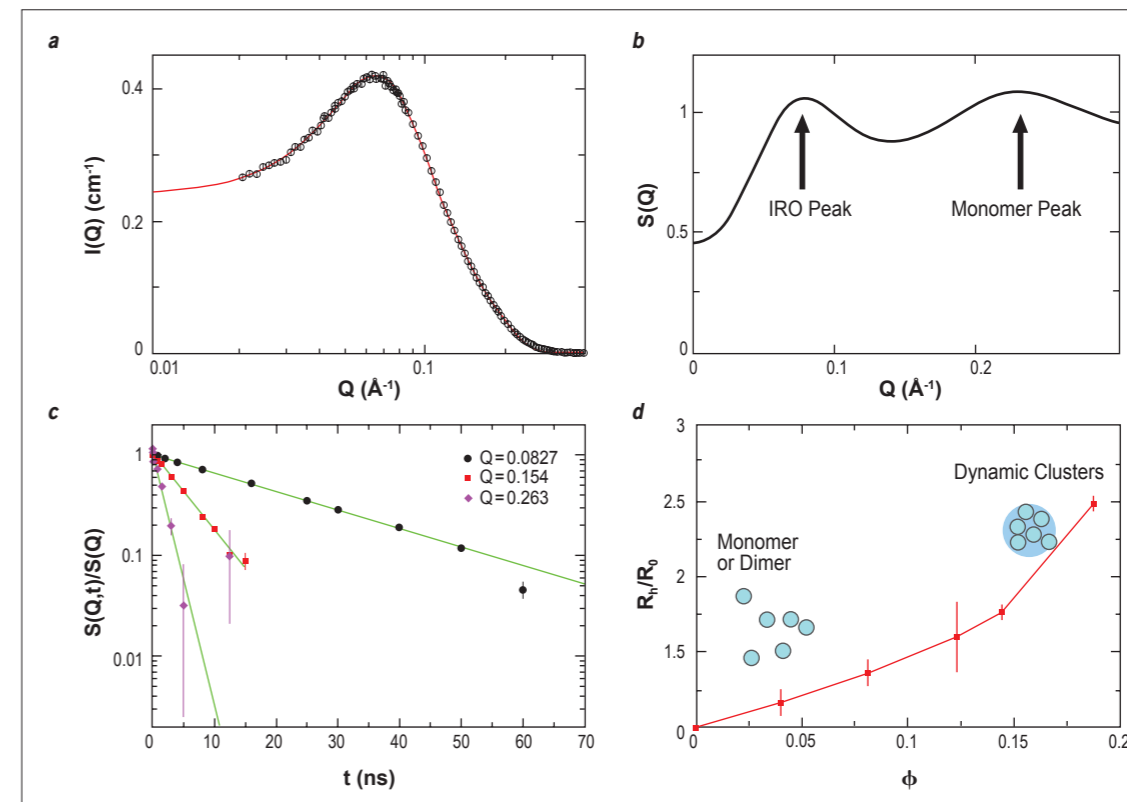


Figure 1: (a) Fitting curve (solid line) together with the experimental points of 5 wt% lysozyme solution measured by SANS. (b) Extracted inter-particle structure factor, $S(Q)$, for the 5 wt% sample. (c) $S(Q,t)/S(Q)$ vs t in the Q range 0.08 to 0.26 \AA^{-1} as extracted by NSE on the 5 wt% sample. (d) Normalised hydrodynamic radius as a function of protein volume fraction.

It would therefore be more appropriate to name it an "IRO" peak. With increasing protein concentration, the IRO peak becomes less evident in our SANS results. The NSE results do nevertheless show slower motion, thus indicating the formation of clusters.

In conclusion, the presence of dynamic clusters in protein solutions has been demonstrated by a combined study of SANS and NSE.

Very few dynamic clusters exist at low protein concentrations, while more and more are formed when the protein concentration increases. In this concentrated regime, the properties of the protein solutions at the short time limit are essentially determined by the properties of the dynamic clusters. These findings constitute a first step toward a complete understanding of this interesting system.

REFERENCES

- A. Stradner *et al.*, *Nature* 432 (2004) 492 [1]
 A. Shukla *et al.*, *Proc. Natl. Acad. Sci. U. S. A.* 105 (2008) 5075 [2]
 L. Porcar *et al.*, *J. Phys. Chem. Lett.* 1 (2010) 126 [3]
 Y. Liu *et al.*, to the *J. Phys. Chem.* DOI: 10.1021/jp.109333c (2010) [4]

Can we design 'greener' solvents? Exploring the structure and dynamics of ionic liquids

Ionic liquids are emerging as a promising class of materials with many applications. A particularly fascinating aspect is the possibility of tailoring their properties through careful choice of the ions. This requires however a thorough understanding of their microscopic structure and dynamics. We studied the behaviour of 1-ethyl-3-methylimidazolium bromide, a simple and representative ionic liquid. Our results highlight how movement in the alkyl chain has a significant impact on the dynamics observed; this in turn helps to explain how macroscopic properties such as viscosity depend on the nature of the molecular constituents of the liquid.

Ionic liquids, organic salts with low melting points ($< 100^\circ\text{C}$), have useful properties and are receiving increasing attention in the chemical industry. They are considered to be promising environmentally-friendly replacements for conventional organic solvents [1]. One remarkable feature of ionic liquids is their level of tunability; they can be obtained by combining different organic cations from several main groups (imidazolium, pyridinium, pyrrolidinium, ammonium, etc.) with a number of different anions ranging from simple halides to complex organic groups. It is therefore possible, in principle, by combining the appropriate cation and anion, to design the liquid required for a particular application. Unfortunately, the molecular interactions conferring macroscopic properties on a liquid are very complex, and we do not yet master the basics for putting this into practice.

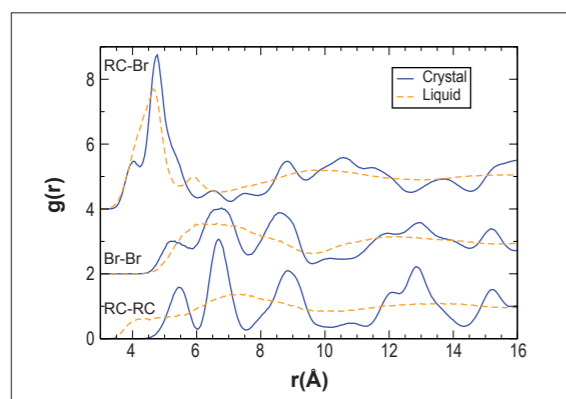


Figure 1: Partial pair distribution functions for the ring centers (RC) of the $[\text{emim}]^+$ cations and the Br^- anions in the crystal and liquid. The bottom curve shows that the cations approach each other much more closely in the liquid [2].

As a first step in this direction we used X-ray diffraction and neutron spectroscopy techniques in combination with molecular dynamics (MD) simulations to explore the atomic structure and dynamics of the prototypic ionic liquid 1-ethyl-3-methylimidazolium bromide, $[\text{emim}]\text{Br}$.

Our MD simulations reproduced the experimental data for the liquid and crystal structures convincingly, and revealed to what extent the molecular arrangement in the crystal is conserved locally in the liquid [2]. It turns out that there is a similar distribution of the Br^- anions around the cation in each phase; surprisingly, however, some of the $[\text{emim}]^+$ cation pairs are much more closely arranged in the liquid than in the crystal, adopting a parallel orientation not found in the ordered phase (**figure 1**).

The dynamics of both phases was studied with quasielastic neutron scattering experiments (QENS) on IN5 at ILL and NEAT at BENSC. The spectra for the crystal exhibit a quasielastic component that can be associated with localised motion, while the liquid spectra can be fitted with two Lorentzians, one assigned to translational diffusion and the other to localised motion.

The MD simulations indicate that the only possible contribution in the QENS time window is from the reorientation of the ethyl chains, labelled 3 in **figure 2a**. **Figures 2b** and **2c** present contour plots of the average spatial distribution of the terminal carbon atom (C_5) of the ethyl chain, along a reference frame based on the plane of the imidazolium ring of the cation, for the crystal and the liquid. In both phases C_5 explores four positions: in the crystal the probability of finding C_5 in two of the four sites is much higher than in the other two, but in the liquid the four sites are equivalent.

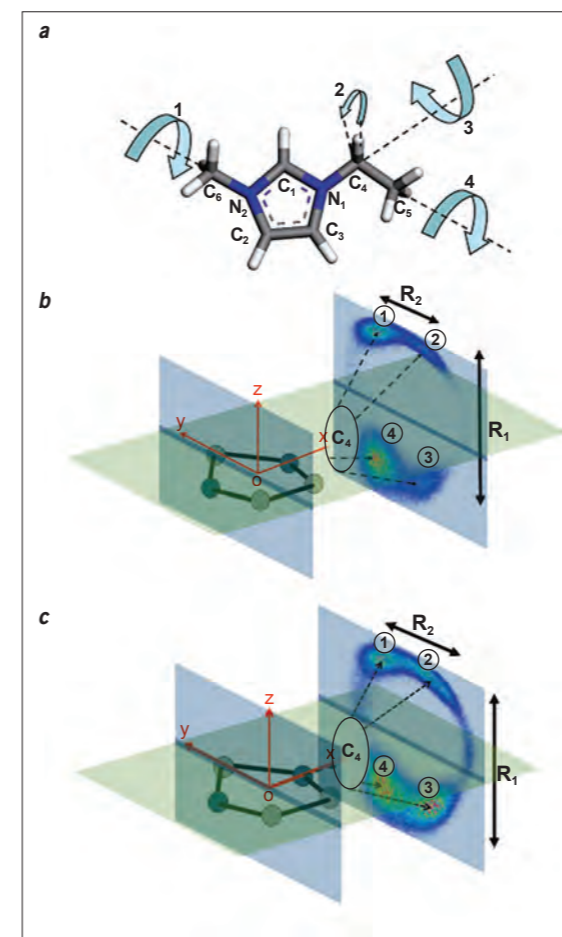


Figure 2: (a) Possible reorientational motions of the $[\text{emim}]^+$ cations: only the ethyl chain rotations (3) fall within the QENS time window. Global molecular rotations (1) are too slow, while methyl rotations (4) and CH_2 motions (2) are too fast to affect the QENS signal; (b,c) spatial distribution of the terminal carbon atom C_5 of the ethyl chain in the crystal (b) and liquid (c) [3]. The numbers 1 to 4 refer to the four positions explored by C_5 as explained in the text.

A fit of this model to the experimental data reproduces the Q -dependence of the elastic incoherent structure factor characterising the localised motion, as shown in **figure 3**. In the crystal, the distance R_1 between the two preferred sites is about 2.5 \AA ; the probability of finding the atom in one of them is about twice that of finding it in one of the other two sites. These other two sites are located at a distance R_2 about 1.1 \AA from the preferred ones in a rectangular configuration. In the liquid phase, R_1 decreases to about 1.9 \AA , R_2 increases to about 1.4 \AA , and the four probabilities become almost equal.

These results provide, for the first time, a microscopic view of the origin of the so-called β -relaxation - a local non-cooperative motion universally observed on glass-formers and showing an Arrhenius temperature dependence - previously observed in a related ionic liquid [4]. They underscore the utility of carrying out computer simulations to interpret the experimental results obtained on systems of this complexity.

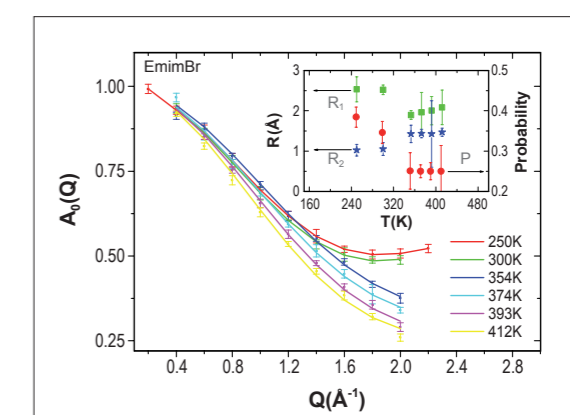


Figure 3: Elastic incoherent structure factor for liquid ($T > 353\text{K}$) and crystal ($T < 300\text{K}$) at several temperatures, fitted to the model illustrated in **figure 2 (b,c)**. The inset shows the temperature dependence of the jump distances R_1 , R_2 , and the probability P of occupying one of the preferred sites, obtained from the fits [3].

REFERENCES

- [1] R.D. Rogers and K.R. Seddon, *Science* 302 (2003) 792-793
- [2] B. Aoun *et al.*, *J. Phys. Chem. B* 114 (2010) 12623-12628
- [3] B. Aoun *et al.*, *J. Phys. Chem. Letters* 1 (2010) 2503-2507
- [4] A. Triolo *et al.*, *J. Phys. Chem. B* 109 (2005) 8549-8557

Turning up the heat on the liquid-liquid transition

The recent report of a liquid-liquid transition in undercooled metastable $(Y_2O_3)_{0.2}(Al_2O_3)_{0.8}$ at 1788 K has generated great theoretical and experimental interest. Claimed to occur close to a liquid-liquid critical point, this first-order transition should be easily identifiable with small-angle neutron scattering (SANS). Our high temperature SANS measurements on molten yttria-alumina, using aerodynamic levitation and laser heating, showed no evidence of the reported transition.

The typical temperature-pressure phase diagram of a single component material, as represented in thermodynamics text books, consists of co-existence lines between the gas, liquid and solid phases, a triple point where all three phases co-exist in equilibrium, and a critical point above which the distinction between high-density gas-like and low-density liquid-like behaviour becomes blurred. In this thermodynamic picture it has long been believed that a first-order transition between two stable liquid phases, represented by an additional co-existence line in the liquid region of the phase diagram, cannot exist. However, recent theoretical calculations and experimental measurements suggest that first-order liquid-liquid transitions between dense liquid phases do in fact occur. However, these liquid-liquid transitions often involve extremely undercooled metastable phases that exist in a "no man's land" of the phase diagram which is accessible only momentarily during the rapid quench of a liquid into a glass [1,2].

The $(Y_2O_3)_x(Al_2O_3)_{1-x}$ ($0 \leq x \leq 1$) system has attracted considerable interest due to evidence of a liquid-liquid transition whereby microscopic droplets, purported to be a second low-density liquid (LDL), form in the bulk high-density liquid (HDL) as a sample is rapidly quenched from its equilibrium state [3]. These droplets remain in the glass obtained at the end of the quench, and the observations are interpreted in terms of the formation of a low-density glass from the LDL phase within the bulk high-density glass derived from the HDL phase. Subsequently, and more dramatically, it has been claimed [4] that such an HDL-LDL transition may be observed under metastable conditions for at least one stoichiometry termed AY20, namely undercooled liquid $(Y_2O_3)_{0.2}(Al_2O_3)_{0.8}$ at 1788 K (cf. melting point $T_m = 2125$ K). In particular, the transition should be observable as a large increase in the SANS intensity if it is characterised by either the nucleation and growth of small droplets of the LDL phase in the bulk HDL phase, or as density fluctuations near the proposed liquid-liquid critical point. Below the transition temperature, 100% LDL should have formed so that the SANS signal returns to a low intensity.

In the present work a SANS measurement using the instrument D22 was made on liquid AY20 at temperatures in the vicinity of the purported transition temperature of $T_{LL} = 1788$ K. In order to maintain the sample at the high temperatures required and to avoid crystallisation of the undercooled liquid, the experiment was carried

out using an aerodynamic levitation and laser heating system (supplied by CEMHTI-CNRS, Orléans) wherein a small (3 mm diameter) droplet of the liquid sample was held under containerless conditions to avoid heterogeneous nucleation. Care was taken to produce a semi-circular incident beam with dimensions just larger than the sample, and the use of 8 m incident beam collimation, plus additional Cd shielding close to the sample, assured a low background intensity in the SANS which was carefully measured and subtracted. **Figure 1** shows the levitation chamber and nozzle assembly with a small glass sphere placed at the sample position.

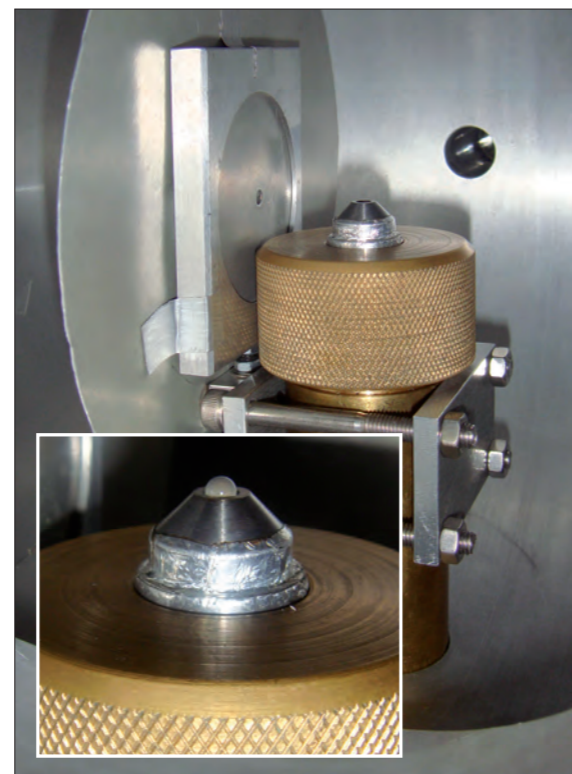
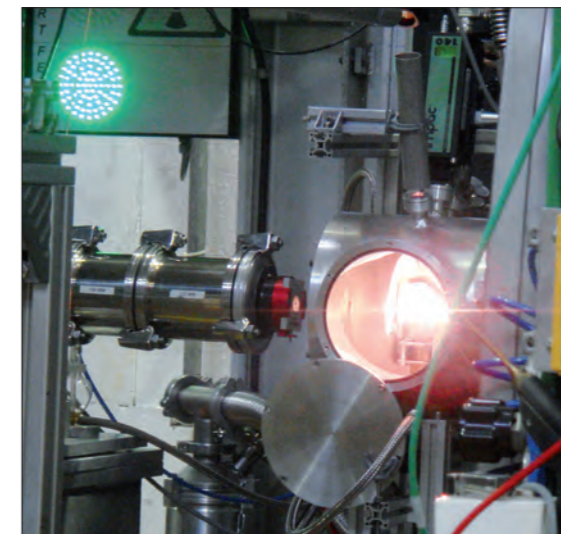


Figure 1: The nozzle assembly within the levitation chamber on D22. The inset shows a close-up of a small spherical glass sample placed on the vanadium nozzle. The beam enters from the left through a semi-circular aperture. The sample is heated by two infra-red CO₂ lasers, one directed downwards on to the top of the sample and the other directed upwards through the aperture of the nozzle.

Figure 2 shows the levitation chamber mounted at the D22 sample position. The glow originates from a levitating sample heated by an infra-red laser. Under experimental conditions, the chamber is closed and filled with the argon-oxygen mixture used as the levitation gas.



As shown in **figure 3**, we observed no enhancement of the SANS intensity in the vicinity of 1788 K for the levitated AY20 sample, a result that contrasts directly with that reported from small angle X-ray scattering measurements [4]. In addition, we were unable to find, in a complementary high-energy wide-angle X-ray scattering study using ID11 at the ESRF [5], any evidence of a structural change associated with a liquid-liquid transition in AY20 as the reported transition temperature is traversed under either quasi-isothermal or rapid-quenching conditions.

Figure 2:

A sample in the levitation chamber on D22 heated to about 2300 K.

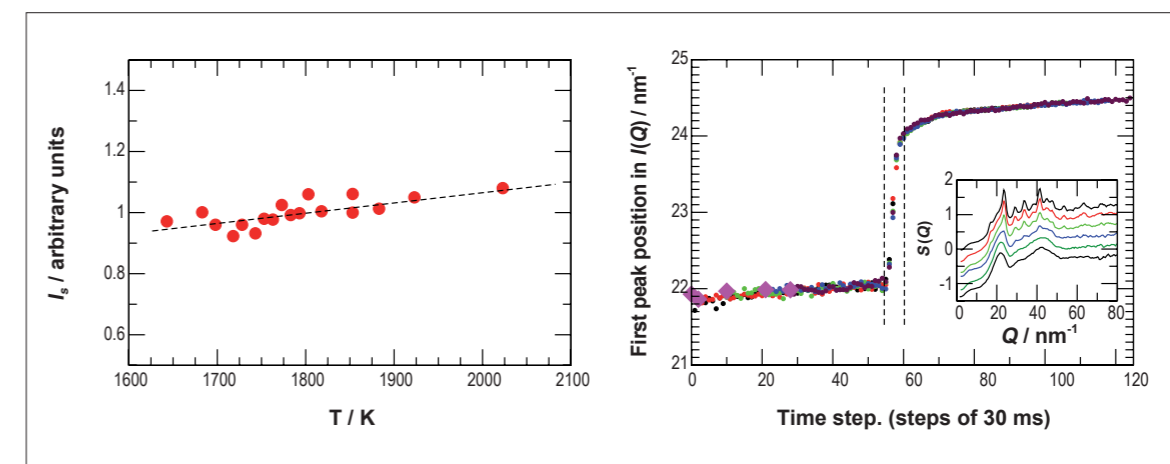


Figure 3: The figure on the left shows the integrated SANS signal as a function of temperature and shows no signature of a rapid rise and fall in signal which is expected if a first-order transition close to a liquid-liquid critical point takes place at 1788 K. The figure on the right gives the evolution of the first peak position in the intensity $I(Q)$ in a time-resolved X-ray diffraction experiment made using ID11 at the ESRF and shows (between the vertical dashed lines) the characteristic crystallisation process that takes place as the sample is rapidly cooled. No liquid-liquid transition is observed before crystallisation. The purple diamonds represent the points measured in X-ray diffraction experiments on the undercooled liquid state down to a minimum temperature of 1573 K. The inset shows the evolution of the diffraction pattern as crystallisation takes place, starting with the equilibrium liquid state at the bottom.

REFERENCES

- P.G. Debenedetti, *Metastable Liquids* (Princeton Univ. Press, Princeton NJ, 1996) [1]
 O. Mishima and H.E. Stanley, *Nature (London)* **396**, 329 (1998) [2]
 S. Aasland and P.F. McMillan, *Nature (London)* **369**, 633 (1994) [3]
 G.N. Greaves *et al.*, *Science* **322**, 566 (2008) [4]
 A.C. Barnes *et al.* *Physical Review Letters* **103**, 225702 (2009) [5]

C. Dicko (University of Lund, Sweden)
 I. Greving, and F. Vollrath (University of Oxford, UK)
 A. Terry (ISIS and University of Oxford, UK)
 P. Callow (ILL)

Small-angle scattering diffractometer D22

Unravelling the secrets of silk production

Spiders and insects have achieved what many industries and laboratories strive to accomplish, namely the controlled assembly of complex mixtures in water into high performance fibres and adhesives, at ambient temperature and pressure. Inspired by the achievements of the natural world, and of the impact they might have on sustainable artificial fabrication, we aim to better understand the relation between molecular assembly and the materials' properties prior to and during processing [1].

Silk is incredibly durable, possessing a tensile strength comparable with steel. There has long been interest in how a silk fibre is assembled from unspun protein precursors (fibroin), much of which has focussed on 'reconstituted' silk fibroin (RSF) proteins, (obtained by breaking down cocoon fibres with high salt concentration). RSF is used partly because it is readily available in large quantities and because it may lead toward the commercialisation of spinning silk 'waste'. Indeed, one of the practical limitations when studying silk is that at any given time each silk worm has only minute amounts of silk's precursor proteins inside its body.

However, to date, we have lacked a suitable silk benchmarking method to evaluate the 'structure-shape-processing' relationship that characterises silk fibre assembly. To address this, we conducted a series [2] of small-angle neutron scattering (SANS) experiments on the D22 instrument.

For the first time, the silk fibroin was extracted in small quantities direct from the glands of silk worms (figure 1a). We demonstrated that the size and shape of native silk proteins in solution can be measured (figure 1c) and we discovered that the size of native silk molecules adopted in solution is larger than that of RSF; this helped to explain, for example, observations from previous studies that RSF forms poorer quality fibres than native precursor proteins [3].

Details of the behaviour of silk fibroin in solution shows that concentration affects the proteins behaviour; at high concentrations the native protein molecules form a compact and predominantly helical structure with a radius of gyration of about 90 nm and they show very little interaction, which is unusual for these values

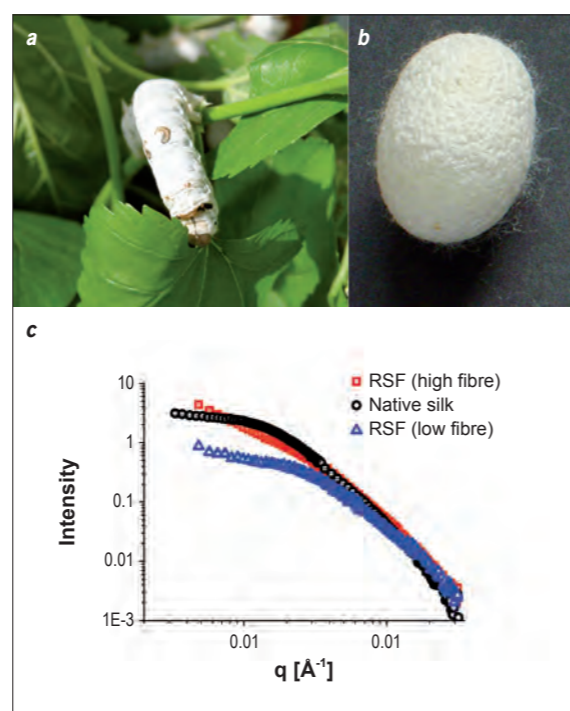


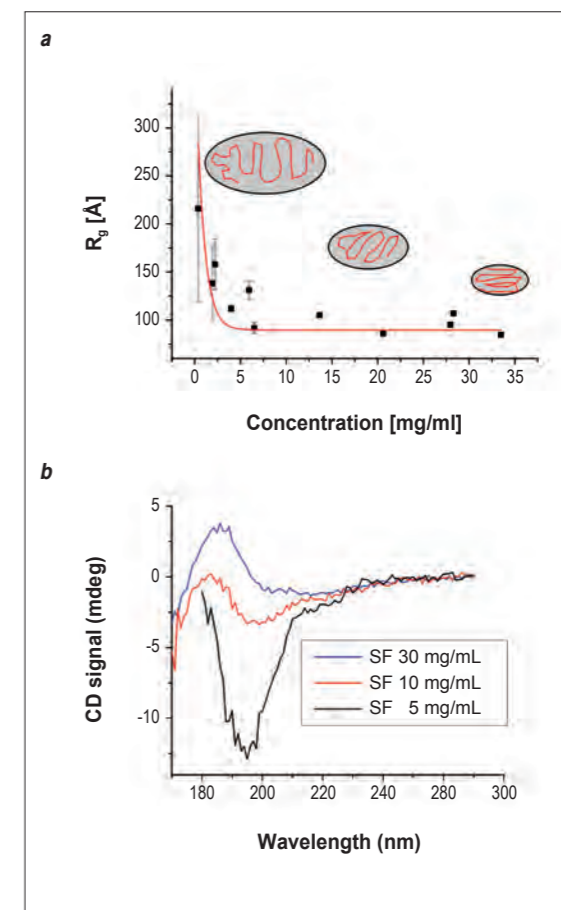
Figure 1: (a) Live *Bombyx mori* silkworm. (b) *Bombyx mori* cocoon, the worm inside is protected during pupation into a moth. (c) SANS data comparing native silk (from the worm) and reconstituted silk fibroin (RSF) from the dissolution of the cocoon in chaotropic salts. Two preparations are compared from either a high or a low fibre concentration.

of concentration; as they are diluted they unfold until they are 130 nm in size (figure 2a and 2b). In simple terms, the effect of decreasing concentration on the silk proteins is analogous to what happens when a neat ball of string unravels to produce freer strands that then become tangled and knotted.

This dependence will have a profound effect on the performance of the material that can be produced and also helps to explain the difficulties found by many research groups using RSF as a spinning material. *In vivo*, however, the silkworms are able to control this process so that the proteins are spun into highly ordered silk filaments as they unfold and begin to flow.

The fact that the proteins can remain stably dispersed at such high concentration is a surprising observation and it is a vital step towards understanding and controlling the liquid precursor [4]. This will be essential in order to synthesise silk and develop new materials with silk's desirable mechanical properties, the key to which lies in answering such questions as how stable is the precursor, and how is it structurally and chemically modified during the spinning process.

Figure 2: (a) Dependence of the radius of gyration (R_g) of native silk proteins as a function of concentration. (b) Circular Dichroism spectra of native silk proteins as a function of concentration. Both results suggest that at low concentration silk proteins are larger in size and predominantly in a random coil conformation, and that at higher concentration silk proteins are smaller in size and predominantly helical.



New insights into the E2:E3BP core assembly of the human pyruvate dehydrogenase multienzyme complex (hPDC)

Pyruvate dehydrogenase multienzyme complex (PDC) is a vital mitochondrial assembly that is ultimately responsible for glucose homeostasis in man. As such, PDC deficiencies are implicated in a wide variety of genetic, metabolic, neurodegenerative and autoimmune diseases. We can now over-express, purify and reconstitute hPDC produced in bacteria allowing us to analyse and mimic many of the genetic and metabolic defects found in the human population. We have employed small-angle X-ray (SAXS) and neutron scattering (SANS) – together with cryo-EM measurements – to obtain the first low-resolution structures of the hPDC pentagonal dodecahedral core.

hPDC is a vast macromolecular machine ($M_r \sim 10$ million) comprising multiple copies of 3 separate enzymes (E1–E3) and a novel accessory polypeptide, E3 binding protein (E3BP). The icosahedral E2:E3BP core forms the central structural framework, required for optimal positioning of and cooperativity with its bound E1 and E3 partners. Using small-angle X-ray /neutron scattering (SAXS/SANS) and cryo-EM, we have generated the first low resolution structures of the E2:E3BP core assembly, distinguishing between conflicting addition (60E2:12E3BP) and substitution (48E2:12E3BP or 40E2:20E3BP) models for its organisation. E2 and E3BP, a related polypeptide, require to be co-expressed for integration of E3BP into the wild-type high M_r core assembly. Alternatively E2 can self-assemble into a 60-meric pentagonal dodecahedron mimicking the situation in a group of E3BP-null patients who still retain partial (10–20%) PDC activity.

The truncated C-terminal halves of E2:E3BP or E2 alone can also form intact cores as the outwardly-extended N-terminal lipoyl domains (LDs) and associated E1 and E3 binding domains (SBDs) are joined in tandem by mobile linkers to the C-terminal assembly providing the flexibility for the lipamide cofactors to visit all 3 active sites during catalysis.

Previously we and others have reported the presence of 12 E3BPs per native core in bovine PDC [1,2] and suggested that they occupied the 12 pentagonal faces of the E2 dodecahedron; however, more recent substitution models [3,4] have proposed that E3BPs can partially replace E2 to varying extents (48E2:12E3BP and 40E2:20E3BP). In this study, we have generated full-length hE2:3BP and hE2 assemblies plus a truncated version involving only the C-terminal domains. Their structures were determined

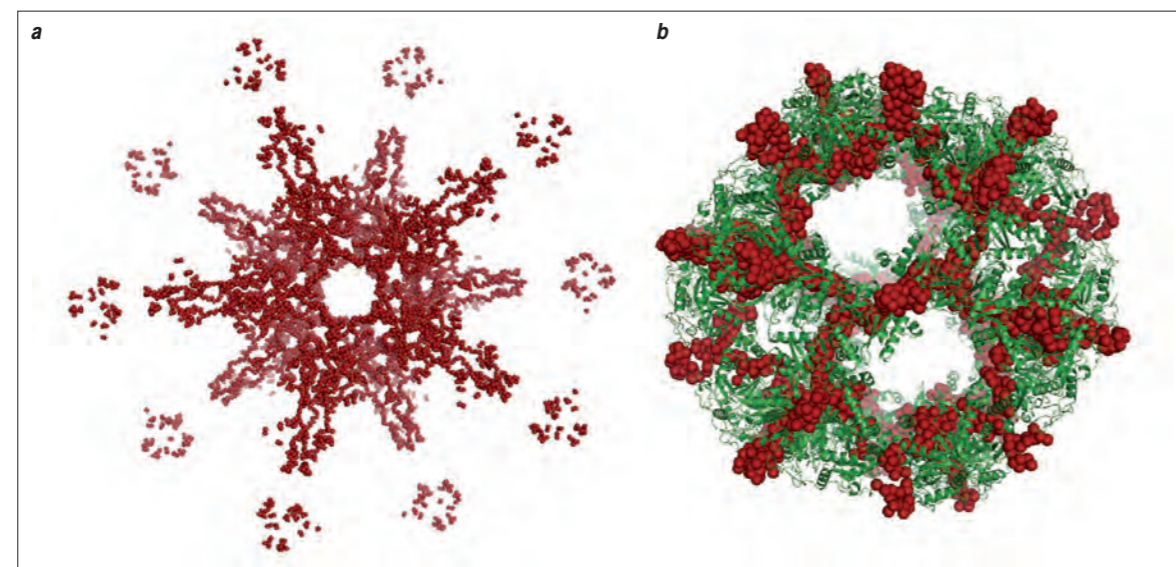


Figure 1: *Ab initio* reconstructions of full-length and truncated (C-terminal) versions of the E2:E3BP core assembly of the hPDC. (a) Solution structure of hE2:E3BP core assembly (visualised along the 5-fold axis of symmetry) reconstructed from SAXS data using GASBOR. (b) similar *ab initio* reconstruction of truncated hE2:E3BP core assembly (red; generated from SANS data using GASBOR) and its superimposition with the *B. stearothermophilus* truncated E2 crystal structure (green).

by SAXS or SANS and compared with native bovine heart E2:E3BP. In addition, cryo-EM reconstructions of full-length hE2:E3BP cores were carried out in the presence or absence of E3.

Our SAXS and SANS studies have revealed that the recombinant human and native bovine core assemblies contain open (unoccupied) pentagonal faces in agreement with the substitution models (figure 1). They have also permitted direct visualisation of the dynamic (disordered) outwardly-extended LDs and SBDs in the intact core assemblies for the first time. These are notably absent in the truncated E2:E3BP core. Moreover, our cryo-EM-reconstructions confirm the present of unoccupied (open) faces on all versions of the core assembly (figure 2). They also highlight that E3 binding induces a greater degree of order at the core surface as judged by the appearance of prominent spikes protruding above the core surface, the expected location of the E3-SBDs. Interestingly, the extensions observed in the SAXS-derived models are longer than in the cryo-EM models in agreement with the

greater ability of the former to detect the disordered and highly-mobile LDs located at the extreme N-termini of E2 and E3BP.

To conclude, our data have provided strong evidence in favour of the substitution model of E2:E3BP core organisation in both recombinant human and native bovine PDCs. Moreover the flexible lipoyl 'swinging arms' of the core assembly have been visualised for the first time and we have shown that E3 binding induces more structural order above the core surface [6].

Our current research is using the enhanced neutron scattering properties of deuterated E3 to determine the numbers of E3s bound per E2:E3BP core and has confirmed a previous report that individual E3 homodimers link pairs of E3BPs in a 1:2 stoichiometry [5]. The presence of this network of E3 cross-bridges is consistent with our cryo-EM observations and represents a novel architectural feature that has important implications for the catalytic mechanism and regulation of PDC.

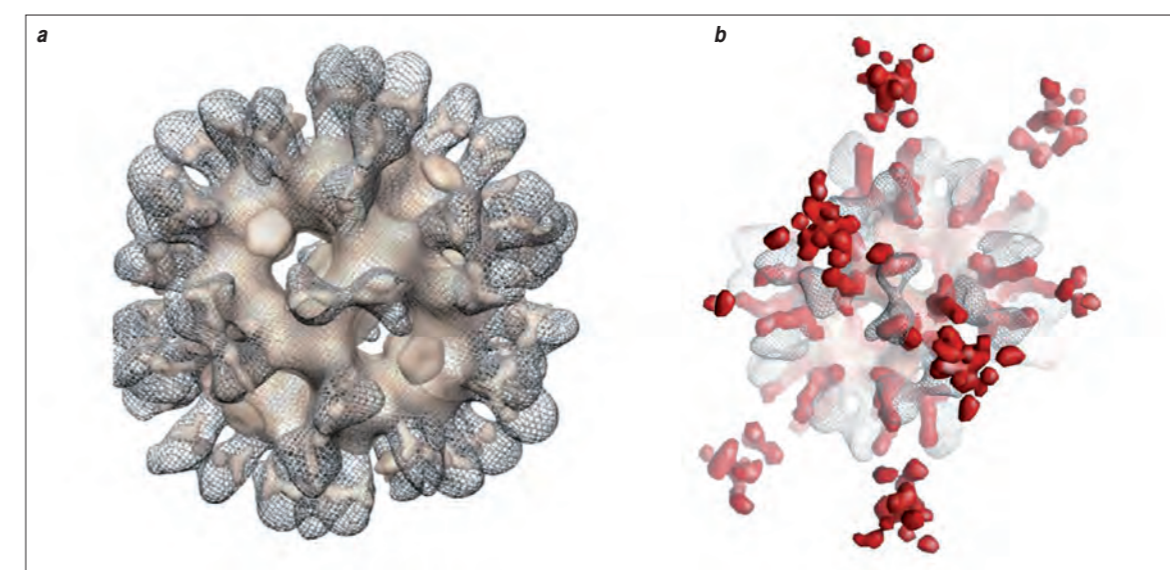


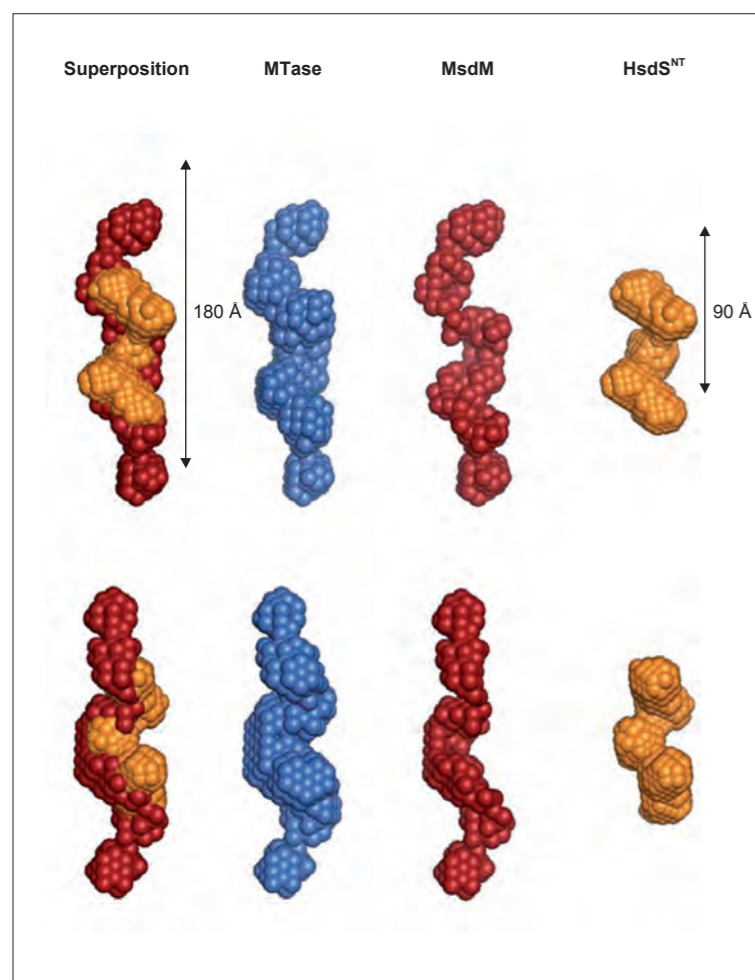
Figure 2: Cryo-EM of the full-length recombinant hE2:E3BP and E2:E3BP:E3 assemblies and comparison with the SAXS-derived model for E2:E3BP:E3. (a) The E2:E3BP core in the absence (semi-transparent surface) and presence of E3 (mesh) showing the appearance of ordered protrusions (spikes) at the core surface in the expected location of the E3BP-SBDs induced by E3 binding. (b) Superimposition of the cryo-EM E2:E3BP:E3 core structure (mesh) and the GASBOR-derived recombinant E2:E3BP SAXS model (red). The peripheral projections visualised in the SAXS data extend well beyond the outer limits of the cryo-EM structure and are consistent with the positioning of the N-terminal, highly-flexible LDs.

REFERENCES

- S.J. Sanderson, C. Miller and J.G. Lindsay / *Eur. J. Biochem.* 236 (1996), 68–77 [1]
 Z.H. Zhou, D.B. McCarthy, C.M. O'Connor, L.J. Reed and J.K. Stoops / *Proc. Nat. Acad. Sci. USA* 98 (2001), 14802–14807 [2]
 Y. Hiromasa, T. Fujisawa, Y. Aso and T.E. Roche / *J. Biol. Chem.* 279 (2004), 6921–6933 [3]
 C.A. Brautigam, R.M. Wynn, J.L. Chuang and D.T. Chuang / *J. Biol. Chem.* 284 (2009), 13086–13098 [4]
 M. Smolle, A.E. Prior, A.E. Brown, A. Cooper, O. Byron and J.G. Lindsay / *J. Biol. Chem.* 281 (2006) 19772–19780 [5]
 S. Vijaykrishnan, S.M. Kelly, R.J.C. Gilbert, P. Callow, D. Bhella, T. Forsyth, J.G. Lindsay and O. Byron, *J. Mol. Biol.* 399 (2010) 71–93 [6]

Structural and functional analysis of the engineered type I DNA methyltransferase EcoR124I_{NT}

Bacteria, like animals, are susceptible to viral infection. While in animals this can lead to a range of symptoms of varying severity, for bacteria the outcome is usually death. Bacterial viruses, or bacteriophages, inject genetic material into the host which then corrupts its metabolism forcing the bacteria to produce hundreds more of them. These newly formed viruses are then released into the environment free to infect more bacteria. It has therefore been vital for bacteria to develop defensive mechanisms which protect them from invasion by foreign DNA. With the rise of antibiotic resistant bacteria, bacteriophages are now being extensively studied as treatments for bacterial infections, however in order to circumvent the bacterial defences we must first understand how they work.



One element that makes up the bacteria's primitive immune system is composed of restriction-modification (R-M) enzymes. These enzymes protect the bacteria by marking its own genetic code at specific points in its DNA. This operation is performed by a methyltransferase (MTase) enzyme which is composed of two different proteins, one which recognises the DNA sequence (the S subunit) and one which labels the DNA (the M subunit). Once the bacteria's own DNA has been marked in this way it is possible for the bacteria to differentiate between its own DNA and any foreign DNA that enters the cell. Should foreign DNA from a bacteriophage, for example, be identified a third protein is recruited to the R-M complex (the R subunit) which then cuts up the foreign DNA before it can cause any damage to the bacteria.

EcoR124I is one of the best studied R-M systems, however structural work on this protein complex has been hampered by the insolubility of the S subunit when not associated with the M subunit. In this study molecular biology techniques were used to engineer a soluble form of the S subunit which could be successfully recombined with the M subunit to form a new R-M enzyme EcoR124I_{NT}, which maintained the characteristics of the naturally occurring EcoR124I. This enabled the specific deuteration of the components of EcoR124I_{NT} at the ILL-EMBL Deuteration Laboratory for small-angle neutron scattering (SANS) experiments that were performed on D22. As a result, through the use of neutron contrast variation and *ab initio* modelling techniques, we were able to determine the structural arrangement of the S and M subunits of the type I R-M methyltransferase EcoR124I_{NT} (figure 1).

Figure 1: *Ab initio* models of M.EcoR124I_{NT} (blue), and the M and S_{NT} subunits in situ (red and orange, respectively). The two rows show mutually perpendicular views of the structures, rotated by 90° around the y-axis.

Our results clearly indicate that the M subunits extend towards the periphery of the complex, whereas the S subunit is located more centrally. The *ab initio* model of the S subunit of EcoR124I_{NT}, in complex with the M subunits, shows a structure that appears to be well conserved when compared to the S subunits of unrelated R-M systems for which data are available. In contrast the M subunit organisation within M.EcoR124I_{NT} appears to be completely novel. The results of the SANS analysis suggests that the M subunits are linked essentially end to end in the MTase, making at most rather limited contacts at the centre of the complex. Even though the free M subunits exist as monomers in solution, there may be relatively weak protein-protein contacts between them in the MTase which are stabilised by interactions with the S subunits.

The overall low-resolution structure we have obtained for M.EcoR124I_{NT} varies significantly from those proposed for the R-M enzymes M.EcoKI, which was determined on the basis of electron microscopy and for M.EcoR124I on the basis of molecular modelling.

However, it should be noted that those models were for complexes formed with DNA and are much more compact, with the M subunits appearing as arms which close to 'hug' the DNA, completely encircling it.

It therefore appears that R-M enzymes undergo significant structural rearrangements on binding to DNA changing from an 'open' conformation with the M subunits extended to a 'closed' conformation with the M subunits bound across the DNA. It may well be that this structural flexibility is necessary to enable these systems to fulfil their duel role of DNA sequence recognition and methylation.

Further studies are underway using M.EcoR124I_{NT} as a model system to determine whether further conformational changes occur as the R subunits are recruited to the complex to enable restriction of foreign DNA.



Figure 2: This work was featured on the cover of the May 2010 issue of the Journal of Molecular Biology.

REFERENCE

J. Taylor, P. Callow, A. Swiderska and G. Kneale, Journal of Molecular Biology 398, (2010) 391-9 [1]

Three-dimensional small-angle scattering model of human platelet integrin $\alpha_{IIb}\beta_3$ in solution

Proteins are an important part of the complex machinery that enables life. There is an obvious need to understand the function of each component of this machinery. In order to understand function, which is closely linked to structure, we need to know the structure of individual biological molecules (protein, DNA, RNA) and of their complexes. In recent years there has been a dramatic increase in the high-resolution structural information available from crystallised protein. However, high-resolution techniques, such as protein crystallography, become difficult to apply to proteins which are difficult to crystallise, as is the case with most membrane proteins.

Integrin $\alpha_{IIb}\beta_3$ is a membrane protein involved in the coagulation of blood. Blood platelets have distinct mechanisms to respond to the different agonists of platelet activation, all of which end up with the acquisition by integrin $\alpha_{IIb}\beta_3$ or glycoprotein IIb/IIIa of the capacity to recognise and bind fibrinogen and other adhesive proteins. Fibrinogen is the major adhesive protein in plasma and fibronectin is the major adhesive protein in the extracellular matrix of subendothelium, the connective tissue between the endothelium and the inner elastic membrane in the inner part of arteries. The binding of fibrinogen to activated $\alpha_{IIb}\beta_3$ and the binding of fibronectin to resting or activated $\alpha_{IIb}\beta_3$ lead to the formation of interplatelet cross-linking and to platelet adhesion to the subendothelium, respectively, and, eventually, to the formation of the platelet plug.

Knowledge of the fibrinogen receptor and the mechanisms by which its activity is induced and modulated is therefore vital to understanding hemostasis and the physiological paths leading to thrombosis, as well as to developing new ways to prevent, detect and treat thrombosis effectively, securely and selectively.

Recent developments in small-angle scattering data analysis methods can provide valuable structural information from high-quality scattering patterns [1] and these methods are being employed to address increasingly complicated questions.

Small-angle scattering is usually described as a low-resolution structural technique that can determine with high precision large distances. These distances can act as very tight constraints on the modelling and refinement of the three-dimensional structure of biological molecules. Small-angle scattering experiments also make it possible to analyse relatively large structures, such as biological macromolecules and their complexes, in nearly physiological environments, and to study directly structural responses to changes in external conditions. In addition, the possibility of using contrast variation by solvent exchange (H_2O/D_2O) or specific deuteration provides added value to small-angle scattering with neutrons (SANS).

Figure 1: Average experimental SANS curve (circles) from $\alpha_{IIb}\beta_3$ in detergent solution. The continuous red line is the theoretical scattering curve obtained from the reconstructed high-resolution structural model of $\alpha_{IIb}\beta_3$, and the continuous black line is the theoretical scattering curve obtained from a possible extended conformation.

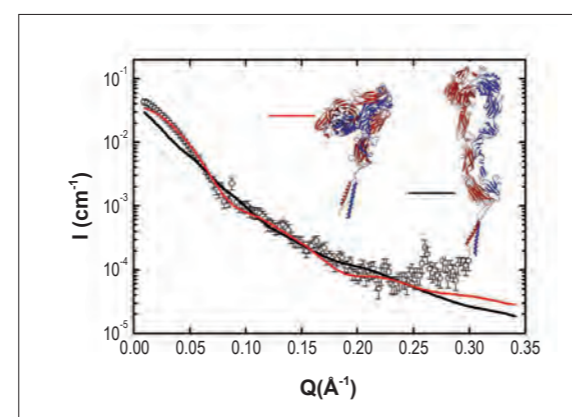
With SANS it is possible to observe the low-resolution structure of native membrane proteins and their functional modifications, both in detergent solutions and in suspensions of membrane proteins reconstituted in single bilayer vesicles. This can be done by contrast matching the scattering of the detergent and the scattering of the lipid vesicles, respectively.

The first stage in attempting to interpret SANS data involves fitting known high-resolution structures into models that can describe the experimental data. For example, we can test whether a known protein crystal structure is consistent with its protein solution scattering profile.

However, this is not always possible, in particular when the protein under study is not crystallisable and only high-resolution structural information from protein fragments is available.

Using shape reconstruction techniques [2], it is possible to obtain the shape envelope of the scattering object from the small-angle scattering curve by using the high-resolution information from different parts of the protein under study.

This was the approach used in this work. We used human $\alpha_{IIb}\beta_3$ integrin in surfactant Triton X-100 solutions and SANS to obtain the low-resolution model of the integrin from measurements obtained on the instrument D22. From SANS data (figure 1) we were able to obtain a low-resolution 3D model of whole $\alpha_{IIb}\beta_3$ in Ca^{2+} /detergent solutions (model projections in figure 2) [3]. Docking of this SANS envelope into the high-resolution structure of $\alpha_{IIb}\beta_3$,



reconstructed from crystallographic [4] and NMR data [5] (inset figure 3), shows that the solution structure is less constrained and makes it possible to assign tentatively the disposition of the α_{IIb} and β_3 subunits and their domains within the model and to identify the structural similarities and differences between the SANS model and the crystallographic models of the recombinant extracellular part of $\alpha_{IIb}\beta_3$ and $\alpha_V\beta_3$, on the one hand, and the cryo-EM model of whole $\alpha_{IIb}\beta_3$, on the other. This extracellular part of the protein, the ectodomain, is in the bent configuration at the top of the model, where α_{IIb} and β_3 occupy the concave and convex sides, respectively, at the arched projection, with their bent knees at its apex. It follows the narrower transmembrane region and the cytoplasmic domains at the bottom end.

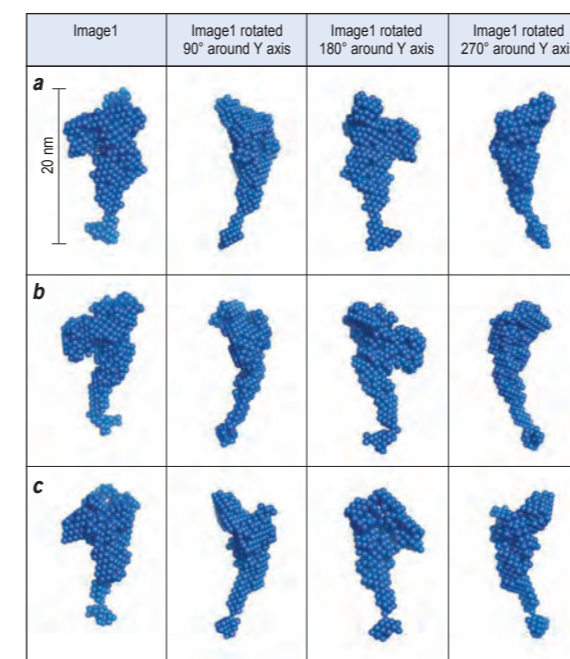


Figure 2: Different projections after 90° rotation along the long axis of three examples of reconstructed three-dimensional *ab initio* sphere models of $\alpha_{IIb}\beta_3$ integrin in detergent solution with Ca^{2+} .

With these results, we have shown how 'low-resolution' models obtained from SANS measurements can be used to understand the conformation of complex proteins, such as membrane proteins, in nearly physiological conditions. At present there are high-resolution crystallographic models for very few whole membrane proteins. The SANS low-resolution models of membrane proteins could play a key role in overcoming this limiting situation. In the future, the low-resolution structure of membrane proteins reconstituted in single bilayer deuterated lipid vesicles, their disposition with respect to the membrane and their structural modification in different functional conditions could be obtained by SANS, provided the deuterated lipid vesicles are made invisible using neutron contrast variation.

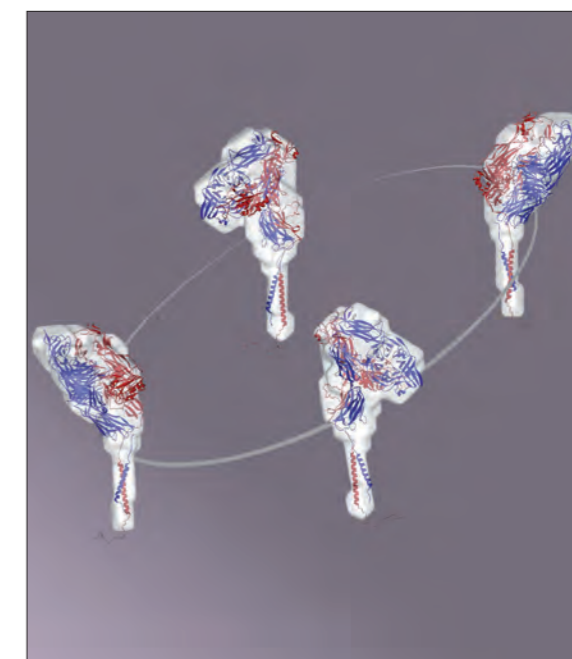


Figure 3: Four different projections of the docking of the high-resolution model available in the literature [3,4] into the low-resolution model obtained by SANS at D22.

REFERENCES

- D.I. Svergun and M.H.J. Koch, Rep. Progr. Phys. 66 (2004) 1735 [1]
 D.I. Svergun, Biophys J. 76 (1999) 2879 [2]
 A. Nogales, C. García, J. Pérez, P. Callow, T.A. Ezquerra, J. González-Rodríguez, Journal of Biological Chemistry 285 (2010) 1023-1031 [3]
 J.P. Xiong, T. Stehle *et al.*, Science 296 (2002) 151 [4]
 O. Vinogradova and A. Velyvis *et al.*, Cell 110 (2002) 587 [5]

P. Langan and A. Kovalevsky (Los Alamos National Laboratory, USA)
 S.A. Mason, V.T. Forsyth and M.P. Blakeley (ILL)
 L. Hanson (University of Toledo, USA)
 J.P. Glusker and H.L. Carrell (Fox Chase Cancer Center, Philadelphia, USA)
 D.A. Keen (ISIS, UK)

Diffraction for single-crystal and fibre diffraction D19
 Neutron protein crystallography station PCS (LANSCE)

Neutron and X-ray vision of a biofuels enzyme

Neutron and X-ray crystallographic structures of several metal ion and ligand complexes of D-xylose isomerase have been determined. These represent different stages in the progression of the biochemical catalytic action of this enzyme which involves isomerisation of certain monomeric sugars. Comprehensive analyses of these crystal structures provide information relevant to a general understanding of hydrogen transfer in enzymes and serve to guide bioengineering efforts to improve the enzyme for applications in the production of fuels and chemicals from lignocellulosic biomass.

Lignocellulosic biomass, the fibrous material found in plant cell walls, is a renewable feedstock which some day could partially replace petroleum-based products. One approach to this conversion of biomass to useful products is to enzymatically break down the polymeric carbohydrate components of biomass (cellulose and hemicellulose) into monomeric sugars. These can then be converted by microorganisms into the required fuels and chemicals. A major product of such hydrolyses of biomass is the pentose sugar, xylose. Derived from hemicellulose, xylose can account for 30% of the total sugar content of biomass, but it cannot be efficiently fermented by industrial strains of yeast. This problem can, however, be addressed by the use of the enzyme D-xylose isomerase which converts xylose into its fermentable *keto* isomer xylulose. To date this enzyme has not performed well when engineered into yeasts (which would be used to effect this conversion). In our present studies, the catalytic mechanism of D-xylose isomerase is being elucidated in detail in order to provide insights that would guide re-engineering of the active site in order to improve the performance of the enzyme in yeast.

D-xylose isomerase is a 43 kDalton enzyme with an alpha-beta barrel ($\beta\alpha_8$) shape. Its active form is a tetramer with four active sites, each containing two metal ion cofactors. The enzymatic

reaction involves opening the ring of the sugar to obtain the open-chain form of this substrate (**figure 1, step 1**). Then isomerisation of this substrate occurs when a H atom is transferred from one adjacent carbon atom to another (**figure 1, step 2**). A key breakthrough in our most recent study was the discovery that by using different metal cofactors it is possible to trap intermediate complexes at different stages along the chemical reaction pathway. This discovery has helped describe the movement of hydrogen atoms in the active sites of the enzyme.

The enzymatic reaction involves the transfer of hydrogen at two different stages. Hydrogen, the smallest of atoms, is often difficult to locate in X-ray diffraction experiments because the power to scatter X-ray depends on the atomic number. This is not the case for neutron diffraction. The hydrogen isotope deuterium scatters neutrons to about the same extent as do carbon or oxygen. Therefore if H can be replaced by D, the location of this hydrogen atom (now D) can readily be detected by neutron diffraction.

By collecting neutron data from the various complexes using neutron diffractometer D19 at the ILL and the neutron Protein Crystallography Station (PCS) at the Lujan Center at Los Alamos National Laboratory it has been possible to map the positions

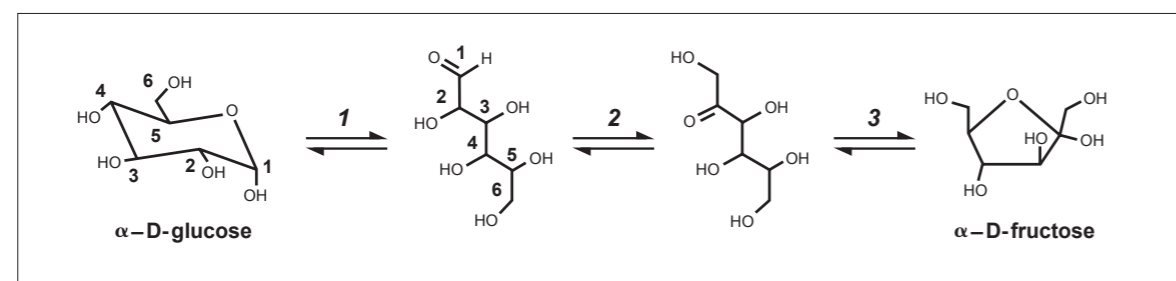


Figure 1: A chemical diagram of the three main stages of the sugar interconversion reaction catalysed by D-xylose isomerase, involving (1) ring-opening, (2) isomerisation (3) ring-closure.

of individual hydrogen atoms as the enzyme moves them, and also to model how specific amino acid residues of the enzyme might be involved in promoting these movements (**figure 2**). Each experiment involved growing a large (several mm³ in volume) crystal of the enzyme in complex with its deuterated substrate and a different species of metal ion, exchanging H₂O in the crystal with D₂O in order to increase hydrogen atom visibility, and then collecting neutron data at room temperature to 1.8 - 2 Å resolution over several days. The neutron data are then combined with X-ray data in an advanced joint "XN" structure refinement process [1] that provides a clearer picture of hydrogen atom positions (and hence possible movements in the active site region).

In the four complexes of D-xylose isomerase that we have studied by both X-ray and neutron diffraction [2,3,4], the side chain of amino acid residue His54 is doubly protonated (on the ring N atoms of histidine) throughout. This challenges the widely accepted role of His54 in donating a proton permanently to the sugar oxygen atom, O5, to promote ring opening. One the other hand,

the side chain of amino acid Lys289 is deprotonated (neutral) in the first two stages and becomes protonated in the last two, suggesting that it may play an unexpected role in ring opening by abstracting a proton from the sugar. Probably the most significant event for the isomerisation step is the deprotonation of the catalytic water in the last stage (to give a hydroxyl ion). The observed variable charges on O5 of the substrate (to aid the enzyme in holding it in place) and on Lys289 (to help in some way the flow of protons to and from the isomerisation site) are important components of the mechanism.

In this study neutron and X-ray crystallographic methods have been combined in order to obtain new insights into the catalytic mechanism of the enzyme D-xylose isomerase. The results are being used to enable new approaches to modifying the enzyme to improve its performance for the production of biofuels and other applications. In particular, specific amino acid residues of the enzyme are being mutated in order to improve the activity of the enzyme over values of pH typically found in the cytosol of yeasts.

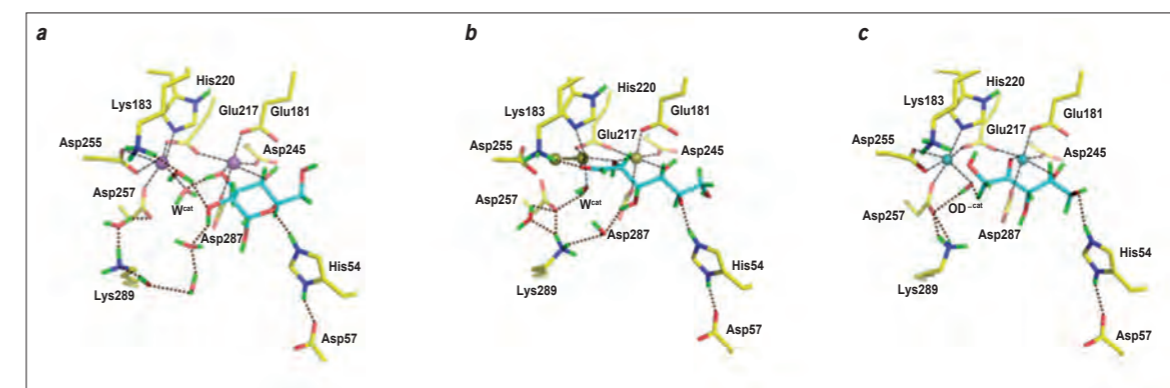


Figure 2: (a) Cyclic substrate glucose bound, (b) linear substrate glucose bound after ring opening has occurred and (c) linear product, xylulose (lacking the C6-terminal CH₂OH group), bound after the ring-opening and isomerisation steps have occurred. Note the interaction of the catalytic OD⁻ with the C1 methylene group of the sugar in (b) and (c). Metal coordination: black dashed lines; H bonding: dotted brown lines; D atoms: green.

REFERENCES

- P.D. Adams, M. Mustyakimov, P.V. Afonine, P. Langan. Acta Crystallographica Section D Biological Crystallography 65, 567-573, 2009 [1]
 B. Bennett, M. Yeager Structure, 18, 657-659, 2010 [2]
 A.Y. Kovalevsky, L. Hanson, S.Z. Fisher, M. Mustyakimov, S.A. Mason, V.T. Forsyth, M.P. Blakeley, D.A. Keen, T.Wagner, H.L. Carrell, A.K. Katz, J.P. Glusker, P. Langan Structure 18, 688-699, 2010 [3]
 J.P. Glusker, H.L. Carrell, A.Y. Kovalevsky, L. Hanson, S.Z. Fisher, M. Mustyakimov, S.A. Mason, V.T. Forsyth, P. Langan. Acta Crystallographica Section D Biological Crystallography 66, 1257-1261, 2010 [4]

The influence of cholesterol on the collective dynamics of the phospholipid acyl chains in model membranes

An important goal in biophysics is to understand the structural, dynamical and functional properties of membranes. Binary lipid membranes serve as simple model systems to understand their far more complex biological counterparts. Cellular membranes are highly enriched in cholesterol and their behaviour – in terms of fluidity or permeability for instance – is strongly influenced by its properties. Collective lateral membrane fluctuations play a crucial role in the transport processes within and across membranes [2]. Neutron three-axis spectrometer experiments have now revealed structural and dynamical properties of physiologically relevant phospholipid/cholesterol membranes [1]. The work shows how picosecond collective molecular motions in this important biological interface are affected and controlled by this key molecular player.

There have been far fewer studies of the dynamics of fluid lipid bilayers containing cholesterol than of their structural aspects, even though the functional properties of a membrane may depend as much on the dynamics as on the structure. We have studied binary mixtures of 1,2-dimyristoyl-sn-glycero-3-phosphatidylcholine (DMPC) and cholesterol at two points in the temperature- and concentration-dependent phase diagram [1], one well within the so-called liquid-ordered L_o -phase (40mol%, 24°C), and one well within the liquid disordered L_d -phase (5mol%, 35°C). **Figure 1(a)** shows a view of the lipids in each of the phases.

Neutron scattering experiments were carried out on the ILL's three-axis spectrometers IN8 and IN12. For each of the two cholesterol ratios, a 400 mg lipid solution was spread on several 300 μm -thick round silicon wafers of a diameter of 5 cm; these were then stacked to produce a 'sandwich sample'. The samples, consisting of several thousand highly oriented lipid bilayers on top of each of twenty

stacked wafers, were kept at constant temperature and relative humidity. **Figure 1(b)** illustrates the scattering geometry used for the reflectivity scans $S(Q_z)$, to determine the lamellar repeat order and spacing D_z , as well as for the in-plane measurement of the elastic $S(Q_x)$ and inelastic structure factors $S(Q_x, \omega)$.

Already the neutron reflectivities $S(Q_z)$ shown in **figure 2** reveal interesting effects: the number of lamellar peaks is visibly higher for 40 mol% cholesterol than for 5 mol%; this is consistent with a reduction in the thermal undulations caused by the frequently reported increase in bending rigidity κ_B . It confirms a higher acyl chain order at higher cholesterol concentration.

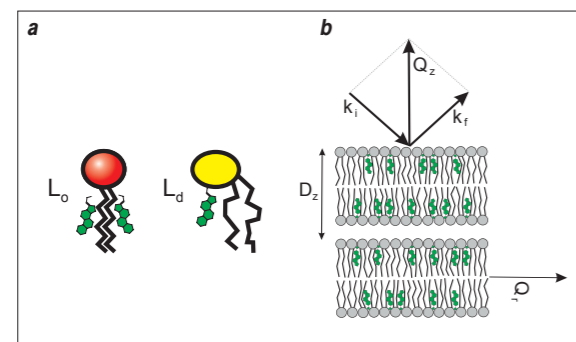


Figure 1: (a) View of the L_o - and L_d -phase. (b) The scattering geometry for reflectivity $S(Q_z)$ and in-plane structure $S(Q_x)$ and dynamics $S(Q_x, \omega)$.

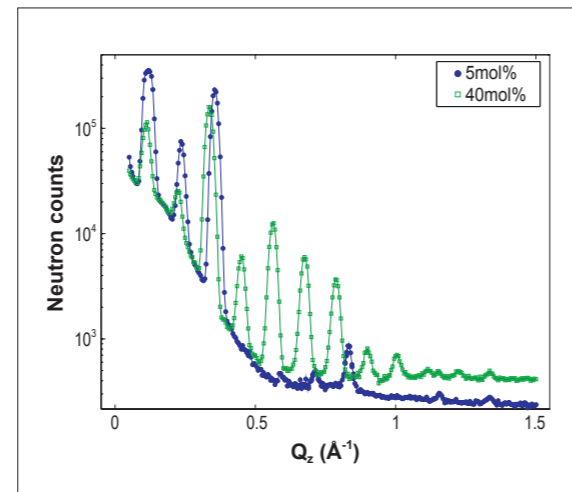


Figure 2: Neutron reflectivities $S(Q_z)$ in the L_d -phase (5mol%) and L_o -phase (40mol%) (IN8).

Nevertheless, the acyl chain correlation peaks $S(Q_x)$ shown in **figure 3** indicate a similar nearest neighbour packing distance of the lipids independent of cholesterol concentration, but different to pure DMPC in the gel phase.

Inelastic neutron scattering experiments shed light on the collective dynamics of the lipid acyl chains for both cholesterol concentrations (**figure 4**). The inelastic structure factor $S(Q_x, \omega)$ was analysed empirically, i.e. by combining a central Lorentzian line-shape (to account for any quasielastic contribution) with two separate damped harmonic oscillator motions (to describe the inelastic excitations).

Over a broad Q_x -range, a pair of sharp excitations can be seen in both phases, which was not observed in the preceding study of pure DMPC [2]. The position and width of the excitations for all Q_x depend only weakly on the phase state. The collective lipid chain dynamics exhibit threshold-type behaviour similar to the effect observed when a drop of oil is inserted into water. The strongest inelastic scattering contribution is observed at the position of the acyl chain correlation peak (**figure 4, centre**). The ring-shaped cholesterol body acts as a rigidifier, so that any acyl chains in its vicinity may be forced to oscillate in phase. Cholesterol filters out certain modes, favouring those commensurate in wavelength

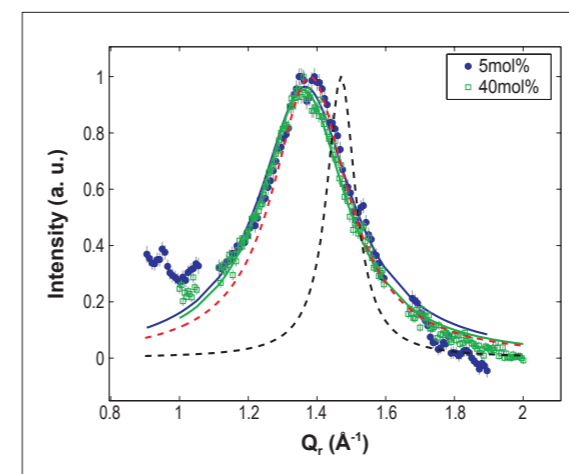


Figure 3: Acyl chain correlation peaks $S(Q_x)$ (normalised, IN8) in the L_d -phase (5mol%) and L_o -phase (40mol%); dotted lines represent pure DMPC in the gel phase (black) and fluid/liquid phase (red).

with the lateral packing distance. The addition of cholesterol changes the chain density fluctuations by reducing the dissipation of propagating sound modes.

In a physiological environment, the molecule is found in membranes adjacent to nerve cells, therefore in membranes which expand while the action potential passes. The role of cholesterol here could be to reduce mechanical dissipation.

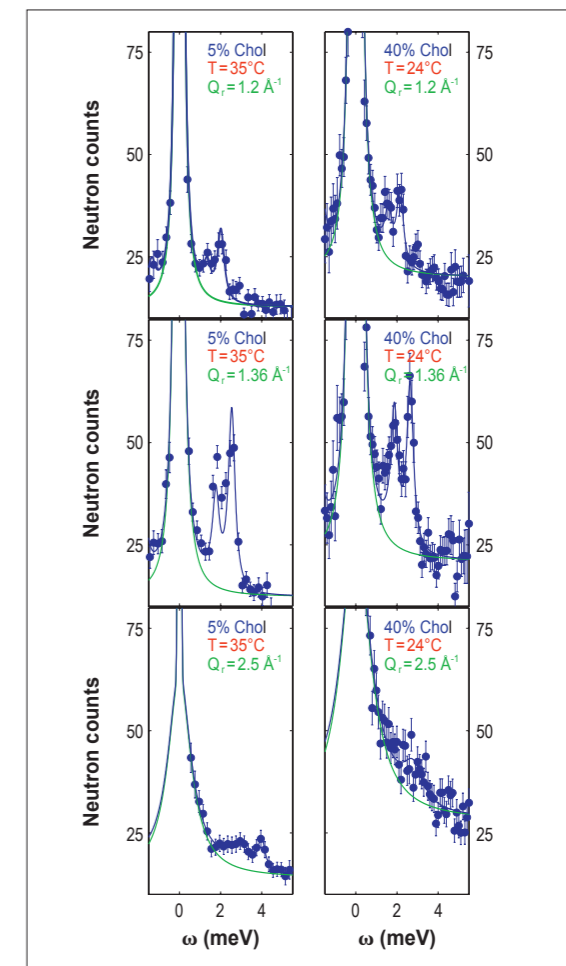


Figure 4: Energy scans $S(Q_x, \omega)$ at various momentum transfers Q_x (IN12); (left column) 5mol%: L_d -phase, (right column) 40mol%: L_o -phase. Fit described in the text.

REFERENCES

- B. Brüning, M.C. Rheinstädter, A. Hiess, B. Weinhausen, T. Reusch, S. Aeffner and T. Salditt, Eur. Phys. J. E 31 (2010), 419 [1]
 M.C. Rheinstädter, C. Ollinger, G. Fragneto, F. Demmel and T. Salditt, Phys. Rev. Lett. 93 (2004), 108107 [2]

Molecular origin and hydration dependence of protein anharmonicity revealed by elastic neutron scattering

Neutron scattering reveals the occurrence of anharmonic dynamics in proteins. In this article we describe how we used homomeric polypeptides as model systems to determine the molecular origin of protein anharmonicity by elastic neutron scattering. We show that methyl group rotations are the main contributors to the first onset of anharmonicity at low temperature, while the so-called dynamical transition above 220 K involves backbone and side-chain fluctuations. We also investigate and highlight the role of hydration on these anharmonic onsets.

Proteins are the molecular machines of living systems. Their dynamics range over several orders of magnitude in time. Functionally relevant anharmonic motions of side chains, such as methyl group rotations or aromatic-ring fluctuations, occur in the subnanosecond time domain. Neutron scattering is a powerful technique for studying protein dynamics in this timescale, which is accessible with the typical energy resolution of neutron spectrometers. In particular, probing the dynamics as a function of temperature makes it possible to explore the energy landscape of proteins [1].

Two main onsets of anharmonicity are present in protein dynamics [2]. Neutron scattering on hydrated protein powders reveals a first onset of anharmonicity at about 100-150 K and a second one at about 230 K (the so-called dynamical transition), both corresponding to anharmonic motions that fall within the timescales accessible with the instrumental resolution available. The role of these motions in the protein function would appear to be crucial. However, until now a complete mapping of the specific dynamical contribution of the different amino acids (the building blocks of protein chains) had not yet been achieved. Indeed, the structural heterogeneity of proteins makes it difficult to identify the contribution of each amino acid.

Using elastic neutron scattering at the IN13 backscattering spectrometer, we have recently shown [3,4] that homomeric polypeptides are suitable systems for identifying and isolating the contribution of the different amino acids to the total mean square displacement of hydrogen atoms. This approach overcomes the problem posed by the intrinsic heterogeneity of proteins: it allows the study of amino acid chains (since the dynamical properties of proteins can be expected to be intimately linked to their chain-like nature) but at the same time makes it possible to measure the dynamic behaviour of each type of residue separately, allowing us to determine the contributions of each type of side chain to the anharmonic transitions and hence identify the transitions' molecular origin.

In particular, we used hydrated powders of the polypeptides poly-glycine, poly-alanine, poly-isoleucine, poly-lysine, poly-phenylalanine and poly-proline (see **figure 1**). The rationale of this choice is as follows: poly-glycine has only α -carbon hydrogens and therefore should provide the "pure backbone" contribution, thus highlighting the role that the backbone plays in anharmonic dynamics; poly-alanine has a side chain composed of a single methyl group and hence should reveal how methyl groups contribute to anharmonic dynamics; poly-lysine does not contain methyl groups;

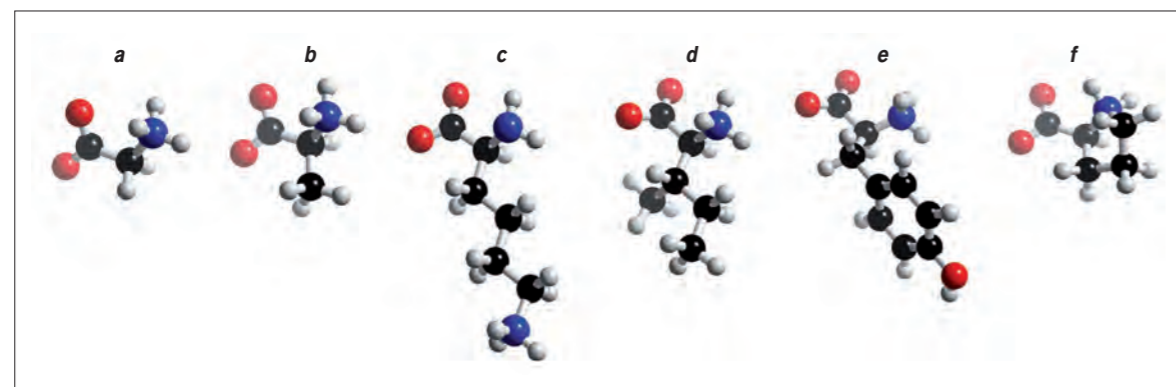


Figure 1: Chemical structure of the six different amino acids of which the homomeric polypeptides studied in this work are composed. From left to right: (a) glycine, (b) alanine, (c) isoleucine, (d) lysine, (e) phenylalanine and (f) proline.

it has four methylene groups and a charged amino terminus and was chosen to identify the methylene contribution; poly-isoleucine has a more complex methyl-group-containing side chain; poly-phenylalanine has a benzyl side chain that does not contain methyl groups; poly-proline has a methylene side chain with the terminus bound to the N atom of the backbone, thus making the polypeptide backbone itself much less flexible.

The results obtained from this research provide the first unambiguous and model-independent experimental evidence for different contributions to anharmonic activations in proteins. Moreover, relevant information has been obtained about the role of water in anharmonic dynamics. The main results can be summarised as follows (**figure 2**):

- 1) the first onset of anharmonicity, at about 150 K as measured with IN13 resolution, is largely attributable to methyl group rotations, as previously suggested although never clearly shown; much smaller contributions from aromatic hydrogen atoms are also present;
- 2) water does not affect this onset: it also occurs in a dry sample and does not change (either in activation temperature or in amplitude) when hydration increases;
- 3) the second onset of anharmonicity, at about 230 K, usually referred to as the dynamical transition, involves backbone fluctuations and also occurs in the absence of side chains; the presence of side chains does not influence the activation temperature but increases the fluctuation amplitude substantially;
- 4) the presence of water on the polypeptide surface is necessary for the dynamical transition to take place;
- 5) the hydration effect is strongly dependent on the structural complexity of the polypeptide: the presence of side chains causes an increase in the mean square displacements (MSD) when hydration increases, while for poly-glycine, where the polypeptide has only the backbone, the amplitude of the fluctuations activated at the dynamical transition is not sensitive to changes in hydration level above 0.2 [g D₂O]/[g poly-glycine].

The present results open up new perspectives about the physical nature of the observed anharmonic onsets. How is their activation temperature related to instrumental resolution? Can the dynamical transition really be considered as a "standard" glass transition?

In order to clarify these points, further investigations are currently ongoing, using other neutron spectrometers with different energy resolutions.

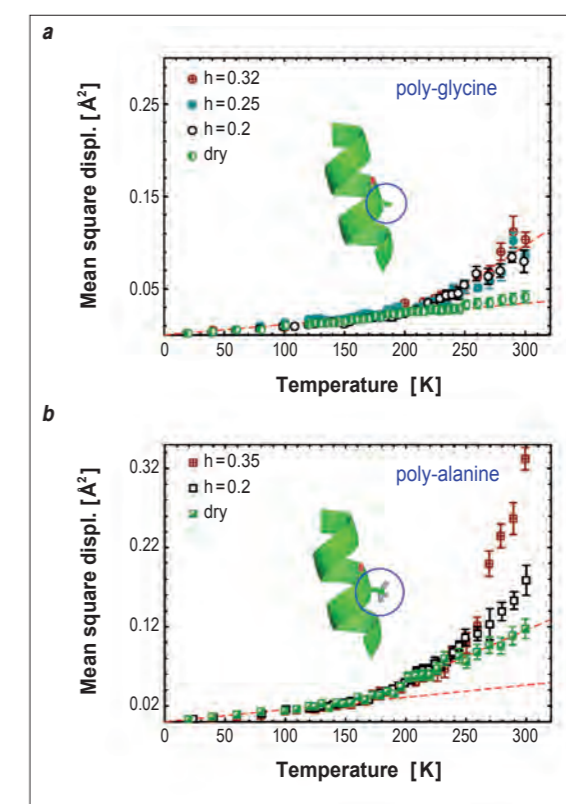


Figure 2: Comparison of MSD in poly-glycine (a) and poly-alanine (b) at different hydration levels. The hydration water effect on anharmonic dynamics depends on the structural complexity of the polypeptides. The local dynamics of methyl side chains is independent of the presence of water and unaffected by the hydration level. Concerning the anharmonic fluctuations involved in the dynamical transition, a minimum number of water molecules are needed to activate large-scale fluctuations. When only the backbone is involved (poly-glycine), the extent of these fluctuations does not increase by increasing the hydration above this threshold; on the contrary, the presence of side chains (poly-alanine) creates a strong hydration dependence.

REFERENCES

- W. Doster, S. Cusack and W. Petry, *Nature* 337 (1989) 754 [1]
 J.H. Roh, V.N. Novikov, R.B. Gregory, J.E. Curtis, Z. Chowdhuri and A.P. Sokolov, *Phys. Rev. Lett.* 95 (2005) 038101 [2]
 G. Schirò, C. Caronna, F. Natali, and A. Cupane, *J. Am. Chem. Soc.* 132 (2010) 1371 [3]
 G. Schirò, C. Caronna, F. Natali, and A. Cupane, *Phys. Chem. Chem. Phys.* 12 (2010) 10215 [4]

The coherent dynamics of protein, hydration water and the protein-water interface in the terahertz window

The structure and dynamics of proteins are the key to understanding how they work and, more generally, how they can accomplish their natural biological role [1]. Once the basic chemical and physical properties of these systems have been determined, we can begin to contemplate the possibility of developing tailored microscopic biological machinery to perform specific biochemical and medical tasks. One crucial step in this direction is to understand the synergic correlation between the protein and solvent dynamics.

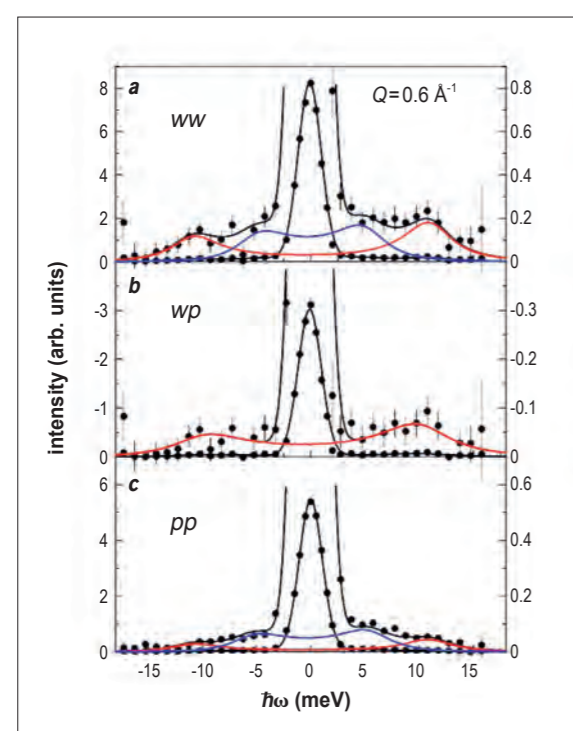


Figure 1: Partial dynamic structure factors of water-water (a), protein-water (b) and protein-protein correlations (c) at $Q=0.6 \text{ \AA}^{-1}$. The full spectra (scale on the left) are superimposed on the magnified spectra (scale on the right), which emphasises the inelastic components. Continuous black lines show the best-fit model function. Blue and red lines show, respectively, the low- and high-frequency DHO employed in the model fitting function.

In this article, we present the results of a neutron spectroscopy study on the collective dynamics of atoms, or groups of atoms, in the Maltose Binding Protein (MBP) at terahertz frequencies. THz dynamics in proteins are thought to be essential for driving functionally relevant movements. However, due to the difficulty of singling out the coherent scattering signal from the generally large incoherent background of single-particle localised motions, the features of collective modes in proteins are still far from being understood.

Thanks to both the availability of fully deuterated samples (produced by the ILL-EMBL Deuteration Laboratory) and the specificity of the BRISP spectrometer, we were able to obtain the very first experimental determination of the separate dynamical contributions that arise from the protein, the protein-water interface and the hydration water.

The three coherent partial dynamic structure factors were extracted by combining the measurements of three MBP samples presenting different protein-water contrast factors, namely a dry protein sample and two samples hydrated at 0.5h and 1.0h (h = grams of D_2O /grams of dry protein), respectively. The data obtained for the three partials were fitted by an empirical model based on the response function of two damped harmonic oscillators (DHOs) (figure 1).

The resulting dispersion curves, plotted in figure 2, reveal that, at meV energies, the coherent dynamics of protein and hydration water closely resemble each other, both displaying two emerging modes [2]. The first mode is dispersionless and localised around 6 meV, while the second one propagates with a speed of about 3200 m/s. Quite strikingly, the two modes are also very similar to those observed in bulk water (see the straight line in figure 2) [3].

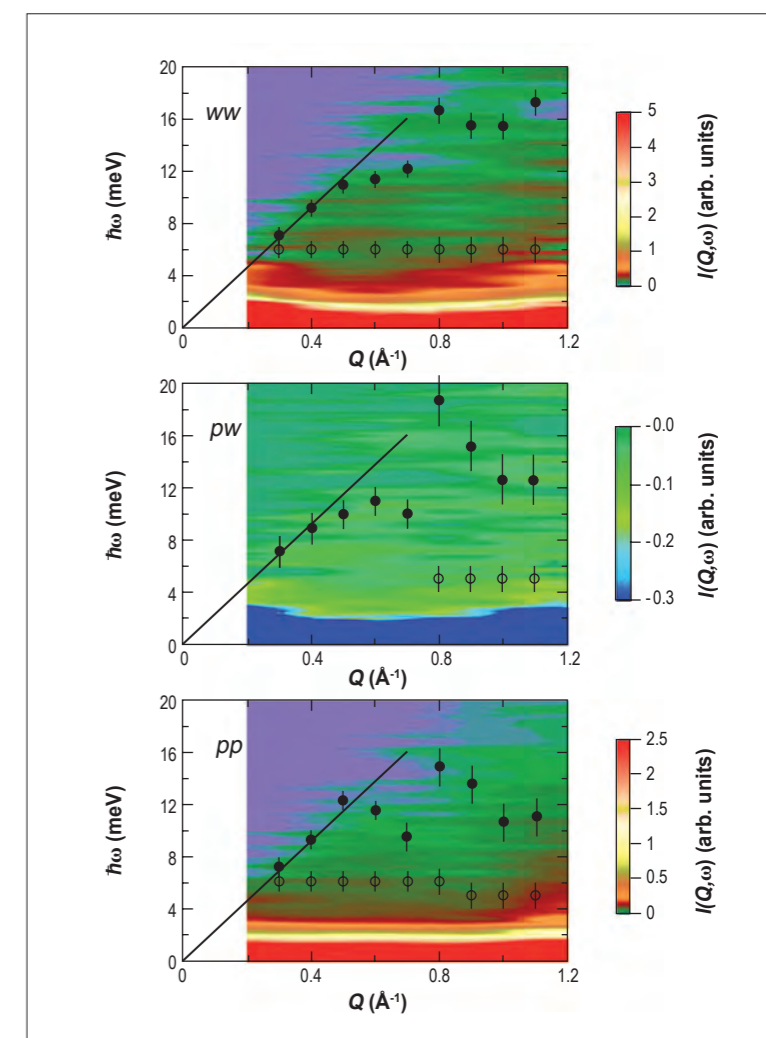
The present approach also provides access to the protein-water interfacial contribution, although with lower statistical quality. Interestingly, this contribution supports a picture where the dispersive thermal fluctuations propagate even through the interface.

Such similarities suggest an intrinsic dynamical affinity between the biomolecule and its solvent, thus allowing THz density fluctuations to propagate without substantial reflection or scattering from the solvent to the protein and vice-versa.

A deeper analysis of the mode's scattering intensities suggests that the dispersive fluctuation in the protein is sustained by molecular subdomains with a total mass of about 60 amu, which is of the order of the average amino acid mass in MBP.

The emerging picture of collective coherent dynamics in the protein-water system suggests a delicate interplay between two interacting networks of oscillators: the hydrogen-bond network of water molecules and the entire collection of the oscillating protein subdomains.

Figure 2: Dispersion curves of the low- (empty circles) and high-frequency (full circles) collective mode, superimposed to the contour plots of the three partial dynamic structure factors. The water-water, protein-water and protein-protein dynamic structure factors are shown in the top, middle and bottom panel, respectively. Straight lines represent the trend of the high-frequency mode in bulk water.



REFERENCES

- K. Henzler-Wildman and D. Kern, Nature 450 (2007) 964 [1]
A. Orecchini *et al.*, J. Am. Chem. Soc. 131 (2009) 4664 [2]
C. Petrillo and F. Sacchetti, Phys. Rev. E 62 (2000) 3611 [3]

V.V. Nesvizhevsky and R. Cubitt (ILL)
 A.Yu. Voronin (Lebedev Institute, Moscow, Russia)
 K.V. Protasov (UJF-CNRS/IN2P3-INPG, Grenoble, France)

Polarised cold neutron beam facility PF1B
 Reflectometer D17

Neutron whispering gallery

The "whispering gallery" effect had already been recognised in ancient times as a phenomenon in air-borne sound waves; it was later recognised in water and more recently for a broad range of electromagnetic waves in the radiofrequency region, from visible light to X-rays. It consists of wave localisation in the vicinity of concave surfaces. For matter waves, it includes a new feature: a massive particle settled in quantum states, with parameters depending on its mass. This article presents the first observation of such an effect [1].

It is thanks to the whispering gallery effect that a sound can reach a person on the opposite side of a building, or even complete a complete circle and produce an echo. Lord Rayleigh explained and quantitatively described this phenomenon in his "Theory of sound" [2], launching in the process the science of acoustics. Whales are believed to exploit a similar effect in the surface layers of sea water, thus enabling them to communicate over long distances. There is an increasing interest in electromagnetic whispering gallery waves across the spectrum from radio to light (the halo effect) and X-ray frequencies [3,4], owing to their multiple applications.

Prior to the present work, no analogous phenomenon has ever been measured with matter waves [5]. Consider the scattering of a cold neutron by a perfect cylindrical mirror with a radius of a few centimeters as shown in **figure 1**. The mirror is described by a

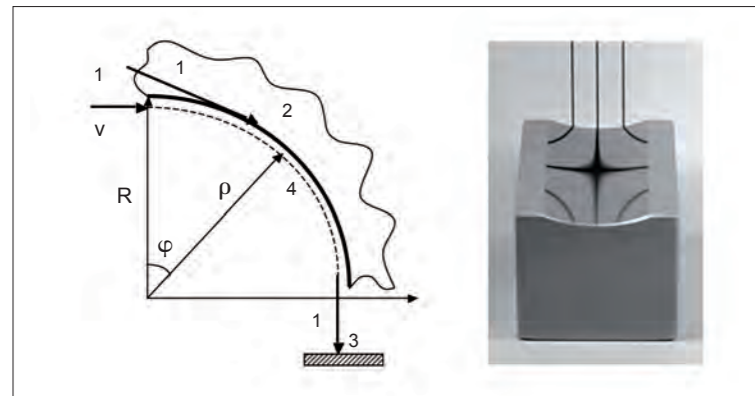


Figure 1: A view of the neutron centrifugal experiment. 1: Classical trajectories of incoming and outgoing neutrons, 2: cylindrical mirror, 3: neutron detector, 4: quantum motion along the mirror surface. **Insert:** A photo of the single-crystal cylindrical silicon mirror used for the experiments presented, with an optical reflection of black stripes for illustrative purposes.

uniform neutron-nuclear optical potential, which reflects neutrons (classically) with radial velocity components lower than the critical velocity corresponding to this potential. The neutron, however, is affected by huge centrifugal acceleration a million times stronger than the Earth's gravitational acceleration. The tangential motion of the neutron is essentially classical, while the quantum effects for the radial motion are dominant. The quantum states are settled in a bounding well of nearly triangular shape. The well is formed by the centrifugal potential and the mirror potential. These are quasi-stationary states, as the probability of tunneling through the trapping potential barrier is never zero, although it could be negligible for deeply bound states [1].

The method used to study the quantum states is based on a continuous variation of the bounding triangle barrier width. The width, the energy and the number of states depend strongly on the neutron velocity. In particular, the transmitted neutron flux increases sharply from zero when the neutron velocity (wavelength) approaches a characteristic cut-off value corresponding to the appearance of the lowest quasi-stationary state.

An alternative method for studying such centrifugal states consists in measuring the radial velocity distribution using a position-sensitive neutron detector, placed at a distance from the mirror. In particular, if a single long-living state is populated, we could directly measure the distribution of radial velocity components in this quantum state. Evidently, the most powerful method consists of combining the two options, i.e. a simultaneous measurement of the scattering angle and the neutron velocity.

A typical scattering pattern is shown in **figure 2**. The feasibility of this experiment was tested at PF1B and the experiment was performed on the D17 instrument at the ILL. The neutrons enter from the entrance edge of a truncated cylindrical mirror (**figure 1**).

The "fingerprints" of the quantum states in **figure 2** have a "V" shape. This can be understood as follows. The average deviation angle is equal to the angular mirror size. The "fingerprint" is centered on this value; thus, the radial velocity distribution is symmetric relative to the zero value. For classical consecutive Garland trajectories of neutrons, the width of the "V" would be exactly proportional to the neutron wavelength (**figure 2**). One manifestation of the centrifugal quasi-stationary states observed consists in the sharp cut-off in the neutron flux wavelength, corresponding to the appearance of the lowest quantum state. Another manifestation is the striped structure inside the "V" shape. This is explained by the interference of a few transmitted quantum states. The theoretical simulation of the data, shown in **figure 2**, reproduces the measurement in detail. Some of the difference between the experimental data and the simulation is probably due to the thin oxide layer on the mirror surface.

In conclusion, under certain conditions this problem can be reduced to a quantum particle above a mirror in a linear potential, the so-called quantum bouncer, in analogy with the neutron quantum motion in the Earth's gravitational field above a flat mirror [6]. These two phenomena provide a first direct demonstration of the weak equivalence principle (the equivalence of the gravitational and inertial masses) in a pure quantum state: although the independence of a free fall on mass does not hold in the quantum limit, the quantum states of a massive body in a locally uniform gravitational field and those in a system moving with equal acceleration are equivalent. Both the centrifugal and the gravitational problems provide an excellent laboratory for studying neutron quantum optics phenomena. Deeply bound whispering-gallery states are long-lived and weakly sensitive to surface potential; highly excited states are short-lived and very sensitive to the wall potential shape. They therefore provide a very promising tool for studying fundamental neutron-matter interactions, quantum neutron optics, and surface physics effects.

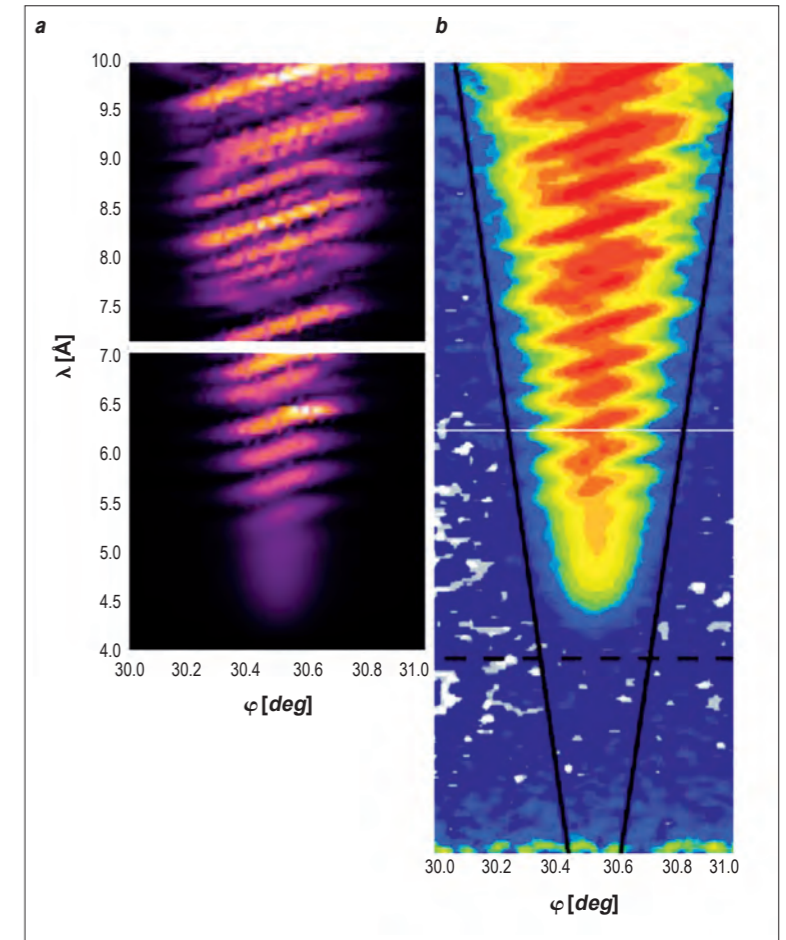


Figure 2: (a) The scattering probability as a function of neutron wavelength (vertical axis) and deviation angle (horizontal axis). The geometrical angular size of the mirror is 30.5° . The inclined solid lines show the signal shape for the classical Garland trajectories. The dashed line illustrates a characteristic wavelength cut-off. (b) Theoretical simulation of the data.

REFERENCES

- V.V. Nesvizhevsky, A.Yu. Voronin, R. Cubitt and K.V. Protasov, *Nature Phys.* (2010) Vol. 6, 114-117 [1]
 J.W. Strutt, *The Theory of Sound*, v.2. s.l.: Macmillan (1878) [2]
 G. Mie, *Ann. Phys.* (1908) Vol. 25, 377-452 [3]
 K.J. Vahala, *Nature* (2003) Vol. 424, 839-846 [4]
 H. Mabuchi and Kimble, *Opt. Lett.* (1994) Vol. 19, 749-751 [5]
 V.V. Nesvizhevsky *et al.*, *Nature* (2002) Vol. 415, 297-299 [6]

M. Jentschel and J. Krempel (ILL)
 W. Urban (ILL and University of Warsaw, Poland)
 J. Dudek and D. Curien (Institute for Subatomic Research, Strasbourg, France)
 B. Lauss (PSI, Villigen, Switzerland)
 G. de Angelis (Legnaro National Laboratories, Italy)
 D. Tonev and P. Petkov (Institute for Nuclear Research and Nuclear Energy, Soa, Bulgaria)

A Test of Tetrahedral Symmetry in Nuclei

Symmetry is a fundamental concept in describing physical systems. Recent theoretical studies based on the nuclear mean field postulated the existence of high rank symmetries leading to nuclei with a tetrahedral shape [1, 2]. In molecules, which are configurations of atoms bound by electromagnetic interactions, the non-trivial point group symmetries are common. Such symmetries in nuclei, with a compact distribution of elementary particles governed by strong interactions, would represent a new class of physical phenomena.

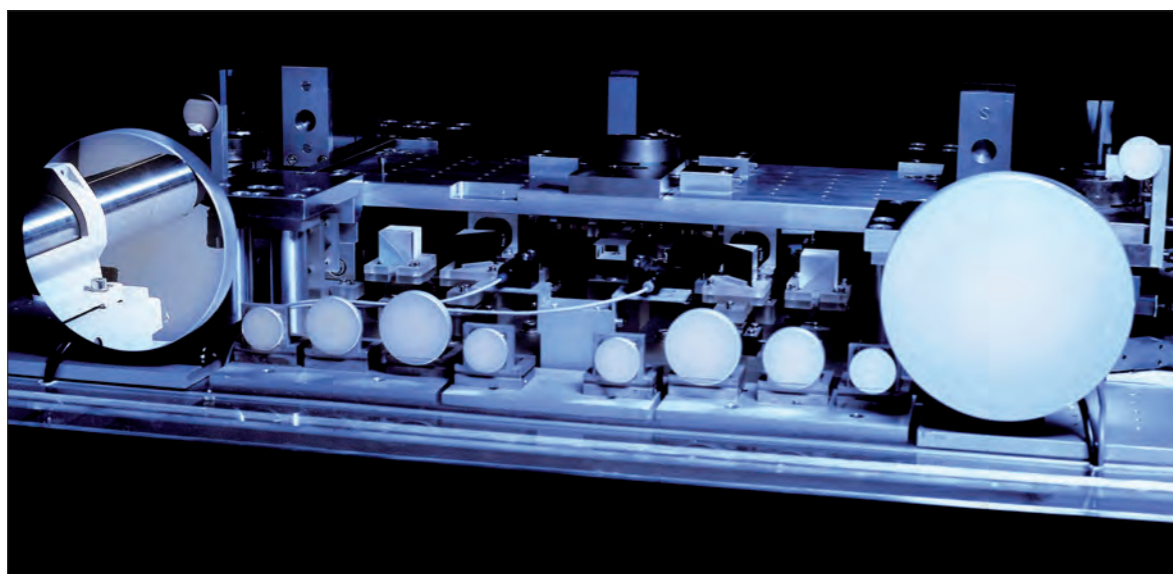


Photo: The high-resolution gamma-ray spectrometer GAMS.

Any experimental verification of this postulate requires the formulation of criteria allowing to distinguishing this new symmetry from others. Theoretical investigation have been made [1] stating that a nucleus with tetrahedral shape should exhibit negative-parity rotational bands (negative parity means that reflection symmetry is violated) with vanishing intra-band transitions. In the same theoretical work it was predicted that tetrahedral shapes are expected all over the nuclear chart, where the nucleus ^{156}Gd , is considered to be the most favourable candidate for an experimental verification.

The lowest odd-spin, negative-parity rotational band in ^{156}Gd may be due to tetrahedral deformation, because the intra-band transitions were not observed at the bottom of the band in previous experiments. It was of interest to investigate the character of this band in order to decide if it is due to a tetrahedral deformation.

The first direct test of tetrahedral symmetry in ^{156}Gd was carried out at the ILL in 2009 [3] exploiting the ultra-high resolution of the gamma-ray spectrometers GAMS4 and GAMS5. The GAMS4 spectrometer was equipped with perfect flat crystals yielding a very high relative energy resolution of $\Delta E/E \approx 10^{-6}$. Its unique energy resolution allows the determination of nuclear states lifetimes using the Gamma Ray Induced Doppler-broadening (GRID) technique. The spectrometer is also capable of measuring absolute energies. The GAMS5 spectrometer, equipped with curved crystals in DuMond diffraction geometry, has the solid angle 10^5 higher than GAMS4, though for the price of a lower energy resolution. Thanks to the diffraction process the detectors at GAMS have a very small background rate and can detect transitions with a dynamical range of 10^6 . All these features make GAMS4 and GAMS5 spectrometers a unique tool for studying the properties of very weak transitions.

In our study we aimed at verifying the presence of the $5^-_1 \rightarrow 3^-_1$ transition in ^{156}Gd and measuring its transition rate. According to the tetrahedral model this intra-band transition located at the bottom of the band, should be absent. The search of the intra-band transition profited from the extraordinary dynamic range of the GAMS5 spectrometer. In order to further increase statistics only a small energy range of γ -rays from 130 keV to 134 keV containing the 131.119(2) keV, reference line was scanned for one week.

The observed spectrum is shown in **figure 1**. The two prominent lines in the spectrum provided a shape calibration for fitting weaker lines (see insert in **figure 1**). One of the observed lines at 131.983(12) keV matches well the energy difference between the 5^-_1 and 3^-_1 levels, measured previously.

To further improve this identification the energy difference between the 5^-_1 and 3^-_1 levels was determined with GAMS4 by measuring energies of the $5^-_1 \rightarrow 4^+_1$ and $3^-_1 \rightarrow 4^+_1$ transitions. After recoil correction the energy difference of the 5^-_1 and the 3^-_1 levels was determined to be $E = 131.9894(19)$ keV. The intensity of the 131.983 keV transition of 0.019(3) is less than 10^{-5} fraction of the strongest line in ^{156}Gd .

Using the GRID technique we measured the lifetimes of the 5^-_1 and 3^-_1 levels in ^{156}Gd . The nuclear state lifetimes were deduced from the measured Doppler broadening of a transition, where corrections for instrument response and thermal broadening have been subtracted. This yielded a lifetime of $\tau = 0.303^{+0.073}_{-0.075}$ ps for the 5^-_1 and $\tau = 0.220^{+0.180}_{-0.030}$ ps for the 3^-_1 state, respectively.

The measured lifetimes and the intensity of the intra-band transition allowed us to calculate the quadrupole moment of the 5^-_1 state to be $Q_0 = 7.1^{+0.7}_{-1.6}$. The large value of this moment,

which is comparable to the intrinsic quadrupole moment, $Q_0 = 6.83(37)$ [4], of the ground state of ^{156}Gd , indicates strong intraband transitions in the disputed lowest odd-spin, negative-parity band in ^{156}Gd . Following the criteria formulated in [1,2] the present work concludes that the negative parity band in ^{156}Gd is incompatible with a description based on tetrahedral symmetry. Therefore, future theoretical investigations should focus on the formulation of alternative criteria and/or the search for new test candidates.

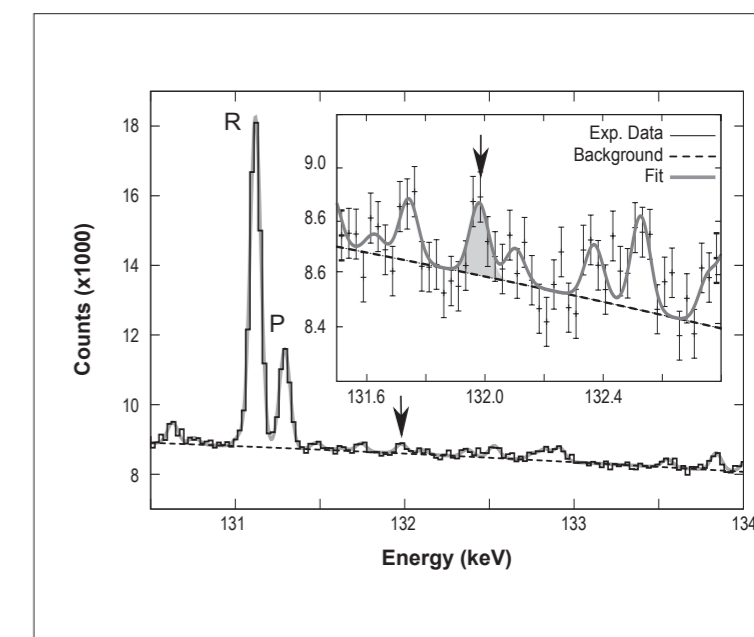


Figure 1: Measured spectrum of the lowest negative parity band in ^{156}Gd . The insert shows the detected intra-band transition.

REFERENCES

- J. Dudek *et al.*, Phys. Rev. Lett. 88, 252502 (2002) [1]
 J. Dudek *et al.*, Phys. Rev. Lett. 97, 072501 (2006) [2]
 M. Jentschel *et al.*, Phys. Rev. Lett. 104, 222502 (2010) [3]
 P.D. Cottle and N.V. Zamfir, Phys. Rev. C 54, 176 (1996) [4]

C. Otjacques, J.-Y. Raty and J.-P. Gaspard (University of Liege, Belgium)
 F. Hippert (LMGP, CNRS, Grenoble-INP, France)
 M. Johnson and H. Schober (ILL)
 C. Bichara (CINaM-CNRS, Marseille, France)

Time-of-flight spectrometer IN6
 Liquids and amorphous diffractometer D4

Dynamical anomaly and negative thermal expansion in tellurium based liquid alloys

Not all liquids expand as their temperature increases, the most famous example being water that contracts between 0°C and 4°C. Some tellurium-based alloys are known to show a negative thermal expansion (NTE) in a narrow concentration range in the liquid phase. Using neutron elastic and inelastic scattering, we demonstrate that this NTE originates from a subtle interplay of quantum mechanical (Peierls-like distortion of the local environment) and statistical (gain in vibrational entropy) effects.

Covalent elements have low coordination numbers (2 for Te, 3 for Sb, 4 for Ge, sometimes referred to as the "valence") leading to the well-known octet rule (the coordination number is equal to 8 minus the number of sp electrons), because of a spontaneous symmetry breaking mechanism imposed by quantum mechanics, called Peierls distortion. This is different from bulk metals for which the highest coordination is favoured. Crystalline antimony for instance, with its 3p electrons and p σ bonding, displays an alternation of aligned short and long bonds (figure 1), instead of the simple cubic structure expected for this element. This leads to the semiconducting (or insulating) behaviour of

the right hand side of the periodic table. The Peierls distortion is not only observed in crystals but also in disordered structures, at least on average, as shown by neutron scattering analysis of covalent liquid and amorphous structures.

If the thermal expansion of materials is the rule - it results from the anharmonicity of the interatomic potential -, there are exceptions [1]. In liquid Te-based alloys showing a NTE, such as GeTe₆ and As₂Te₃, we have observed a noticeable change of the structure factor S(Q) and a red shift of the density of vibrational states (vDOS) (figure 2) close to the melting point, precisely in the temperature range where the NTE occurs [2, 3].

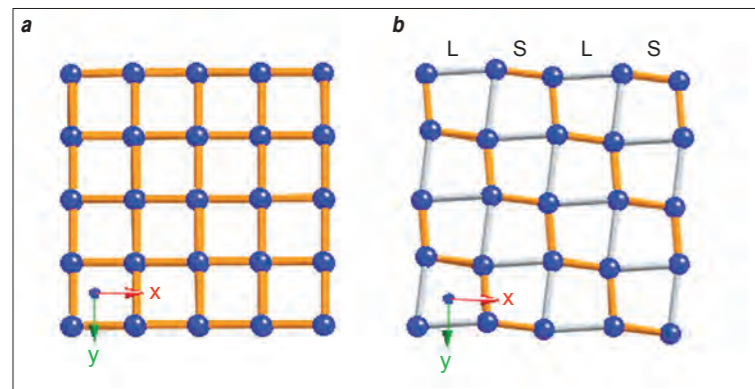


Figure 1: Symmetry breaking of the simple cubic structure induced by an electronic instability (Peierls distortion) in column V elements (As, Sb, Bi). (a) (001) plane of the undistorted structure. (b) Distorted structure: alternation of short and long distances LSLSLS in the <100> directions. In 3D, the distorted structure has a rhombohedral symmetry. By alternating germanium and tellurium atoms on the structure, one gets the β and α phases of GeTe respectively.

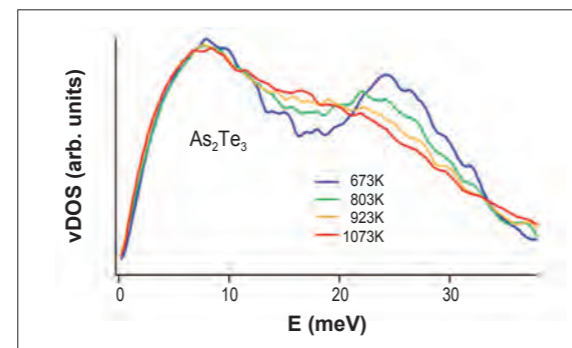


Figure 2: Density of vibrational states in liquid As₂Te₃ obtained from inelastic neutron scattering on IN6. A red shift of the high energy modes is observed as the temperature increases. It corresponds to a softening of the shortest interatomic bonds.

We have explained the driving force of this NTE, which differs substantially from that of water, by combining inelastic neutron experiments (performed on IN6) with *ab initio* calculations and heat capacity measurements. At the melting point the octahedral symmetry of the local order in the liquid is broken by a Peierls-like distortion that leads to a coordination number significantly lower than 6. At higher temperature, the symmetry is restored by an entropic effect leading to a smaller volume and a larger number of neighbours, as in the ($\alpha \rightleftharpoons \beta$) transition in crystalline GeTe. The red shift, observed when increasing temperature, results from a softening of the shortest chemical bonds with a larger vibrational amplitude that increases the entropy. For instance in GeTe₆ the vibrational entropy symmetrises the position of the Ge atom in a cage of Te atoms as sketched in figure 3. Since longer bonds shrink more than shorter bonds elongate, the atomic volume is reduced in this process, while the electrical conductivity shows a significant increase, related to the reduction of the electronic gap. It is worth mentioning that the red shift effect has been first studied by *ab initio* Molecular Dynamics before doing the experiment in order to check that the effect would be observable.

In conclusion, the original NTE occurring in some liquid Te-based alloys results from competing electronic and entropic effects. It is associated with a liquid-liquid crossover between a low temperature less dense phase and a high temperature more dense phase that is more conducting. In other Te-based alloys used as "phase-change" materials [4], a similar phenomenon occurs: the system switches from a less dense amorphous phase to a denser crystalline phase with a much higher conductivity which qualifies these materials for data storage.

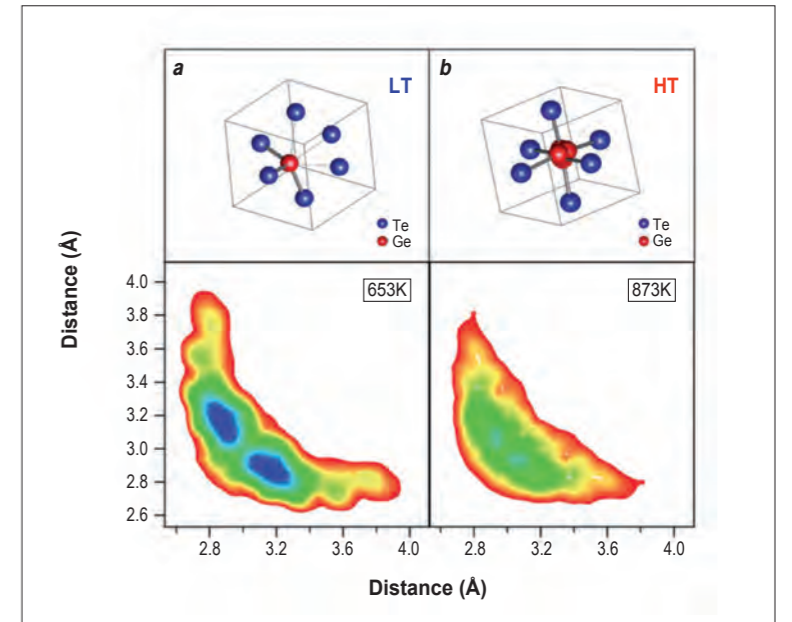


Figure 3: (a) Sketch of the structure of liquid GeTe₆ just above the melting temperature: the Ge atom is in a large volume distorted octahedral environment. (b) At higher temperature, the local environment of Ge atom inside a shrunk octahedral cage becomes more symmetric and the vibrational entropy becomes larger. Three-body correlation function for almost aligned triplets of atoms, centered on Ge atoms, calculated on simulated GeTe₆ structures. At 653 K (lower left panel) two maxima show the Peierls distortion; they merge at 873 K (lower right panel).

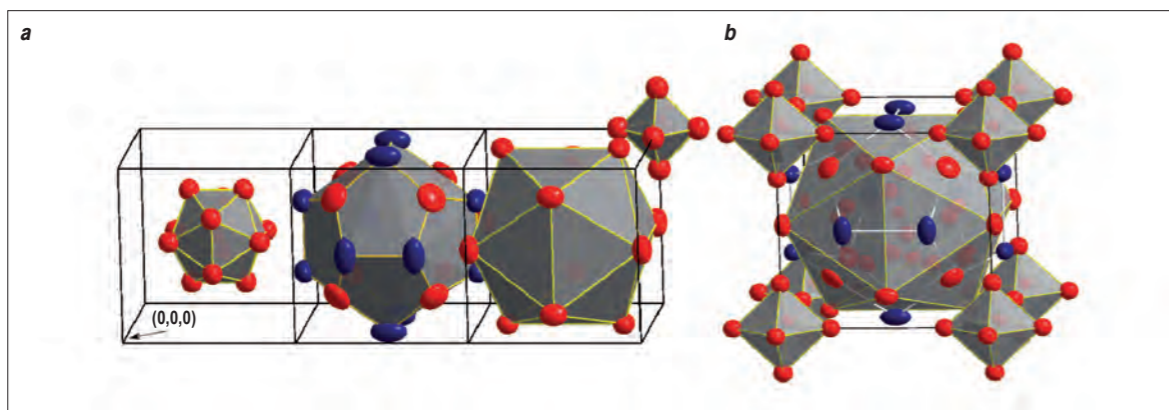
REFERENCES

- G.D. Barrera, J.A.O. Bruno, T.H.K. Barron and N.L. Allan, J. Phys.: Cond. Matter 17 (2005) R217 [1]
 C. Otjacques, J.-Y. Raty, M.-V. Coulet, M. Johnson, H. Schober, C. Bichara, and J.-P. Gaspard, Phys. Rev. Lett. 103 (2009) 245901 [2]
 C. Otjacques, J.-Y. Raty, F. Hippert, H. Schober, M. Johnson, R. Céolin and J.-P. Gaspard, Phys. Rev. B 82 (2010) 054202 [3]
 K. Shportko, S. Kremers, M. Woda, D. Lencer, J. Robertson and M. Wuttig, Nature Materials 7 (2008) 653 [4]

H. Euchner (ITAP, Stuttgart, Germany)
 M. Mihalkovic (Slovak Academy of Science, Bratislava, Slovakia)
 H. Schober, S. Rols and M.R. Johnson (ILL)
 M. de Boissieu (SIMAP, Grenoble, France)
 S. Ohhashi, A.-P. Tsai (Tohoku University, Sendai, Japan)

Anomalous vibrational dynamics in Mg_2Zn_{11}

Quasicrystals are complex, long range ordered materials without translation invariance. This lack of lattice periodicity makes the understanding of physical properties a challenging problem. One way to approach such non-periodic materials is to investigate structures that consist of similar atomic building blocks. In this context we have extensively studied Mg_2Zn_{11} , a compound which shows interesting vibrational properties and exhibits intermediate structural complexity in between the Laves phase $MgZn_2$ [1] and alloys of higher complexity or quasicrystals [2].



Mg_2Zn_{11} consists of 39 atoms in a cubic unit cell and can be described as a packing of atomic clusters. As depicted in **figure 1** the structure is built up from subsequent cluster shells at the body centre, notably a Zn icosahedron with a Zn atom at its center, followed by a dodecahedron of Zn and Mg atoms and a second Zn icosahedron. These clusters - so called Pauling triacontahedra - are linked by Zn octahedra at the vertex of the unit cell (**figure 1b**). By combining X-ray single crystal and neutron powder diffraction data, the existing model of Mg_2Zn_{11} [3] was refined and it could be shown that the innermost Zn site is only partially occupied (30% vacancy, 70% Zn), a result which turned out to be important for stability and dynamics of the system.

The analysis of the diffraction data furthermore provided evidence of strongly anisotropic thermal ellipsoids, especially for the Mg and Zn atoms of the dodecahedral shell (**figure 1a** second shell), related to the local environment and the non-ideal coordination of these atoms, opening space for vibrational motion.

Inelastic neutron scattering (INS) experiments were conducted on polycrystalline samples of Mg_2Zn_{11} at the IN4 and IN6 time-of-flight spectrometers. From these experiments we extracted the generalised vibrational density of states (GVDOS) which

Figure 1: (a) Cluster building blocks of Mg_2Zn_{11} : Inner Zn icosahedron, dodecahedron of Mg (blue) and Zn (red) atoms, outer icosahedral shell of Zn atoms with Zn octahedron at the corner (from left to right). (b) Structure as a cubic packing of Pauling triacontahedra linked by Zn octahedra.

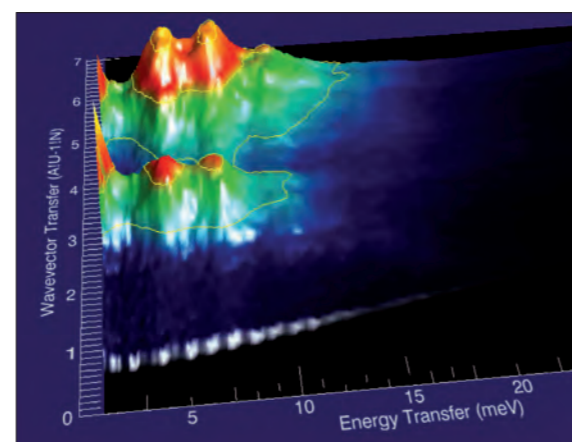


Figure 2: Dynamic structure factor of Mg_2Zn_{11} , as determined from inelastic neutron scattering at 300 K.

is essentially the sum over the weighted partial densities of states (weighted by the Debye-Waller factor and the ratio of scattering power and mass of the Mg and Zn atoms, respectively). The GVDOS of Mg_2Zn_{11} exhibits an excess of modes at low energies, a very unusual behaviour for a metallic alloy. This excess of modes and the resulting increase of sound velocity becomes evident by comparing the GVDOS of Mg_2Zn_{11} to that of the $MgZn_2$ Laves phase (**figure 2**), another Mg-Zn alloy which shows the behaviour of a simple crystal. Furthermore, many sharp, well developed features are visible, indicating that despite structural complexity, several families of *eigenmodes* retain their distinct character.

The impact of the Zn/vacancy disorder on the GVDOS was investigated by *ab initio* methods, using the harmonic approximation. These calculations yielded good agreement with the experimental data after a frequency rescaling for a model with 50% vacancy at the cluster center (**figure 3**). From the experimentally determined temperature dependence of the GVDOS (IN4) on the one hand and from the qualitative behaviour extracted from molecular dynamics (MD) simulations on the other, we could show that the differences at higher energies can be accounted for by including temperature. The observed differences at low energies (modes at 2-3 meV) seem to be artifacts which occur due to the fact that the true energetic ground state (i.e. the exact vacancy distribution) cannot be obtained from *ab initio* calculations due to limitations in system size.

Since the simulation results were found in accordance with the experimental data, we used the *ab initio* phonon *eigenvectors* to relate features of the GVDOS to distinct atomic motions. Vibrational modes in complex structures cannot be meaningfully analysed one by one, therefore we applied a systematic microscopic interpretation by merging modes with a high degree of mutual similarity. For groups of modes with similar energies and vibrational characteristics, we analysed the time-averaged distributions, which illustrate characteristic atomic motions. We could clearly

demonstrate that the prominent modes with anomalously low energy at about 5 meV and 7 meV, respectively, correspond to motions dominated by the Zn atoms of the outer shells (i.e. only weak contributions of the Mg and the inner Zn icosahedron atoms), while the modes at about 13 meV can be attributed to vibrations of the inner Zn icosahedron, which is consistent with the fact that this group of modes is very sensitive to the vacancy content.

In summary, the comparison between the GVDOS of Mg_2Zn_{11} and that of the simple $MgZn_2$ Laves phase showed striking differences between these two Mg-Zn compounds, which, however, seem to originate not only from the higher structural complexity but also from some peculiarities of the Zn-Zn interaction in Mg_2Zn_{11} . The exceptional low energy features of Mg_2Zn_{11} could be reproduced by our simulations and a good overall agreement between experimental and calculated vibrational properties was obtained. Furthermore, pronounced features of the GVDOS could be related to atomistic motions, dominated by certain structural units of the compound, a concept interesting for tailoring functional materials with distinct dynamical properties.

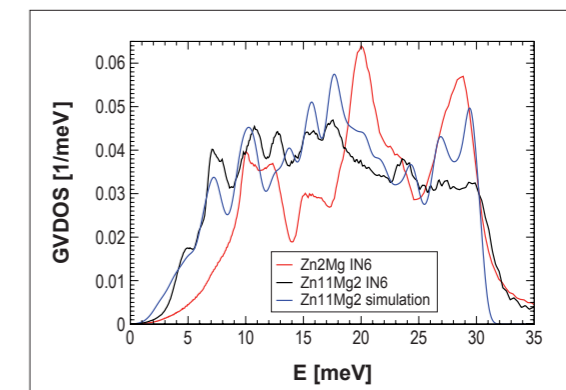


Figure 3: Experimental and calculated GVDOS of Mg_2Zn_{11} in comparison with the GVDOS of $MgZn_2$ at 300 K.

REFERENCES

- P. Brommer *et al.*, Z. Kristallogr. 224 (2009) 97-100 [1]
 M. de Boissieu *et al.*, Nature 6 (2007) 977-984 [2]
 S. Samson, Acta Chem. Scand. 3 (1949) 835-843 [3]

J. Bossy (Institut Néel, Grenoble, France)
 H.R. Glyde (University of Delaware, USA)
 T. Hansen (ILL)

Time-of-flight spectrometer IN5
 High-intensity two-axis diffractometer D20

Superflow in Amorphous Solid Helium

In 2004, Kim and Chan observed a superfluid fraction in solid helium. This remarkable discovery extended superfluidity to all three phases of matter - gases, liquids and solids - and created an entire new field of physics [1]. Perfect crystalline helium is not expected to be a superfluid. However, superflow via defects such as vacancies, dislocations or amorphous regions in the solid is predicted. We have created entirely amorphous solid helium in small pore diameter porous media such as MCM-41. Using D20 we have shown that the confined solid has no Bragg peaks and therefore no crystalline regions. Using IN5, we find there are no phonons. This new amorphous quantum solid is an exciting candidate for superflow in solids and neutrons are playing a critical role.

Helium is a simple atom. It has a light mass, 4 nucleus surrounded by two tightly bound electrons in a stable unit. The ^4He - ^4He interaction is equally simple. Yet at low temperature the atomic de Broglie wavelength is long and helium displays rich and fascinating quantum properties. Below 2 K liquid helium becomes superfluid

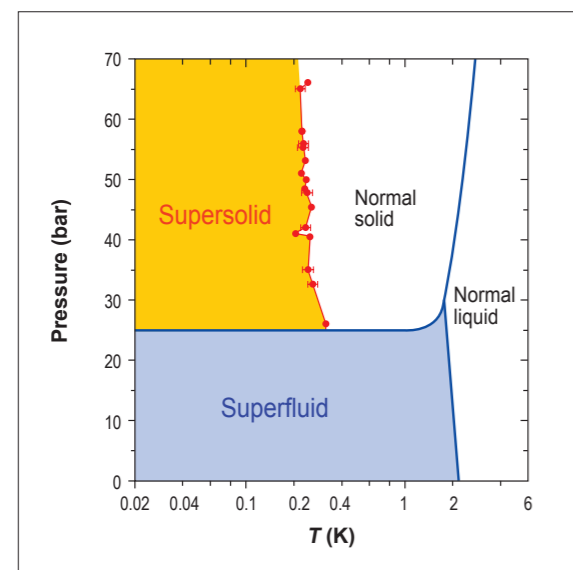


Figure 1: Phase diagram of helium showing the supersolid phase (from reference [2]).

and flows without friction. Since there is no friction, superfluid helium in a container remains motionless when the container is oscillated, as if it is massless. Indeed the superfluid fraction is determined in this way. Equally, below 2 K, some liquid helium condenses into a single quantum state, denoted Bose-Einstein condensation (BEC). BEC is the driver of superflow.

Under a pressure of 25 atmospheres (25.33 bar) or more, helium solidifies. Atomic diffusion is rapid and the solid anneals readily into one or a few large single crystals. Remarkably, in 2004 superflow in solid helium was reported [2]. Below a temperature of 0.2 K, a fraction of the solid ceased to oscillate in an oscillator exactly as the liquid. There is a supersolid phase (see figure 1). However, like superconductivity in the copper oxide and iron base superconductors, the mechanism of this superflow remains a mystery.

Although supersolidity is now confirmed in several laboratories, the observed fraction that is superfluid varies dramatically, from 0.015 to 20 % depending upon how the solid is prepared. This suggests that the superflow is via defects, vacancies, dislocations, grain boundaries or amorphous regions in the solid. Interestingly, the shear modulus of solid helium also increases with decreasing temperature exactly as the superfluid component. This suggests that the two are related and both dependent on the mobility of defects or dislocations. Equally interesting, path integral Monte Carlo calculations predict a large superfluid fraction and BEC in amorphous solid helium.

We have created amorphous solid helium by confining it in porous media. If the pore diameter is less than 50 Å, the solid is entirely amorphous. Helium is highly attracted to the rough pore walls. When helium first enters the pores, it forms an amorphous layer on the walls. Subsequent solid helium grows as an amorphous solid away from the walls. If the pore diameter is small enough the pores are filled entirely with amorphous solid. Using the instrument D20 we have measured the static structure factor, $S(Q)$, of liquid and solid helium in 34 Å diameter gelsil and in 47 Å diameter MCM-41. As shown in figure 2, the static structure factor, $S(Q)$, of solid helium at lower temperature ($T < 1.1$ K) is very similar to that of the liquid at higher temperature ($T > 1.8$ K). No Bragg peaks, characteristic of a crystal, are observed in the solid. In addition we have measured the excitations of the amorphous solid on the instrument IN5. No phonons characteristic of a crystalline solid are observed. Rather, the dynamic response is spread over a wide energy range quite different from the crystalline solid. Analysis of this data is in progress.

In summary, we have shown that amorphous solid helium can be made. This opens a path to demonstrating whether superflow is indeed possible via amorphous helium. Equally we can test whether amorphous solid helium has BEC. In addition the dynamics of a highly

quantum amorphous solid can be investigated for the first time. Superflow in solid helium remains a fascinating field and neutrons are playing a critical role in discovery.

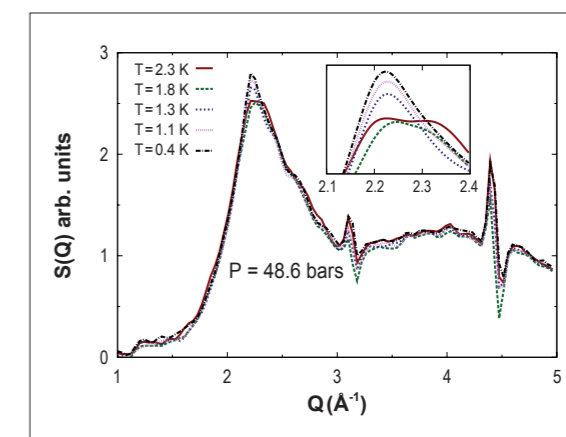


Figure 2: The static structure factor, $S(Q)$, of helium at pressure 48.6 bars in MCM-41. Helium in MCM-41 is liquid at temperatures greater than 1.3 K and solid below 1.1 K. The amorphous solid below 1.1 K has no Bragg peaks. The liquid and solid $S(Q)$ differ only in the peak region of $S(Q)$ (from reference [3]).

REFERENCES

- PACS Index 67.80.bd, supersolid ^4He [1]
 E. Kim and M.H.W. Chan, Science 305, 1941 (2004), Nature (London) 427, 225 (2004) [2]
 J. Bossy, H.R. Glyde, and T. Hansen, Phys. Rev. B 81, 184507 (2010) [3]

MILLENNIUM PROGRAMME
AND TECHNICAL DEVELOPMENTS

The TYREX helium 3 filling station.

MILLENNIUM PROGRAMME
NEW EXPERIMENTAL TECHNIQUES
TECHNICAL AND COMPUTING DEVELOPMENTS

2010 saw excellent progress on the Millennium projects, with nearly all project milestones attained. With 4 years of the second Millennium phase behind us we have already invested 55% of the 43 M€ budget allocated (over 23 M€). In real terms this means the successful upgrade of the D11 small-angle neutron diffractometer, of the vertical reflectometer D17, and of IN4C the thermal time-of-flight spectrometer. LAGRANGE, a hot neutron spectrometer with a beryllium filter option, was delivered to the ILL just before the end of the year.

Of course instruments take space, and we were therefore happy to see the new extension to the ILL 7 guide hall emerging. The hall is now ready to host two new instruments: the small-angle diffractometer D33, and IN16B, a back-scattering spectrometer. It will also soon be sporting two new guides for the instruments. Most of the components for these projects have already arrived or are in their final manufacturing phase.

If we have achieved so much, it has been through frenetic activity on all fronts, not so far removed, from Charlie's "Modern Times"!

At the same time we have continued our focus on new or enhanced sample environment facilities, as well as the further development of ILL's instrument control software NOMAD. These are improvements which benefit the entire suite of ILL instruments; they contribute to the increasing sophistication and higher performance of experiments and are already providing concomitant gains in our scientific output.

If we have achieved so much, it has been through frenetic activity on all fronts, not so far removed, I have to say, from Charlie's "Modern Times"! The plans seem to have been well laid, however, and the coordination good; given excellent team spirit and collaboration across the services and divisions we were able to manage this technically complicated and logistically challenging programme.

The M-1 phase continues of course. The 2011-2014 period is looming, and other projects are already at the detailed design or fabrication point; others are being examined for advanced feasibility. ThALES and WASP are well advanced, for example, together with the projects to provide the infrastructure they need – the H5 guide and the extension to the ILL 22 guide hall. The work on the H5 guide will require good coordination with the Maintenance Service (SAE-DA) and the Reactor Division, given the need to replace the horizontal cold source on H5's beamtube.

The Projects and Techniques Division's (DPT) services also provide support on a day-to-day basis for our users' experiment programme; it is our role, within ILL's mission of progress in science, to minimise technical disorders that could lead to loss of beamtime (currently at less than 7%). Equally important however is the role we play in the research and development process. The new results we have obtained in a partnership with the University of Augsburg, FRM2 and HZB on the potential of diamond monochromator crystals, illustrate the opportunities to be seized to improve the performance of hot neutron instruments. To take another example, we have been pursuing the need for more user-friendly software, so that users can more easily simulate experiments or control the instruments. The new software will encourage the adoption of neutron techniques by scientific communities seeking different tools for their research but with little experience in neutron technology.

The DPT's energy and achievements in 2010 have certainly been impressive. I would like to thank all those across the ILL who have made this possible, and who, most importantly, generate confidence for the future. For it is projects, ideas, and energy, that keep the ILL moving. I should also note the significant changes in 2010 at management level, with the arrival of three new DPT heads of service. Michel Thomas retired after a long and successful career at the Institute and it is now Yoann Calzavara's turn to maintain the high standards of quality and efficiency at Projects and Calculations. Frédéric Descamps and Ken Andersen have also departed to explore new paths in their careers, handing over to Paolo Mutti at Instrument Control and Electronics and to Pierre Courtois at Neutron Optics – both have accepted the challenges with calm and enthusiasm. The year also saw the retirement of DPT secretary Barbara Standke after a remarkable career dedicated to the ILL.

It is true that, in financial terms, 2010 has announced difficult times ahead, but, with our experienced staff and new faces, this has in no way dulled our determination to continue innovation and deliver the ambitious technical services our users require.

José Luis Martínez
Associate Director



Millennium Programme 2010

Phase M-1 of the Millennium Programme (2007-2014) has now reached "cruising speed". This ambitious phase covers the upgrade of 4 instruments, the construction of 4 new instruments, the upgrade of 3 key neutron guides, as well as ongoing improvements to advanced sample environment equipment and instrument control software. The extra space needed to house the new instruments also means extending both neutron guide halls. The total budget for phase M-1 is 43 M€, 55% of which has already been spent at the end of 2010.

The 4 instrument upgrades are close to completion. The upgrade of **D11** (small-angle diffractometer) was finished in 2009, as were the improvements to **D17** (vertical reflectometer). The **IN4C** upgrade project (thermal time-of-flight spectrometer) was completed in 2010. The new monochromator has been installed and aligned and its three faces (one with graphite and two with copper crystals) are now fully operational. The new sapphire filter is proving to be extremely efficient in reducing undesirable fluctuating background. Thanks to the small-angle detector and new collimator system, the signal can now be explored at low Q (mostly magnetic). Finally, following extensive testing, the upgraded electronics of the old Fermi chopper will guarantee the reliability of this important component. The average gain factor achieved by these three projects is 3.7 (3 for D11, 4 for D17 and 4 for IN4C).

Also in 2010, the ILL received delivery of all the components for the secondary spectrometer **LAGRANGE** (Beryllium-filter hot neutron spectrometer). The main elliptical analyser (see **figure 1**), which comprises 620 pyrolytic graphite crystals, is now in the alignment stage and, in parallel to this, testing of the Beryllium-filter cooling system and the global shielding is being conducted. The final commissioning of the instrument with neutrons is scheduled for the second quarter of 2011. The entire secondary spectrometer was manufactured on time by the firm Tekniker (Spain), within the framework of a dedicated Spanish contribution to the ILL. The final gain factor compared with the previous Be-filter spectrometer is expected to be between 50 and 100, depending on the efficiency of the shielding system (reduction of background).

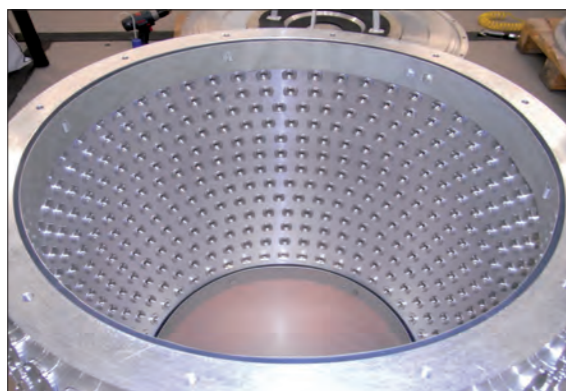


Figure 1: Elliptical analyser for the instrument LAGRANGE. One highly oriented pyrolytic graphite (HOPG) crystal will be placed in every hole (total 620).

Significant progress was made in 2010 on the new instrument and guide projects concerning the **neutron guide hall ILL7**. The first step involved extending the guide hall itself, which was completed in the last quarter of 2010. The new space available will make it possible to host two new instruments, **D33** (a small-angle diffractometer) with the new guide **H14** and **IN16B** (a high-resolution back-scattering spectrometer) with the associated dedicated neutron guide (**H112**); **H14** is a long and complex neutron guide, which splits into 4 branches and will deliver neutrons to the instruments **D33**, **LADI**, **IN11** and **IN12**. The three instruments already available will be relocated to different sites in the ILL7 guide hall in order to take greater advantage of the enhanced characteristics of the new **H14** guide.

Most of the components for **D33** (see **figure 2**) are in the manufacturing or final detailed design stage. The main components will be delivered to the ILL in early 2011 and the assembly process will begin at the reserved site in ILL7. In particular, we expect to receive the main aluminium tube in February 2011, followed shortly afterwards by the collimation system.

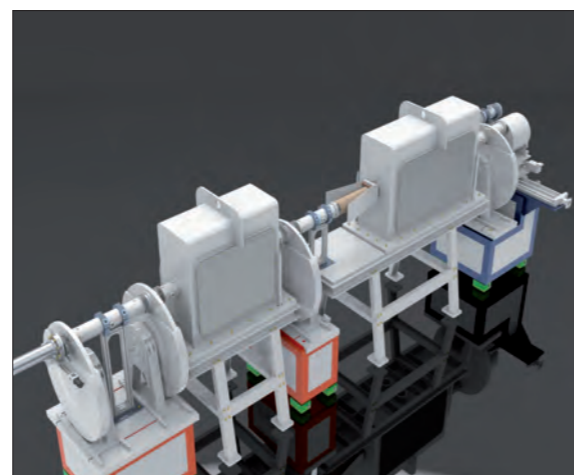


Figure 2: Final design of the collimation system together with the 4-disk chopper and the velocity selector for **D33**.

Rapid progress is being made with the installation of the **guide H14** and the final elements of the guide are expected to be installed in summer 2011 (see **figure 3**). The 4 instruments on the **H14** guide are due to be commissioned either in the last cycle of 2011 or the first cycle of 2012.

H112 and **IN16B** are also progressing according to schedule. The different guide supports have already been prepared and most of the guide elements have been delivered to the ILL. Complete installation and alignment of the **H112** guide is scheduled for summer 2011. The various components of the complex **IN16B** spectrometer have already been manufactured and installation will start during the first cycle of 2011 at the reserved site in the ILL7 guide hall. The main aluminium vacuum chamber (see **figure 4**) has already been manufactured and vacuum tested, as have the elements of the deflector and final element of the focusing neutron guide. The main components of the Phase Space Transformer (PST), in particular the sophisticated cassette system, are ready and every element has been tested individually.

The work undertaken in 2010 and the work planned for 2011 will bring all the Millennium projects in the ILL7 guide hall to a close. In 2010, we also started making progress with the next stage, namely the three projects that concern the ILL 22 guide hall. In particular, the new cold neutron triple-axis spectrometer (**ThALES**) entered the detailed design phase, following completion of the feasibility and conceptual design phases. This project will be completely outsourced and financed by our Czech partner (Charles University of Prague). The contract is expected to be signed in early 2011.

The new wide angle spin-echo instrument **WASP** is also making progress in the feasibility and conceptual design phases. The instrument will be sited in the new extension of the ILL22 neutron guide hall, where the complex magnetic coil system and polarisation analyser supermirrors will be installed. Preparation of the complex supermirrors was started well in advance, because a total 3330 supermirrors will be needed to cover a scattering angle of 90 degrees.

The new (**ThALES**, **WASP**) and existing (**D16**, **SuperADAM**, **D22** and **IN15**) instruments in the neutron guide hall ILL22, will be supplied with neutrons from an upgraded **H5 neutron guide**. The preliminary design of this very complex guide started in 2010 and the final detailed design should be finished in early 2011.



Figure 3: Elements of the **H14** neutron guide. The lower part goes to **IN12** and **D33** and the upper part to **LADI** and **IN11**.



Figure 4: Main aluminium vacuum chamber for **IN16B**.

Fortunately, the excellent results achieved with the Millennium Programme have encouraged our partners to upgrade some of the **CRG instruments** with their own budgets.

Of particular note is the progress made with the upgrade of **D1B**. Its new banana detector covers 130 degrees (compared with only 80 degrees previously), with a resolution of 0.1 degrees (previously 0.2 deg). The new detector is now ready and undergoing final tests in our Neutron Detector Service. It is due to be installed on **D1B** during the first cycle of 2011 (see **figure 5**).

The cold neutron triple-axis spectrometer **IN12** will undergo a complete upgrade - financed by FZ Jülich - covering everything from its monochromator to its analyser system. The upgraded instrument will take advantage of the new improved characteristics of the guide **H14** and its new end-guide position. Final commissioning is expected for the first cycle of 2012.

Finally, the spin-echo spectrometer **IN15** will also be upgraded and improved with specific support from the BMBF and FZ Jülich. A completely new system of optimal-precession magnetic coils will be implemented, including an improved power supply and a more robust cooling system.



Figure 5: New detector for **D1B** covering a scattering angle of 130 degrees.

B. Ouladdiaf, M-H. Lemée-Cailleau, J. Archer, J.R. Allibon, P. Decarpenrie and J. Rodriguez-Carvajal (ILL)
 A.W. Hewat (ILL and NeutronOptics, Grenoble, France)
 S. York and D. Brau (Photonics Science Limited, Sussex, UK)
 G.J. McIntyre (ILL and University of Durham, UK)

CYCLOPS - a new fast reciprocal-space explorer

This article describes the key technical aspects of CYCLOPS. Laue patterns subtending large solid angle are read out in less than 3 s to allow real-time exploration of reciprocal space and rapid data collection through phase transitions. The first results have exceeded our expectations, and promise exciting new applications for neutron Laue diffraction.

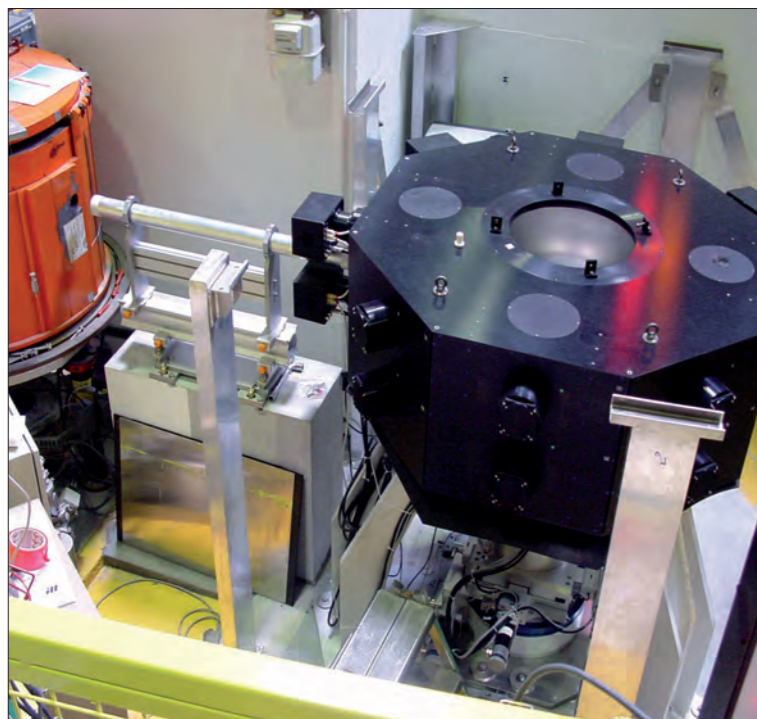


Figure 1: General view of CYCLOPS.

The Laue method, in which the single crystal is maintained fixed in an incident white beam, is one of the most efficient diffraction techniques not only for exploring reciprocal space but also for quantitative structure determination. With its large solid angle of detection, the Laue diffractometers LADI and VIVALDI has shown the advantages of the Laue technique compared to conventional monochromatic single-crystal diffractometers [1]. It is however limited in some applications by the slow readout of its image-plate detector. In contrast, on the CCD Laue diffractometer OrientExpress, the 1680x1320 pixel image is read out in less than 0.2 s [2].

The new Laue diffractometer CYCLOPS (**C**ylindrical **C**cd **L**ae **O**ctagonal **P**hoto **S**cintillator) retains the advantages of VIVALDI while providing real-time readout and higher data-collection efficiency when exposures are short. CYCLOPS is composed of an octagonal

detector, essentially eight copies of the OrientExpress detector. The large-area neutron scintillator behind each octagonal face is viewed via f0.95 close-focus lenses by two high-performance thermoelectrically cooled image-intensified CCD cameras. The neutron scintillators are 0.21 mm-thick ASTND screens based on ZnS:Ag, with ⁶LiF added to provide high neutron-capture efficiency. The coupling between the intensifier and the CCD is ensured via a fibre-optic taper to give maximum transmission and high sensitivity.

The total active area of 8 x (166x410) mm² is rendered as a single image of 7680x2400 pixels, each pixel being 172 μm on edge. The modular nature of the octagonal detector facilitates construction and maintenance, each dual-CCD camera unit being independent mechanically and electronically. There are presently five dual-CCD cameras. The sample table includes a heavy-duty ω rotation table and X,Y and Z translations. The free diameter around the sample is 365 mm, three times larger than that of VIVALDI, allowing a considerably wider range of sample environments, including pressure cells, furnaces and cryomagnets. CYCLOPS is located at the end of the H24 thermal guide at the position previously occupied by OrientExpress. The latter has been moved 3 m downstream to use the beam transmitted by CYCLOPS.

Figure 1 shows the housing of the detector with the first five dual-CCD units. The operation of all dual-CCD cameras is controlled via a PC using a customised dialog box in a software package from Photonic Science. The exposure of all cameras is synchronised to occur simultaneously, although they transfer their images to the PC serially. The images are then geometrically corrected and stitched together to form a single image. The total readout time is about 3 s for five dual-CCD cameras units. In routine operation of CYCLOPS, a software application runs as a client of the standard ILL diffractometer-control software MAD, which itself runs on a Linux workstation to allow the automated collection and storage of series of Laue patterns when changing external parameters.

As with VIVALDI and LADI, the data from CYCLOPS can still be displayed, indexed and scaled to a common wavelength using CCP4 Laue-suite software [3]. However, a new Laue software package, including indexation and intensity integration, is under development in collaboration between the ILL and ANSTO.

Figure 2 shows the observed and indexed Laue pattern from a 3 mm-diameter ruby crystal obtained from the five dual-CCD units

presently on CYCLOPS. Nine such patterns at different positions in crystal rotation ω were recorded, each for one minute, and analysed to extract the integrated intensities. The main results show good agreement between refined predicted and observed spot positions. The refined structural parameters are in agreement with those in the literature. A complete structure determination can therefore be achieved in just a few minutes.

An example studied with CYCLOPS is the phase transition of the two-dimensional multiferroic Pr(Sr_{0.1}Ca_{0.9})₂Mn₂O₇, where the interplay between charge, orbital and spin order gives rise to coupling between electric and magnetic order parameters. Pr(Sr_{0.1}Ca_{0.9})₂Mn₂O₇ undergoes two charge-order transitions, one at T_{C01} ≈ 405 K and the second at T_{C02} ≈ 300 K. The charge-order transition is followed by an antiferromagnetic ordering at T_N ≈ 150 K [4].

A Laue thermodiffraction experiment was performed on CYCLOPS between 1.5 K and 320 K using the standard ILL orange cryostat. **Figures 3a** and **3b** show the Laue patterns of the Pr(Sr_{0.1}Ca_{0.9})₂Mn₂O₇ crystal taken in 60 s at 320 K and 1.5 K, respectively [5]. The pattern at T = 320 K corresponds to the charge-orbital ordered phase characterised by the satellite reflections around the nuclear peaks as shown in the inset. The pattern at T = 1.5 K shows both additional spots characteristic of long-range antiferromagnetic order and two-dimensional diffuse-scattering lines along the principal zone axes, which disappear at high temperature.

Due to its fast readout and low γ sensitivity, Laue diffraction patterns with large solid angle are now measurable within just a few seconds. CYCLOPS provides a unique instrument for exploring a large volume of reciprocal space under various experimental conditions of temperature, pressure and magnetic fields, allowing structural and magnetic phase transitions as well as incommensurate structures to be investigated in real time. Thanks to the fast readout, *in situ* and thermodiffraction experiments can now be performed on single crystals with a similar time resolution to powder samples.

Figure 3: (a) Laue pattern from Pr(Sr_{0.1}Ca_{0.9})₂Mn₂O₇ taken in 60 s exposure time at T = 320 K. **Inset:** Satellite reflections due to charge ordering. (b) Laue pattern from Pr(Sr_{0.1}Ca_{0.9})₂Mn₂O₇ taken in 60 s exposure time at T = 1.5 K.

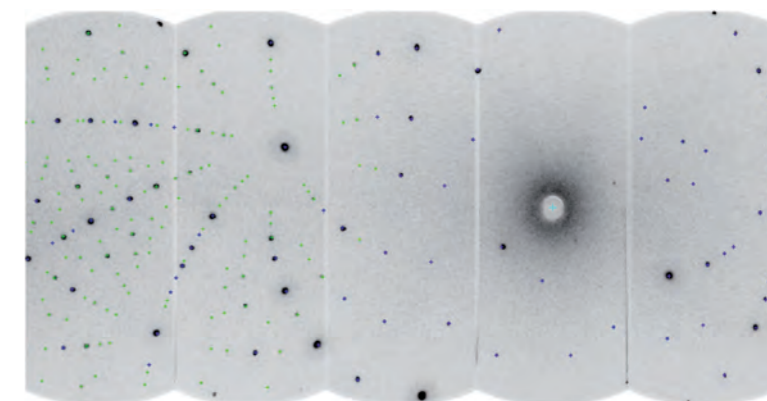
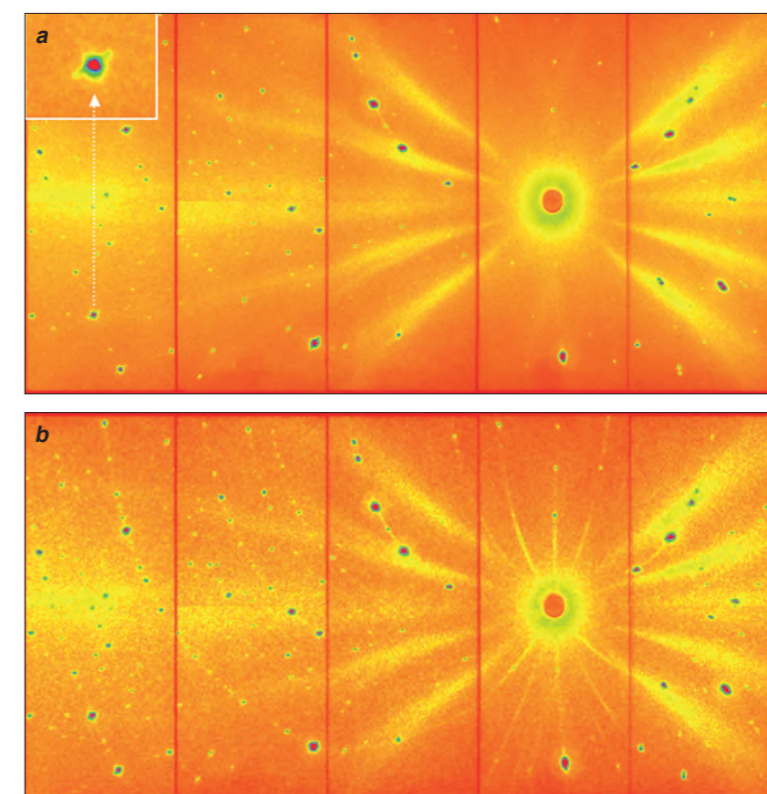


Figure 2: Indexed and observed Laue diffraction pattern from a 3 mm-diameter standard ruby crystal in 60 s exposure time.



REFERENCES

- C. Wilkinson, J.A. Cowan, D.A.A. Myles, F. Cipriani, and G.J. McIntyre, Neutron News 13 (2002) 37 [1]
- G.J. McIntyre, M.H. Lemée-Cailleau, and C. Wilkinson, Physica B 385-386 (2006) 1055
- B. Ouladdiaf, J. Archer, G.J. McIntyre, A.W. Hewat, D. Brau, and S. York, Physica B 385-386 (2006) 1052 [2]
- J.W. Campbell, Q. Hao, M.M. Harding, N.D. Nguti, and C. Wilkinson, J. Appl. Cryst. 31 (1998) 496 [3]
- Y. Tokunaga, T. Lottermoser, Y. Lee, R. Kumal, M. Uchida, T. Arima, and T. Yoshinori, Nat. Mater. 5 (2006) 937 [4]
- We would like to thank Tapan Chatterji for providing the double perovskite crystal [5]

10 GPa precision control over a broad temperature range

Under the ILL's Millennium Programme Sample Environment Modernisation project, the ILL has re-launched pressure activity with the aim of strengthening its user support, modernising its equipment and covering a much broader pressure range. After successfully commissioning a fast cryogen-free cryostat enabling measurements at 10 GPa down to 3K, we can now present a fast high-precision automatic pressure controller for continuously loaded pressure cells and Paris-Edinburgh presses.



ILL's sample environment team has revamped its existing equipment (clamps and pressure generators, for example) and acquired two 4 GPa VX-1 and two 10 GPa VX-5 Paris-Edinburgh presses [1]. These presses are used at room temperature with a liquid pressure transmitter and at very low temperatures with helium gas. Thanks to the very fruitful collaboration established several years ago with S. Klotz's team at Paris's Pierre et Marie Curie University, we can now provide top-class technical support to users unfamiliar with high-pressure techniques; this has led to a number of very successful experiments [2-4].

To further facilitate the use of the 0.5 GPa continuously-loaded pressure cells and Paris-Edinburgh presses, we have also designed and constructed a new rack, in collaboration with colleagues from the CNRS. The rack is capable of charging the device with up to 0.2 GPa of helium gas in 20 minutes, controlling ramps at 3 MPa/min (30 bar/min), and maintaining constant pressure with variations around the set point of less than 20 kPa (200 mbar). In combination with a VX-5 press it allows rapid and precise regulation of the sample pressure up to 10 GPa, at temperatures down to 3 K in our cryogen-free cryostat.

To achieve these performances we use a 0.3 GPa compressor, two high-precision 0.2 GPa valves [5], and a buffer. A Eurotherm controller maintains the gas in the buffer above the pressure

Figure 1: Successful commissioning by Claude Payre (left) and Jean-Luc Laborier (right) of the high-pressure controller on the D20 powder diffractometer.

required by the user and regulates the sample pressure by opening and closing the valves. One valve releases the pressure, and the other injects the gas available in the buffer. To adjust the pressure in the press or cell rapidly, the controller automatically disables the regulation loop and controls the compressor (or relief valve) directly.

The innovative principle underlying the 0.2 GPa isolation valve is the elastic deformation of materials and the absence of a stuffing box (O-ring). The use of a flexible seal between the valve body and the needle stem can create a number of problems, such as leaks and pollution, and, above all, a significant amount of friction rendering it difficult to open or close the valve and causing significant hysteresis. The valve is operated by compressed air (6 bar). A licensing arrangement has been agreed between the CNRS and Autoclave Engineers France for marketing the device.

Efforts have been made to simplify the use of the rack on the instruments by ensuring ease of installation and a very simple user interface. Once the power and compressed air lines are connected it is simply a matter of connecting the press or cell, switching it on and entering the set point. In the event of power loss, overpressure, or a shutdown of the compressed air line, the rack automatically ceases to function, releasing the pressure applied to the sample. The rack shown in **figure 1** was commissioned in 2010 and a second device is under construction.

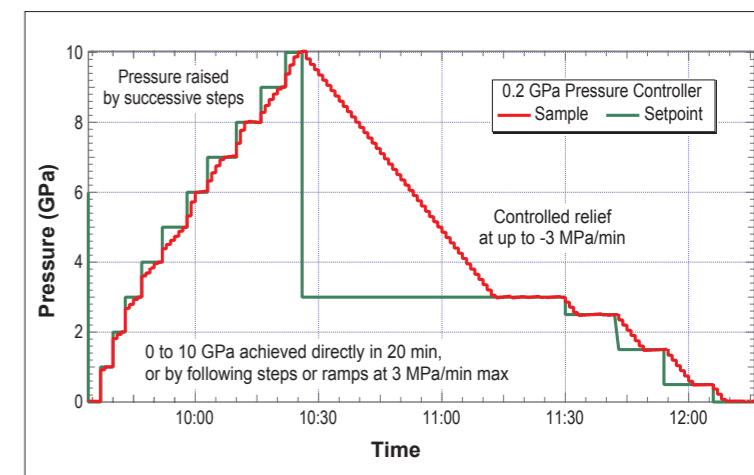


Figure 2: Automatic evolution of the pressure applied to the sample in the VX-5 press after successively changing the set point.

REFERENCES

- [1] S. Klotz, G. Hamel and J. Frélat, High Pressure Research 24 1 (2004) 219
- [2] S. Klotz, T. Strässle, A.L. Cornelius, J. Philippe and T. Hansen, Phys. Rev. Lett. 104 (2010) 115501
- [3] S.A.J. Kimber, A. Kreyssig, Y.-Z. Zhang, H.O. Jeschke, R. Valentí, F. Yokaichiya, E. Colombier, J. Yan, T.C. Hansen, T. Chatterji, R.J. McQueeney, P.C. Canfield, A.I. Goldman and D.N. Argyriou, Nature Materials 8 (2009) 471
- [4] S. Klotz, L.E. Bove, T. Strässle, T.C. Hansen and A.M. Saitta, Nature Materials 8 (2009) 405
- [5] Patent CNRS n° 04 00 515, valve distributed by Autoclave France under licence number L0813 - <http://www.autoclave-france.fr>

P. Courtois (ILL)
 K.H. Andersen (ESS, Lund, Sweden)
 A.K. Freund (ILL and Via Cordis, Bordeaux, France)
 S. Gsell, M. Fischer and M. Schreck (University of Augsburg, Germany)
 G. Borchert (FRM2, Garching, Germany)
 M. Skoulatos (HZB, Berlin, Germany)

Diamond mosaic crystals: the ultimate material for neutron monochromators

Diamond single crystals are potentially the best material for neutron monochromators. The enormous challenge of growing thick diamond crystals with a suitable mosaic spread has been overcome by a research team at the University of Augsburg. It is now possible to make crystal plates that are 0.1 cm thick with a surface area of approximately 2 cm² and a mosaic spread of 0.2°. Experiments carried out at the ILL have confirmed the predicted high reflectivity of these crystals. It is now planned to build a composite system by stacking several crystal plates on top of one another. This monochromator should produce the highest performance levels ever achieved at short wavelengths and would thus represent a significant breakthrough for hot neutron instrumentation.

Figure 1: Theoretical neutron peak reflectivity as a function of wavelength for diamond (thickness 0.5 cm), Cu and Ge crystals (thickness 0.8 cm) with the same mosaic spread of 0.3°.

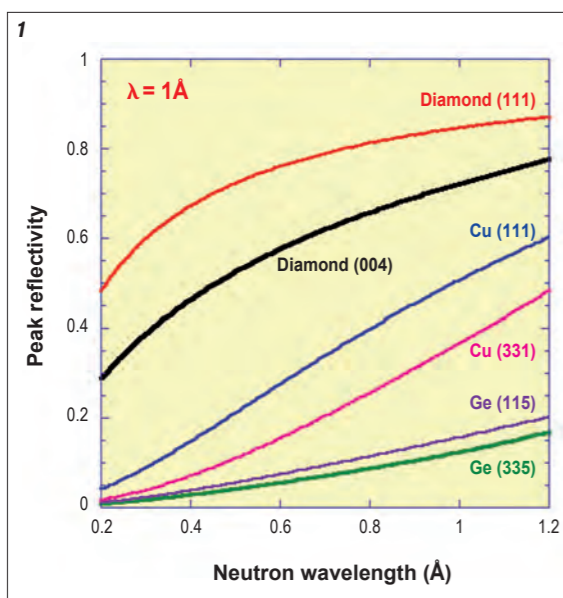
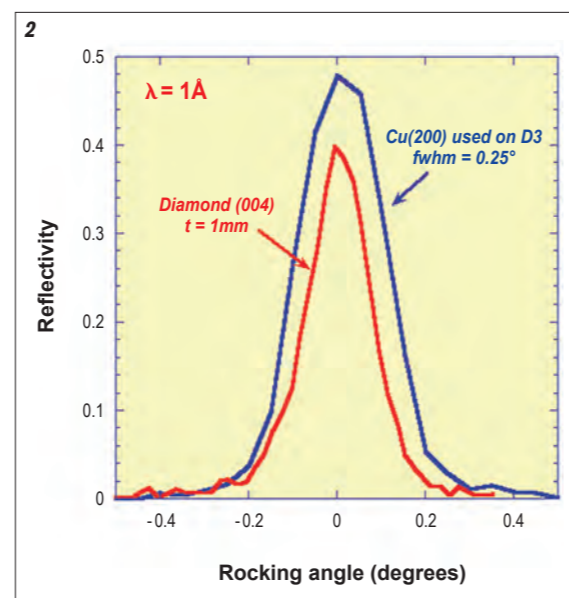


Figure 2: Neutron rocking curves of a 0.1 cm-thick diamond (004) crystal and a Cu (200) crystal monochromator.



Thanks to its ideal crystalline and nuclear properties, diamond offers the highest performance levels of all existing materials for neutron applications [1]. It has a very compact structure with a small unit cell composed of 8 carbon atoms with a large coherent scattering length and very small incoherent and absorption cross-sections. A sufficiently thick crystal with an appropriate mosaic distribution would theoretically be the ultimate neutron monochromator. A research group at the University of Augsburg has succeeded in producing diamond crystals using plasma chemical vapour deposition. Crystalline layers are grown in the <001> direction on a very thin iridium (001) film coated onto a thick layer of yttria-stabilised zirconia deposited on a silicon (001) wafer [2].

The mosaic spread should be comparable to the divergence of the incoming neutron beam, which is typically 0.3°. The flux provided by a crystal monochromator is proportional to the integrated reflectivity, i.e. the product of rocking curve width × peak reflectivity. The optimum crystal thickness depends on several parameters, such as the neutron energy, the mosaic spread and the reflection used. Calculations predict that the (004) reflection of a 0.5 cm-thick diamond crystal with a mosaic spread of 0.3° reaches 80% of its maximum peak reflectivity in the wavelength range 0.3 - 1 Å. Such a crystal would outperform Cu and Ge mosaic crystals as shown in figure 1.

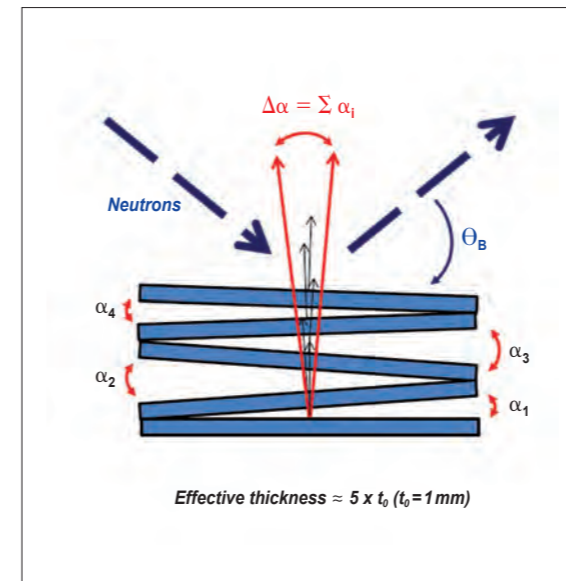


Figure 3: A 0.5 cm-thick composite crystal system is obtained by stacking thinner crystals at angles α_i .

Many samples 1 cm × 1 cm in size and up to 0.2 cm thick were characterised on the test diffractometer T13C at the ILL at a wavelength of 1 Å [3]. The peak reflectivity measured on several crystals just 0.1 cm thick and with a mosaic spread of 0.15° was close to that of Cu, which is the reference material presently used at the ILL (see figure 2). Because the synthesis of 0.5 cm-thick diamond crystals with a mosaic distribution of 0.3° is still quite difficult, we propose the stacking of several plates as shown in the diagram in figure 3. This technique has already been successfully used for Cu monochromators [4].

As a first step, we built a stack of two 0.1 cm-thick crystals. The orientation of each crystal was controlled using neutron diffraction on T13C. We measured a peak reflectivity of 45% for

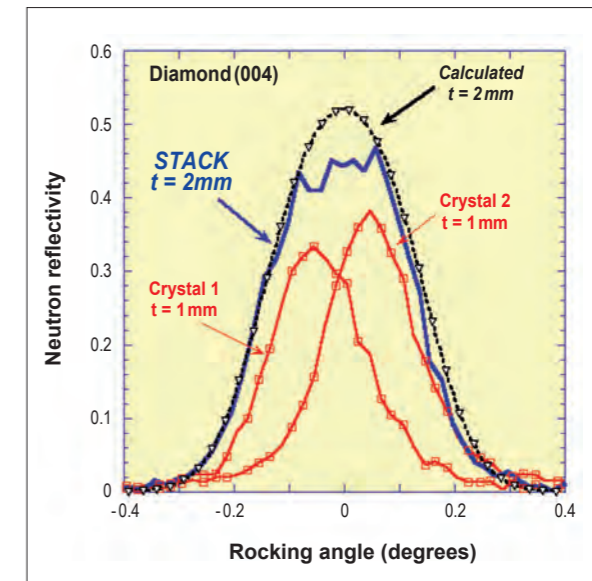


Figure 4: Calculated and experimental peak reflectivity for $\lambda = 1 \text{ \AA}$ obtained for a stack of two 0.1 cm-thick diamond crystals.

a mosaic spread of 0.31° at 1 Å (see figure 4), corresponding to 80% of the theoretical values for a 0.2 cm-thick crystal with the same mosaic spread. Even at this early stage, the performance of such a composite system in terms of integrated reflectivity exceeds by 16% that of the best existing Cu crystal. Extrapolation for a 0.5 cm-thick stack produces 60% higher reflectivity.

It has therefore been well established that a composite diamond crystal system makes it possible to increase the flux substantially, in particular for hot neutrons. Further reflectivity measurements are planned at smaller wavelengths on D9. We are currently aiming to build a full-scale diamond monochromator that will achieve unprecedented performance levels for a hot source instrument at the ILL.

REFERENCES

- A.K. Freund, J. Appl. Cryst. 42 (2009) 36-42 [1]
- S. Gsell, T. Bauer, J. Goldfuss, M. Schreck, and B. Stritzker, Appl. Phys. Lett. 84 (2004) 4541 [2]
- A.K. Freund, S. Gsell, M. Fischer, M. Schreck, K.H. Andersen, P. Courtois, G. Borchert and M. Skoulatos, Proc. Conf. NOP 2010, Nucl. Instr. Meth. Phys. Res. (2010), in press [3]
- B. Hamelin, ILL Annual Report (1996) [4]

NOMAD – A new way of thinking experiments

After an initial phase of heavy debugging, ILL's new instrument control software has reached maturity. NOMAD's stability - our prime concern with respect to our users - is no longer an issue. Its software/hardware interaction has been optimised to minimise beamtime losses and the user interface has been dramatically improved, both in terms of response time and the quality and quantity of information available in real time. New techniques have been developed to facilitate the interaction between users and hardware. Non-expert users can now control the instrument and perform complex operations by just clicking on the interface.

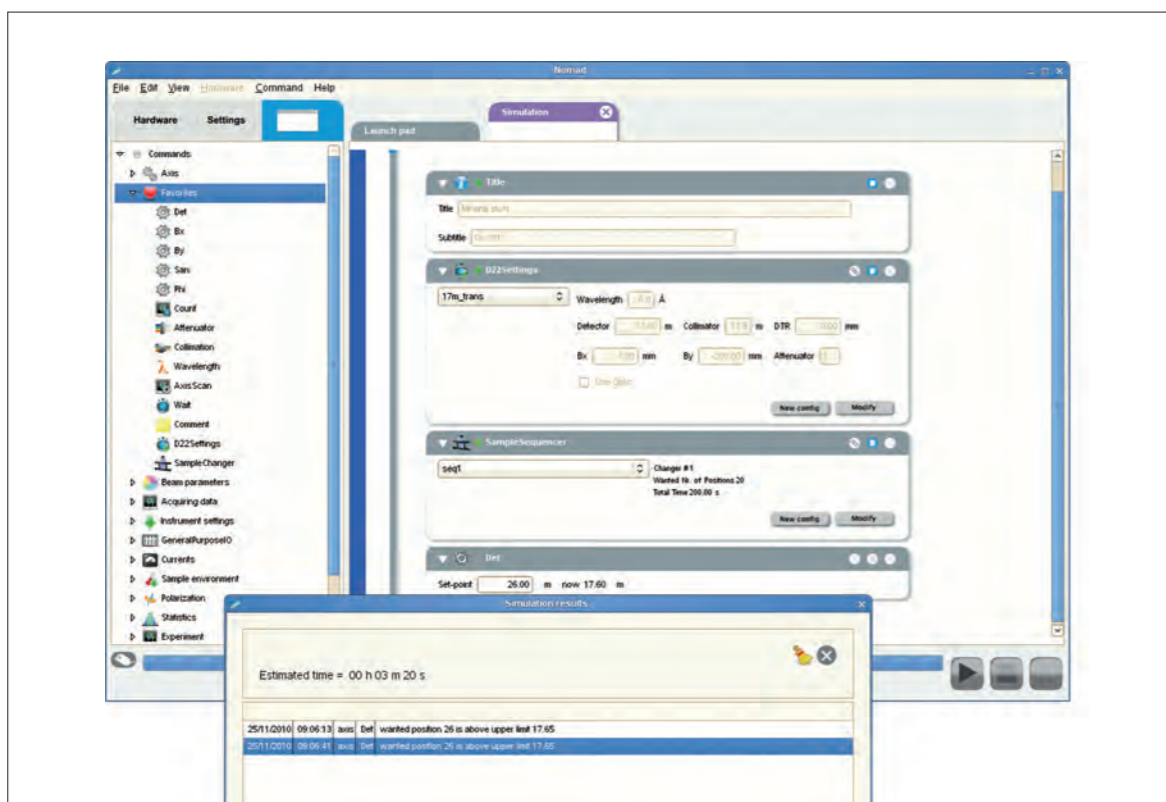


Figure 1: The NOMAD simulator allows users to check the estimated runtime and the quality of the configuration requested.

Fighting for performance

The stability and performance of our instrument control software are major concerns for our users. Stability is an issue since the software must guarantee the reliable execution of operations without constant supervision by scientists. Performance is crucial, to minimise dead time and to maximise the use of the available beamtime. Both aspects are linked to the quality of the coding; it needs to be rigorous and well documented.

Huge efforts have been invested in improving the development procedures to ensure constant progress from release to release. An automatic compilation server checks the consistency of the current release nightly, performing a series of automatic validation tests. There is a complete set of documents available on the server and the graphical user interface architecture, as well as on every single driver and controller.

The high level of integration achieved between software and hardware has allowed real-time operations never achieved before. Double buffering on the acquisition electronics has reduced data storage latency to a minimum, making a data flux of up to 1 TB per day possible. The reactor's long winter shutdowns provide the perfect opportunity for stress-testing our software on the instruments without disturbing scientific activity. NOMAD boots up in seconds, thanks to careful tuning of the server operations and flow of events between server and user interface. It handles hundreds of graphical objects and is now more reactive to user input.

A few clicks are all it takes to identify the errors in a particular sequence of instructions which could lead to the stoppage of an experiment overnight or even damage the equipment (figure 1). NOMAD's simulator allows users to simulate (via the graphical

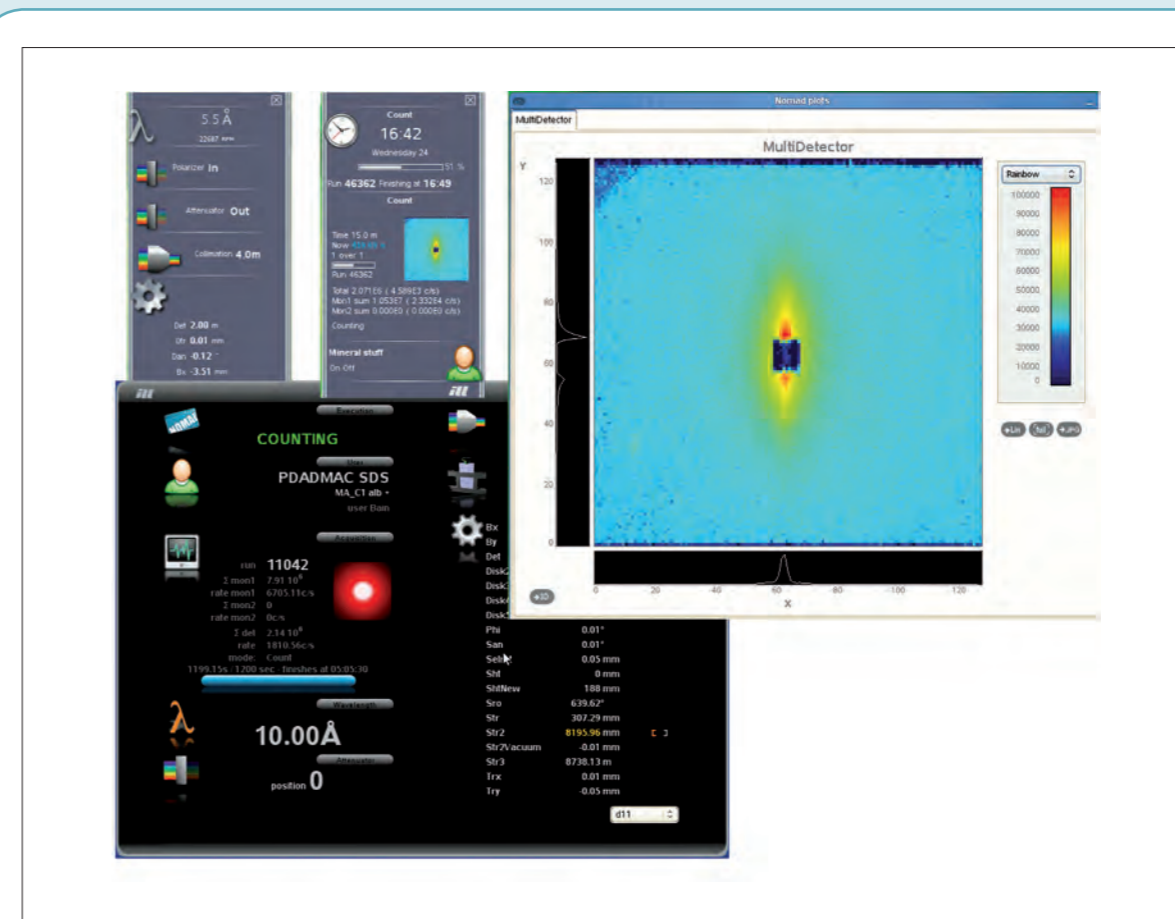


Figure 2: A complete set of local and web-based monitor spies display real-time data as the measurement progresses.

interface or in command line mode) all the operations foreseen for the instrument, from a real configuration baseline. All the warnings are then displayed, as well as the estimated duration of the script, thus allowing for corrections and optimisation of the running time.

A graphical user interface to control your instrument

The overall increase in instrument efficiency at ILL has resulted in a significant reduction in the average length of an experiment. In addition, our neutron instruments are becoming more attractive to non-expert users, thus opening them up to a broader scientific community.

With its intuitive drag-and-drop approach, the NOMAD graphical user interface (GUI) provides for a simpler configuration of the measurement process. Complex structures such as for-loops and counting sequences can be defined in the work area and saved for later use. The essential data on instrument status is constantly available via a set of spy monitors (figure 2), and the data from the detector or scan are displayed in real time. The data can also be retrieved remotely, thanks to a web-based system allowing the user to monitor experiment progress. Users preferring the less intuitive but more efficient command line approach can use the unix-like shell, or the command line available within the interface itself. A range of constantly developing instrument settings allows scientists to perform complex operations on their instrument without losing sight of the physical quantities they want to measure.

User-centred development

Today's reality in instrumentation includes a high variety of setup and sample environments, ToF, kinetics, field control unit acquisitions - multiple configurations, in short.

Thanks to its graphical configuration interface NOMAD offers unique possibilities for modifying instrument layout to match the requirements of a specific experiment. There are configurable alarms on the critical hardware to inform users, via sms and email, of any malfunction during the experiment. Statistical estimators, optimisation routines and automatic scans help scientists exploit to the full the beamtime available. With over 125 drivers NOMAD can control all the sample environment hardware, performing on-line liquid height adjustments, magnetic field closed loop control, and much more.

NOMAD is now running well on a third of the ILL's instrument suite, and it is becoming a standard for many of the groups in the Projects & Techniques Division. We are using it daily for testing the quality and performance of the monochromators, for setting up detectors, tuning new mechanics and preparing sample environments.

Deployment across the entire suite of instruments continues, and the goal is to extend its functionality further, to guarantee our users even better levels of instrument performance and stability.

M. Boehm, A. Filhol, J. Kulda and M. Johnson (ILL)
 Y. Raoul (ILL and Forschungszentrum Jülich, Germany)
 W. Schmidt and K. Schmalzl (Forschungszentrum Jülich, Germany)

The vTAS suite: a simulator for classical and multiplexed three-axis neutron spectrometers

You need a bit of experience to navigate through the four dimensions of momentum and energy (Q, ω) space with a three-axis spectrometer (TAS) if you want to avoid getting lost in reciprocal space or crash-land in real space. The vTAS suite provides graphical assistance for the preparation and performance of inelastic neutron scattering experiments on TAS instruments, including the latest multiplexed instrumental configurations such as FlatCone, IMPS and UFO. vTAS is a platform-independent public-domain software tool available for download from the ILL homepage.

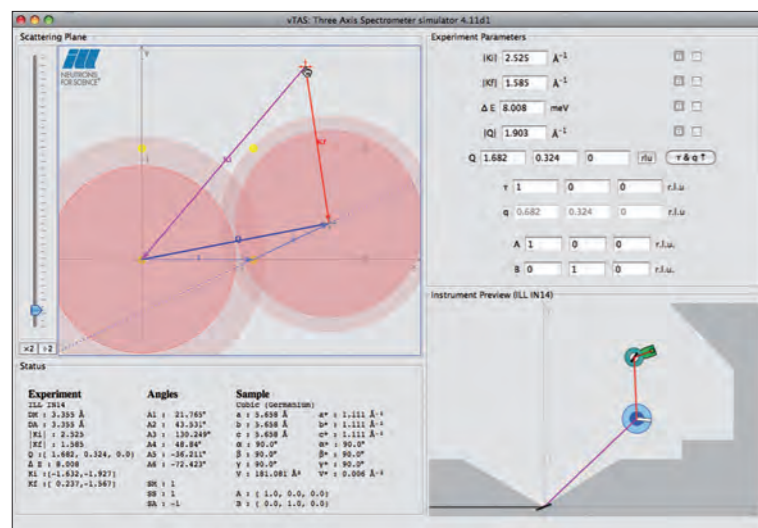


Figure 1: The graphical interface of vTAS. Top left: view of the scattering plane with the scattering triangle. Top right: area for defining experimental parameters. Bottom left: status of instrument and sample. Bottom right: instrument position within the instrument zone (top view).

In order to investigate the relationships between the momentum and energy of collective excitations in liquid and crystalline samples, three-axis spectrometers can access arbitrary points in diverse Brillouin zones within a certain maximum momentum (Q about $0.1 - 6 \text{ \AA}^{-1}$) and energy transfer range (ΔE about $0.1 - 100 \text{ meV}$).

Classical TAS configurations are based on three components with independent vertical rotation axes: the monochromator defining the

incident neutron energy E_i , the analyser measuring the scattered neutron energy E_f and the sample stage between them, defining the momentum transfer Q and its coordinates in the reciprocal space of the sample. Efforts to increase data acquisition rates over the last decade have resulted in generalisations of the traditional point-by-point constant- Q and constant- E scanning techniques by introducing multiplexed analysers such as the RITA spectrometer (Re-Invented Triple-Axis) [1,2], IN8-IMPS [4], IN12-UFO [5] and the wide-angle FlatCone multianalyser array [3].

In all these variants, the simple analyser-detector system of the classical spectrometer is replaced by a multitude of analyser-detector units multiplying the number of scanning points for the same acquisition time. Different layouts imply different geometrical constraints in real space, and these transform to more complex trajectories in reciprocal space. Setting up efficient data collection strategies therefore becomes much less intuitive, to the extent that a graphical representation of the scattering geometry becomes a necessity.

The vTAS software suite was developed to provide graphical assistance for TAS experiments. It consists of three independent applications: vTAS, covering the classical TAS and FlatCone configurations, vIMPS (IN8-IMPS) and vUFO (IN12-UFO, developed in collaboration with JCNS).

It was important for the developers that the functionality and layout of the suite meet the demands not only of experienced users but also of students and scientists new to inelastic neutron scattering. vTAS was kept platform-independent to provide a simulation and tutorial tool easily accessible from outside the ILL [5].

The graphical interactive interface is composed of three active panes (figure 1): a view of the scattering plane with the scattering triangle, an instrument preview pane, and an area for defining the experiment parameters. Any modification made in one of the panes (through mouse or keyboard input) will be promptly reflected in the others. Movements can be constrained in order to simulate different instrument scanning modes. vTAS allows for modifications to the instrument configuration, including the definition of zone walls. This provides the flexibility required to extend the standard ILL instrument suite to instruments on other neutron sources.

A simple data-viewer mode can be activated by dragging and dropping ILL data files onto vTAS, (figure 2) displaying the points measured in the scattering plane and refreshing the instrument position.

The maintenance and future development of the vTAS suite will depend on its level of acceptance by the user community. It is a compact application in its present state, but it could be extended in various directions.

There is a demand for example for resolution calculations as an important additional feature, and this is currently being tested. vTAS will also provide a protocol for calling and communicating with external programmes such as Restrax [6] and McStas [7], instead of incorporating algorithms in its own code.

The implementation of the new instrument configuration renders the present two-dimensional representation ambiguous, and we are therefore discussing and testing the possibility of animations in 3D.

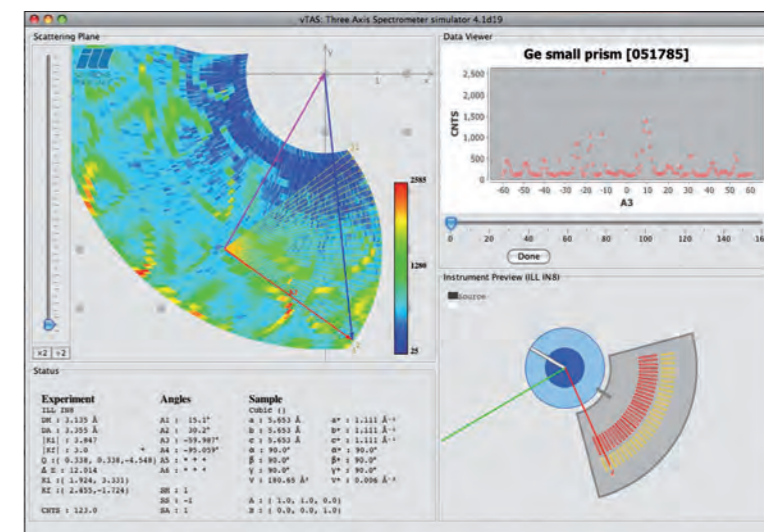
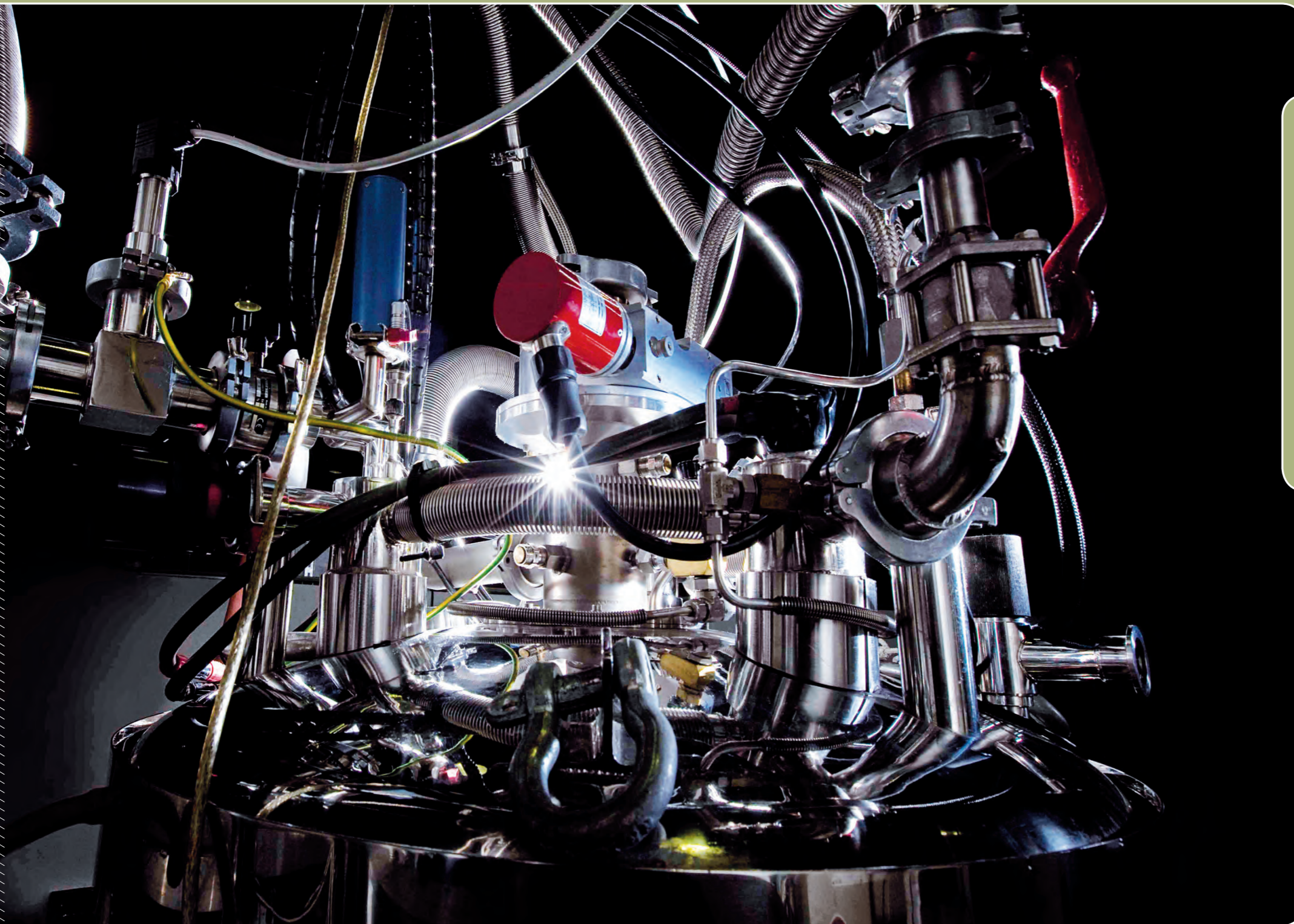


Figure 2: The vTAS interface in data-viewer mode for the FlatCone option.

Finally, the ILL is currently implementing a major programme to replace its existing instrument control software with the new NOMAD software (see article on p.86). There have been plans to integrate a graphical simulator in NOMAD from the very beginning, and vTAS will obviously provide valuable experience for this. From the user point of view, the similarity between the more widely used vTAS software and the new instrument control software should improve the visibility and accessibility of the instruments.

REFERENCES

M. Kempa *et al.*, Physica B 385-386 (2006) 1080-1082 [1]
 e.g. K. Lefman *et al.*, Physica B 385-386 (2006) 1083-1085 [2]
 M. Jimenez-Ruiz *et al.*, Physica B 385-386 (2006) 1086-1088 [3]
 W. Schmidt *et al.*, Physica B 385-386 (2006) 1073-1076 [4]
 (<http://www.ill.eu/html/instruments-supports/computing-for-science/cs-software/all-software/vtas/>) [5]
 J. Šaroun, J. Kulda, Physica B 234-236 (1997) 1102-1104. J. Šaroun, J. Kulda, <http://neutron.ujf.cas.cz/restrax/> (2007) [6]
 P. Willendrup, E. Farhi, K. Lefmann, "McStas 1.7 - a new version of the flexible Monte Carlo neutron scattering package", Neutron News 350 (2004) e735-e737 - <http://neutron.isroe.dk/> [7]



The single-crystal diffractometer D23.

USER PROGRAMME BEAMTIME STATISTICS INSTRUMENT LIST

The ILL User Support team is dedicated to helping all visiting researchers to make the most of its facilities. If you are coming to the ILL to carry out experiments, the User Office is here to give you the organisational and administrative support you need to successfully perform your experiments.

Neutron beams and instrument facilities are free of charge for proposers of accepted experiments. Scientists affiliated to the Institute's member countries will also, in general, be assisted with necessary travel and daily subsistence for a limited period. The User Support Team makes all arrangements for accommodation and will process claims for expenses after you have completed your experiment.

If you would like more information about the Institute's facilities, application for beamtime, user support and experimental programme, please visit our web-site:

<http://www.ill.eu/users>

User programme

THE ILL VISITORS CLUB

All administrative tools for our scientific visitors are grouped together and directly accessible on the web, thanks to the Visitors Club. All information is presented in a user-friendly environment. After having logged in with your own personal identification, you will have direct access to all the available information which concerns you. Users with particular responsibilities have privileged access to other tools, according to their role. The ILL Visitors Club includes the electronic proposal and experimental reports submission procedures, and electronic peer review of proposals. Additional electronic services have also been put in place: acknowledgement of proposals, subcommittee results, invitation letters, user satisfaction forms and so on.

PROPOSAL SUBMISSION

There are different ways of submitting a proposal to the ILL:

- Standard submission – twice a year – via the Electronic Proposal System (EPS)
- Long-Term Proposals – once a year - via the Electronic Proposal System (EPS)
- EASY access system (EASY) throughout the year
- Director's Discretion Time (DDT) throughout the year
- Special access for proprietary research and industrial users

Submission of a standard research proposal

Applications for beamtime should be submitted electronically, via our Electronic Proposal Submission system (EPS), available on the Visitors Club web-site. Proposals can be submitted to the ILL twice a year, usually in February and in September. The web system is activated two months before each deadline. Submitted proposals are divided amongst the different colleges (see box below) according to their main subject area.

The ILL scientific life is organised into 10 colleges:

- College 1** - Applied Metallurgy, Instrumentation and Techniques
- College 2** - Theory
- College 3** - Nuclear and Particle Physics
- College 4** - Magnetic Excitations
- College 5A** - Crystallography
- College 5B** - Magnetic Structures
- College 6** - Structure and Dynamics of Liquids and Glasses
- College 7** - Spectroscopy in Solid State Physics and Chemistry
- College 8** - Structure and Dynamics of Biological Systems
- College 9** - Structure and Dynamics of Soft-condensed Matter

⁽¹⁾ If you are not yet registered in the Visitors Club and you wish to join it, you can register directly at <http://club.ill.eu/cv/>

Proposals are judged by a Peer Review Committee of the Subcommittees of the ILL Scientific Council. Subcommittee members are specialists in relevant areas of each College and they evaluate the proposals for scientific merit and recommend to the ILL Management the award of beamtime to the highest-priority proposals.

Before the meeting, the subcommittee receives a report on the technical feasibility and safety of a proposed experiment from the appropriate College at the ILL. Two proposal review rounds are held each year, approximately six weeks after the deadline for submission of applications.

There are normally 4 reactor cycles a year, each of which lasts 50 days. Accepted proposals submitted by February will receive beamtime in the second half of the year and those submitted by September, in the first half of the following year.

More detailed information on application for beamtime and deadlines is given on our website at <http://www.ill.eu/users/proposal-submission/>.

Easy Access System

The Easy Access System (EASY) grants diffraction beamtime to scientists from ILL member countries, who need a rapid structural characterisation of samples and data analysis. Access is open all year long, and it does not go through the ILL standard proposal round and consequent peer review system.

The system offers one neutron day per cycle, on four instruments (D2B, D16, VIVALDI and OrientExpress) to perform very short experiments at room temperature. The users will not be invited to the ILL, but will send their samples to one of two designated ILL scientists, who will be responsible for the measurements and sample radiological control. The ILL will ship back the sample once the measurement is finished. You can apply for EASY beamtime on the Visitors Club. More information is available at http://club.ill.eu/cvDocs/EASY_Guidelines.pdf.

Long-Term Proposals

Users from ILL member countries can also apply for extended periods of beamtime, by submitting a Long-Term Proposal (LTP). Its purpose is to facilitate the development of instrumentation, techniques or software – which could be beneficial to the ILL community as a whole – through the award of beamtime over several cycles. The total amount of beamtime that may be allocated to LTPs on any particular instrument is capped at 10%, and beamtime is not awarded to LTPs to perform science beyond essential testing.

LTPs can be submitted once a year at the autumn proposal round using the specific LTP application form. The primary criterion for acceptance of a LTP is the excellence of the science that it will ultimately enable. The length of LTP projects is expected to be 3 years typically, with continuation approved at the end of each year,

based on an annual report; a final report is also required at the end of the project. More details are given at

<http://www.ill.eu/users/proposal-submission/>

Submission of a proposal to the Director's Discretion Time

This option allows a researcher to obtain beamtime quickly, without going through the peer-review procedure. DDT is normally used for 'hot' topics, new ideas, feasibility tests and to encourage new users. Applications for Director's Discretion Time can be submitted to the Head of the Science Division, Prof. Andrew Harrison, at any time.

Access for proprietary research and industrial users

The ILL's mission is to provide neutrons for both public and industrial research. In November 2010 we appointed a business development officer who is charged with communicating more widely the services we can offer to the industry. He will also facilitate and coordinate centrally industrial R&D at the ILL, in particular access to the ILL's scientific expertise and instrument suite. He will work closely with the ILL "Industrial Liaison and Consultancy Group"(ILC) to assess the feasibility of the experiments and the quotation of the services. The ILC Group is composed of scientists with considerable experience and expertise in neutron techniques applied to industrial R&D; it ensures rapid access and total confidentiality for industrial companies, and provides specialised technical and scientific support. To apply for proprietary beam time, please contact the Business Development Office at industry@ill.eu or by phone at +33(0)4 76 20 72 01 or consult the web site under <http://www.ill.eu/industry/>.

Experimental reports

Users are asked to complete an experimental report on the outcome of their experiments. The submission of an experimental report is compulsory for every user who is granted ILL beamtime. Failure to do so may lead to rejection in case of application for beamtime for a continuation proposal.

All ILL experimental reports are archived electronically and searchable via the web server as PDF files (under <http://club.ill.eu/cv/>). Experimental reports for experiments performed in 2010 are included in the CD-ROM of this year's Annual Report.

COLLABORATIVE RESEARCH GROUP INSTRUMENTS

The ILL provides a framework in which Collaborating Research Groups (CRGs) can build and manage instruments at the ILL to carry out their own research programmes. CRGs represent a particularly successful form of long-term international scientific collaboration. They are composed of scientists from one or two research disciplines, and often multinational, carrying out a joint research programme centred around a specific instrument.

CRGs enjoy exclusive access to these instruments for at least half of the beamtime available. The CRGs provide their own scientific and technical support and cover the general operating costs of these instruments. If there is demand from the user community and the resources are available, the beamtime reserved for ILL can be made accessible to users via the subcommittees.

There are currently three different categories of CRG instruments:

- **CRG-A** in which the external group leases an instrument owned by the ILL. They have 50% of the beamtime at their disposal and for the remaining 50% they support ILL's scientific user programme.
- The **CRG-B** category owns their instrument and retains 70% of the available beamtime, supporting the ILL programme for the other 30%.
- Finally, **CRG-C** instruments are used full time for specific research programmes by the external group, which has exclusive use of the beam.

SUPPORT LABORATORIES

The opportunities we offer to our users extend beyond the privileges of access to the world's leading suite of neutron instruments. The ILL - in collaboration with the ESRF and other institutes - is actively responding to the needs of scientists unfamiliar with neutron techniques and in need of training and support facilities. New support facilities have been already set up on the ILL site. For more information see the chapter "More than simply neutrons", p.105.

User and beamtime statistics

THE ILL USER COMMUNITY

The ILL welcomed 1056 users in 2010, including 213 from France, 202 from Germany and 228 from the UK (figure 1). Many of our visitors were received more than once (for a total of 1753 visits).

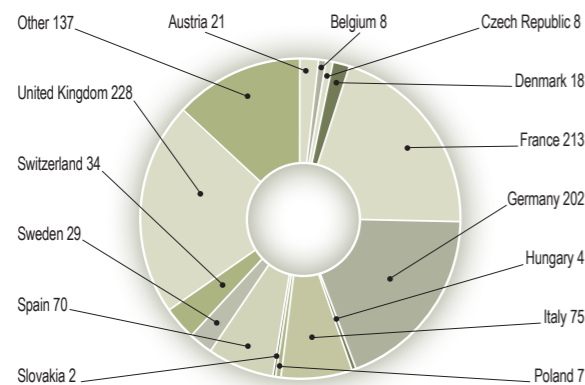


Figure 1: National affiliation of ILL users in 2010.

We value feedback from our users as an indicator of how well our facility is fulfilling their needs and to initiate actions when this is not the case (see figure 2). The User Satisfaction Form is a means of finding out what our users think of the facility. Users who have just finished an experiment at the ILL are asked to complete the questionnaire on the Visitors Club and give us their views on different topics. User comments are made available to managers for their information and actions when appropriate.

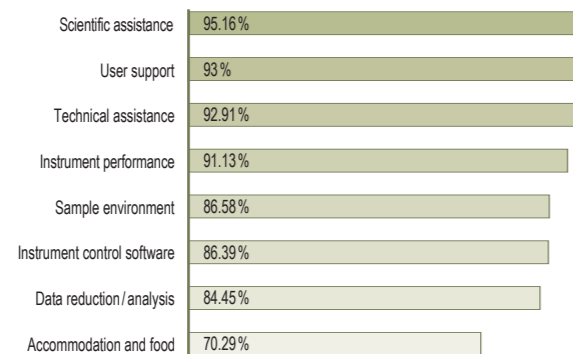


Figure 2: User satisfaction survey results for 2010.

INSTRUMENTS

The instrumental facilities at the ILL are shown in the schematic diagram on page 98.

The list of instruments as of December 2010 is summarised below. Besides the 28 ILL instruments, there are 10 CRG-instruments (marked with an asterisk *):

- powder diffractometers: D1B*, D2B, D20, SALSA
- liquids diffractometer: D4
- polarised neutron diffractometers: D3, D23*
- single-crystal diffractometers: D9, D10, D15*
- large scale structures diffractometers: D19, LADI, VIVALDI
- small-angle scattering diffractometer: D11, D22
- low momentum-transfer diffractometer: D16
- reflectometers: SuperADAM*, D17, FIGARO
- diffuse scattering and polarisation analysis spectrometer: D7
- three-axis spectrometers: IN1, IN8, IN12*, IN14, IN20, IN22*
- time-of-flight spectrometers: BRISP*, IN4, IN5, IN6,
- backscattering and spin-echo spectrometers: IN10, IN11, IN13*, IN15, IN16
- nuclear physics instruments: PN1, PN3
- fundamental physics instruments: PF1, PF2, S18*

LADI and IN15 have a special status, since they are joint ventures of the ILL with other laboratories: in the case of LADI with EMBL and for IN15 with FZ Jülich and HZB Berlin. Cryo-EDM is a CRG-C instrument and is not available as a 'user' instrument. The two-axis diffractometer D1A was decommissioned in summer 2010. D15 was dismantled in December 2010.

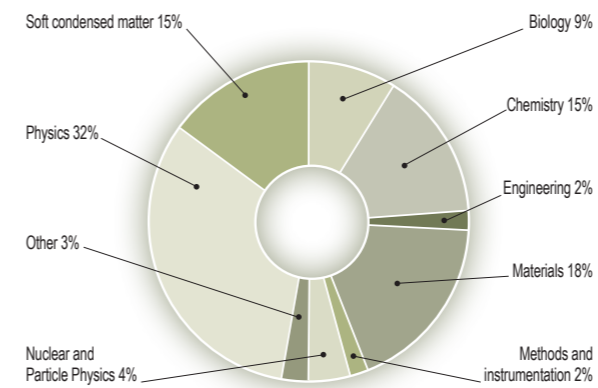
Details of the instruments can be found on the web at <http://www.ill.eu/instruments-support/instruments-groups/>.

BEAMTIME ALLOCATION & UTILISATION FOR 2010

Overall, the Subcommittees of the Scientific Council examined 1142 proposals requesting 7754 days for 2010, out of which 670 proposals received beamtime, allocating 3726 days of beamtime on the different instruments.

The distribution of beamtime for these experiments amongst the different research areas is given in figure 3a, together with the impact of science carried out at the ILL on many of the challenges facing society today (figure 3b).

3a



3b

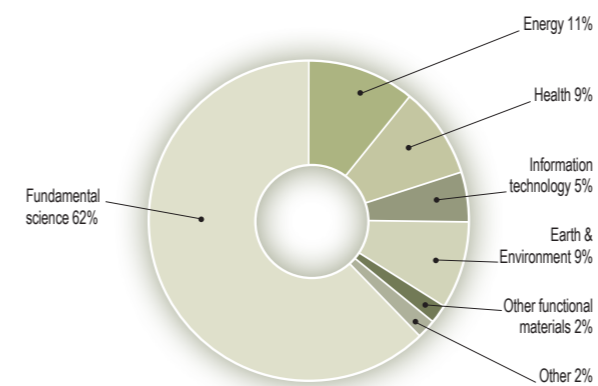


Figure 3: Beamtime allocation in 2010: (a) distribution amongst the different research areas; (b) impact on different areas of research.

In 2010, the member countries of the ILL were: France, Germany, UK, Austria, Belgium, the Czech Republic, Denmark, Hungary, Italy, Poland, Slovakia, Spain, Sweden and Switzerland. Poland rejoined ILL as a scientific member on 1st of July 2010, therefore it doesn't appear as a member country in the table.

In calculating the statistics of beamtime per country, shown in table 1a, the attribution is based on the location of the laboratory of the proposers, not their individual nationality. For a proposal involving laboratories from more than one member country, the total number of days is divided amongst the collaborating countries,

All countries

Country	Requested days	Requested in %	Allocated days	Allocated in %
AR	5.01	0.06	3.39	0.09
AT	65.31	0.84	37.22	1.00
AU	88.19	1.14	37.26	1.00
BE	45.20	0.58	15.77	0.42
BG	0.35	0.00	0.35	0.01
BR	18.93	0.24	7.55	0.20
BW	2.00	0.03	1.67	0.04
CA	28.03	0.36	5.83	0.16
CH	221.89	2.86	129.72	3.48
CN	24.67	0.32	4.00	0.11
CY	0.67	0.01	0.00	0.00
CZ	100.02	1.29	36.35	0.98
DE	1264.93	16.31	620.34	16.65
DK	53.60	0.69	18.73	0.50
EG	1.00	0.01	0.00	0.00
ES	273.17	3.52	160.46	4.31
ESRF	48.41	0.62	27.61	0.74
FI	39.83	0.51	16.25	0.44
FR	1186.43	15.30	536.75	14.40
GB	1389.80	17.92	764.37	20.51
GR	4.00	0.05	0.00	0.00
HU	22.13	0.29	11.97	0.32
IL	7.33	0.09	3.67	0.10
ILL	1298.42	16.74	654.71	17.57
IN	109.09	1.41	34.92	0.94
IR	0.83	0.01	0.00	0.00
IT	505.10	6.51	213.72	5.74
JP	64.02	0.83	23.67	0.64
KR	16.00	0.21	0.00	0.00
LV	11.67	0.15	0.00	0.00
MX	3.60	0.05	3.40	0.09
NL	42.53	0.55	28.85	0.77
NO	1.60	0.02	0.00	0.00
PL	36.20	0.47	20.92	0.56
PT	7.60	0.10	0.80	0.02
RO	11.74	0.15	8.87	0.24
RU	146.47	1.89	85.21	2.29
SE	117.88	1.52	61.35	1.65
SI	3.33	0.04	1.00	0.03
SG	2.00	0.03	2.00	0.05
SK	10.67	0.14	8.00	0.21
TH	8.00	0.10	0.00	0.00
US	444.97	5.74	134.48	3.61
ZA	6.25	0.08	5.25	0.14
Total	7754.25	100.00	3726.4	100.00

Table 1a: Distribution amongst the different countries of beamtime requested and allocated in 2010 during the Subcommittees of the Scientific Council.

and weighted by the number of people for each country. Local contacts are not counted as proposers except when they are members of the research team.

In **table 1b**, the beamtime requested by and allocated to scientists from ILL, ESRF or EMBL is allocated to the member countries according to a weighting system based on the fractional membership of the country of the institute concerned. When a proposal involves collaboration with a non-member country, the allocated time is attributed entirely to the collaborating member country (or countries), and weighted by the number of people for each member country. Proposals for which all proposers are from non-member countries therefore do not appear in this table.

Table 1b: Distribution amongst the Associate and scientific-member countries of beamtime requested and allocated in 2010 during the Subcommittees of the Scientific Council. Poland does not appear in the table because it rejoined ILL on 1st July 2010.

Only member countries				
Country	Requested days	Requested in %	Allocated days	Allocated in %
AT	118.71	1.59	56.56	1.55
BE	55.76	0.75	21.23	0.58
CH	296.59	3.97	163.13	4.46
CZ	110.18	1.48	40.51	1.11
DE	1869.06	25.03	910.15	24.89
DK	57.03	0.76	21.27	0.58
ES	367.73	4.92	209.80	5.74
FR	1806.97	24.20	817.97	22.37
GB	1996.08	26.73	1056.87	28.91
HU	30.63	0.41	15.88	0.43
IT	591.81	7.92	255.82	7.00
SE	153.90	2.06	77.46	2.12
SK	13.93	0.19	9.53	0.26
Total	7468.37	100.00	3656.10	100.00

A more complete view of beamtime use is given in **table 2**. Request and allocation of beamtime as well as the number of scheduled experiments refer to standard submissions to the subcommittee meetings. The effective number of days given to our users takes into account also Director's Discretion Time and CRG time for CRG instruments.

INSTRUMENT PERFORMANCE

Table 2 also gives a summary of instrument performance for 2010. For each cycle, a record is kept of any time lost from the total available beamtime and the reasons for the lost time are analysed for all the instruments. The table gives a global summary for the year.

Overall 3753 days were made available to our users in 2010 on ILL and CRG instruments, which represents about 81 % of the total days of operation. 187 days were used by ILL scientists to carry out their own scientific research. About 8 % of the total beamtime available on the ILL instruments is allowed for tests, calibrations, scheduling flexibility, minor breakdowns recuperation and student training.

Beam days delivered for science in 2010 amount to 3940 (used for users and internal research).

A total of 740 experiments were scheduled. During 2010 the reactor operated for 3 cycles, representing 150 days of neutrons (see § Reactor Operation, p.102).

In 2010, 322 out of 4660 days were lost due to various malfunctions, which represent less than 7 % of the total available beamtime. The breakdown by reasons for beamtime losses is shown in **figure 4b**.

Detailed comments on the larger beamtime losses (above 25 days) are as follows:

- IN4 lost about 60 days because of the failure of the new Fermi chopper rotor during its commissioning and of the same chopper electronics later in the year.
- One of the two GAMS spectrometers (GAMS-4) was not operational for one cycle: the instrument was dismantled to allow the installation of the new GAMS-6.
- PN1 lost 45 days because the cabling of new vacuum interlocks - by an external company - was completed well after the contractual delivery date.

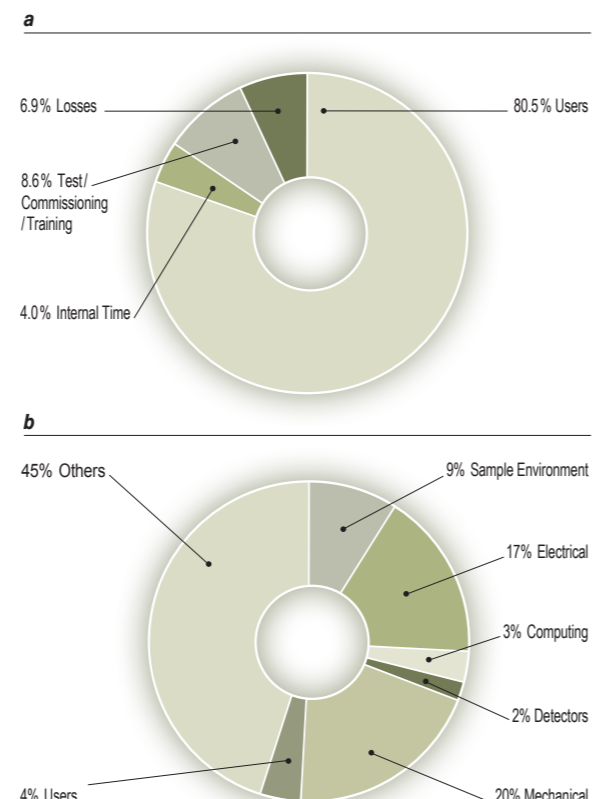


Figure 4: (a) Use of ILL beamtime (b) Reasons for beamtime losses.

Instrument	Days requested	Days allocated*	Number of scheduled experiments	Available days	Days used for users**	Days lost	Days for commissioning /test/training	Days for internal research
SuperADAM	36	39	6	119	86	8	18	7
BRISP	151	44	5	119	87	5	27	0
D10	259	127	15	119	115	3	0	1
D11	234	109	59	119	91	13	15	0
D15	16	37	5	119	102	9	4	4
D16	230	116	24	119	107	1	7	4
D17	207	109	34	119	89	1	19	10
D19	190	130	16	119	93	0	22	4
D1A	28	25	9	45	34	4	2	5
D1B	63	63	23	119	100	1	14	4
D20	290	95	44	119	103	5	5	6
D22	352	84	41	119	97	1	19	2
D23	73	42	6	119	101	5	13	0
D2B	221	105	52	119	107	2	7	3
D3	116	88	10	119	91	6	6	16
D4	141	60	14	68	63	1	4	0
D7	104	84	12	119	94	0	19	6
D9	253	113	16	119	100	3	14	2
FIGARO	196	83	30	119	89	2	28	0
IN1	82	34	8	51	35	0	15	1
IN10	116	100	13	119	102	2	2	13
IN11	248	104	14	105	94	1	3	7
IN12	94	25	4	69	55	2	5	7
IN13	149	53	8	119	77	8	29	5
IN14	299	120	18	119	100	7	3	9
IN15	283	71	9	119	101	5	7	6
IN16	305	118	22	119	91	13	11	4
IN20	330	125	19	119	103	3	6	7
IN22	102	42	5	119	111	7	1	0
IN4	230	112	26	119	48	68	3	5
IN5	266	120	32	119	101	3	9	6
IN6	263	129	32	119	107	3	9	0
IN8	229	111	17	119	106	1	11	1
LADI	310	92	10	69	64	1	2	2
PF1B	285	138	11	119	111	8	0	0
PF2/nb set-up	191	132	10	138	122	0	8	6
PN1	233	109	12	119	70	45	4	0
PN3/Gams4+5	246	194	10	188	97	64	3	24
S18	58	22	3	119	107	3	7	2
SALSA	120	95	18	119	97	1	13	8
VIVALDI	130	101	17	119	105	7	7	0
Total	7754	3726	740	4660	3753	322	401	187
Percentage of the total available beamtime					80.5%	6.9%	8.6%	4.0%

* 'days allocated' refers to only those days reviewed by the subcommittees (i.e., excluding CRG days and DDT).

** 'days used' refers to the total number of days delivered to users (i.e., including CRG days for CRGs and DDT).

PF2 consists of different set-ups where several experiments are running simultaneously. The values given are averages for these positions. D4 and IN1 share the same beam port and cannot be run simultaneously.

Table 2: Beamtime request/allocation (via standard subcommittees and DDT together) by instrument and instrument performance. CRG instruments are in green.

Instruments list - December 2010

ILL instruments

D1A (50%)	powder diffractometer	decommissioned in summer 2010
D2B	powder diffractometer	operational
D3	single-crystal diffractometer	operational
D4 (50% with IN1)	liquids diffractometer	operational
D7	diffuse-scattering spectrometer	operational
D9	single-crystal diffractometer	operational
D10	single-crystal diffractometer	operational
D11	small-angle scattering diffractometer	operational
D16	small momentum-transfer diffractometer	operational
D17	reflectometer	operational
D19	single-crystal diffractometer	operational
D20	powder diffractometer	operational
D22	small-angle scattering diffractometer	operational
FIGARO	horizontal reflectometer	operational
IN1 (50% with D4)	three-axis spectrometer	operational
IN4	time-of-flight spectrometer	operational
IN5	time-of-flight spectrometer	operational
IN6	time-of-flight spectrometer	operational
IN8	three-axis spectrometer	operational
IN10	backscattering spectrometer	operational
IN11	spin-echo spectrometer	operational
IN14	three-axis spectrometer	operational
IN16	backscattering spectrometer	operational
IN20	three-axis spectrometer	operational
PF1	neutron beam for fundamental physics	operational
PF2	ultracold neutron source for fundamental physics	operational
PN1	fission product mass-spectrometer	operational
PN3 - GAMS	gamma-ray spectrometer	operational
SALSA	strain analyser for engineering application	operational
VIVALDI	thermal neutron Laue diffractometer	operational

CRG instruments

SuperADAM	reflectometer	CRG-B operational
BRISP	Brillouin spectrometer	CRG-B operational
CRYO EDM	installation for the search of the neutron electric dipole moment	CRG-C operational
D1B	powder diffractometer	CRG-A operational
D15	single-crystal diffractometer	CRG-B decommissioned in december 2010
D23	single-crystal diffractometer	CRG-B operational
GRANIT	gravitation state measurement	CRG under construction
IN12	three-axis spectrometer	CRG-B operational
IN13	backscattering spectrometer	CRG-A operational
IN22	three-axis spectrometer	CRG-B operational
S18	interferometer	CRG-B operational

Jointly funded instruments

LADI (50%)	Laue diffractometer	operational with EMBL
IN15	spin-echo spectrometer	operational with FZ Jülich and HZB Berlin

Test and characterisation beams

CT1, CT2	detector test facilities
CYCLOPS	Laue diffractometer
TOMOGRAPHY	neutrography
OrientExpress	Laue diffractometer
T3	neutron optics test facility
T13A, C	monochromator test facility
T17	cold neutron test facility

INSTRUMENT LAYOUT 2010

The IN5 multitube position-sensitive detectors.

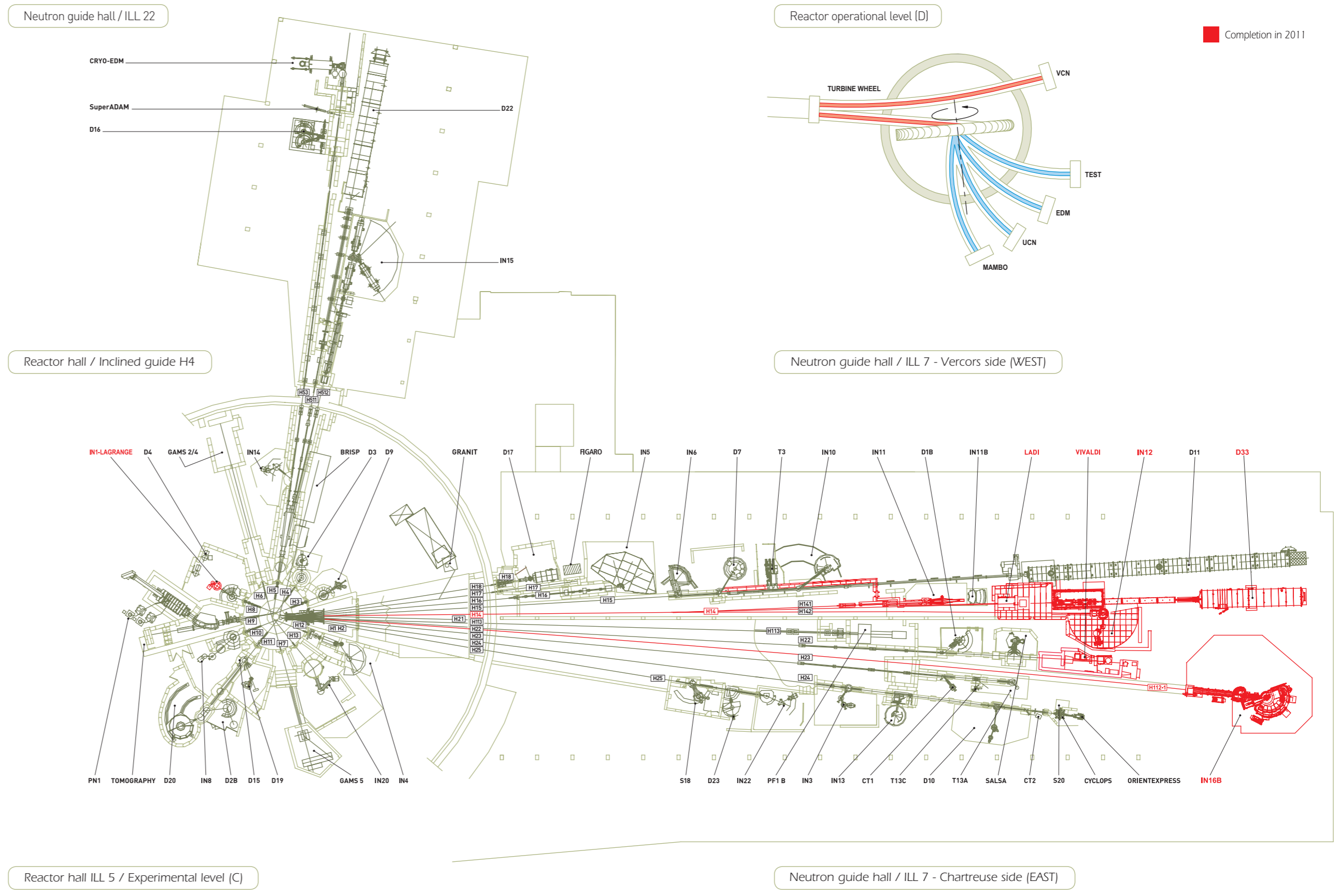
Instruments list - December 2010

ILL instruments		
D1A (50%)	powder diffractometer	decommissioned in summer 2010
D2B	powder diffractometer	operational
D3	single-crystal diffractometer	operational
D4 (50% with IN1)	liquids diffractometer	operational
D7	diffuse-scattering spectrometer	operational
D9	single-crystal diffractometer	operational
D10	single-crystal diffractometer	operational
D11	small-angle scattering diffractometer	operational
D16	small momentum-transfer diffractometer	operational
D17	reflectometer	operational
D19	single-crystal diffractometer	operational
D20	powder diffractometer	operational
D22	small-angle scattering diffractometer	operational
FIGARO	horizontal reflectometer	operational
IN1 (50% with D4)	three-axis spectrometer	operational
IN4	time-of-flight spectrometer	operational
IN5	time-of-flight spectrometer	operational
IN6	time-of-flight spectrometer	operational
IN8	three-axis spectrometer	operational
IN10	backscattering spectrometer	operational
IN11	spin-echo spectrometer	operational
IN14	three-axis spectrometer	operational
IN16	backscattering spectrometer	operational
IN20	three-axis spectrometer	operational
PF1	neutron beam for fundamental physics	operational
PF2	ultracold neutron source for fundamental physics	operational
PN1	fission product mass spectrometer	operational
PN3 - GAMS	gamma-ray spectrometer	operational
SALSA	strain analyser for engineering application	operational
VIVALDI	thermal neutron Laue diffractometer	operational

CRG instruments		
SuperADAM	reflectometer	CRG-B operational
BRISP	Brillouin spectrometer	CRG-B operational
CRYO EDM	installation for the search of the neutron electric dipole moment	CRG-C operational
D1B	powder diffractometer	CRG-A operational
D15	single-crystal diffractometer	CRG-B decommissioned in december 2010
D23	single-crystal diffractometer	CRG-B operational
GRANIT	gravitation state measurement	CRG under construction
IN12	three-axis spectrometer	CRG-B operational
IN13	backscattering spectrometer	CRG-A operational
IN22	three-axis spectrometer	CRG-B operational
S18	interferometer	CRG-B operational

Jointly funded instruments		
LADI (50%)	Laue diffractometer	operational with EMBL
IN15	spin-echo spectrometer	operational with FZ Jülich and HZB Berlin

Test and characterisation beams	
CT1, CT2	detector test facilities
CYCLOPS	Laue diffractometer
TOMOGRAPHY	neutrography
OrientExpress	Laue diffractometer
T3	neutron optics test facility
T13A, C	monochromator test facility
T17	cold neutron test facility



■ Completion in 2011

REACTOR OPERATION

REACTOR OPERATION

This ILL High Flux Reactor (HFR) produces the most intense neutron flux in the world: 1.5×10^{15} neutrons per second per cm^2 , with a thermal power of 58.3 MW.

The main moderator is the ambient D_2O coolant surrounding the core which delivers intense beams of thermal neutrons to 11 beamlines and to four neutron guides. A graphite hot source operating at 2400 K delivers hot neutrons - energies up to 1 eV and wavelengths down to 0.3 Å - to 3 beamlines.

Two liquid deuterium cold sources at 25 K deliver cold neutrons - energies down to 200 μeV and wavelengths up to 20 Å - to some 17 instruments. An ultra-cold neutron source fed from the top of one of the cold sources delivers neutrons vertically through the reactor pool to 5 instruments on the operational floor of the reactor.

The reactor operates 50-day cycles, with each cycle of operation followed by a shutdown period during which the fuel element is changed and a number of checks are carried out. Occasional longer shutdowns allow for equipment maintenance. There are normally 4 reactor cycles per year - when the maintenance programme allows it -, supplying 200 days of neutron flux for scientific use.

The ILL reactor usually operates four 50-day cycles per year, producing 200 days of beamtime for the experimental programme

As part of the ILL's determination to guarantee the safety and reliability of its facilities over future years, the Reactor Division runs a 'key reactor components programme', the aim of which is to ensure the development and replacement as necessary of the essential main components of the reactor. The current plans under this programme cover the period up to 2016.

The Laue diffractometer LADI.

Cycle no.	Start of cycle	End of cycle	Number of days of operation	Number of days of scheduled	Number of unscheduled shutdowns
158	15/06/10	30/07/10	45	50	1
159	26/08/10	19/09/10	24	50	1
160	28/10/10	17/12/10	50	50	0
Total			119	150	2

Only 3 cycles were planned in 2010, and overall 119 days of scientific activity were provided.

We lost less than one week during the first cycle due to the unexpected radioactivity of the H11 plug. The second cycle was unfortunately interrupted because the static bearing of one pump - needed in case of loss of coolant - broke. As a consequence, a filtering of the primary circuit was necessary, which was carried before out the restart of the third cycle, during which the reactor ran impeccably.



The new anti-turbulence grid.

The exceptionally long 2010 winter shutdown was used to carry out an important maintenance programme and to perform a number of major operations, such as:

- the replacement of the reactor anti-turbulence grid and the fuel element holder
- the replacement of two safety rods and the V7 vertical channel
- the installation of the gaseous decay tank
- the H11 shielding and collimation plug maintenance
- the installation of the new Drac river water intake filters
- the refurbishment of the cold sources helium compressors control system
- the ILL now ensures environmental monitoring for the Institute and the CEA's (the French nuclear organisation) nuclear activities.

The Key Reactor Components Programme continues

The ILL continues to invest in the Key Reactor Components Programme (KRC) designed to ensure the long-term safety and reliability of the Reactor till 2030. The aim is to upgrade or replace a number of key components. Work on this started in 2005 and our plans now extend to 2016, to be fully prepared for the next ten-yearly safety review by the nuclear authorities.

A Project Management Committee is now in charge of controlling the schedule, the budget and the organisation of the KRC programme.

The operations performed this year include, amongst others, the installation of important safety systems as part of our reactor safety plan (the ultimate core reflood system and the seismic depressurisation circuit).

The AG3NET aluminium alloy supply progressed very well and allowed us to order the fabrication of spare beam tubes, which will be replaced in the near future.



Addition of nitrogen on a gamma spectrometer in the environmental laboratory.

Operations foreseen during the 2011 winter shutdown

The long 2011 winter shutdown will be used to perform a number of important operations, such as:

- the replacement of the H10 beam tube (feeding IN8)
- the removal of the IH4 beam tube (feeding D15, now dismantled)
- the replacement of two safety rods
- the maintenance of the control rod mechanism, the vacuum relief valve and natural convection dampers
- the replacement of heavy water pumps
- the recabling of the motor of a primary pump.

Radioactive waste and effluents

The ILL's activities in 2010 generated waste and effluents respecting the regulatory limits applicable to our installation, as follows:

Evacuation of radioactive waste	Quantity
Decay bin (60 l)*	8
5 m ³ pre-concreted crate (low and intermediate level waste)	0
5 m ³ crate (low and intermediate level waste)	0
200 l drums of "incineratable" (laboratory waste)	0
HDPE drums 120 l (laboratory waste)	7
30 l cylinders (liquid)	3

* Waste stocked in these decay bins is still quite active and requires several years of interim storage before meeting ANDRA's specifications for processing as intermediate-level waste.

Gaseous effluents	Released in 2010 (TBq)
Tritium	7.8
Rare gas	0.74
Carbone-14	0.46
Iodine	0.0000034
Aerosols	0.000000095

Liquid effluents	Released in 2010 (TBq)
Tritium	0.24
Carbone-14	0.00021
Iodine	0.0000011
Other activation products	0.000077

MORE THAN SIMPLY NEUTRONS



The backscattering spectrometer IN16.

SCIENTIFIC SUPPORT LABORATORIES
FUTURE DEVELOPMENTS OF THE EPN-CAMPUS
TRAINING

In order to maintain their ranking on the international scene, European research institutes must optimise their resources and develop synergies at every level.

The ILL is firmly committed not only to build high-performance instruments but also to offer the best scientific environment to the user community and it has established successful collaborations with neighbouring institutes over the years. After the successful Partnership for Structural Biology and the Materials Science Support Laboratory, we have now launched a Partnership for Soft Condensed Matter. In parallel, the ILL and the ESRF have been working on plans to transform our joint site into a research campus – the **European Photon and Neutron science campus**, or **EPN-campus for short** - with a truly international reputation.

In addition, the ILL has teamed up with the other institutes located on the *Polygone scientifique* science park (where our Institute is located) for the GIANT partnership, a project which aims to develop our neighbourhood into a world-class science and technology park.

The ILL is firmly committed not only to build high-performance instruments but also to offer the best scientific environment to the user community

In the light of the essential role played by PhD students in its scientific life, the ILL has decided to raise the total number of PhD grants. The new ILL PhD programme aims at promoting four scientific fields: nanoscience, soft condensed matter, biology and magnetism. However, the award of a grant depends essentially on the quality of the proposals and high quality proposals from other fields are of course also considered.

Scientific support laboratories

Partnership for Structural Biology

The Partnership for Structural Biology (PSB) contains a powerful set of technology platforms that are contributed by the various partner institutes (ILL, ESRF, EMBL, IBS, and the unit for host-pathogen interactions). These platforms include advanced capabilities that complement the powerful neutron scattering facilities available to ILL users: synchrotron X-rays, electron microscopy, NMR, high-throughput methods (soluble expression and crystallisation), and a range of biophysical techniques such as isothermal calorimetry and surface plasmon resonance. A joint SANS/SAXS platform is being developed and there is also an initiative to develop a joint X-ray/neutron low resolution crystallography capability. The aim of the PSB is to enhance the interdisciplinary capabilities of each of the facilities co-located on the site. Further details are provided on its website <http://www.psb-grenoble.eu/>

Deuteration Laboratory

Of particular interest to ILL's biology users is the ILL-EMBL Deuteration Laboratory (D-Lab). The aim of the platform is to provide a focus for European scientists wishing to make their own deuterated materials for neutron scattering or NMR experiments. The D-Lab has had a decisive impact on biological neutron scattering globally, now imitated at other institutes for neutron scattering around the world. Closer to home, it plays a key role for the ILL user community, now implicated in 40% of successful proposals for beam-time for experiments on biological systems. More information is given at: <http://www.ill.eu/sites/deuteration/>

Materials Science Support Laboratory

The joint ILL-ESRF Materials Science Support Laboratory provides a range of support to our users in engineering materials science, from advice with experimental proposals to advanced sample metrology. In particular, the Laboratory works with users to optimise the experimental methodology before the start of an experiment. This takes the form of standardised specimen mounting, digitisation of samples, definition of measurement macros and liaising with the

instrument responsible. It is recommended that users arrive at the ILL a day or two prior to the start of an experiment to enable these off-line preparations to be performed. More information may be found on the MSSS's website <http://www.ill.eu/sites/mssl/>

Partnership for Soft Condensed Matter

The recently-established Partnership for Soft Condensed Matter (PSCM) will allow users to characterise samples before their experiments at both the ILL and ESRF and will facilitate the performance of complementary *in situ* measurements. By early 2013, the PSCM will be able to host 20 to 30 scientists and technicians working in the laboratories and office space of the new Science Building of the joint ESRF/ILL campus. In these laboratories, scientists will prepare experiments with highly complex self-assembled and non-equilibrium soft matter systems which cannot be easily transported to Grenoble. Many materials related to nanotechnologies, life sciences, environment and renewable energy are, in fact, soft matter systems. Users wishing to use the facility in conjunction with neutrons or synchrotron radiation measurements should indicate this when submitting their request for beamtime. Further details can be found at <http://www.ill.eu/instruments-support/labs-facilities/pscm/>

Computation-Laboratory

The Computation-Laboratory (C-Lab) offers support to ILL users for atomistic simulations using classical and *ab initio* methods. Typical applications for simulations are structure, magnetism and phonons in crystals and liquid/glass structure and dynamics. As samples become more complex, simulations can provide key, complementary information that will help to interpret experimental data and understand how systems behave. Scientists and thesis students at the ILL benefit from the software, hardware and expertise of the C-Lab and users can benefit via their local contacts. In order to improve access to simulations for users, they are now able to request simulation support for their neutron scattering experiments on the official ILL proposal forms by ticking the appropriate box. For more information see <http://www.ill.eu/instruments-support/computing-for-science/home/>

Future developments of the EPN-campus

The ILL and ESRF have launched an ambitious project to extend the facilities already offered by our international site, the newly-established **European Photon and Neutron science campus, or EPN-campus** for short (www.epn-campus.eu).

The new scientific and technological installations will be complemented by other more general improvements, such as the new Science Building, a new site entrance, a despatch and reception platform, a bigger restaurant and internal roadways.

Under the French *Contrat de Projets entre l'Etat et la Région*, significant funding is available for projects in our Rhône-Alpes region. Additional funding will also be granted through ESFRI, the European Strategy Forum on Research Infrastructures.

The ILL 20/20 project

ILL 20/20 is part of the European Strategy Forum for Research Infrastructures (ESFRI) Road Map, the European Commission's strategic initiative to develop the scientific integration of Europe and to strengthen its international outreach.

The mission of ESFRI is to support a coherent and strategy-led approach to policy-making on research infrastructures and to facilitate multilateral initiatives leading to the better use and development of research infrastructures in Europe.

Assisted by EU infrastructure funding, the ILL 20/20 project has a budget of 171 M€. It focuses on the maintenance of key neutron source components, the construction of instruments and other infrastructures and aims to boost the average efficiency of the ILL instruments by a factor of more than 10.



The new Science Building, to be built by September 2012 on the EPN science campus.



The extension of the ILL7 guide hall - which is now 118m long - was completed on 8 November, right on schedule.

Grenoble and the future

The Grenoble metropolitan authorities have launched an ambitious development plan, the GIANT partnership (Grenoble Isère Alpes Nano Technologies), aiming to reinforce links between education, research and industry to foster the technological breakthroughs that will be the economic drivers of the future. GIANT's aim is to respond to major challenges confronting our society today, such as communication technologies, renewable energies and environmental problems, bioscience and human health.

GIANT hosts leading European laboratories - the ESRF light source, the ILL neutron source and the EMBL for molecular biology - major French research institutions - CEA and CNRS - and highly innovative institutions from the academic world - Grenoble Ecole de Management (Grenoble EM), Grenoble Institute of Technology (Grenoble INP) and the University Joseph Fourier (UJF). These eight institutions have joined forces, driven by a common goal: to become one of the world's top campuses in research, higher education, and technology transfer to industry.

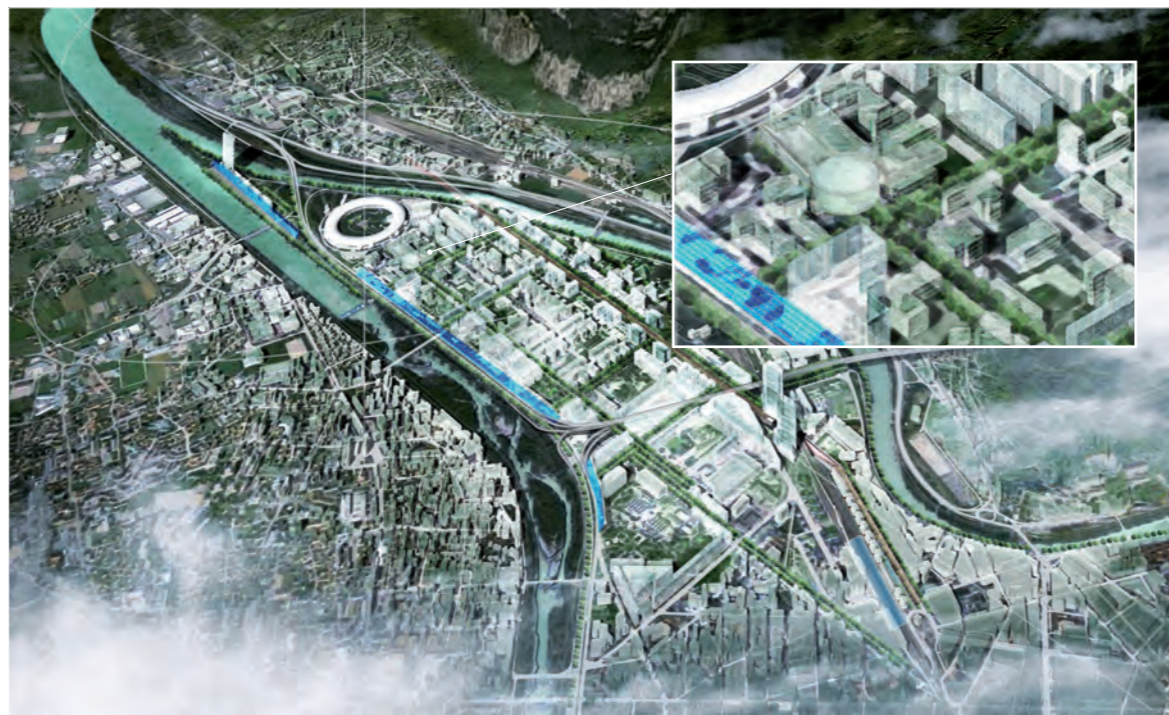
The city's two main hives of intellectual activity, the university campus and the *Polygone Scientifique* science park where ILL has its home, are to benefit from a major redevelopment programme.

A sizeable portion of the city's surface area is to be transformed in what is one of France's top five urban development initiatives. The changes to come will have a major and highly beneficial social impact on the science park as a whole, and our users will be amongst the happy beneficiaries.

The *Polygone Scientifique* is to be developed both in economic terms - to multiply the links between research and industry - and through major replanning - by bringing the *Polygone* closer to the city centre via improved transport and housing infrastructure. As a consequence, the ILL will be linked to the town centre via a new tramline by 2013.

From a scientific point of view, the project will be based on specialised activity clusters. The laboratory and university structures in the fields of biotechnology or energy, for example, will be relocated together to improve the potential for synergy and the links with industrial partners. The ILL will also benefit from the pooling of local skills and resources.

Architect's view of the Grenoble peninsular project for 2020
© CEA/Grenoble/Vasconi.



Training

The ILL PhD programme

Through the new ILL PhD programme, our student body has grown in strength over recent years, and now numbers 35 students of many different nationalities, wholly or partially supported by the ILL. In the last call for proposals for PhD projects, 40 proposals were submitted, of which 9 projects were selected and subsequently students were recruited. Six of these students have already started their PhD work at the ILL and the other three will do so early in 2011.

Since the students work in different disciplines, their **annual clip session** gives them the opportunity to exchange new ideas and to get to know one another better. The 2010 clip session on 19 April once again challenged the students to present their work in five minutes. This event was entertaining as ever, with some presenting about their levitating samples as fast as their mouths could go, and others attempting to discuss all the data from their thesis in the given time.

Throughout the year the PhD student representatives also organise **student seminar sessions**, which prove invaluable

for both practising talking in front of a friendly audience, and discovering more about the work of other students.

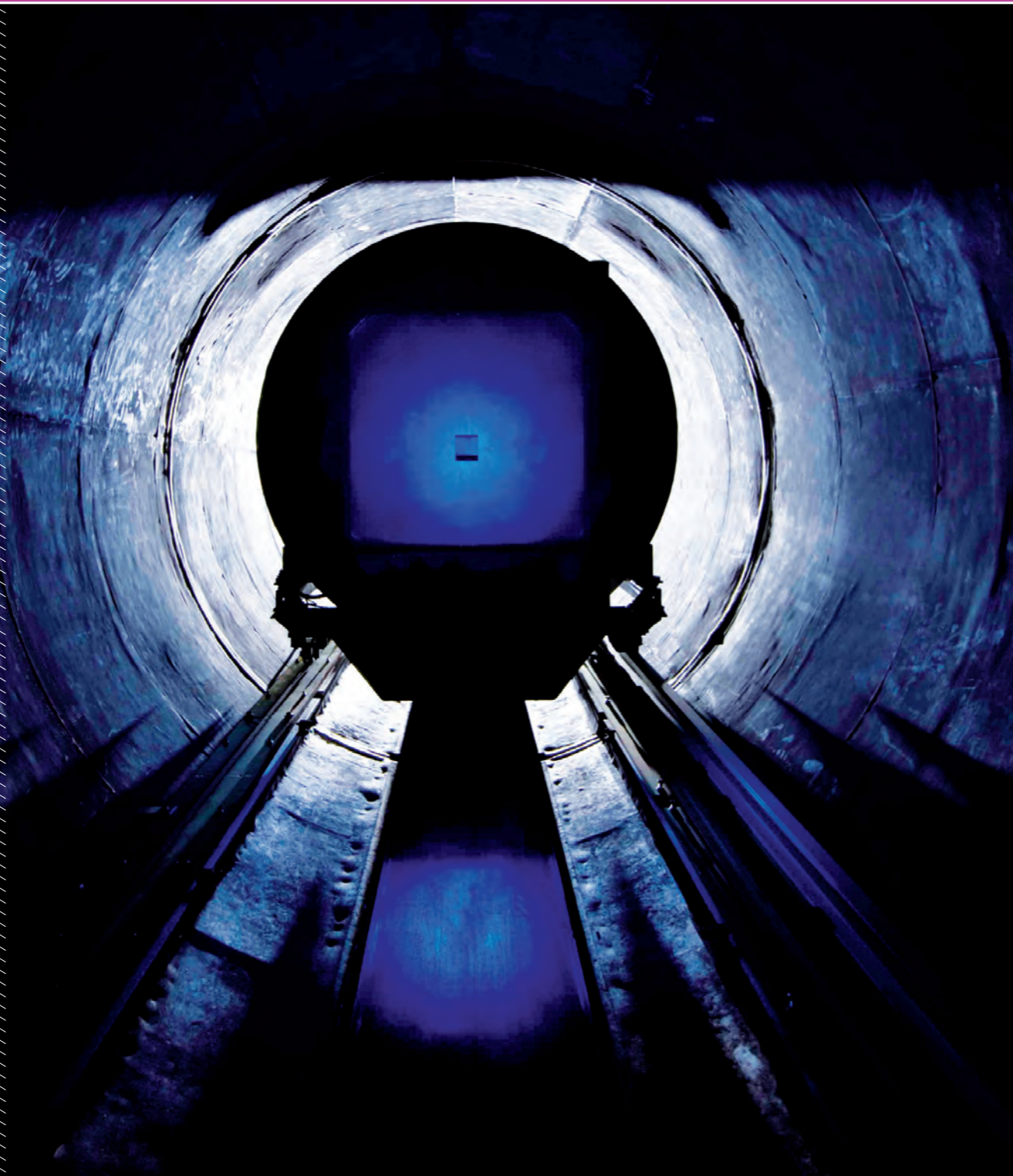
In 2010, the students were also given a brilliant **lecture course** - organised by Garry McIntyre - which spanned all areas of neutron science, and left them all much wiser.

TP CESIRE

2010 also saw a significant strengthening of the ties between the ILL and the Grenoble universities. After having signed an agreement in 2008 with University Joseph Fourier of Grenoble (UJF) to establish two *Associate Professorship Chairs for Large-scale facilities* (one for the ILL and one for the ESRF), the ILL has now agreed with UJF to offer interested master and PhD students the opportunity to take part in real neutron scattering experiments within the framework of the so called **TP CESIRE**. Coordinated by Arno Hiess and thanks to the number of ILL scientists interested in this project, experiments with appropriate topics and experimental set-up are constantly selected for this purpose. Seventeen UJF master students participated since autumn 2010 in seven TP CESIRE performed on both ILL and CRG instruments.



The ILL PhD students during their clip session on 19 April.



The detector and vacuum tube of the small-angle scattering instrument D11.

**ILL workshops
and schools in 2010**

20 January

MAM2010, Membranes and molecules - Symposium
in honour of Peter Timmins and Roland May
<http://www.ill.eu/news-events/past-events/2010/mam2010/>

26 - 30 January

Flipper 2010, Workshop on Single-Crystal Diffraction
with Polarised Neutrons
<http://www.ill.eu/news-events/past-events/2010/flipper-2010/>

14 - 19 February

GRANIT 2010, Les Houches
<http://www.ill.eu/news-events/past-events/2010/granit-2010/>

3 - 5 March

CONFIT 2010, Dynamics in confinement
<http://www.ill.eu/news-events/past-events/2010/confit2010/>

17 - 19 March

NOP 2010, International Workshop on Neutron Optics,
Alpe d'Huez
<http://www.ill.eu/news-events/past-events/2010/nop2010/>

2 - 7 May

FullProf School 2010
<http://www.ill.eu/news-events/past-events/2010/fpschool-2010/>

7 August

QFS2010, Quantum Fluids and Solids, Satellite workshops at ILL
<http://www.ill.eu/news-events/past-events/2010/qfs-2010-and-its-satellite-workshops/>

15 - 17 September

ILL2020 Vision User Meeting
<http://www.ill.eu/news-events/past-events/2010/ill2020/>

21 - 23 October

SENSE 2010 Superconductivity Explored
by Neutron Scattering Experiments
<http://www.ill.eu/news-events/past-events/sense2010/>

25 - 26 October

SuperADAM: advanced neutron reflectometry
for solving questions related to the physics and chemistry
of thin films, interfaces, and nanostructures
<http://www.ill.eu/news-events/past-events/superadam/>

Short reports on the ILL workshops can be found in the ILL News
for Reactor Users (June and December 2010 issues)
<http://www.ill.eu/top-links/publications/ill-news/>

ILL chronicle 2010

16 January

Public exhibition 'GIANT'

24 February

Visit of Prof. Jerzy Szwed,
Deputy Minister of the Polish Ministry of Science and Higher Education

5 March

Meeting of the Directors of all major neutron facilities

25 - 26 March

Hercules XX, a symposium celebrating the 20th anniversary of Hercules,
the Higher European Research Course for Users of Large Experimental Systems

13 - 16 April

Meetings of the ILL Scientific Council and its Subcommittees

29 - 30 April

Meeting of the Subcommittee on Administrative Questions (SAQ).

4 June

Celebration of the CPER projects
(science building, site entrance and extension of the restaurant)

24 - 25 June

Meeting of the Steering Committee in Saclay (Paris)

15 - 17 September

ILL2020 Vision User Meeting

21 September

Visit of the board of Directors of the Los Alamos National Laboratory

25 September

ILL Family Day

19 - 22 October 2009

Meetings of the ILL Scientific Council and its Subcommittees

21 - 27 October

ILL stand at the French Science Festival

16 November

Visit of the Spanish National Research Council (CSIC)

28 - 29 October

Meeting of the Subcommittee on Administrative Questions (SAQ)

1 - 2 December

Meeting of the Steering Committee in Grenoble

Visits & events

The Directors of all major neutron facilities from Europe, the US, Australia, Japan and China gathered at the ILL on 5 March 2010.



Richard Wagner, the ILL director, welcomes Pr. Jerzy Szwed on his arrival at ILL.



ILL welcomes a delegation of the Spanish National Research Council on 16 November 2010: José Luis Martínez (ILL Associate Director, first from the right) and Javier Campo (Zaragoza University, second from the left) accompany Prof. Carmen Peláez Martínez (Vice-president) and Prof. José Vicente García Ramos (Deputy), on a visit to the ILL reactor.



In January 2011, India signed up with the ILL for four years. In the picture, representatives of our new partner (the Bhabha Atomic Research centre) meet the ILL management.

French Science Festival & ILL family Day

French Science Festival.



ILL family Day.

Happy users

"Where there's a wheel - There's a way".
Virginia Garcia (from Tekniker, Spain)
on SALSAs measuring stress profiles
in a train's wheel.



Matthew Dunstan and Chris Ling
(Sydney University) on OrientExpress.



From left to right: David Chisnal
and Holly Hedgeland (Cavendish Lab, Cambridge)
with Peter Fouquet (ILL) on IN11.



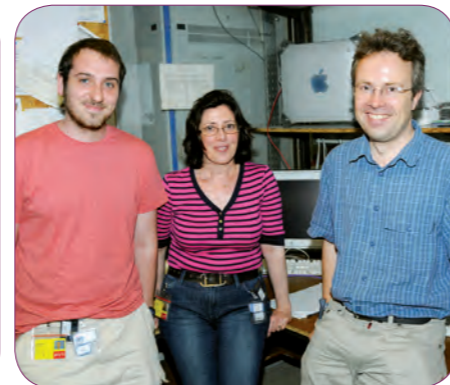
From left to right: Emma Sparr, Tommy Nylander,
and Agnes Michanek (Lund University) with Hanna Wacklin during
their experiment on RNA-lipid interactions on FIGARO.



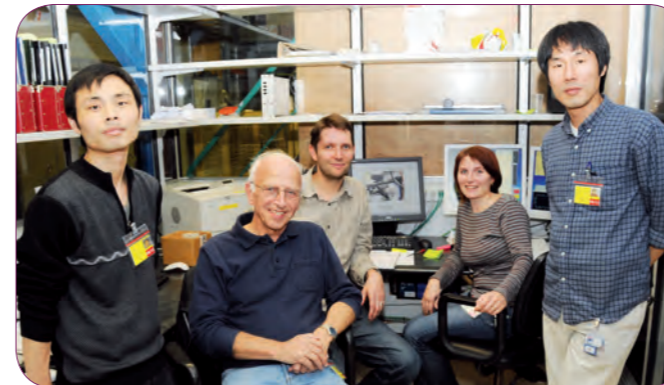
From right to left: Colin Broholm (John Hopkins University, US),
Dimitri Argyriou (HZB, Berlin), Wei Bao (Renmin University, China)
with Arno Hiess (ILL) on IN3, preparing the experiments on Fe(Te/Se)
(see p.12).



Enjoying a little break from their experiment on PF2 (from the left):
Thomas Brenner (ILL), Christian Siemens, Christian Düsing, Christian Plonka-Spehr,
Sybille Komposch (University of Mainz), Christian Pruner (University of Salzburg)
and Jürgen Klepp (University of Vienna).



From the left: Gregor Sneddon and Valeria Arrighi
(University Heriot-Watt, Edinburgh)
with Tilo Seydel (ILL) on IN10, during a very
successful experiment on the dynamics
of strongly hydrogen-bonded polymer blends.



From left to right (front): Mengjun Xue, Gerhard Findenege
and Tae-Gyu Shin (TU Berlin) during their experiment on D16.
At the back, the instrument responsables, Bruno Demé
and Viviana Cristiglio.



From left to right: Imre Varga (Elte TTK University, Budapest)
with the ILL team, Richard Campbell, David Bowyer and Ralf Schweins,
during a joint FIGARO/D11 experiment.

User support

Philippe Dercapentrie purging a closed cycle cryostat.



Simon Wood plumbing in the cooling circuit for the solid/liquid sample cells for FIGARO.

Alain Daramsy on D20, cooling down the cryostat equipped with the new 4GPa Paris-Edinburgh pressure press.



Gilles Rignon during his "ronde" in the experimental halls.



Philippe Chevalier on IN20, cooling down the cryostat.

Passing it on

Here is a small selection of the many changes in personnel in 2010

Katja Mayer-Jenkins retired after 34 years of loyal service to the ILL (amongst which 32 in the User Office). Alison Mader (former secretary in the Science Division) joined the SCO team.



Peter Timmins retired in January this year. Robert Cubitt (former ILL scientist) is now the new Head of the Large-Scale Structure Group.

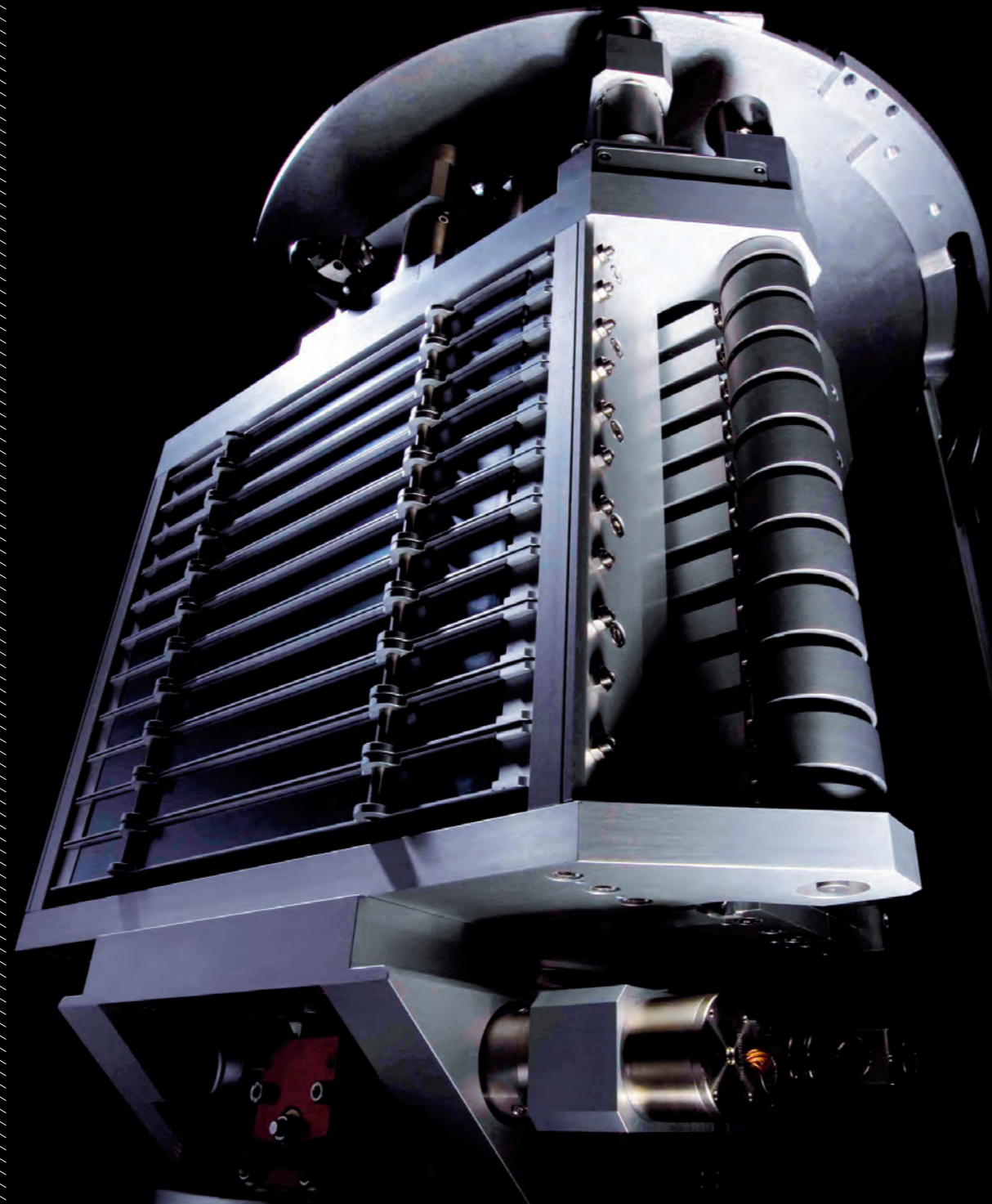
Garry McIntyre - ILL senior fellow - moved to ANSTO (Australia), where he got a position as Research Leader in hard condensed matter.



Ken Andersen - Head of the Neutron Optics Service - left the ILL in September and joined the ESS team in Lund. He has been replaced by Pierre Courtois (former Head of the Monochromator Group).

Barbara Standke retired in July. She worked as personal assistant to six ILL Directors.





The new double-focusing monochromator for the hot-neutron instruments IN1 and D4.

FACTS AND FIGURES ORGANISATION CHART

2010 was again a busy year during which the ILL's Administrative Division conducted a host of interesting and challenging projects

Important milestones included the updating of the ILL Statutes and the completion of preparatory work for the renewal of the ILL's Intergovernmental Convention, both of which involved a dedicated working group of representatives of the Associates. The year also saw the drafting and signing of a large number of contracts in a variety of areas: scientific collaborations, scientific grants, the renewal of CRG contracts and commercial contracts.

The first phase of the the "Jobs, skills and recognition" project - which aims to improve career perspectives for ILL staff - was brought to a successful close with the finalisation of 60 job profiles covering each of the jobs present at the Institute, including the core responsibilities for each of these profiles. The next phase was launched at the end of 2010 and involves defining the skills associated with each job profile.

Negotiations on the revision of a number of major points in the ILL Collective Agreement, which expired on 6 January 2011, were also conducted in 2010. The human resources service and ILL's top and middle management were closely involved in conducting these changes, contributing to the drafting and communicating of proposals. Amongst the major topics addressed were a new scheme for salary advancements and regrading, and a redefinition of the conditions for retirement and early retirement (CAA).

A major step forward achieved by the Administration Division in 2010 was the introduction of changes in the way in which the ILL will be audited in the future. For the first time in the ILL's history, the annual accounts from 2011 onwards will be audited exclusively by external statutory auditors appointed by the Steering Committee. The Audit Commission, which will no longer be an organ of the Association, will continue to perform special audits at the request of the Steering Committee or the Management, or at its own initiative.

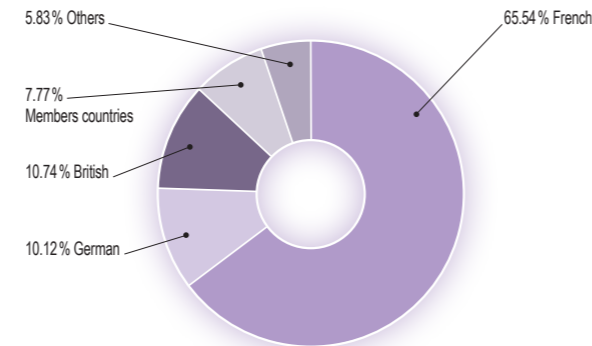
Industrial return, which helps to provide the ILL with the best products and services at an optimal price, was improved thanks to efforts to develop procurement opportunities in different countries. As these improvements remain uneven from one country to another, further efforts will be needed in the future to improve the national balance.

Work within the framework of the *Contrat de Projets Etat-Region* (CPER) project, which involves both the ILL and ESRF, progressed well. This contract provides for financial contributions from the regional and local authorities and the city of Grenoble for the modernisation of the **European Photon and Neutron science campus**, or EPN-campus for short, on which the ILL, among others, is located. In particular, the final design studies were completed for the construction of the Science Building, which will accommodate chemistry labs, a partnership for soft condensed matter and other laboratories. The coordination of views between the ESRF and ILL and the identification of possible savings on this project in the context of the budget reductions announced for both institutes are important milestones that were achieved in 2010.

STAFF

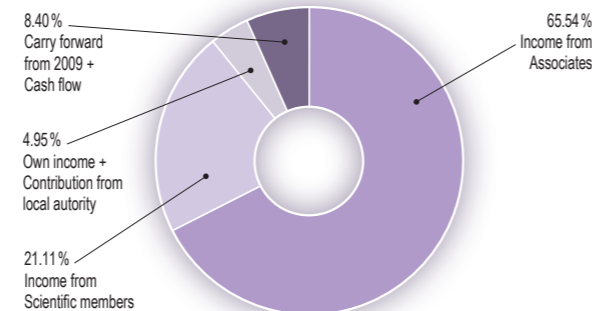
- 489 people including 66 experimentalists in the scientific sector and 28 thesis students
- 320.5 French, 49.5 German, 52.5 British, 38 from Scientific Member countries and 28.5 from others.

Staff on 31/12/2010		%
French	320.5	65.54
German	49.5	10.12
British	52.5	10.74
Scientific Members	38	7.77
Others	28.5	5.83
Total	489	100

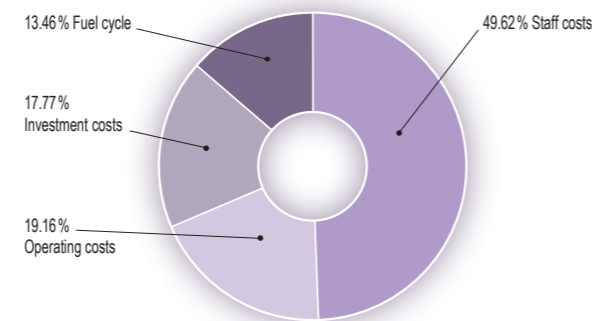


BUDGET 2010: 88.5M€ (excluding taxes)

Income	M€	%
Income from Associates	57.989	65.54
Income from Scientific Members	18.680	21.11
Own income + Contribution from local authority	4.380	4.95
Carry forward from 2009 + Cash flow	7.433	8.40
Total	88.481	100

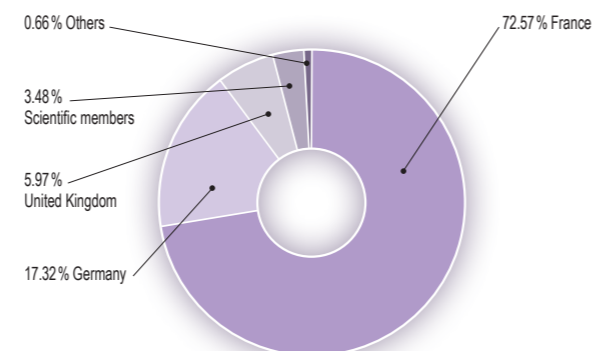


Expenditure	M€	%
Staff costs	43.900	49.62
Operating costs	16.950	19.16
Investment costs	15.724	17.77
Fuel cycle	11.907	13.46
Total	88.481	100



DISTRIBUTION OF ILL PURCHASES

Income	M€	%
France	19,06	72.57
Germany	4,55	17.32
United Kingdom	1,567	5.97
Scientific Members	0,913	3.48
Others	0,173	0.66
Total	26.263	100
French captive market	10,36	-
Total captive / non captive	36.623	-



NAME
Institut Max von Laue - Paul Langevin (ILL)

FOUNDED
17 January 1967. International Convention signed until 31 December 2013.

ASSOCIATES
France
Commissariat à l'Energie Atomique (CEA)
Centre National de la Recherche Scientifique (CNRS)

Germany
Forschungszentrum Jülich (FZJ)

United Kingdom
Science & Technology Facilities Council (STFC)

COUNTRIES WITH SCIENTIFIC MEMBERSHIP

Spain
Ministerio de Ciencia e Innovación (MICINN)

Switzerland
Staatssekretariat für Bildung und Forschung (SBF)

Italy
Consiglio Nazionale delle Ricerche (CNR)

CENI (Central European Neutron Initiative)
Consortium, composed of:
- Austria: Österreichische Akademie der Wissenschaften
- Czech Republic: Charles University of Prague
- Hungary: Research Institute for Solid State Physics and Optics on behalf of the Hungarian Academy of Sciences (MTA)
- Slovak Republic: Comenius University Bratislava

BELPOLSWENI (the Belgian-Polish-Swedish Consortium)
- Belgium: Belgian Federal Science Policy Office (BELSPO)
- Sweden: Swedish Research Council (SRC)
- Poland: Polish Academy of Sciences

Denmark
Danish Agency for Science, Technology and Innovation
Interim scientific membership 01/07/2009 - 30/06/2011

India (from 1 January 2011)
Bhabha Atomic Research Centre (BARC)
Interim scientific membership 01/01/2011 - 31/12/2012

SUPERVISORY AND ADVISORY BODIES

- Steering Committee, meeting twice a year
- Subcommittee on Administrative Questions, meeting twice a year
- Audit Commission, meeting once a year
- Scientific Council with 9 Subcommittees, meeting twice a year

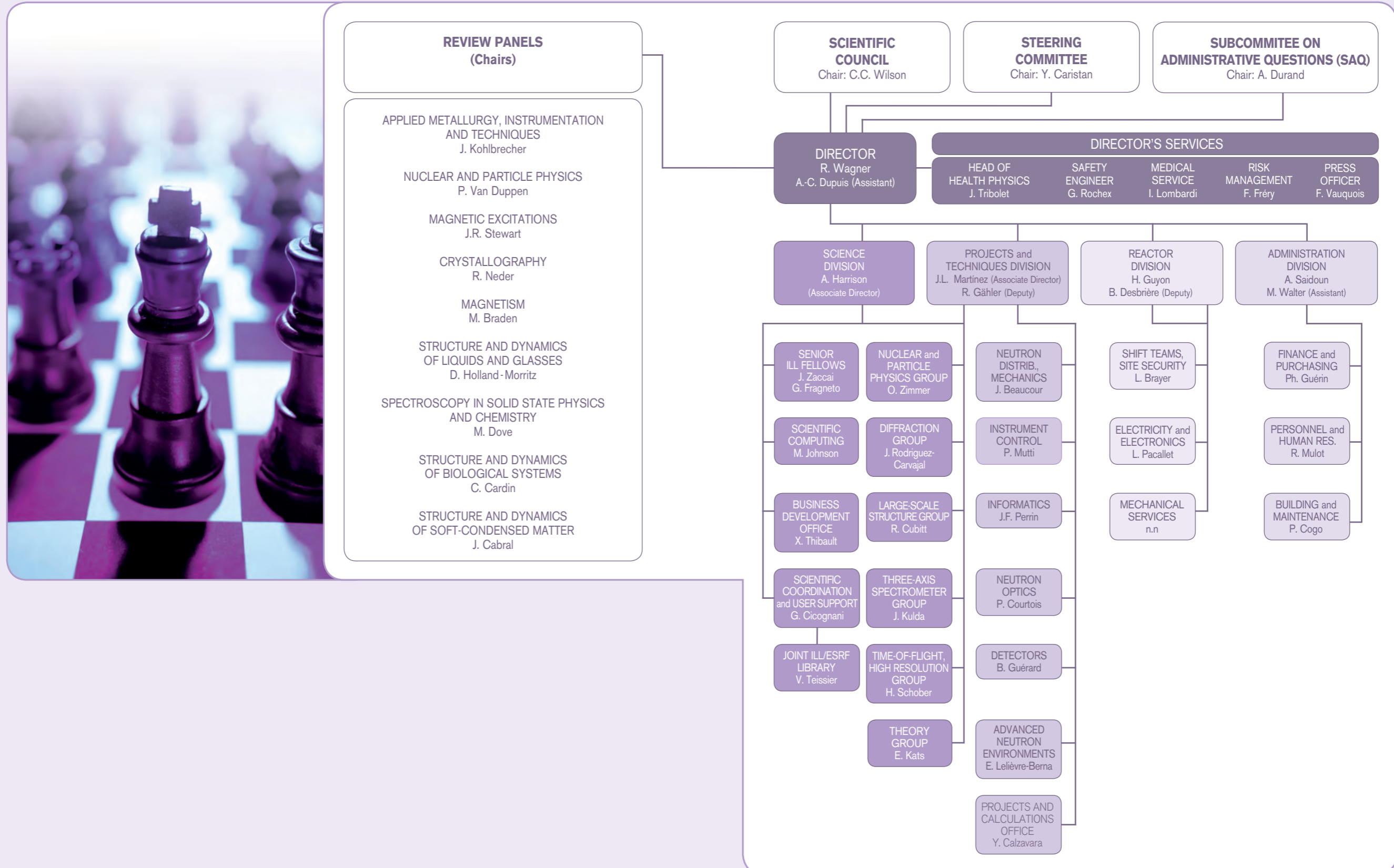
REACTOR

- 58 MW, running 3 cycles in 2010 (with cycles of 50 days)

EXPERIMENTAL PROGRAMME

- 740 experiments (allocated by subcommittees) on 28 ILL-funded and 10 CRG instruments
- 1056 visitors coming from 35 countries
- 1142 proposals submitted and 670 accepted

Organisation chart - December 2010



Publications

In 2010, the ILL received notice of 652 publications by ILL staff and users

The distribution by subject is as follows:

Applied physics, instrumentation and techniques	36
Materials science and engineering	48
Theory	21
Nuclear and particle physics	61
Magnetic excitations	50
Crystallography	119
Magnetic structures	88
Liquids and glasses	22
Spectroscopy in solid state physics and chemistry	49
Biology	52
Soft matter	106

ILL PhD studentships

PhD students at ILL in 2010	35
PhD theses completed in 2010	6

